CHARACTERIZATION AND MODELING OF THERMO-MECHANICAL FATIGUE CRACK GROWTH IN A SINGLE CRYSTAL SUPERALLOY

A Dissertation
Presented to
The Academic Faculty

By

Benjamin Scott Adair

In Partial Fulfillment
Of the Requirements for the Degree
Doctor of Philosophy in the
George W. Woodruff School of Mechanical Engineering

Georgia Institute of Technology

August, 2013

CHARACTERIZATION AND MODELING OF THERMO-MECHANICAL FATIGUE CRACK GROWTH IN A SINGLE CRYSTAL SUPERALLOY

Approved by:

Dr. W. Steven Johnson, Co-Advisor
School of Materials Science and Engineering, George W. Woodruff School of Mechanical Engineering
Georgia Institute of Technology

Dr. Stephen D. Antolovich, Co-Advisor
School of Materials Science and Engineering, George W. Woodruff School of Mechanical Engineering
Georgia Institute of Technology

Dr. Richard W. Neu
George W. Woodruff School of Mechanical Engineering, School of Materials Science and Engineering
Georgia Institute of Technology

Dr. Shuman Xia
George W. Woodruff School of Mechanical Engineering
Georgia Institute of Technology

Dr. Julian Rimoli
Daniel Guggenheim School of Aerospace Engineering
Georgia Institute of Technology

Date Approved: June 26, 2013

ACKNOWLEDGMENTS

I owe much thanks to my advisors Dr. Steve Johnson and Dr. Stephen Antolovich for their extensive guidance throughout this project. I have learned more than I ever imagined from their continual support and mentoring. Additionally, I would like to thank Dr. Richard Neu, Dr. Shuman Xia and Dr. Julian Rimoli for being on my committee, reviewing my work and providing their technical insight.

Without the financial support of Pratt & Whitney this research would have never been possible, and for that I am greatly appreciative. I am also extremely grateful for project direction and technical oversight provided by Dr. Alexander Staroselsky, Shawn Gregg, Venkat Seetharaman and Keith Kersey.

The support provided by fellow graduate students Matt O'Rourke, Vince Barker, Patxi Fernandez-Zelaia and Mike Hirsch was immeasurable and much appreciated. I am also much indebted to research engineer JD Huggins for all of his help with experimental set-ups and keeping the equipment running. Finally, I would also like to express my sincere gratitude to my family and friends; they have continually given me the support I needed to be successful in graduate school.

TABLE OF CONTENTS

ACKNOWLEDGMENTS iii

LIST OF TABLES vii

LIST OF FIGURES viii

LIST OF SYMBOLS AND ABBREVIATIONS xvi

SUMMARY xix

CHAPTER 1: INTRODUCTION 1

1.1: Motivation 1
1.2: Research Objectives 6
1.3: Dissertation Overview 8

CHAPTER 2: LITERATURE REVIEW AND BACKGROUND 10

2.1: History of Superalloys 10
2.2: History of Single Crystal Ni-Base Superalloys PWA1480 and PWA1484 12
2.3: Superalloys Composition, Microstructure and Processing 13
2.3.1: Composition 13
2.3.2: Microstructure 15
2.3.3: Processing 20
2.4: Mechanical Properties of Superalloys 23
2.5: History of Fatigue Life Prediction 27
2.5.1: Stress-Life Approach 27
2.5.2: Strain-Life Approach 28
2.5.3: Fracture Mechanics Approach 29
2.5.4: Crack tip Stresses and Strains Approach 34
2.6: Fatigue Crack Service Life Prediction Methodologies 37
2.6.1: Safe-Life (Life-to-First-Crack) 37
2.6.2: Damage-Tolerant (Retirement for Cause) 38
2.6.3: Equivalent Initial Flaw Size 39
2.7: Thermo-Mechanical Fatigue Behavior of Superalloys 41

2.7.1: Fatigue Crack Initiation 41
2.7.2: Fatigue Crack Propagation 42
2.7.3: Effect of Microstructure on Propagation Rates 44
2.7.4: Effect of Environment on Propagation Rates 48
2.7.5: Effect of Operating Conditions on Propagation Rates 53
2.7.6: Effect of Crystal Orientation on Propagation Rates 57

CHAPTER 3: EXPERIMENTAL METHODS 59

3.1: Material 59
3.2: Specimens 62
3.2.1: Specimen Design 62
3.2.2: Specimen Uniform Stress vs. Uniform Displacement 65
3.2.2: Specimen Preparation 73
3.3: TMF and Monotonic Testing 75
3.3.1: Thermo-Mechanical Fatigue Crack Growth Test Equipment 76
3.3.2: Monotonic and Cyclic Round Bar Test Equipment 81
3.3.3: Inert Environment Test Equipment 82
3.3.4: Testing Standards 86
3.4: Secondary Orientation Using Metallography 88
3.5: SEM Crystallographic Plane Measurement Technique 89
3.6: Crack Growth Non-Interaction Modeling 90

CHAPTER 4: EXPERIMENTAL RESULTS 93

4.1: Material Analysis 93
4.2: Secondary Orientation Determination 96
4.3: Monotonic and Cyclic Property Determination 101
4.4: Isothermal Constant Amplitude Testing 110
4.4.1: Effect of Secondary Orientation 111
4.4.2: Effect of Temperature 115
4.4.3: Effect of R-Ratio 118
4.4.4: Effect of Environment 122
4.5: Aged Microstructure Testing 124
4.6: Temperature Interaction Testing 128
4.7: Load Interaction Testing 134
4.8: Semi-Realistic Spectrum Testing 145

CHAPTER 5: CRACK SURFACE MORPHOLOGY 158

5.1: Isothermal Constant Amplitude Crack Surface Morphology 159
5.2: Temperature and Load Interaction Crack Surface Morphology 166
5.3: Crack Surface Morphology Mapping 170

CHAPTER 6: MODELING 175

6.1: Crack Path Trajectory 176
6.2: Crack Plane Determination Via SEM 180

CHAPTER 7: CONCLUSIONS, RESEARCH SIGNIFICANCE AND RECOMMENDATIONS FOR FUTURE WORK 184

7.1: Conclusions 184
7.1.1: Isothermal Constant Amplitude Conclusions 184
7.1.2: Temperature Interaction Conclusions 185
7.1.3: Load Interaction Conclusions 185
7.1.4: Semi-Realistic Spectrum Conclusions 186
7.1.5: Crack Surface Morphology 186
7.1.6: Overall Conclusions 186
7.2: Research Significance 187
7.3: Recommendations for Future Work 188

APPENDIX 191

A.1: Procedure for cold-mounting, grinding, polishing, and etching 192
A.2: Initial TMF Test Rig Startup Tasks 193
A.3: TMF Test Procedure Setup and Initialization 194
A.4: TMF Test Rig Shutdown Procedure 195
A.5: Semi-Realistic Spectrum #1 Loads and Temperatures 196
A.6: Semi-Realistic Spectrum #2 Loads and Temperatures 198
A.7: Semi-Realistic Spectrum #3 Loads and Temperatures 200

REFERENCES 201

LIST OF TABLES

Table 2.1: Some Compositions of Wrought Superalloys [14] 14

Table 2.2: Some Compositions of Cast Superalloys [14] 14

Table 2.3: Compositions of Second Generation Single Crystal Superalloys [11] 15

Table 2.4: Number of Active Slip Systems by Crystallographic Orientation 26

Table 3.1: Material Orientation Details for 24 Fatigue Crack Growth Specimens and 12 Tensile Specimens 60

Table 3.2: Material Orientation Details for 14 Tensile Specimens 60

Table 3.3: Material Orientation Details for 30 Fatigue Crack Growth Specimens 61

Table 3.4: Comparison of Sent Specimen Correction Factors 69

Table 4.1: PWA1484 Nominal Chemical Composition in Weight Percent 93

Table 4.2: PWA1484 Uncontrolled Slab Primary and Secondary Orientations 100

Table 4.3: Temperature, Strain Rate and Strain Range for Monotonic and Cyclic Testing 101

Table 4.4: PWA1484 Slow and Fast Yield Strength Values 106

Table 4.5: PWA1484 Slow and Fast Modulus Values 106

LIST OF FIGURES

Figure 1.1: Turbine Blades in the (a) Polycrystalline, (b) Directionally Solidified and (c) Single Crystal Forms [1] 2

Figure 1.2: Schematic of a Basic Turbojet Gas Turbine Engine [3] 3

Figure 1.3: Schematic of a Basic Turbofan Gas Turbine Engine [3] 3

Figure 1.4: Turbofan Engine Blade Failure: (Bottom) Fractured Blade Toot (Top) Perforated Engine Nacelle [7] 5

Figure 2.1: Increase of Turbine Entry Temperature TET Made Possible by Gains in Alloy and Manufacturing Technologies [14] 12

Figure 2.2: PWA1484 Microstructure: (a) Dendrites Along with Interdendritic Regions (b) Cuboidal γ' Phase in γ Matrix Material [24] 16

Figure 2.3: Distribution of the γ' Phase in a Polycrystalline Superalloy [25] 17

Figure 2.4: Crystal Structure of Ni_3Al γ' Showing the Distribution of Aluminum and Nickel Atoms 18

Figure 2.5: Microstructure and XRD Results of a Single Crystal Superalloy with <001> Orientation [26] 19

Figure 2.6: Schematic of Dendrite Side Branching Directions [26] 19

Figure 2.7: The Production of Turbine Blade Alloys by Investment Casting [11] 21

Figure 2.8: Different Types of Grain Selectors for Use during Investment Casting [11] 22

Figure 2.9: Details of the Starter Block and Pig-Tail Grain Selector from the Trent 800 High-Pressure Turbine Blade Casting [11] 23

Figure 2.10: Yield Stress as a Function of Temperature for Single Crystal Superalloys [11] 25

Figure 2.11: Creep Performance as a Function of Crystallographic Orientation for Mar-M247 [41] 26

Figure 2.12: S-N Curve Showing the Effect of Surface Condition on the Fatigue Life of Steel [45] 28

Figure 2.13: Strain-Life Curve Showing Strain Range Versus Cycles to Failure [50] ... 29

Figure 2.14: The Three Different Crack Tip Loading Modes: K_I, K_{II} and K_{III} [56]..... 30

Figure 2.15: Constant Amplitude Crack Growth Data 31

Figure 2.16: Three Regions of Crack Growth Rate 32

Figure 2.17: Derivation of the Material Design Curve and Predicted Safe Cyclic Life [81]..... 38

Figure 2.18: Schematic Representation of the Retirement for Cause Approach Where Inspections Are Used to Extend Damage Tolerance [81]..... 39

Figure 2.19: The Equivalent Initial Flaw Size Can Be Used as Starting Point for Probabilistic Life Prediction [85]..... 40

Figure 2.20: A Non-Crystallographic Fatigue Crack Initiation at a Micropore in PWA1480 [17]..... 42

Figure 2.21: A Crystallographic and Non-Crystallographic Fracture Initiated from a Micropore in PWA1484 [17]..... 44

Figure 2.22: Variation of the Creep Rupture Life of the Single-Crystal Superalloys TMS-75 and TMS-82+ as a Function of the Amount of γ' Phase [111]..... 47

Figure 2.23: Effect of Temperature on Crack Growth in IN100; R = 0.1, Frequency = 0.167 Hz [115]..... 49

Figure 2.24: Fatigue Crack Growth Rates in PWA1484 at Temperature from 27°C to 871°C [87]..... 51

Figure 2.25: Fatigue Crack Growth Rates in PWA1484 at R=0.1, R=0.5 and R=0.7 [87] 54

Figure 2.26: Effect of Overload Ratio (OLR) on Crack Growth in IN100; T = 649°C, R = 0.5, Freq = 0.167 Hz, CBO = 40 [115]..... 55

Figure 2.27: Effect of Number of Cycles Between Overloads (CBO) on Crack Growth in IN100; T = 649°C, R = 0.5, Freq = 0.167 Hz, OLR = 1.5 [115]..... 56

Figure 2.28: PWA1484 Fatigue Crack Growth Rates for <001>/<110> Loaded Specimens at 593°C, R=0.5 and 20Hz [147]..... 58

Figure 3.1: Cast Slabs for Single Edge Notch Specimen Laue Analysis, Showing Setup on Laue System..... 61

Figure 3.2: Cast Slabs for Single Edge Notch Specimen Laue Analysis, Showing Definitions of Beta, Delta, and Gamma..... 62

Figure 3.3: Single Edge Notch Tension Specimen with Dimensions..... 64

Figure 3.4: Round Bar Tensile Specimen with Dimensions 65

Figure 3.5: ABAQUS FEM For Uniform Stress (Left) and Uniform Displacement (Right) 66

Figure 3.6: FRANC2D SENT Specimen Crack Tip Mesh 67

Figure 3.7: FRANC2D Stress Intensity Factor as a Function of Crack Length 68

Figure 3.8: Comparison of Stress Intensity Factors for Uniform Stress and Uniform Displacement Conditions 70

Figure 3.9: Comparison of Correction Factors Calculated Using the Boundary Force Method [151] 71

Figure 3.10: Comparison of Uniform Stress and Uniform Displacement Correction Factors for a SENT Specimen 72

Figure 3.11: Thermocouple Placement in the Center of the Specimen Just Below the Crack Path 75

Figure 3.12: Semi-Realistic Fighter Jet Flight Spectrum Showing Cyclic Mechanical and Thermal Loading [115] 76

Figure 3.13: MTS Load Frame Used for Thermo-Mechanical Fatigue Testing 78

Figure 3.14: Water Cooled Pyramid Teeth Wedges 79

Figure 3.15: Ambrell Hotshot 3.5 kW Induction Heater (Left) and Heating Station (Right) 79

Figure 3.16: Specimen in Test Rig Showing Unique Coil Design and Twin Cooling Fans 80

Figure 3.17: Monotonic Tensile Specimen in Test Rig Showing Coil Design and High-Temperature Axial Extensometer Placement 82

Figure 3.18: Acrylic and Silicone Inert Environment Chamber 83

Figure 3.19: Ultra High Purity Argon Tanks with High Precision Low Flow Regulator 84

Figure 3.20: OXIGRAF Fast Oxygen Analyzer 85

Figure 3.21: Inert Environment TMF Test Set-Up 86

Figure 3.22: X, Y and Z Faces of Single Edge Notch Tension Specimen for Metallographic Inspection 88

Figure 3.23: Mounted Specimens after Grinding, Polishing and Etching 89

Figure 3.24: SEM and Cross Product Approach to Determining Crystallographic Fracture Planes 90

Figure 3.25: MATLAB Code and Paris Coefficients and Exponents used for Non-Interaction Fatigue Crack Growth Modeling 92

Figure 4.1: Fully Heat Treated PWA1484 Microstructure Showing Cuboidal γ' Precipitates on the Order of 0.4 μm 94

Figure 4.2: Fully Heat Treated PWA1484 Microstructure Showing High Volume (>0.60) Fraction of Precipitate 95

Figure 4.3: PWA1484 Slab 23831 Secondary Dendritic Orientation 96

Figure 4.4: PWA1484 Slab 23832 Secondary Dendritic Orientation 96

Figure 4.5: PWA1484 Slab 23833 Secondary Dendritic Orientation 97

Figure 4.6: PWA1484 Slab 23834 Secondary Dendritic Orientation 97

Figure 4.7: PWA1484 Slab 23835 Secondary Dendritic Orientation 97

Figure 4.8: PWA1484 Slab 23836 Secondary Dendritic Orientation 98

Figure 4.9: PWA1484 Slab 23838 Secondary Dendritic Orientation 98

Figure 4.10: PWA1484 Slab 23843 Secondary Dendritic Orientation 98

Figure 4.11: PWA1484 Slab 23844 Secondary Dendritic Orientation 99

Figure 4.12: PWA1484 Slab 23845 Secondary Dendritic Orientation 99

Figure 4.13: PWA1484 Slab 23847 Secondary Dendritic Orientation 99

Figure 4.14: PWA1484 Slab 23848 Secondary Dendritic Orientation 100

Figure 4.15: Stress Strain Curves under Slow and Fast Strain Rates for PWA1484 102

Figure 4.16: Stress Strain Curves Under Fast Strain Rates for PWA1484 103

Figure 4.17: Stress Strain Curves Under Slow Strain Rates for PWA1484 104

Figure 4.18: PWA1484 Yield Strength as a Function of Temperature [164] 105

Figure 4.19: PWA1484 Modulus as a Function of Temperature [164] 106

Figure 4.20: PWA1484 Cyclic Stress Strain Curves at 649°C 107

Figure 4.21: PWA1484 Cyclic Stress Strain Curves at 816°C 108

Figure 4.22: PWA1484 Cyclic Stress Strain Curves at 982°C 108

Figure 4.23: PWA1484 Strain Life Results for 649°C, 816°C and 982°C 109

Figure 4.24: PWA1484 Fatigue Crack Growth Rates for All Isothermal Constant Amplitude Tests 112

Figure 4.25: PWA1484 Fatigue Crack Growth Rates for Uncontrolled Secondary Orientation Isothermal Constant Amplitude Tests 113

Figure 4.26: PWA1484 Fatigue Crack Growth Rates for Controlled Secondary Orientation Isothermal Constant Amplitude Tests 114

Figure 4.27: PWA1484 Fatigue Crack Growth Rates for R Ratio=0.7 Constant Amplitude Tests 116

Figure 4.28: PWA1484 Fatigue Crack Growth Rates for R Ratio=0.1 Constant Amplitude Tests 117

Figure 4.29: PWA1484 Fatigue Crack Growth Rates for 649°C Constant Amplitude Tests 119

Figure 4.30: PWA1484 Fatigue Crack Growth Rates for 816°C Constant Amplitude Tests 120

Figure 4.31: PWA1484 Fatigue Crack Growth Rates for 982°C Constant Amplitude Tests 121

Figure 4.32: PWA1484 Fatigue Crack Growth Rates for 982°C Argon Constant Amplitude Tests 123

Figure 4.33: PWA1484 Fatigue Crack Growth Rates for 649°C, R=0.1 Aged Microstructure Constant Amplitude Tests 126

Figure 4.34: PWA1484 Fatigue Crack Growth Rates for 649°C, R=0.7 Aged Microstructure Constant Amplitude Tests 127

Figure 4.35: Temperature Interaction Testing Between 649°C and 982°C Schematic . 128

Figure 4.36: Temperature Interaction Testing Between 649°C and 982°C for 1, 10 and 100 Alternating Cycles at R=0.1 Along with Non-Interaction Predictions 130

Figure 4.37: Temperature Interaction Testing Between 649°C and 982°C for 20 and 50 Alternating Cycles at R=0.1 Along with Non-Interaction Predictions 131

Figure 4.38: Temperature Interaction Testing Between 649°C and 982°C for 1, 10 and 100 Alternating Cycles at R=0.7 Along with Non-Interaction Predictions 132

Figure 4.39: Temperature Interaction Testing Between 649°C and 982°C for 20 and 50 Alternating Cycles at R=0.7 Along with Non-Interaction Predictions 133

Figure 4.40: Overloads Were Applied Every 800 Cycles During Load Interaction Testing 135

Figure 4.41: 1.3x Overload Testing at 649°C, 816°C and 982°C Along with Non-Interaction Predictions 136

Figure 4.42: 1.6x Overload Testing at 649°C, 816°C and 982°C Along with Non-Interaction Predictions 137

Figure 4.43: 2.0x Overload Testing at 649°C, 816°C and 982°C Along with Non-Interaction Predictions 138

Figure 4.44: 1.3 x Overload Testing at 982°C Along with Non-Interaction Prediction 139

Figure 4.45: 1.6x Overload Testing at 982°C Along with Non-Interaction Prediction. 140

Figure 4.46: 2.0x Overload Testing at 982°C Along with Non-Interaction Prediction. 141

Figure 4.47: 1.3x Overload Testing at 982°C Along with Non-Interaction Prediction Shifted Over 142

Figure 4.48: 1.6x Overload Testing at 982°C Along with Non-Interaction Prediction Shifted Over 143

Figure 4.49: 2.0x Overload Testing at 982°C Along with Non-Interaction Prediction Shifted Over 144

Figure 4.50: Fighter Jet Flight Spectrum Showing Cyclic Mechanical and Thermal Loading [115] 146

Figure 4.51: Two Hour Semi-Realistic Spectrum with Constant 1 Hz Cycling 147

Figure 4.52: Non-Interaction Prediction for Two Hour Semi-Realistic Spectrum with Constant 1 Hz Cycling 148

Figure 4.53: Two Hour Semi-Realistic Spectrum with Constant 1 Hz Cycling Test #1 149

Figure 4.54: Two Hour Semi-Realistic Spectrum with Constant 1 Hz Cycling Test #2 150

Figure 4.55: Non-Interaction Prediction for Two Hour Semi-Realistic Spectrum with Constant 1 Hz Cycling at 80% Load 151

Figure 4.56: Two Hour Semi-Realistic Spectrum with Constant 1 Hz Cycling Test #3 152

Figure 4.57: Two Hour Semi-Realistic Spectrum with Twenty One 1 Hz Loading Cycles and Dwell Time 153

Figure 4.58: 3.5 Minute Semi-Realistic Spectrum with Twenty One 1 Hz Loading Cycles 154

Figure 4.59: Non-Interaction Prediction for Spectrums with Twenty One Loading Cycles 155

Figure 4.60: Results for Twenty One Loading Cycle Spectrums with Crack Length Plotted as a Function of Time 156

Figure 4.61: Results for 21 Loading Cycle Spectrums with Crack Length Plotted as a Function of Number of Flights 157

Figure 5.1: PWA1484 Fracture Surface Displaying Wire EDM Notch, Crystallographic Pre-Cracking and Flat Fracture at 1 Hz, 982°C and R=0.1 160

Figure 5.2: PWA1484 Fracture Surface Displaying Crystallographic Pre-Cracking Composed Predominantly of γ' Shearing at 1 Hz, 982°C and R=0.1..... 161

Figure 5.3: PWA1484 Fracture Surface Displaying Flat Fracture Composed Predominantly of γ' Avoidance at 1 Hz, 982°C and R=0.1..... 162

Figure 5.4: PWA1484 Fracture Surface Displaying Flat Fracture Composed of γ' Avoidance with Some γ' Shearing Visible (indicated with arrows) at 1 Hz, 982°C and R=0.1..... 163

Figure 5.5: PWA1484 Fracture Surface Displaying Fast Fracture Region Composed of Crystallographic Cracking at 1 Hz, 816°C and R=0.1..... 164

Figure 5.6: PWA1484 Fracture Surface Displaying Flat Fracture Comprised of Fatigue Striations along with Crystallographic Cracking at 1 Hz, 649°C and R=0.7 165

Figure 5.7: PWA1484 Fracture Surface Displaying Flat Fracture with Snowflake Pattern Possibly Formed During Casting at 1 Hz, 649°C and R=0.7 166

Figure 5.8: PWA1484 Fracture Surface Displaying Temperature Striations Created During 50 Alternating Cycle Block Testing at 1 Hz, 649°C/982°C and R=0.7 167

Figure 5.9: PWA1484 Fracture Surface Displaying Different Sized γ' Created During 50 Alternating Cycle Block Testing at 1 Hz, 649°C/982°C and R=0.7..... 168

Figure 5.10: PWA1484 Fracture Surface Displaying Temperature Striations Created During 20 Alternating Cycle Block Testing at 1 Hz, 649°C/982°C and R=0.7 169

Figure 5.11: PWA1484 Fracture Surface Displaying Crystallographic Overload Regions Created During 2.0x Overload Testing at 1 Hz, 982°C and R=0.1 170

Figure 5.12: Octahedral and Cubic Planes Relative to Specimen Primary and Secondary Crystallographic Orientations [170] 171

Figure 5.13: Typical Fracture Surface Morphology for PWA1484 Testing at 1 Hz, 649°C to 982°C for R=0.1 and R=0.7 172

Figure 5.14: Fracture Surface Morphology Correlated to da/dN for 982°C and R=0.7 174

Figure 6.1: Crystallographic Fracture that Occurred Around a ΔK of 25MPa$\sqrt{m}$ Invalidating the Fatigue Crack Growth Rate Test Results..... 175

Figure 6.2: Assuming a Controlled Primary Orientation of [001] the Specimen Axes and Crystallographic Axes Can be Related by One Angular Measurement..... 177

Figure 6.3: Crack Path Trajectory Model Definitions for Vectors on the (111) Plane.. 177

Figure 6.4: Crack Path Trajectory Model Normal and Shear Stress Predictions for $(111)[0\bar{1}1]$ 179

Figure 6.5: Three Dimensional Elastic Anisotropic RSS Values for the Twelve Slip Systems as a Function of Theta [74]..... 180

Figure 6.6: PWA1484 Fracture Surface Displaying Crystallographic Cracking at 1 Hz, 816°C and R=0.7, Crack Plane Determination Point 1..... 181

Figure 6.7: PWA1484 Fracture Surface Displaying Crystallographic Cracking at 1 Hz, 816°C and R=0.7, Crack Plane Determination Point 2..... 182

Figure 6.8: PWA1484 Fracture Surface Displaying Crystallographic Cracking at 1 Hz, 816°C and R=0.7, Crack Plane Determination Point 3..... 183

LIST OF SYMBOLS AND ABBREVIATIONS

a	Crack Length
AES	Auger Electron Spectroscopy
APB	Anti-Phase Boundary
APBE	Anti-Phase Boundary Energy
ASTM	American Society for Testing and Materials
BFM	Boundary Force Method
BSE	Back-Scattered Electrons
C	Paris Equation Coefficient
CBO	Cycles between Overload
CT	Compact Tension
da/dN	Fatigue Crack Growth Rate (m per cycle)
Δa	Change in Crack Length
ΔK	Stress Intensity Range
DS	Directionally Solidified
E	Modulus of Elasticity
ESET	Eccentrically-Loaded Single Edge Tension
EDM	Electrical Discharge Machining
EDS	Energy-Dispersive X-ray Spectroscopy
EIFS	Equivalent Initial Flaw Size
ENSIP	Engine Structural Integrity Program
η	Efficiency
f(a/b)	Correction Factor
FCC	Face Centered Cubic
FCG	Fatigue Crack Growth
FCGR	Fatigue Crack Growth Rate
FCP	Fatigue Crack Propagation
FCPR	Fatigue Crack Propagation Rate
G	Energy Release Rate

γ	Gamma Phase Matrix of Superalloy
γ'	Strengthening Precipitate Phase
HIP	Hot Isostatic Pressing
K	Stress Intensity Factor
K_C	Fracture Toughness (Critical Stress Intensity Factor)
K_{IC}	Plane Strain Fracture Toughness
$K_{opening}$	Crack Opening Stress Intensity Factor
K_{max}	Maximum Stress Intensity Factor
K_I	Opening Stress Intensity Factor
K_{II}	In-Plane Shear Stress Intensity Factor
K_{III}	Out-of-Plane Shear Stress Intensity Factor
m	Paris Equation Exponent
n	Walker's Equation Exponent
N	Number of Cycles
NDI	Nondestructive Inspection
OAR	Oxygen Affected Region
OLR	Overload Ratio
π	Pi (3.1415926)
P/M	Powder Metallurgy
PLC	Portevin–Le Chatelier
PSCL	Predicted Safe Cycle Limit
R	Load Ratio
RFC	Retirement for Cause
SEM	Scanning Electron Microscopy
SENT	Single Edge Notch Tension
SWT	Smith-Watson-Topper
SIF	Stress Intensity Factor
σ	Remotely Applied Stress
S-N	Stress-Life
T	Temperature
TMF	Thermo-Mechanical Fatigue

TPNC	Transprecipitate Non-Crystallographic
UHV	Ultra-High Vacuum
XPS	X-ray Photoelectron Spectroscopy
XRD	X-ray Diffraction
<001>	Family of Primary Crystallographic Directions
[001]	A Primary Crystallographic Direction
{001}	Family of Crystallographic Planes

SUMMARY

Turbine engine blades are subjected to extreme conditions characterized by significant and simultaneous excursions in both stress and temperature. These conditions promote thermo-mechanical fatigue (TMF) crack growth which can significantly reduce component design life beyond that which would be predicted from isothermal/constant load amplitude results. A thorough understanding of the thermo-mechanical fatigue crack behavior in single crystal superalloys is crucial to accurately evaluate component life to ensure reliable operations without blade fracture through the use of 'retirement for cause' (RFC).

This research was conducted on PWA1484, a single crystal superalloy used by Pratt & Whitney for turbine blades. Initially, an isothermal constant amplitude fatigue crack growth rate database was developed, filling a void that currently exists in published literature. Through additional experimental testing, fractography, and modeling, the effects of temperature interactions, load interactions, oxidation and secondary crystallographic orientation on the fatigue crack growth rate and the underlying mechanisms responsible were determined. As is typical in published literature, an R Ratio of 0.7 displays faster crack growth when compared to R = 0.1. The effect of temperature on crack growth rate becomes more pronounced as the crack driving force increases. In addition secondary orientation and R Ratio effects on crack growth rate were shown to increase with increasing temperature. Temperature interaction testing between 649°C and 982°C showed that for both R = 0.1 and 0.7, retardation is present at larger alternating cycle blocks and acceleration is present at smaller alternating cycle

blocks. This transition from acceleration to retardation occurs between 10 and 20 alternating cycles for R = 0.1 and around 20 alternating cycles for R = 0.7. Load interaction testing showed that when the crack driving force is near K_{IC} the overload size greatly influences whether acceleration or retardation will occur at 982°C. Semi-realistic spectrum testing demonstrated the extreme sensitivity that relative loading levels play on fatigue crack growth life while also calling into question the importance of dwell times. A crack trajectory modeling approach using blade primary and secondary orientations was used to determine whether crack propagation will occur on crystallographic planes or normal to the applied load. Crack plane determination using a scanning electron microscope enabled verification of the crack trajectory modeling approach.

The isothermal constant amplitude fatigue crack growth results fills a much needed void in currently available data. While the temperature and load interaction fatigue crack growth results reveal the acceleration and retardation that is present in cracks growing in single crystal turbine blade materials under TMF conditions. This research also provides a deeper understanding of the failure and deformation mechanisms responsible for crack growth during thermo-mechanical fatigue. The crack path trajectory modeling will help enable "Retirement for Cause" to be used for critical turbine engine components, a drastic improvement over the standard "safe-life" calculations while also reducing the risk of catastrophic failure due to "chunk liberation" as a function of time. Leveraging off this work there exists the possibility of developing a "local approach" to define a crack growth forcing function in single crystal superalloys.

CHAPTER 1: INTRODUCTION

1.1: Motivation

Gas turbine engines are constantly being pushed to their operational limits in the pursuit of more thrust, better fuel economy and longer more economical life. These operational limits are set by the capabilities of the advanced engineering materials used in the combustor and turbine sections of these engines. In addition, the operational limits are also set realizing that the current state of life prediction for the engine components is very imprecise, dictating a lot of conservatism in design.

Superalloys are known for maintaining excellent mechanical properties at temperature and, as such, are the material of choice for use in the hot section of gas turbine engines. The base alloying element for superalloys can be nickel, cobalt, nickel-iron and tungsten with the most popular by far being nickel. These superalloys come in polycrystalline, directionally solidified and single crystal forms, shown in Figure 1.1. Turbine disk materials are commonly made with polycrystalline material, while the turbine blades that they hold are made out of single crystal and directionally solidified materials. Single crystal blades are commonly used in aircraft engines while directionally solidified blades are usually used in the larger land based power generating turbines with both variants seeing and able to withstand temperatures above 1000°C. Disks see larger loads but are exposed to cooler working environments than the blades with disk temperatures usually being below 750°C.

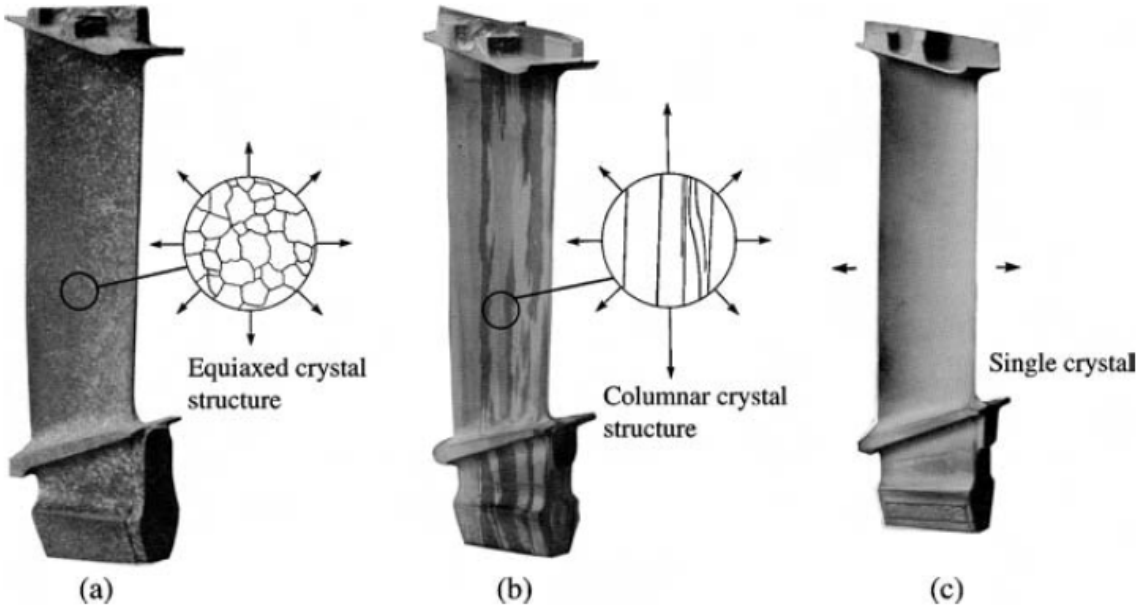

Figure 1.1: Turbine Blades in the (a) Polycrystalline, (b) Directionally Solidified and (c) Single Crystal Forms [1]

Two types of gas turbine engines can be seen in Figure 1.2 and Figure 1.3. The first is a schematic of a turbojet while the second is a schematic of a turbofan. In a gas turbine engine air first enters the compressor where pressure is increased before being mixed with fuel and ignited in the combustor. This expanding gas is used to impart mechanical energy into a turbine which powers the compressor via a shaft. Thrust is created by the momentum difference between the incoming ambient air and the hot exhaust gas. Gas turbine engine efficiency calculated using the Carnot cycle is a function of the input gas temperature over the combustor gas temperature as seen in Equation 1.1. T_1 is the maximum combustor temperature while T2 is the ambient input gas temperature [2].

$$\eta = \frac{T_1 - T_2}{T_1} \tag{1.1}$$

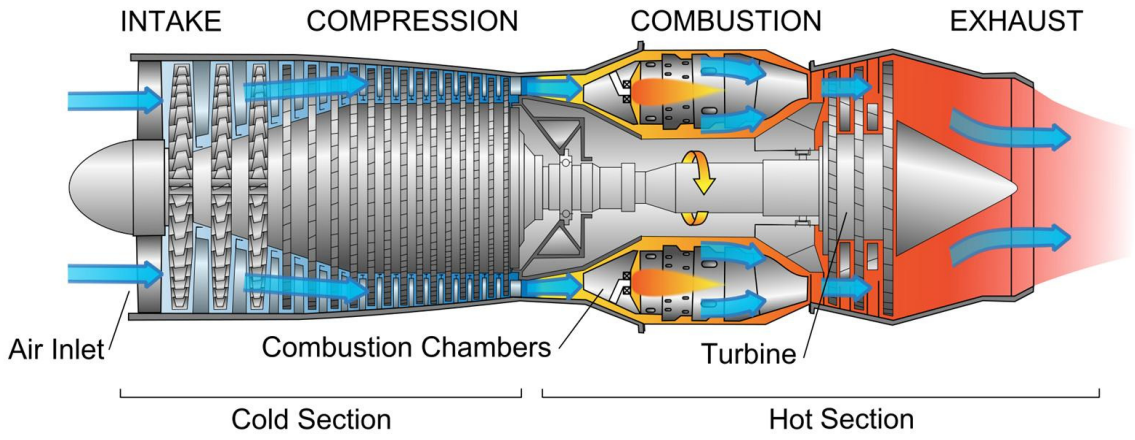

Figure 1.2: Schematic of a Basic Turbojet Gas Turbine Engine [3]

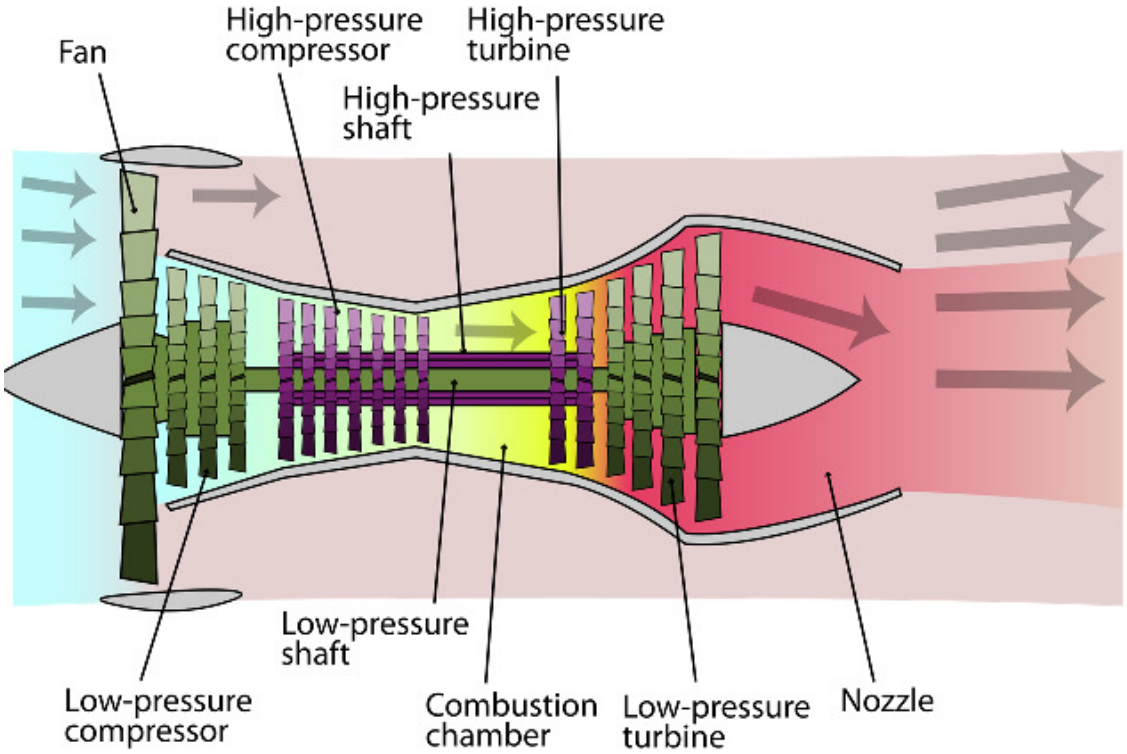

Figure 1.3: Schematic of a Basic Turbofan Gas Turbine Engine [3]

It is certainly not feasible to decrease the ambient input gas temperature of airborne applications so in order to increase efficiency the combustor gas temperature has to be increased. This increase in temperature is made possible by the continued technological advances of superalloys. These advances are not only in the materials that are used but also through better understanding of failure modes, underlying mechanisms and enhanced life prediction models.

These components are subjected to extreme conditions characterized by significant changes in both stress and temperature. These conditions coupled with an extremely corrosive environment promote thermo-mechanical fatigue (TMF) crack growth which can significantly reduce component design life. A thorough understanding of this thermo-mechanical fatigue crack behavior of hot section superalloys is crucial to accurately predict component life to ensure reliable operations without disk or blade fracture through the use of 'retirement for cause' (RFC). Implemented in 1985 by the USAF, for economic and safety reasons, RFC stipulates that components are retired from service when their unique fatigue life is utilized as opposed to the predicted life for the entire population of the same component [4].

This was reinforced by the failure of a turbofan engine on a Boeing 737 during October of 2000, due to a chunk of turbine blade separating and causing damage downstream [5]. A failure attributed to turbine disk chunk liberation occurred on June 2, 2006 at Los Angeles International Airport. An engine on an American Airlines Boeing 767 had a failure of the high pressure turbine stage 1 disk. It was shown that as a result of an

intergranular fatigue crack during high powered ground operation of the engines, a chunk of disk material was liberated causing catastrophic failure of the left engine [6]. A more recent event attributed to turbine blade failure occurred on August 30th 2010 as a Qantas Boeing 747-438 was taking off from San Francisco International airport en route to Sydney, Australia. The failure was initiated by the fatigue fracture of a low pressure stage 2 turbine blade, which led to rotor imbalance and significant damage to the engine nacelle [7]. The turbine blade root and hole in the engine nacelle can be seen in Figure 1.4. Fatigue cracking leading to chunk liberation in turbine blades is not only an issue with jet engines but is also a problem among land based power generating turbines [8, 9].

Figure 1.4: Turbofan Engine Blade Failure: (Bottom) Fractured Blade Toot (Top) Perforated Engine Nacelle [7]

In order to work and be applied properly RFC must be based on a proper understanding of the physical phenomena responsible for fatigue crack propagation. As a first step in building a good modeling foundation, one needs a good understanding of the crack growth mechanisms as a function of temperature, frequency and stress intensity range. These models can then be used to create inspection intervals that when coupled with advanced nondestructive inspection techniques ensure proper retirement of superalloy engine components.

Furthermore RFC needs to be based on a proper understanding of fatigue crack propagation [4]. Better understanding of the fatigue crack growth will lead to superior lifetime estimation in superalloys which will lead to more objectively based inspection intervals that can be introduced to prevent this from happening.

1.2: Research Objectives

Superalloys in gas turbine engines are exposed to strenuous flight profiles involving large temperature and load excursions. This thermo-mechanical cycling introduces many frequency, load and temperature interaction effects that are not thoroughly understood. In order to add to the currently available body of knowledge this project focuses on the TMF crack growth characterization and modeling of single crystal PWA1484 through the use of single edge notch tension, (SENT), round bar tension specimens and fractography with the following objectives:

1. Round bar specimens will be tested to determine monotonic and cyclic properties from 316°C to 982°. The effect of strain rate on monotonic properties will also be researched.

2. SENT specimens will be tested isothermally at 649°C, 816°C and 982°C using constant amplitude cyclic loading. These tests will be performed at R Ratios of 0.1 and 0.7 at a frequency of 1 Hz. Specimens with uncontrolled secondary orientations and controlled secondary orientations will be tested to determine the effect of secondary orientation on the fatigue crack growth rate. These data points will form the basis of the PWA1484 library which will be compared to existing published data and used for non-interaction predictive modeling.
3. Testing in an argon purged environment will be undertaken to ascertain the effect of oxygen. In addition stress free and stressed microstructure aging at 982°C will be performed to determine the effect on the fatigue crack growth rate at 649°C.
4. SENT specimens will be tested bithermally at 649°C and 982°C using constant amplitude cyclic loading with alternating blocks of 1, 10, 20, 50 and 100 cycles. The effect of temperature interactions will be considered to determine crack growth interactions between high and low temperature fatigue.
5. Load interaction testing will be performed at 649°C, 816°C and 982°C while applying single repeated overloads of 1.3x, 1.6x and 2.0x every 800 cycles. The retardation caused by overloads will be examined at different overload ratios and temperatures.
6. Semi-realistic spectrum testing will be performed to determine life variability and the effect of relative loading levels. Spectrums with and without dwell times will also be run to determine the effect of dwell times on life.
7. Fracture surfaces will be examined using a scanning electron microscope to determine failure modes and mechanisms. Through metallography the secondary dendrite arms will be used to determine the secondary orientation of the uncontrolled specimens.
8. A crack trajectory modeling approach using blade primary and secondary orientations will be used to determine whether crack propagation will occur on

crystallographic planes or normal to the applied load. Crack plane determination using a scanning electron microscope will enable verification of the crack trajectory modeling approach.

1.3: Dissertation Overview

The first chapter discusses the motivation for this thermo-mechanical fatigue crack growth of a single crystal superalloy project. This chapter also includes a list of the research objectives of this study. A relevant background is provided in the second chapter that discusses the history, composition, microstructure, processing and mechanical properties of superalloys. Also provided is an overview of the most common fatigue analysis and fatigue crack service life prediction methodologies. In addition the second chapter contains an in depth review of the thermo-mechanical fatigue crack growth behavior of superalloys. This section discusses the varied factors that are responsible for the fatigue crack growth rate. Experimental methods are discussed in the third chapter. This chapter includes details about the material, specimen design, specimen stress intensity factor and preparation and the thermo-mechanical testing process. Also included are the process for secondary orientation determination using metallography, the SEM crystallographic plane measurement technique and crack growth non-interaction modeling. Experimental results are presented in the fourth chapter. This chapter includes results from a material analysis, secondary orientation results and monotonic and cyclic property determination. Then the experimental results chapter discusses the isothermal constant amplitude and temperature and load interaction fatigue crack growth rates. Next this chapter discusses the results from semi-realistic spectrum testing. Lastly this chapter will discuss the crack surface morphology. The modeling is

found in fifth chapter with discussions on the crack path trajectory modeling and crack plane determination via SEM. Conclusions and future recommendations along with research significance can be found in the sixth chapter.

CHAPTER 2: LITERATURE REVIEW AND BACKGROUND

2.1: History of Superalloys

With the invention of the jet engine in the 1930's by Frank Whittle there was demand for materials that could withstand the high turbine entry temperatures [10]. Starting in the 1940's, the turbine entry temperature had increased so much that a new high temperature alloy had to be created to withstand the harsh gas turbine engine environment. This new high temperature material had to fulfill several requirements:

1. The material needed to have excellent mechanical properties at high temperatures especially as it approached its melting point.
2. It needed to be able to resist time dependent deformation such as creep when loaded at high temperatures for long dwell periods.
3. This material would also have to be able to withstand a corrosive operating environment due to the byproducts of combustion [11].

Many materials can satisfy two of these requirements but very few can satisfy all three. For example titanium, which is used for compressor blades and discs, is lightweight and strong, but has poor oxidation resistance and at high temperatures can catch on fire [12]. On the other hand ceramics are creep and oxidation resistant but have low toughness and are brittle. Due to their creep oxidation resistance ceramics have found use as thermal barrier coatings that increase the operational limit of superalloy components.

Several different base alloying elements such as cobalt, nickel and tungsten were looked at but nickel was chosen as the solvent of choice because of several factors:

1. Nickel has an extremely stable face centered cubic lattice structure that does not go through any phase changes from room temperature up to its melting point of 1453°C.
2. Nickel is also very tough and ductile which makes it resistant to fatigue and fracture.
3. The diffusion rate of nickel and substitutional elements is very low which affords it excellent creep resistance [11].

Some other materials are better than nickel in certain areas but when factoring in price and density, nickel clearly emerges as the basic alloying element for superalloys. With the base alloying element of nickel chosen, Nimonic alloy 75 was the first Superalloy developed in support of the Whittle gas turbine engine [13]. As seen in Figure 2.1 the first superalloys where wrought for all components [14]. In the mid 1950's the introduction of vacuum induction melting and casting at Special Metals in Utica, NY, prevented aluminum and titanium from oxidizing which allowed the production of cast alloys that had fewer contaminants [11]. Since then casting technologies have advanced so that alloys can be directionally solidified (DS) so that there are no transverse grains [15] and eventually led to the casting of single crystals that have no grain boundaries [16]. Due to the added expense of using and verifying grain selection processes, polycrystalline materials are still very prevalent as lower temperature turbine disk materials.

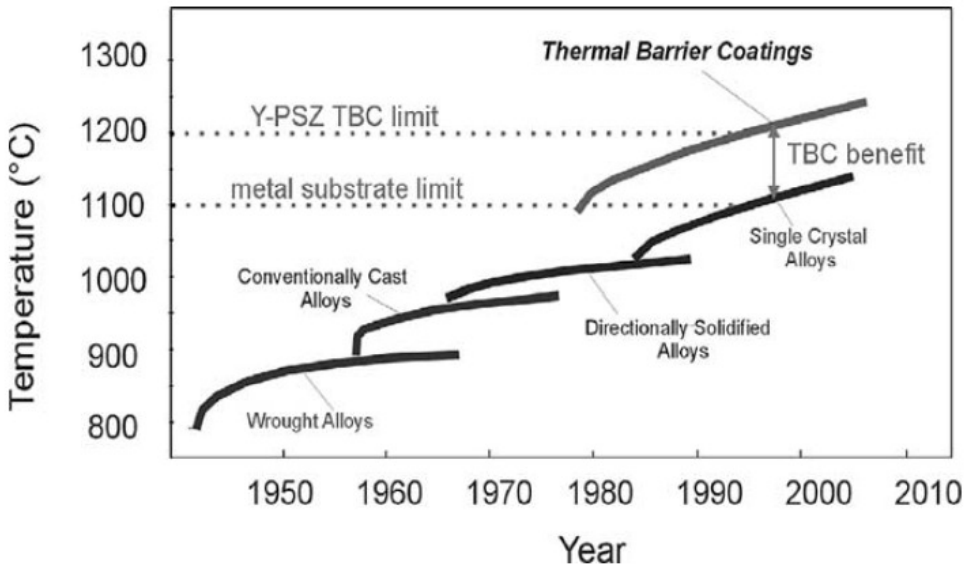

Figure 2.1: Increase of Turbine Entry Temperature TET Made Possible by Gains in Alloy and Manufacturing Technologies [14]

2.2: History of Single Crystal Ni-Base Superalloys PWA1480 and PWA1484

In the early 1980's commercial engines starting using first generation single crystal PWA1480, shortly after PWA1480 was used in military applications [17]. The development of this material was driven by the need for more creep and oxidation resistance during the extended dwell cycles seen during commercial flight. PWA1484 first entered military service in 1986 as turbine blades for the F100-PW-229 afterburning turbofan engine on the F-16 Fighting Falcon and F-15E Strike Eagle fighter aircraft. It was not until 1990 that PWA1484 was first used for commercial applications. The addition of 3.0% rhenium to second generation PWA1484 greatly improves the creep and oxidation resistance over PWA1480 [17].

2.3: Superalloys Composition, Microstructure and Processing

2.3.1: Composition

There are many different superalloys composed of a similar pool of elements but each having a slightly different percent weight configuration. This is primarily due to gas turbine engine manufacturers and material suppliers coming up with there own proprietary blends. The numerous superalloys can also be attributed to the many different alloying elements which can be seen for some common wrought and cast alloys in Table 2.1 and Table 2.2. Removing or slightly modifying a single alloying element can have a large effect on the mechanical properties. A common trend is for superalloys to be composed of approximately 55% nickel by weight followed by chromium, cobalt, tungsten, aluminum, molybdenum and titanium in decreasing percent weight order [14]. Aluminum and titanium play a major role in nickel base superalloys through the formation of γ' [18]. Most of a superalloys mechanical properties are derived from the γ' participate. These two elements can have a deleterious effect on a superalloys oxidation resistance which is why the role of chromium is so pivotal. Chromium has a low tendency to form intermetallic compounds even at elevated temperature [19].

In comparing wrought to cast superalloys it can be seen that iron is no longer used in any cast superalloys whereas cast superalloys are now using more rhenium and tantalum. In comparing polycrystalline (IN100) to single crystal (PWA1484) superalloys, some elements such as carbon and boron which strengthen grain boundaries and zirconium which promotes grain boundary cohesion are absent from the grain boundary free, single crystal materials.

Table 2.1: Some Compositions of Wrought Superalloys [14]

Alloy	Cr	Co	Mo	W	Nb	Al	Ti	Ta	Fe	Hf	C	B	Zr	Ni
Astroloy	15.0	17.0	5.3	-	-	4.0	3.5	-	-	-	0.06	0.030	-	Bal
Hastelloy S	15.5	-	14.5	-	-	0.3		-	1.0	-	-	0.009	-	Bal
Haynes 230	22.0	-	2.0	14.0	-	0.3		-	-	-	0.10	-	-	Bal
Incoloy 925	20.5	-	-	-	-	0.2	2.1	-	29.0	-	0.01	-	-	Bal
Inconel 718	19.0	-	3.0	-	5.1	0.5	0.9	-	18.5	-	0.04	-	-	Bal
LSHR	13.0	21.0	2.7	4.3	1.5	3.5	3.5	1.6	-	-	0.03	0.030	0.050	Bal
Nimonic 75	19.5	-	-	-	-	-	0.4	-	3.0	-	0.10	-	-	Bal
N18	11.5	15.7	6.5	0.6	-	4.35	4.35	-	-	0.45	0.02	0.015	0.03	Bal
Pyromet 860	13.0	4.0	6.0	-	0.9	1.0	3.0	-	28.9	-	0.05	0.01	-	Bal
Rene 95	14.0	8.0	3.5	3.5	3.5	3.5	2.5	-	-	-	0.15	0.010	0.05	Bal
Udimet 500	18.0	18.5	4.0	-	-	2.9	2.9	-	-	-	0.08	0.006	0.05	Bal
Waspaloy	19.5	13.5	4.3	-	-	1.3	3.0	-	-	-	0.08	0.006	-	Bal

Table 2.2: Some Compositions of Cast Superalloys [14]

Alloy	Cr	Co	Mo	W	Al	Ti	Ta	Nb	Re	Ru	Hf	C	B	Zr	Ni
CM247LC	8.0	9.3	0.5	9.5	5.6	0.7	3.2	-	-	-	1.4	0.07	0.015	0.010	Bal
CMSX-10	2.0	3.0	0.4	5.0	5.7	0.2	8.0	-	6.0	-	0.03	-	-	-	Bal
GTD-111	14.0	9.5	1.5	3.8	3.0	5.0	3.15	0.07	-	-	-	0.1	0.014	0.007	Bal
GTD-222	22.5	19.1	-	2.0	1.2	2.3	0.94	0.8	-	-	-	0.08	0.004	0.02	Bal
IN100	10.0	15.0	3.0	-	5.5	4.7	-	-	-	-	-	0.18	0.014	0.06	Bal
IN-792	12.4	9.2	1.9	3.9	3.5	3.9	4.2	-	-	-	-	0.07	0.016	0.018	Bal
Mar-M246	9.0	10.0	2.5	10.0	5.5	1.5	1.5	-	-	-	1.5	0.15	0.015	0.05	Bal
PWA1480	10.0	5.0	-	4.0	5.0	1.5	12.0	-	-	-	-	-	-	-	Bal
PWA1484	5.0	10.0	2.0	6.0	5.6	-	9.0	-	3.0	-	0.1	-	-	-	Bal
PWA1497	2.0	16.5	2.0	6.0	5.6	-	8.25	-	5.95	3.0	0.15	0.03	-	-	Bal
Rene 80	14.0	9.0	4.0	4.0	3.0	4.7	-	-	-	-	0.8	0.16	0.015	0.01	Bal
Rene N6	4.2	12.5	1.4	6.0	5.75	-	7.2	-	5.4	-	0.15	0.05	0.004	-	Bal

Since single crystal superalloys first emerged in 1980 there have been five generations, categorized mostly by the amounts of elements rhenium and ruthenium. First generation superalloys such as CMSX-6 and PWA1480 do not have any rhenium or ruthenium. Whereas second generation superalloys such as PWA1484 and CMSX-4 have approximately 3% rhenium [20]. For third generation superalloys, such as René N6 and CMSX-10 the amount of rhenium was increased to approximately 6%. PWA1497 and TMS-138 are fourth generation superalloys which add ruthenium to the composition mix. The compositions for common second generation single crystal superalloys can be seen

in Table 2.3. Rhenium increases the superalloys' melting temperature which leads to greater thermal stability of the gamma matrix and gamma prime phase which increases creep performance through impediment of diffusion. Increased stability leading to additional strength at high temperatures is obtained by the addition of ruthenium which increases the solubility of high temperature elements in the gamma prime phase [21]. Fifth generation superalloys aim to improve on the fourth generation by increasing ruthenium and chromium content for even more phase stability and oxidation resistance, respectively.

Table 2.3: Compositions of Second Generation Single Crystal Superalloys [11]

Alloy	Cr	Co	Mo	Re	W	Al	Ti	Ta	Nb	Hf	Ni	Density (g/cm^3)
CMSX-4	6.5	9	0.6	3	6	5.6	1	6.5	—	0.1	Bal	8.70
PWA1484	5	10	2	3	6	5.6	—	8.7	—	0.1	Bal	8.95
Rene N5	7	8	2	3	5	6.2	—	7	—	0.2	Bal	8.70
MC2	8	5	2	—	8	5	1.5	6	—	—	Bal	8.63
TMS-82+	4.9	7.8	1.9	2.4	8.7	5.3	0.5	6	—	0.1	Bal	8.93

2.3.2: Microstructure

Superalloys all have a common microstructure which consists of the following phases, which can be seen in Figure 2.2 and Figure 2.3.

Gamma Phase (Denoted γ) – This is the extremely stable FCC matrix material that the other phases, carbides and borides exist in. Elements such as cobalt, chromium, molybdenum, ruthenium and rhenium can be found in this phase [11, 22, 23]

Gamma Prime Phase (Denoted γ') – This ordered Ni_3Al FCC-like precipitate is found embedded in the matrix material and plays a pivotal roll in conferring strength to the superalloy. Gamma prime displays the cubic, $L1_2$, crystal structure

with Al atoms at the corners and Ni atoms at the center of the cube faces as seen in Figure 2.4. This precipitate phase contains elements such as aluminum and titanium for promoting the formation of γ' and tantalum for solid solution strengthening. This phase is called gamma double prime when talking about nickel-iron superalloys and superalloys with large quantities of niobium [11, 22, 23].

Carbides and Borides – Carbon and boron react with other elements to form these strengthening agents which can be found along the grain boundaries of the gamma phase. The presence of these along the grain boundaries hinder grain boundary sliding greatly increasing the rupture strength at high temperatures [22, 23]. These two elements are absent in single crystal superalloys where grain strengthening agents are not needed.

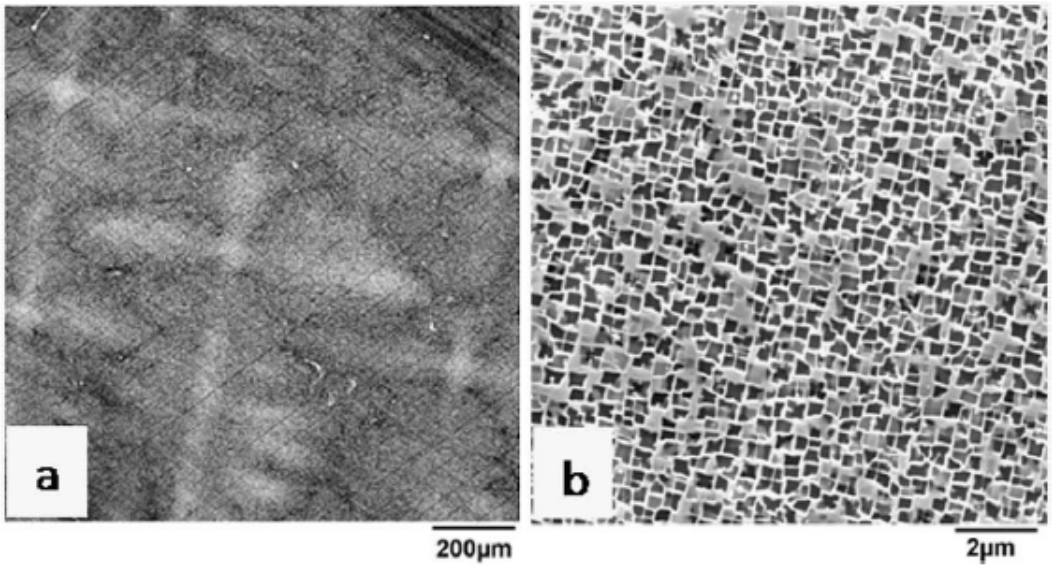

Figure 2.2: PWA1484 Microstructure: (a) Dendrites Along with Interdendritic Regions (b) Cuboidal γ' Phase in γ Matrix Material [24]

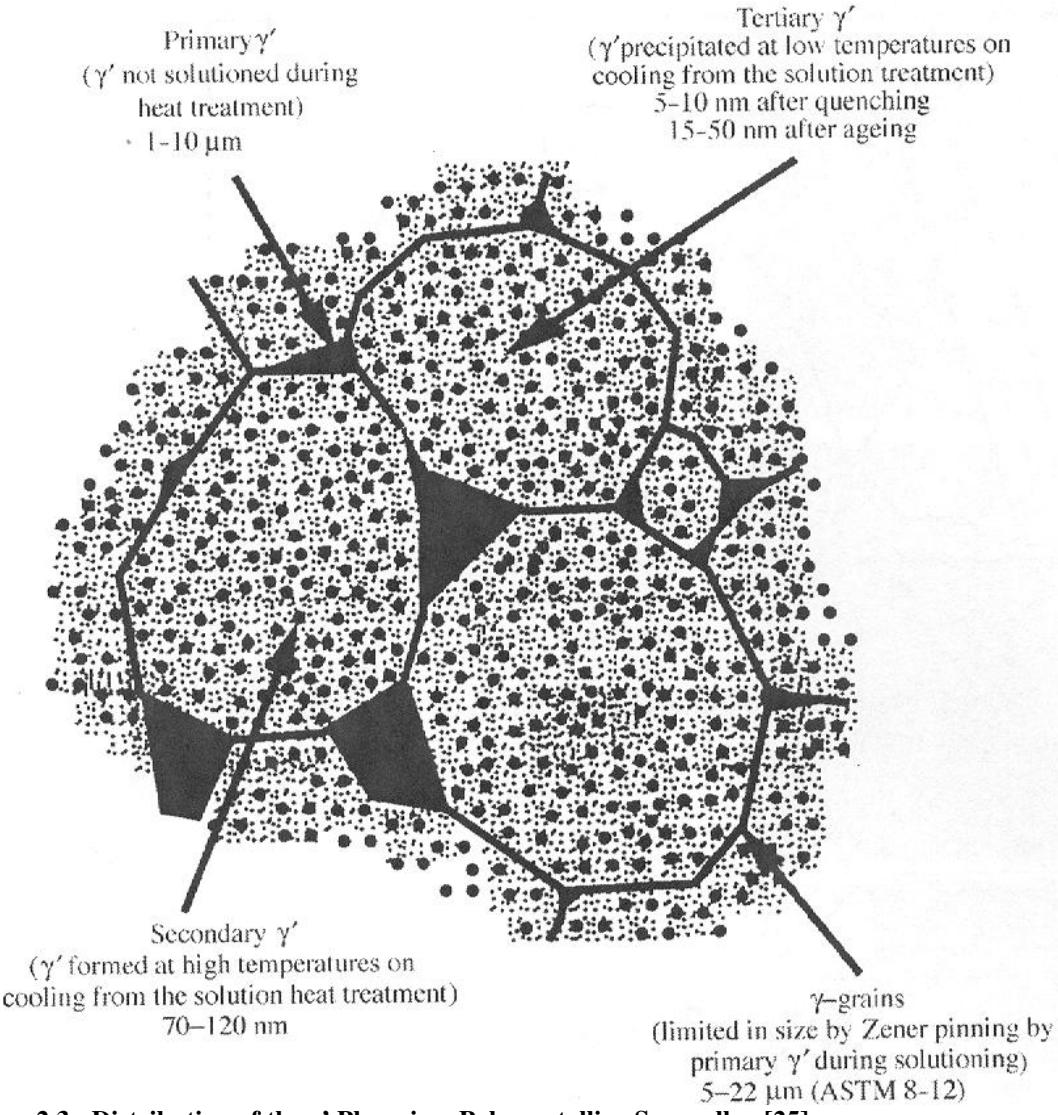

Figure 2.3: Distribution of the γ' Phase in a Polycrystalline Superalloy [25]

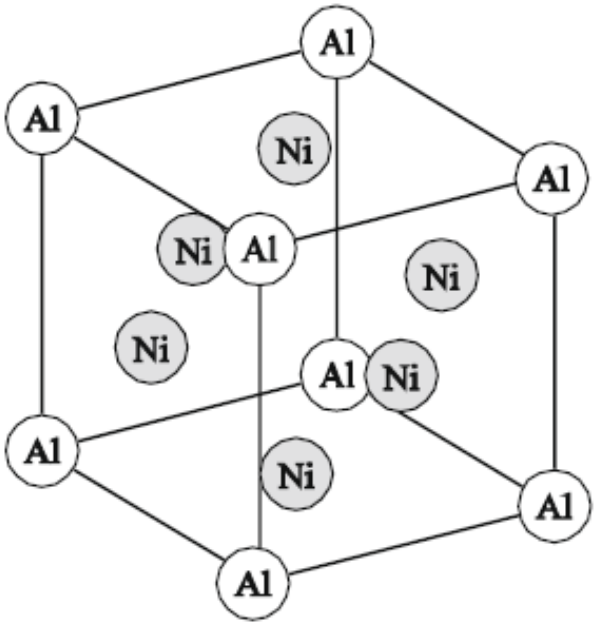

Figure 2.4: Crystal Structure of Ni_3Al γ' Showing the Distribution of Aluminum and Nickel Atoms

PWA1484 are precipitation strengthened single crystal nickel-base superalloys following the Ni-Cr-Al system. Nickel based superalloys have a cubic crystal structure and during the casting process of <001> crystals the continuous primary dendrites form in the direction of the casting with secondary dendrite arms (perpendicular to casting) defining the interdendritic spacing in the shape of 'plus' signs [26]. These secondary dendritic arms can be seen in Figure 2.5. It has been shown that these arms occur along the <001> family of crystallographic directions [27]. This information can be used to roughly calculate crystal orientation in the absence of more sophisticated methods such as Laue Back-Reflection of X-Rays. Application of this technique is demonstrated in Figure 2.6.

The γ' precipitate volume fraction of PWA1484 is approximately 0.6 with the remainder being the γ matrix. A large negative mismatch parameter exists between the γ' and γ matrix [17, 28]. The Ni_3Al blocky γ' strengthening phase is 0.35 to 0.6 μm. The high

volume fraction of γ' prohibits dislocation bypass at low and intermediate temperatures forcing precipitate shearing. In addition PWA1484 has a second ultra fine spherical γ' precipitate that forms in the γ matrix between the larger γ' precipitate. This spherical precipitate is on the order of 30 nm [17, 28].

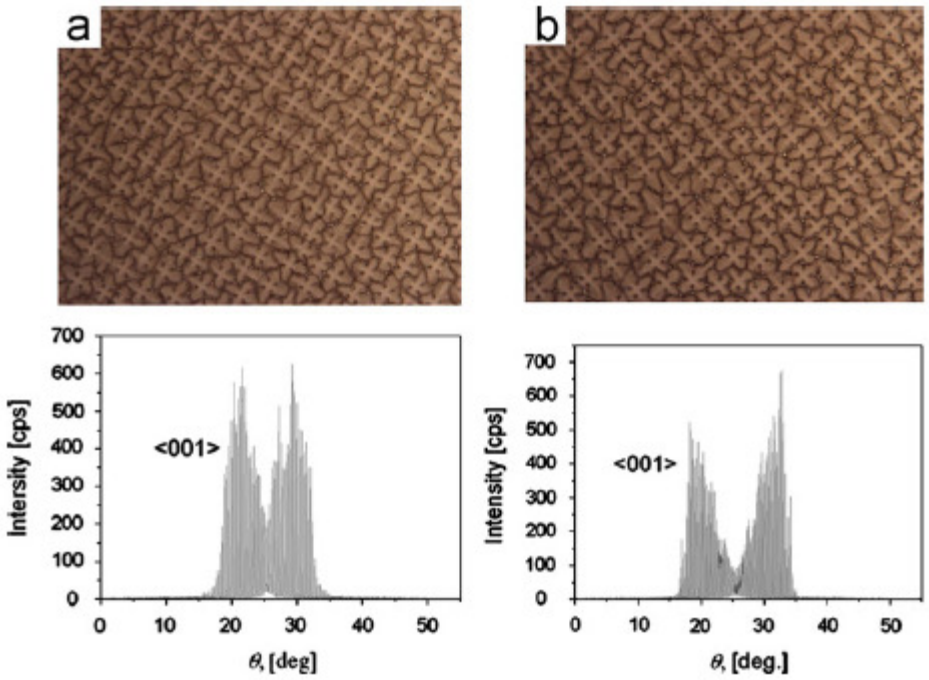

Figure 2.5: Microstructure and XRD Results of a Single Crystal Superalloy with <001> Orientation [26]

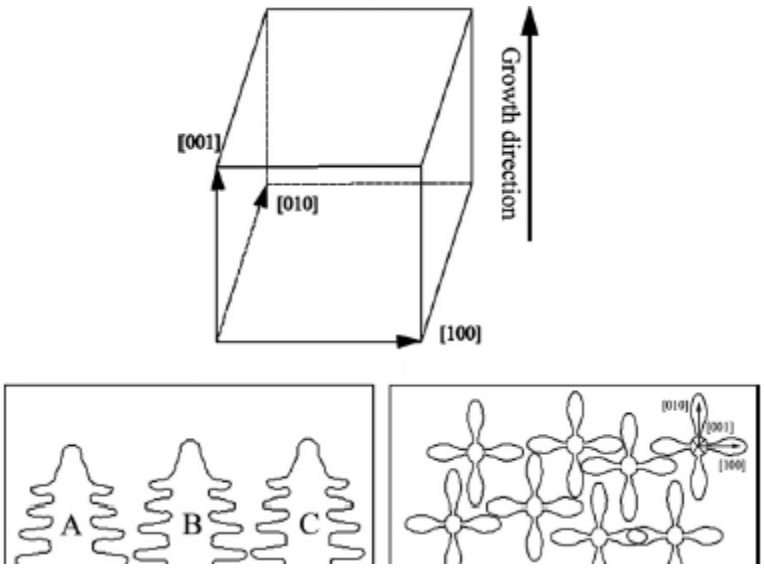

Figure 2.6: Schematic of Dendrite Side Branching Directions [26]

2.3.3: Processing

Gas turbine engine blades were initially produced by extrusion or forging [29]. In the 1970's blades started being produced by investment casting. This allowed the manufacture of hollow blades to allow cooling passages and decreased the overall weight of the blades. Today virtually all turbine blades are manufactured using investment casting [30].

The 'lost-wax' process involves the following steps. Molten wax if first injected into master molds made out of metal. These wax blades are then arranged in clusters so several blades can be cast at once. These clusters are then dipped into a ceramic slurry several time to get a thick coat and fired to melt out the wax and strengthen the ceramic mold. The molten superalloy (~1550°C) is then poured into the mold under vacuum. After cooling the blades are removed from the ceramic molds. The sprue, runners and grain selector are removed and any final machining is now performed such as milling, grinding and wire EDM [31, 32]. These steps can be seen in Figure 2.7.

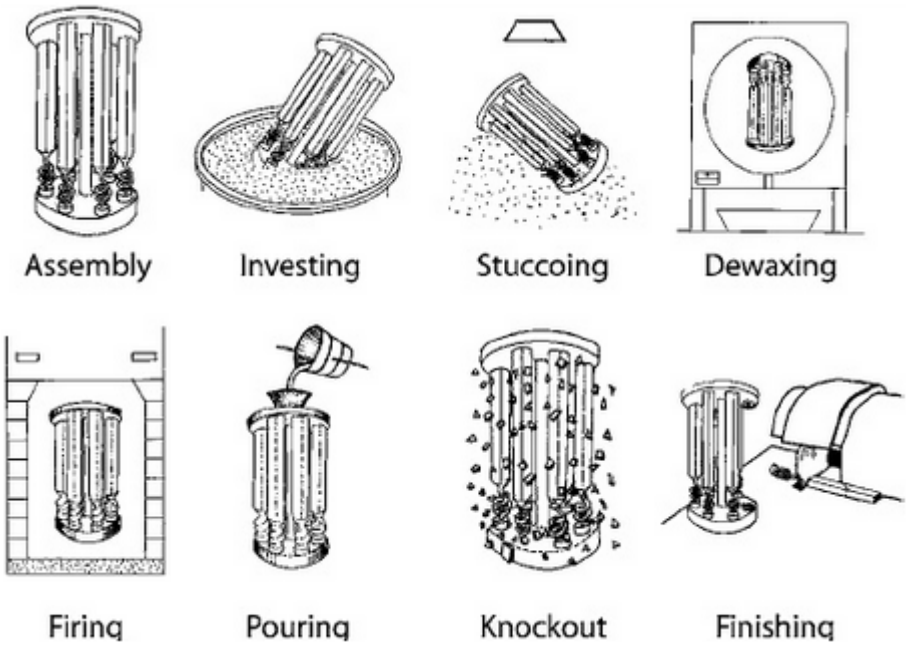

Figure 2.7: The Production of Turbine Blade Alloys by Investment Casting [11]

Single crystals can be produced through either a grain selector method or from already established seed crystals. In both cases investment casting is used to get the near net shape before final machining of the turbine blade. The grain selector method uses a pig tail shaped spiral at the bottom of the wax mold. Different types of grain selectors can be seen in Figure 2.8. This spiral is placed on a chilled plate and as the metal solidifies moving up the pig tail a single grain is selected and enters the main casting cavity. This method produces a crystal whose longitudinal axis is in the [001] direction, while the other two axes are uncontrolled [33]. If an orientation other than [001] is preferred, or if the secondary orientation is to be controlled, the blade is cast using a seed-crystal. This seed crystal has a known primary and secondary orientation and is only partially re-melted ensuring new growth is consistent with the seed [11].

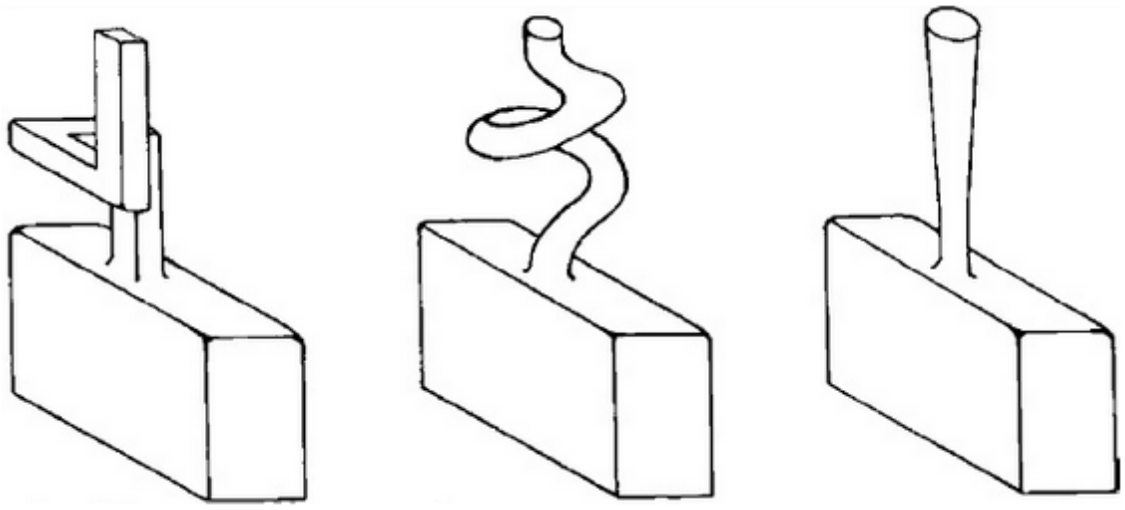

Figure 2.8: Different Types of Grain Selectors for Use during Investment Casting [11]

A starter block and pig-tail grain selector along with the bottom half of a Trent 800 high-pressure turbine blade casting can be seen in Figure 2.9. Looking closely one can see columnar grains in the starter block before passing through the grain selector.

Figure 2.9: Details of the Starter Block and Pig-Tail Grain Selector from the Trent 800 High-Pressure Turbine Blade Casting [11]

2.4: Mechanical Properties of Superalloys

Superalloys unique combination of composition and microstructure are what give superalloys their exceptional mechanical properties at high temperature. These properties are so valuable that lattice block and metallic foam superalloys are being developed to create light weight structural components [34]. Superalloys maintain creep strength and damage tolerance at high temperatures by severely impeding dislocations, the carriers of creep, from entering the gamma prime phase. Dislocations traveling through the gamma

phase have to travel in pairs through what is known as anti-phase boundary (APB) order strengthening.

Superalloys are quite unusual in as much as that unlike most alloys the yield strength increases with temperature up to about 800°C, seen in Figure 2.10 [11]. The main source of strength increase occurs in the γ' phase. The creation of APB takes energy and this energy increase means higher stresses must be applied to move dislocations through the lattice. In γ' phase the cross slip of dislocations from the octahedral to cubic plane combined with the APB order strengthening are primarily responsible for yield strength increasing with temperature. These entanglements are known as Kear-Wilsdorf locks named so after the scientists who first discovered them [35]. De Bussac, Webb and Antolovich [36] were the first to develop a physical model for this cross slip of dislocations. These locks have been found to be reversible with only a small percentage of the work hardening created at high temperature remaining at lower temperatures. Also, at elevated temperatures, gamma prime coarsening will inhibit dislocation movement, requiring increased stress for additional deformation [37]. Above approximately 800°C a preference for thermally activated slip on the cubic plane leads to a sudden drop in yield strength [38, 39].

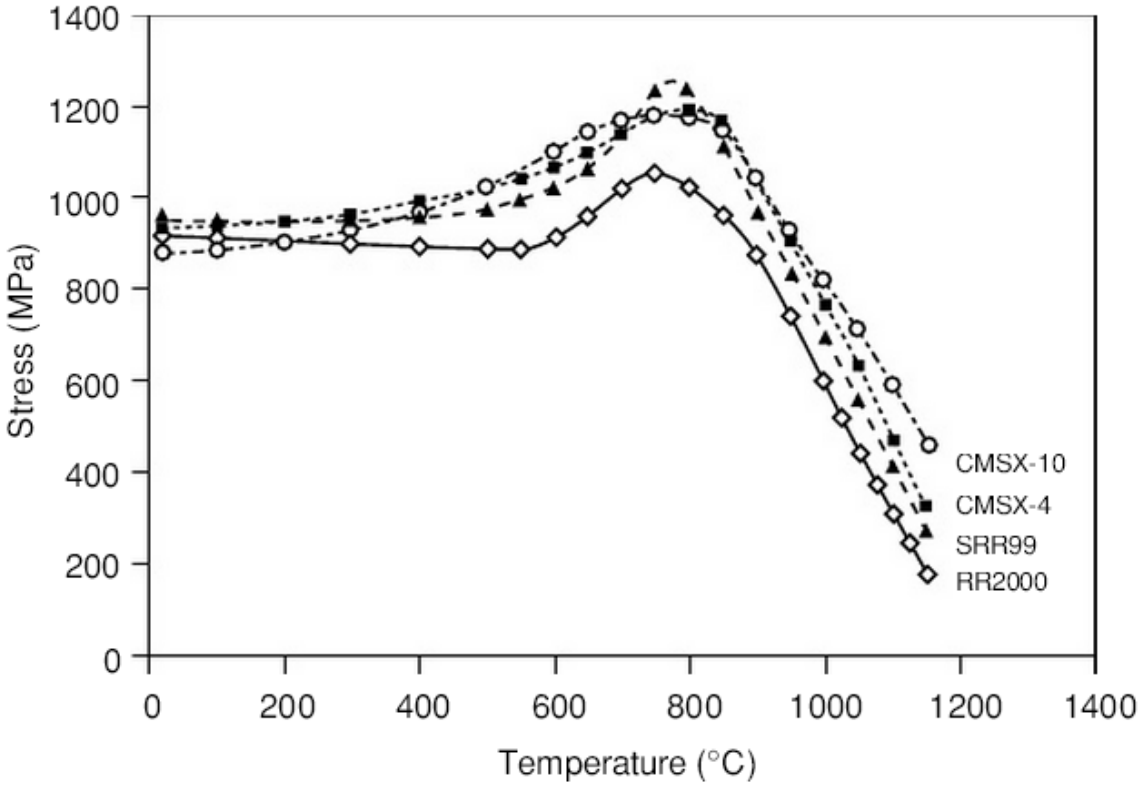

Figure 2.10: Yield Stress as a Function of Temperature for Single Crystal Superalloys [11]

Single crystal superalloys have highly orthotropic properties. Almost always, turbine blades are produced with the primary loading direction being aligned within +/-5° of the primary crystallographic orientation of [001]. The secondary orientation is not usually controlled and is considered a random variable [40]. Every crystal structure has an associated set of slip systems. The activation of a particular slip system is dependent upon the crystal orientation with respect to the axis of loading. The [001] direction has the most number of active slip systems according to Schmidt factor calculations. These active slip systems can be seen in Table 2.4. The 3 cube active slip systems in the [111] orientation are questionable as what has been seen is alternating slip on octahedral planes. These large number of active slip systems are what create an abundance of crystallographic fracture opportunities in single crystal superalloys where Mode I ΔK

solutions are incorrect. Figure 2.11 clearly shows the anisotropic nature of single crystal superalloys, with the creep performance being very dependent on the crystallographic orientation.

Table 2.4: Number of Active Slip Systems by Crystallographic Orientation

Orientation	Primary Slip System	Number of Slip Systems Active
[001]	Octahedral	8 Oct.
[011]	Octahedral	4 Oct.
[111]	Octahedral	6 Oct.+3 Cube
[123]	Octahedral	1 Oct.

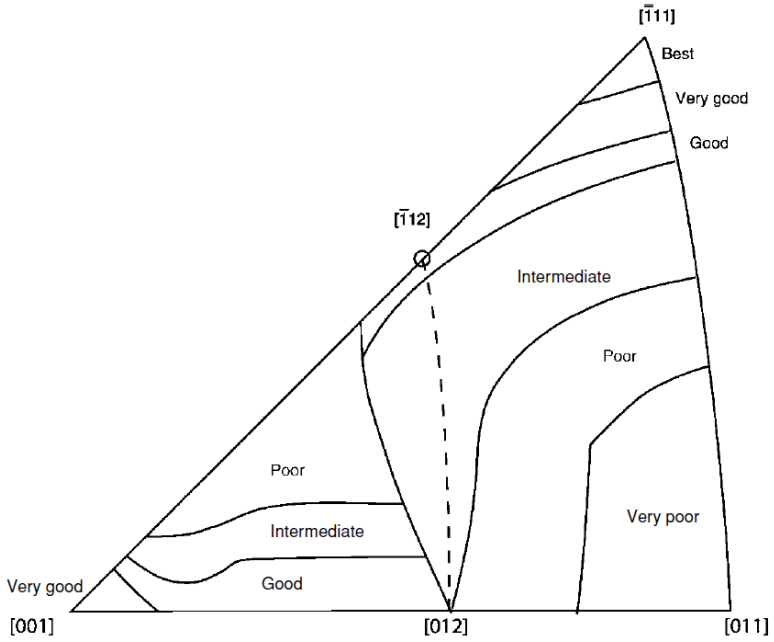

Figure 2.11: Creep Performance as a Function of Crystallographic Orientation for Mar-M247 [41]

2.5: History of Fatigue Life Prediction

Fatigue is characterized as the repeated cyclic loading of structures or components leading to damage or premature failure. In general these stresses are well below the material yield strength making life prediction even more difficult. Add in cyclic temperature effects and you have thermo-mechanical fatigue the single largest contributor of failure in turbine engine superalloys. The fatigue life of a component is broken into three parts; initiation, propagation and fracture stages. There are three main fatigue life prediction methods; stress-life, strain-life and crack growth using a fracture mechanics approach. When dealing with single crystal materials, which are highly anisotropic, a local approach to life prediction becomes very important.

2.5.1: Stress-Life Approach

Stress-life is by far the oldest approach to fatigue life prediction. First used by the German engineer Wöhler [42-44] in the 1850's to predict failure of railroad axles, it was the most widely used approach for over 100 years later. Wöhler is credited with the creation of S-N curves, which can be plotted linearly on a log-log scale as alternating stress versus cycles to failure. An example of an S-N curve can be seen in Figure 2.12. Stress-life works well for simplified geometries under high cycle fatigue, but in low cycle situations where plasticity is encountered a different method is required. Stress-life takes into account both initiation and propagation of a crack up to component failure and is thus dependent upon the size of the sample.

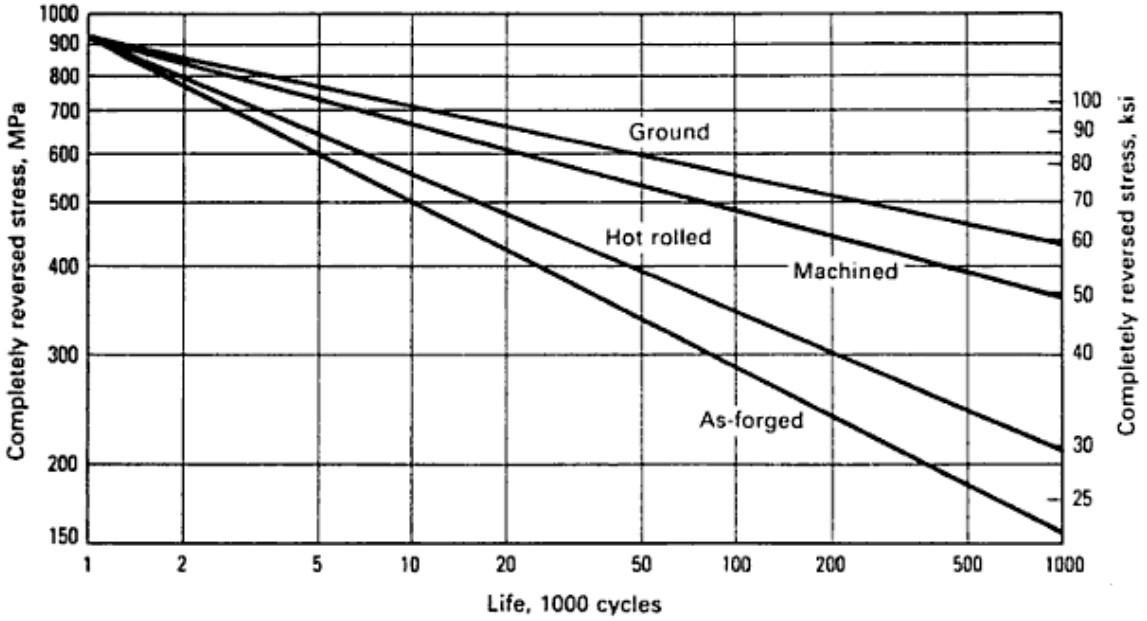

Figure 2.12: S-N Curve Showing the Effect of Surface Condition on the Fatigue Life of Steel [45]

2.5.2: Strain-Life Approach

In the 1950's Coffin and Manson [45, 46] discovered that strain-life could also be plotted linearly on log-log scale as strain amplitude versus cycles to failure. An example of a strain-life curve can be seen in Figure 2.13. Strain life is the preferred approach for areas encountering plasticity, complicated geometries and notched components. Strain control is used around notches due to strain being a more fundamental indicator of damage, especially for materials that do not work harden. No rational design would have large component cross sections experience plasticity but in localized areas such as notches plasticity can occur. Strain-life is mostly used for determination of crack initiation and but can also be used to model fatigue crack propagation rates and notch life [47-49].

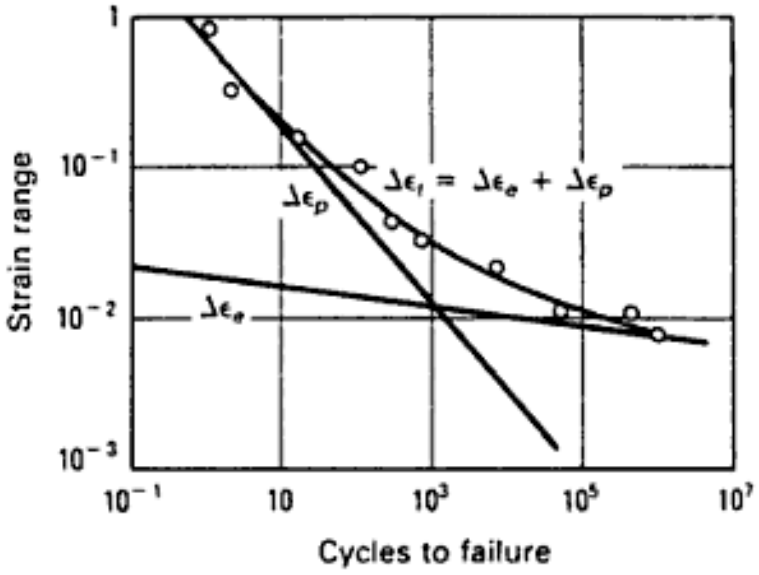

Figure 2.13: Strain-Life Curve Showing Strain Range Versus Cycles to Failure [50]

2.5.3: Fracture Mechanics Approach

Griffith [51] first postulated in 1920 that crack propagation will occur if the total energy of the system is decreased by doing so. This simple energy balance was only accurate for brittle materials so separately in the late 1940's Irwin and Orowan [52, 53] added a term to account for the plastic deformation found in ductile materials. George Irwin developed the concept of the strain energy release rate (G), which is the energy required to create a new area of crack extension. In 1956 Irwin [54] synthesized many results into what is now called the fracture mechanics approach. Fundamental to that approach are the so-called field equation as shown in Equation 2.1.

$$\sigma_{ij} = \frac{K}{\sqrt{2\pi r}} f_{ij}(\theta) \tag{2.1}$$

Where K is the stress intensity factor, 'f' is a trigonometric factor and 'r' is the distance from the crack tip. George Irwin demonstrated that G is related to the stress intensity factor, K though Equation 2.2.

$$G = \frac{K^2}{E} \tag{2.2}$$

Equation 2.1 can be reordered to solve for the stress intensity factor, seen in Equation 2.3.

$$K = \sigma\sqrt{\pi a}\, y \tag{2.3}$$

Where σ is the far field stress, 'a' is the crack length and 'y' is a loading, crack length and geometry correction factor. There are multiple K solutions for many different loading and specimen geometries [55]. The three modes of loading that can be applied to a crack are seen in Figure 2.14.

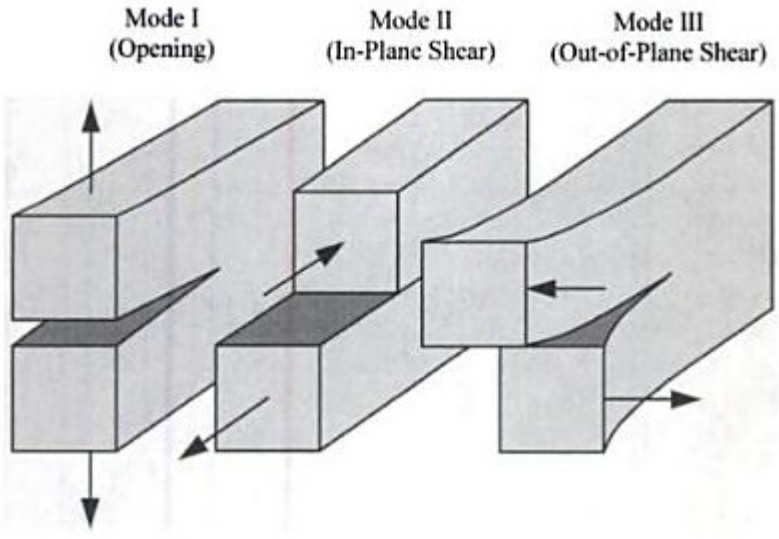

Figure 2.14: The Three Different Crack Tip Loading Modes: K_I, K_{II} and K_{III} [56]

The fracture mechanics approach applies only to existing cracks and is used for the propagation portion of fatigue. After initiation of the crack, growth data is taken by measuring the crack length as a function of the number of applied cycles. As can be seen in Figure 2.15 much of the fatigue life is spent with the crack length relatively small. Increased crack length leads to an increase in growth rate. This can be seen more clearly when the derivative of a as of function of N is taken to provide da/dN.

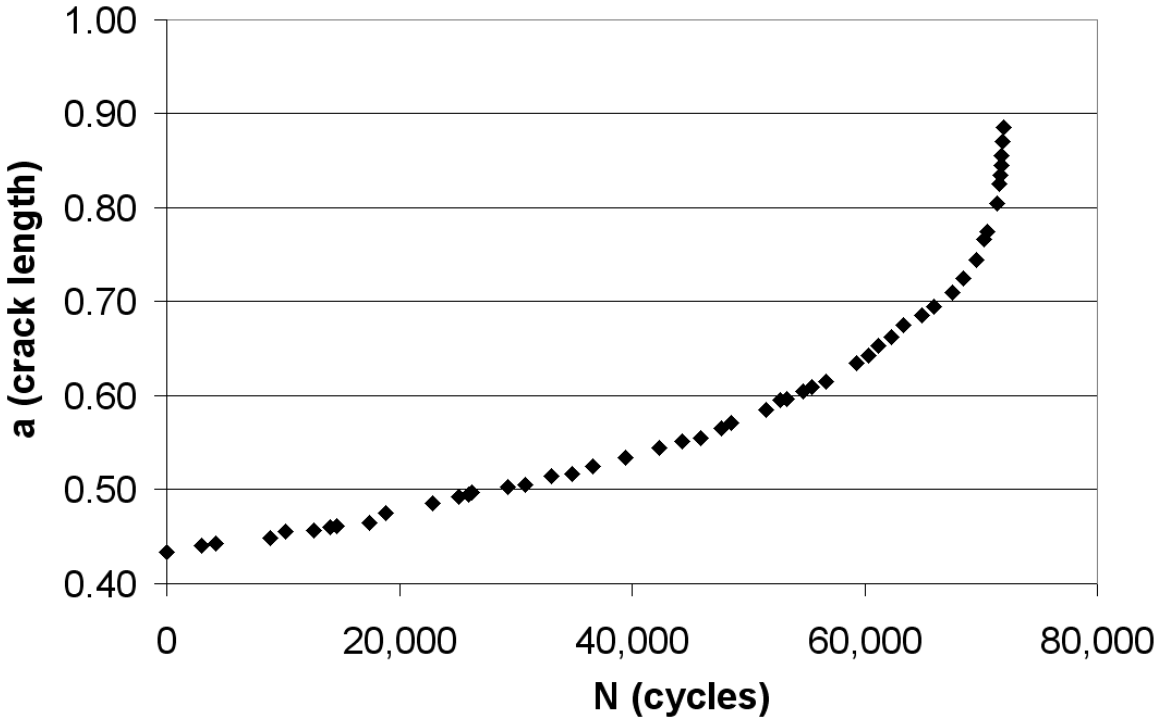

Figure 2.15: Constant Amplitude Crack Growth Data

$$\Delta K = \Delta\sigma\sqrt{\pi a}\, y \qquad \textbf{(2.4)}$$

da/dN can then be plotted as a function of ΔK, which is seen as Equation 2.4. ΔK is the difference between the max and min stress intensity factor also known as the stress intensity factor range. When plotted on a log-log plot the data actually takes the form of

a sigmoidal function. This curve can be split into regions I, II and III as seen in Figure 2.16.

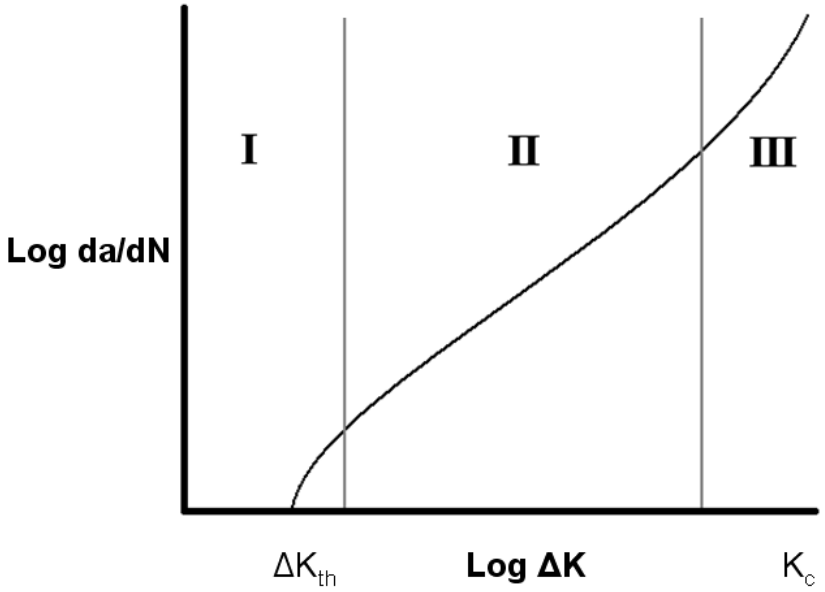

Figure 2.16: Three Regions of Crack Growth Rate

Region I is referred to as near threshold area of the da/dN vs. ΔK curve. Below the stress intensity threshold crack growth does not occur. Threshold is material dependent and also depends on many factors such as R ratio, frequency and temperature. It would be ideal to design components to be exposed only to stress's below the threshold stress intensity. Due to the low stress required to achieve this, it is often impractical to accomplish this. Even then there are small cracks that may still form and propagate ten times faster than long cracks below this threshold level.

Region III is known as the fast fracture area of the da/dN vs. ΔK curve. Once crack growth enters this region it is very difficult to predict this very short and unstable portion

of propagation life. For this reason the region is usually ignored during engineering design. The critical stress intensity, K_c, is more commonly known as the critical fracture toughness and once reached leads to fracture.

Region II is where most of the crack propagation life takes place and can be plotted linearly as logarithmic da/dN versus logarithmic ΔK. The idea of using the fracture mechanics approach and applying it to fatigue crack growth was proposed by Paris, Gomez and Anderson [57] in 1961. Building on this, in 1963 Paris and Erdogan [58] predicted a power law function for region II that was verified by crack growth data with log-log linearity. This relationship can be seen in Equation 2.5.

$$\frac{da}{dN} = C\Delta K^m \tag{2.5}$$

C is known as the Paris equation coefficient and m is known as the Paris equation exponent. C and m values for various materials can readily be found in publications with most values of m for Superalloys falling between 2 and 4. The equation below forms the basis for most fracture mechanics based life estimation models. Knowing the current crack length, a, C and m the change in crack length per cycle can be calculated and added iteratively using Equation 2.6.

$$\frac{da}{dN} = C\left(\Delta\sigma\sqrt{\pi a}\,y\right)^m \tag{2.6}$$

Many different variations of the da/dn vs. ΔK relationship have been proposed to capture behavior at small and large ΔK and to take into account R ratio effects. Two of the more

popular equations are the Forman's and Walker's [59-61] equations seen as Equations 2.7 and 2.8 respectively.

$$\frac{da}{dN} = \frac{C\Delta K^m}{(1-R)K_c - \Delta K} \tag{2.7}$$

$$\frac{da}{dN} = C\left[(1-R)^m K_{\max}\right]^n \tag{2.8}$$

2.5.4: Crack tip Stresses and Strains Approach

A lot of theoretical work has been performed looking at the crack tip stress fields in crystals and single crystals [62-67]. In addition a strain intensity approach has successfully been used to determine fatigue crack growth rates at high temperature in superalloys [68]. This work along with experimental studies examining the strain fields in front of single crystal crack tips [69-73] has laid a solid foundation for the creation of 3 dimensional stress field single crystal crack tip modeling [74-77]. The Smith-Watson-Topper and Fatemi-Socie Paramter critical plane approach has shown promise in the prediction of fatigue crack initiation life [78]. Another option would be to combine shear and normal strains using something like Socie's parameter. This new driving function could then be used to model crack growth in a way similar to how ΔK operates in isotropic materials.

Fatigue crack growth work performed on single crystal CMSX-2 by Antolovich [79] has opened the door for a generalized single crystal model based on a local approach. He stated that in order to create a proper model that takes into account both the changing

intrinsic and extrinsic variables a combined mechanics and mechanisms approach is more appropriate than the usual phenomenological approach. He developed an understanding of the mechanisms of crack advance and the effect of intrinsic and extrinsic variables upon these mechanisms.

The conclusions of Antolovich's [80] work are as follows:

> "The results of this research program show that regardless of testing conditions, two distinct morphologies develop on the fracture surfaces when CMSX-2 single crystals are subjected to fatigue loading. These two morphologies have been shown to correspond to two distinct mechanisms of crack advance which can be related to two fundamental dislocation/precipitate interactions: (1) bypassing and (2) shearing. Furthermore, these mechanisms have been shown to be directly linked to the applied state of stress. This strongly implies that the specimen geometry will play a controlling role in what mechanisms of crack advance operate.
>
> The mechanism of crack advance was also shown to be dependent upon intrinsic variables and other extrinsic variables besides applied state of stress. The primary intrinsic variable which was shown to control the mechanisms of crack advance was the strength of the γ' precipitates. Specifically, increasing the resistance of the γ' precipitates to dislocation motion with increasing temperature was shown to promote crack advance by γ' avoidance instead of γ' shearing.

The primary conclusions of this research are:

> Two different fundamental crack growth mechanisms have been identified for the single crystal nickel base superalloy CMSX-2 for five different

temperature/environment combinations: (1) precipitate shearing and (2) precipitate bypassing.

The primary controlling factors for transitions between cracking mechanisms have been identified as (1) stress fields, (2) temperature and (3) environment. Crack growth on {111} planes has been attributed to dislocation shearing of γ' precipitates. Crack growth which avoids γ' precipitates has been attributed to dislocation segregation to the γ matrix.

A 3-dimensional FEA which models the observed crack geometries has been employed to determine the stress fields ahead of the crack tip. The FEA did not require unrealistic assumptions regarding the crack tip geometry or an assumed state of stress or strain.

The stress fields predicted by FEA have been correlated to the mechanisms of crack growth. Crystallographic crack growth has been associated with regions of high shear stresses resolved in the direction of the Burgers vector and low normal stresses to the plane containing the Burgers vector. γ' avoidance by the crack has been correlated to low shear stresses resolved in the direction of the Burgers vector and high normal stresses to the faces of the γ' precipitates.

Increasing temperature has been shown to increase the amount of γ' avoidance by the crack due to increased resistance to dislocation movement within the γ' precipitates."

2.6: Fatigue Crack Service Life Prediction Methodologies

2.6.1: Safe-Life (Life-to-First-Crack)

The safe-life, also known as the life-to-first-crack approach to lifing is the most conservative of all life prediction techniques. Safe-life assumes new parts are defect free and as soon as the component reaches a predetermined cycle count based on studies of smooth bar specimens, the critical gas engine element is replaced regardless of the state of the particular part. With improving NDI techniques, the acceptable crack size is decreasing, with current capabilities being between 0.38mm and 0.75mm [81-83]. In the case of turbine disks, spin tests are performed to determine the number of cycles required to grow a crack to the NDI detection limit. A predicted safe cyclic life (PSCL) is then calculated where only 1 in 750 disks would have a NDI detection limit, to 95% confidence. Assuming a scatter factor of 6, the -3σ quartile is located a factor of $\sqrt{6}$ below the geometric mean of the spin testing data, seen in Figure 2.17. This lower confidence bound corresponds to a $6^{1.645/6\sqrt{n}}$ life safety factor.

Where n is the test sample size and a 95% confidence level corresponds to 1.645. The predicted safe cyclic life of the component is then calculated using the following equation:

$$PSCL = \frac{\sqrt[n]{\prod_{i=1}^{n} N_i}}{2.449x6^{(1.645/6\sqrt{n})}} \quad \textbf{(2.9)}$$

Where $N_{i,}$ are the individual spin test results. This life prediction technique is very conservative as the crack length to promote fast fracture is most likely larger than the NDI detection limit.

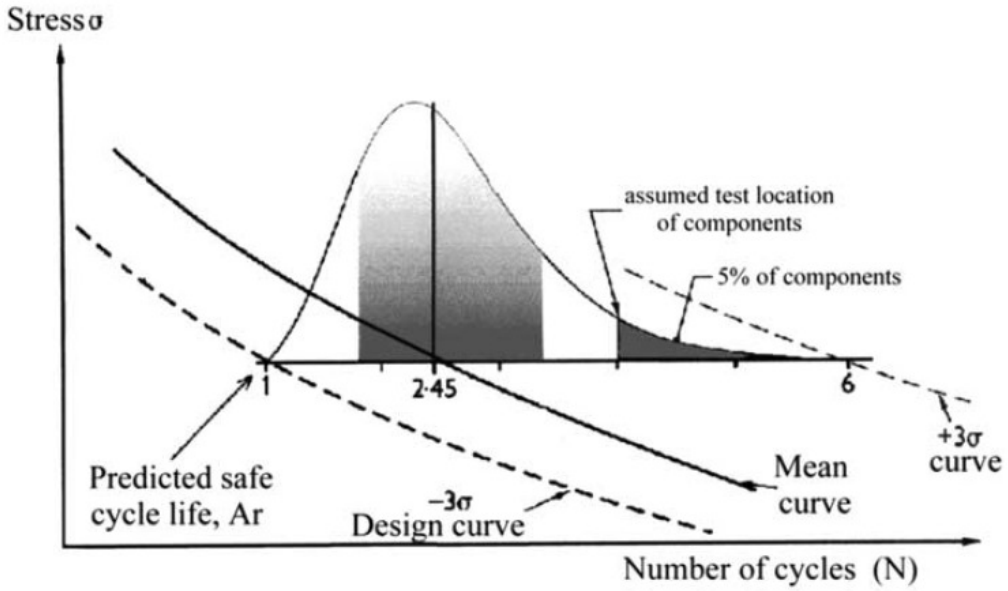

Figure 2.17: Derivation of the Material Design Curve and Predicted Safe Cyclic Life [81]

2.6.2: Damage-Tolerant (Retirement for Cause)

The damage-tolerant, also known as the retirement for cause approach came about due to the life monitoring requirements in the Engine Structural Integrity Program (ENSIP) introduced in the 1970's [84]. This lifing approach is based on the premise that even new components may have flaws that grow in a predictable manner until a critical crack length is reached. This initial flaw size is assumed to be the NDI detection limit. This limit is combined with fracture mechanics and fatigue crack growth data to determine the fatigue life. Integrating the Paris expression creates the following equation for calculating the number of cycles for failure:

$$N_f = \frac{2}{(m-2)Cf^m(\Delta\sigma)^m\pi^{m/2}}\left[\frac{1}{(a_{NDI})^{(m-2)/2}} - \frac{1}{(a_{crit})^{(m-2)/2}}\right] \quad \textbf{(2.10)}$$

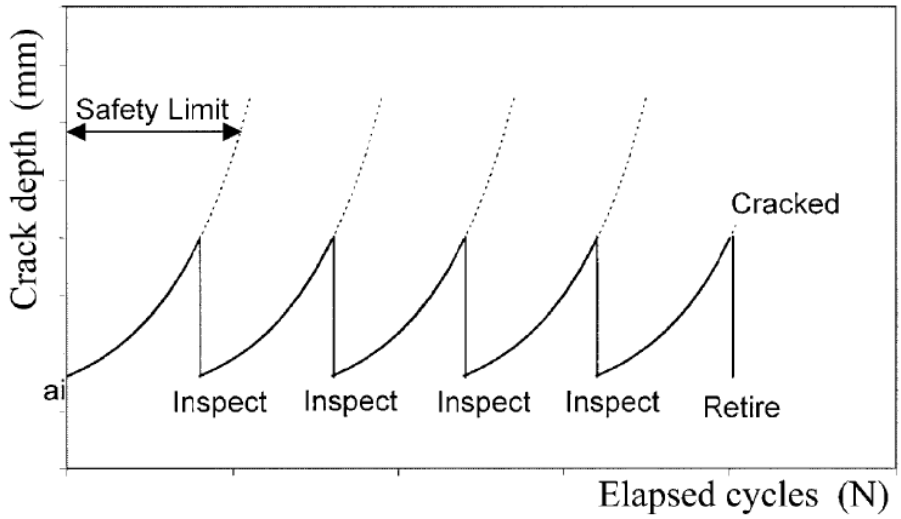

Figure 2.18: Schematic Representation of the Retirement for Cause Approach Where Inspections Are Used to Extend Damage Tolerance [81]

This calculated fatigue life is then used to set up NDI intervals as seen in Figure 2.18. The initial inspection interval is usually ½ of the calculated fatigue life. To maximize the life of the component additional inspection intervals are added with decreasing cyclic duration. This combination of damage tolerance and risk analysis creates the foundation for the U.S Air Force retirement for cause methodology.

2.6.3: Equivalent Initial Flaw Size

The equivalent initial flaw size (EIFS) approach takes into account both initiation and propagation unlike the above mentioned damage tolerant approach that only looks at the propagation life. In that aspect this approach could be thought of as being similar to the safe-life approach but not nearly as conservative. The initiation life of a fatigue crack is

very difficult to predict, being a complicated function of material type, processing, environment, geometry and loading spectrum. It is often difficult to come to a general consensus on what is the definition of a crack. The key is being able to properly determine, initiation time, which is the number of cycles it takes to reach a crack size that is detectable using NDI techniques. Being able to properly predict this adds more fidelity to a model than just setting the initial crack size to the NDI limit. Using data available the EIFS is determined by extrapolating back to a time or cycle count equal to zero. As shown by Johnson [85], these EIFS distributions, seen in Figure 2.19, can then be used as a more precise starting point for probabilistic and damage tolerance approaches to FCG life prediction.

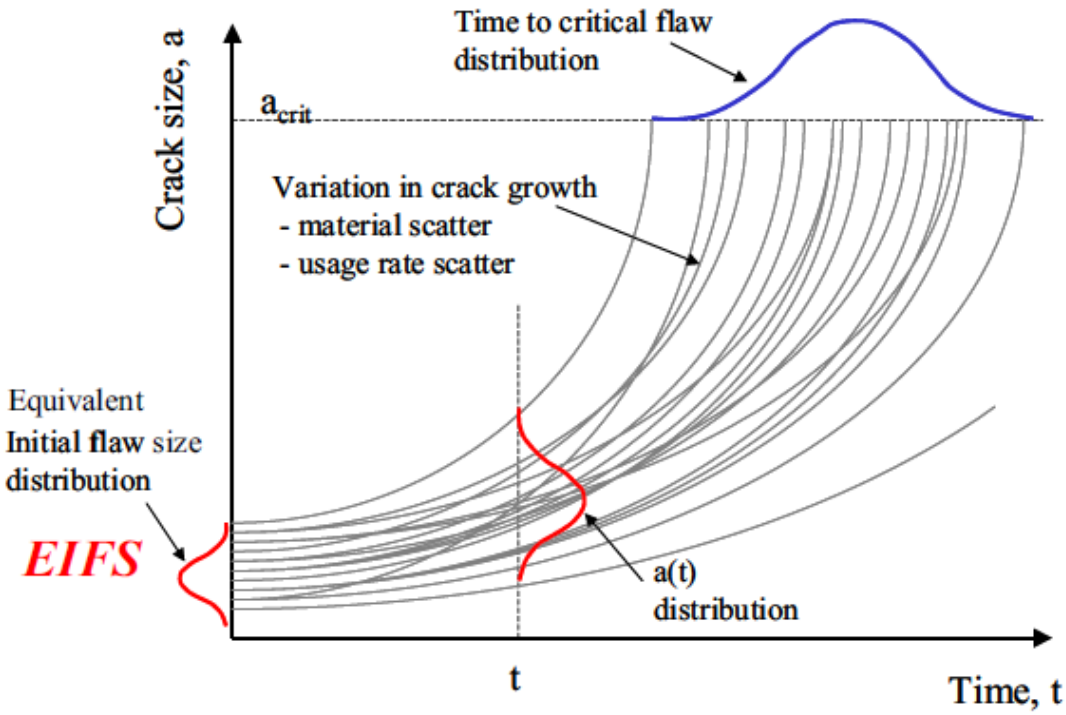

Figure 2.19: The Equivalent Initial Flaw Size Can Be Used as Starting Point for Probabilistic Life Prediction [85]

2.7: Thermo-Mechanical Fatigue Behavior of Superalloys

2.7.1: Fatigue Crack Initiation

It is important to note that the initiation mode in single crystal superalloys usually determines the initial mode of crack propagation. For these materials crack initiation predominantly falls into two categories, crystallographic, along {111} slip planes and non-crystallographic. In both cases the site of initiation is usually located at a micropore or tantalum carbide (TaC). An example of a non-crystallographic fatigue crack initiation at a micropore is shown in Figure 2.20. The environment, stress level and temperature are mainly what determines the type of initiation [17]. At low stresses and temperatures fatigue crack initiation is chiefly crystallographic in nature. At higher stresses and temperatures the initiation transitions to non-crystallographic. Work performed by DeLuca and Cowles [86] has also shown fatigue crack initiation to occur at the γ and γ' interface leading to cracking in the <001> family of directions due to the interface lying perpendicular to the cubic plans.

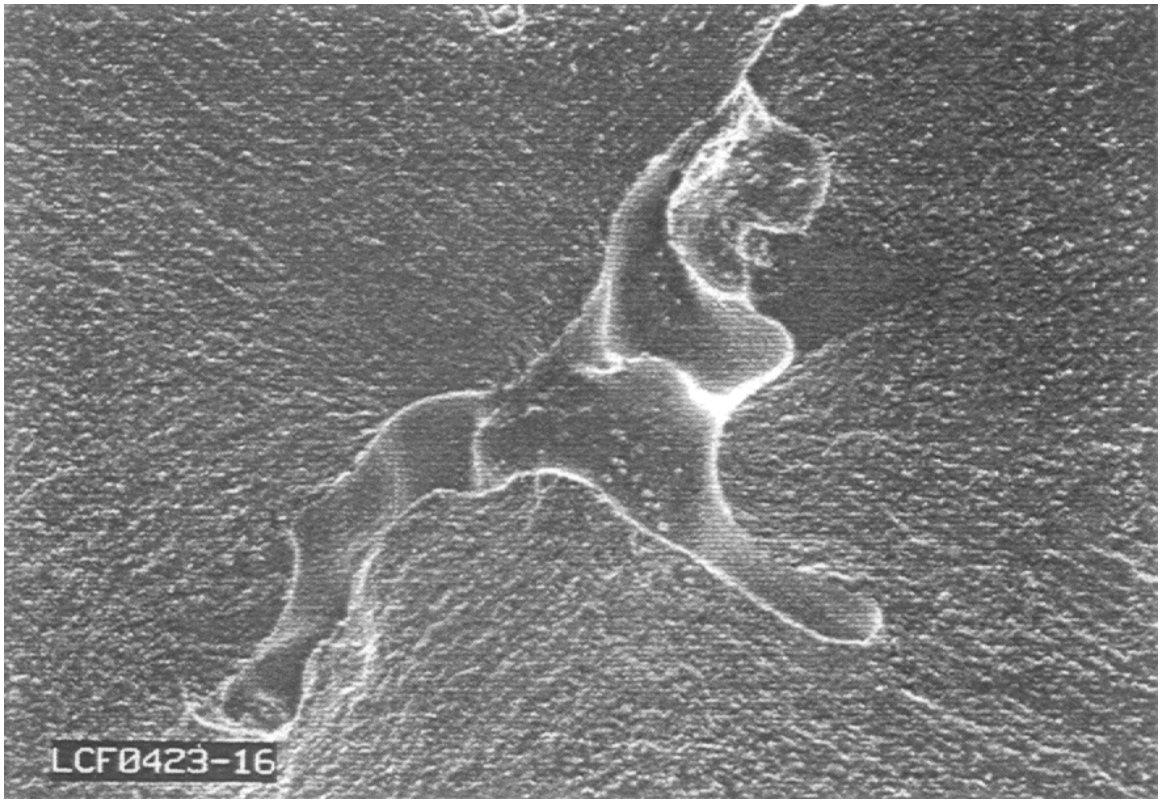

Figure 2.20: A Non-Crystallographic Fatigue Crack Initiation at a Micropore in PWA1480 [17]

2.7.2: Fatigue Crack Propagation

The fatigue crack propagation behavior of single crystal superalloys is mainly dependent on temperature, frequency, orientation and stress intensity [87, 88]. Studies have shown that three different fracture modes exist for single crystal superalloys. Two are crystallographic in nature while the third is non-crystallographic [89-91]. An example of two different fracture modes emanating from a micropore is shown in Figure 2.21. Common at low temperatures and stresses the first crystallographic mode is perpendicular to the applied load on the {001} family of planes. The mode I stress intensity calculations have been found to remain valid during this type of cracking [89, 92]. The second crystallographic mode is also common at lower temperatures with fracture occurring on the {111} global octahedral planes [93-97]. These fracture planes

can vary significantly from the plane normal to the applied loading. As such a mixed mode approach (mode I and II) must be taken when calculating the stress intensity factor. Realizing a need for a modified stress intensity factor taking into account resolved shear stress on octahedral planes at the crack tip, Chen and Liu [98] formulated the resolved shear stress intensity coefficient (RSSIC). Telesman and Ghosn [87] took this one step further and defined the resolved shear stress intensity parameter:

$$K_{RSS} = \lim_{r \to 0} \tau_{RSS} \sqrt{2\pi r} \tag{2.11}$$

Where the resolved shear stress is calculated by projecting the stress tensor at the crack tip on an outward normal plane in the direction of the Burgers vector [99]:

$$\tau_{RSS} = \vec{b} \cdot [\sigma] \vec{n} \tag{2.12}$$

Lerch and Antolovich [100] discussed how the preferred crack plane can be determined by considering the {111} plane with the largest combination of shear stress in the direction of the Burgers vector along with the stress normal to that plane. Furthering this idea Telesman and Ghosn [87] proposed the octahedral stress intensity factor which also takes into account the stresses normal to the {111} octahedral planes:

$$\Delta K_{OCT} = \left[\left(\Delta K_{RSS} \right)^2 + \left(\Delta K_{ION(111)} \right)^2 \right]^{1/2} \tag{2.13}$$

At higher temperatures, slower frequencies and larger stress intensity factors crack growth in single crystal nickel superalloys has shown to propagate transprecipitate non-crystallographic (TPNC) through both γ and γ' phases [17, 91]. As this crack growth is

perpendicular to the applied loading mode I stress intensity factor solutions are appropriate.

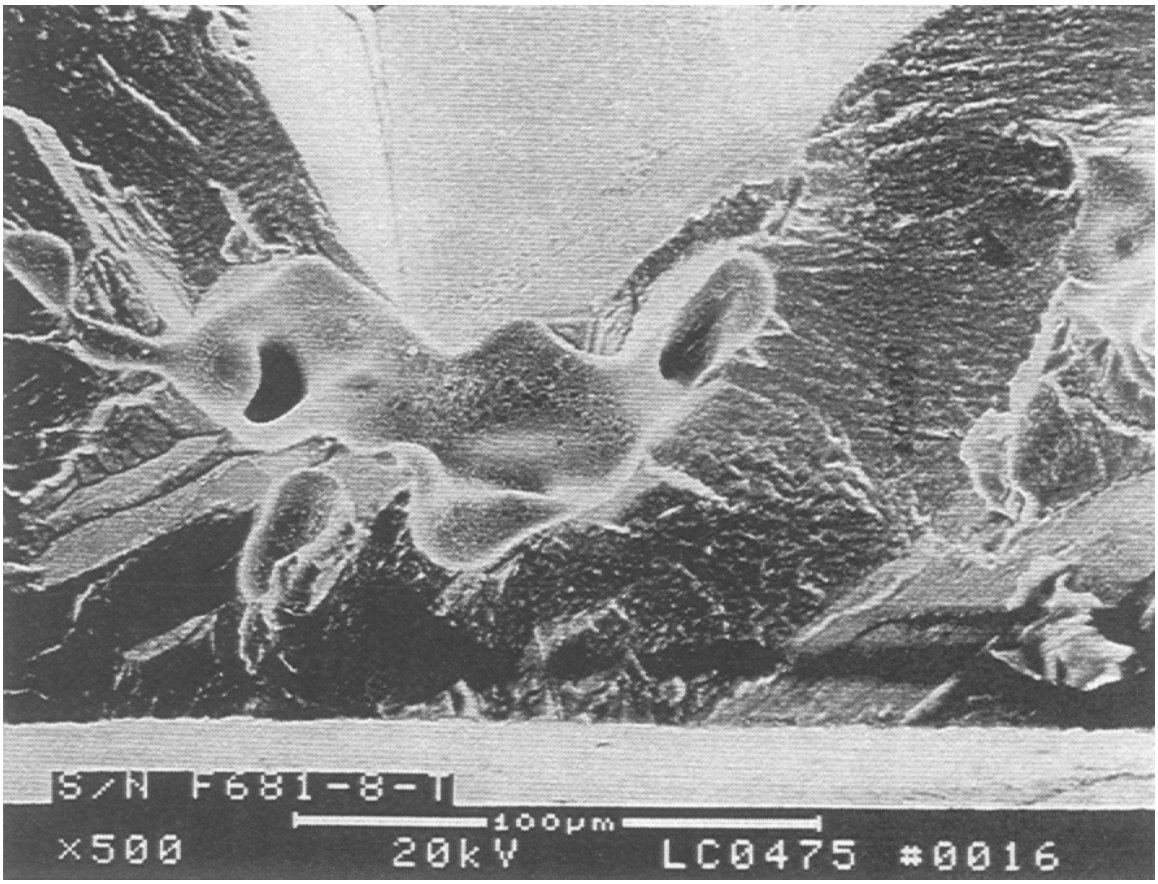

Figure 2.21: A Crystallographic and Non-Crystallographic Fracture Initiated from a Micropore in PWA1484 [17]

2.7.3: Effect of Microstructure on Propagation Rates

As mentioned in Section 2.4 it is well known that the gamma prime phase is responsible for giving superalloys their superior strength at high temperature. This is primarily through the phases' ability to disrupt the translation motion of dislocations. It has been shown that fine and coarse γ' react differently during plastic deformation; the underlying failure mechanism of fine precipitates is by shearing while coarse γ' are avoided by a

process known as Orowan looping [101]. It is reasonable to believe that changing the size and distribution of the gamma prime phase through the chemical composition and heat treatment would have a profound effect on the fatigue crack growth rate [102]. There have been many tests performed looking at the effect of gamma prime morphology on FCGR, with sometimes contradicting results. Antolovich and Jayaraman [103, 104] performed fatigue crack growth rate testing on two different sized gamma prime Waspaloy materials. Through testing it was shown that decreasing the precipitate size from 100 nm to 10 nm resulted in decreased FCGR of almost 5x [105]. Testing by Bowman [106] showed that the fatigue crack propagation rate can be slowed by decreasing the volume fraction of gamma prime and by decreasing the precipitate size. Work performed by Boyd-Lee [107] has shown that increased uniformity in the distribution of gamma prime leads to a slower FCGR. Conversely, testing performed by Gayda and Miner [108] on P/M Astroloy showed that the fatigue crack growth rate decreased as the gamma prime size and volume fraction were increased through aging to increase strength. These results could have been confounded by simultaneously changing both the gamma prime size and volume fraction. Even though the effect of changing precipitate size and distribution is not entirely clear the general consensus is that decreasing gamma prime size and the volume fraction decreases the FCGR.

Work done by Telesman et al. [109] on a low solvus, high refractory superalloy showed that a super-solvus heat treatment slowed the FCGR by a factor of 10x over a sub-solvus heat treatment. This work also showed that the super-solvus heat treatment had much more effect on the FCGR than any chemical composition which affects the

microstructure. On top of that it has been shown that cooling rates of turbine disks play a large part in gamma prime precipitate size. Gabb et al. [110] noticed that uneven cooling between the disk bore and rim led to a variation of precipitate sizes, with the faster cooling rim having a desired uniform precipitate size. On the other hand, the slower cooling bore had a bimodal mix of large and small size precipitates. Reed [11] states that to create strength and fatigue resistance the gamma prime phase should be optimized with γ' forming agents Al, Ti and Ta to achieve a volume fraction between 60% and 70% and heat treatments should be appropriately applied to ensure a homogeneous allocation. Supporting this statement the creep performance as a function of fraction of strengthening phases can be seen in Figure 2.22.

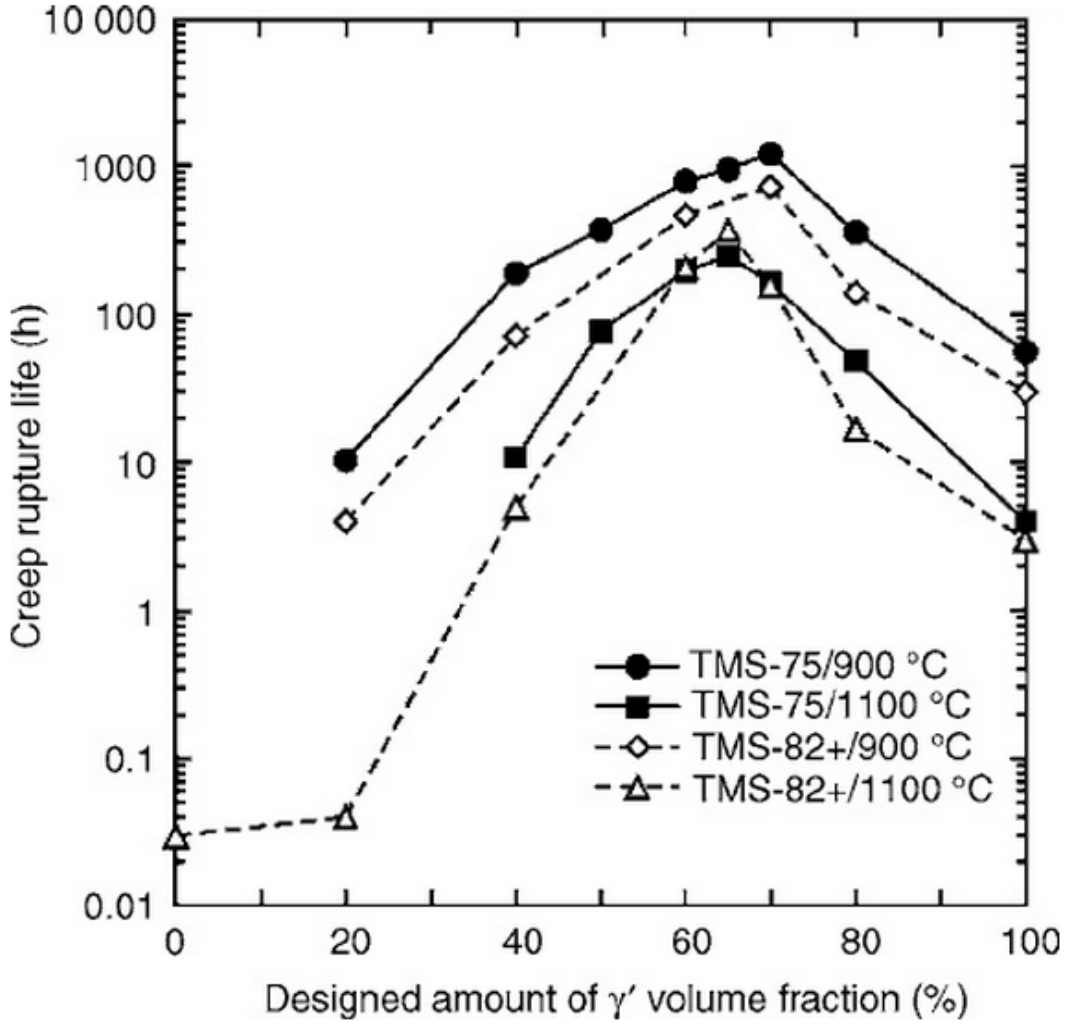

Figure 2.22: Variation of the Creep Rupture Life of the Single-Crystal Superalloys TMS-75 and TMS-82+ as a Function of the Amount of γ' Phase [111]

A review of high temperature fatigue crack propagation of nickel based superalloys done by Pineau and Antolovich [112] shows the importance of not only γ' but also slip mode on the fatigue crack growth rates of superalloys. Looking at model alloys it was shown that an increase in planar reversible slip leads to a larger plastic yield zone at the crack tip causing a decrease in fatigue crack growth rates [113]. Factors such as low anti phase boundary energy (APBE), low stacking fault energy, low lattice parameter mismatch and large grains promote planar reversible slip. Pineau and Antolovich [112] had the following to say about single crystal superalloy, CMSX-2:

"In Ni-base single crystals the fracture surface morphology is related to the environment, to the fundamental nature of the precipitate and to the ratio of the normal to shear stress at the crack front. Crystallographic fracture surfaces are promoted by low temperature (soft γ' easily sheared, reduced environmental effect) in areas where the normal to shear ratio is low. At higher temperatures the fracture surface is macroscopically flat where the normal to shear ratio is high because the γ' is harder (not easily sheared) and the normal stress promotes fracture at the oxygen-enriched γ/γ' interface. In this case the microscopic appearance of the fracture surface is γ' avoidance. Because of the highly irregular fracture surface, the utility of using a simple stress intensity to characterize fracture behavior is called into question."

2.7.4: Effect of Environment on Propagation Rates

The role that temperature plays on the fatigue crack growth rate has been extensively studied for many different superalloys. Work with single crystal superalloy CMSX-6 by Martínez-Esnaola et al. [114] and IN100 compact tension specimens by Larsen et al. [115] validates the commonly held notion that increasing temperature leads to an increase in crack growth rate. This trend can be seen in Figure 2.23. This same trend was seen by Henderson and Martin [116] in their research with single crystal SRR99. Gabb et al. [110] looked at the effect of temperature on the TMF crack growth rate of ME3, also known as René 104. Their research showed that the crack growth rate increased with temperature at R ratios of -0.25, 0.05, 0.25 and 0.5. In going from 25°C to 650°C the crack growth rate increased almost ten times. A 90 second dwell at maximum stress was used to determine the effect of temperature on the dwell crack growth rate. The dwell crack growth rates at R ratios of 0 and 0.05 also increased with temperature although with

a stronger correlation showing the strong effect that time at temperature plays on crack growth rate.

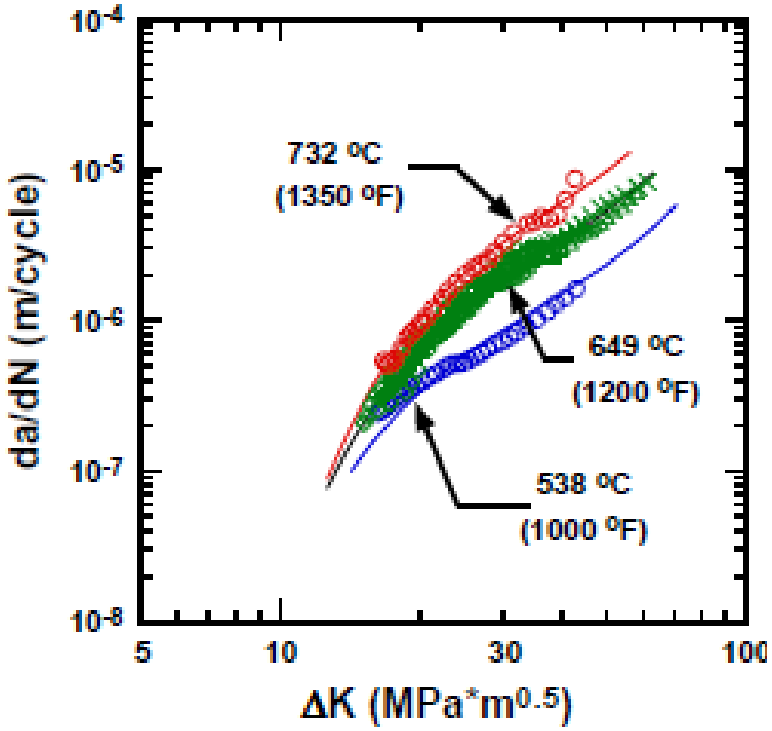

Figure 2.23: Effect of Temperature on Crack Growth in IN100; R = 0.1, Frequency = 0.167 Hz [115]

The fatigue crack growth rates of single crystal superalloys change with temperature due to the underlying change in damage mechanism. At room temperature and low ΔK values, heterogeneous slip promotes FCG along {111} crystallographic planes. This, 'planar slip', is due to only a few slip systems being activated at these lower temperatures. This heterogeneous slip behavior can also be seen at higher temperatures for high cyclic frequencies. As temperature increases and more slip systems become active the slip becomes more homogeneous with the FCG happening along {001} crystallographic facets. In addition to increasing temperature this homogeneous slip is

also seen at larger ΔK values. Micromechanisms of fracture also change with increasing temperature and as a function of frequency. At low temperatures fracture is predominantly crystallographic. This crystallographic fracture extends up to high temperatures at high cyclic frequencies and in the absence of an oxidizing environment. At low cyclic frequencies in high temperature oxidizing environments chemical attack occurs in areas of weakness, not unlike polycrystalline superalloys [11, 56, 112, 117]. In the case of single crystal superalloys irregular gamma primes and interdendritic pores are attacked promoting interdendritic fracture [118, 119]. Work performed by Telesman and Ghosn [87] with PWA1484 demonstrates an interesting phenomenon that temperature has on the fatigue crack growth rate of PWA1484. As seen in Figure 2.24 the FCGR increases for the most part with increasing temperature. Above 760°C increasing temperature actually leads to a decrease in fatigue crack growth rate at the lower values of ΔK. As ΔK increases the FCGR at 871°C transitions to be one of the fastest growth rates as one would expect. This phenomenon has been explained by Antolovich et al. [120] on their work with René 80.

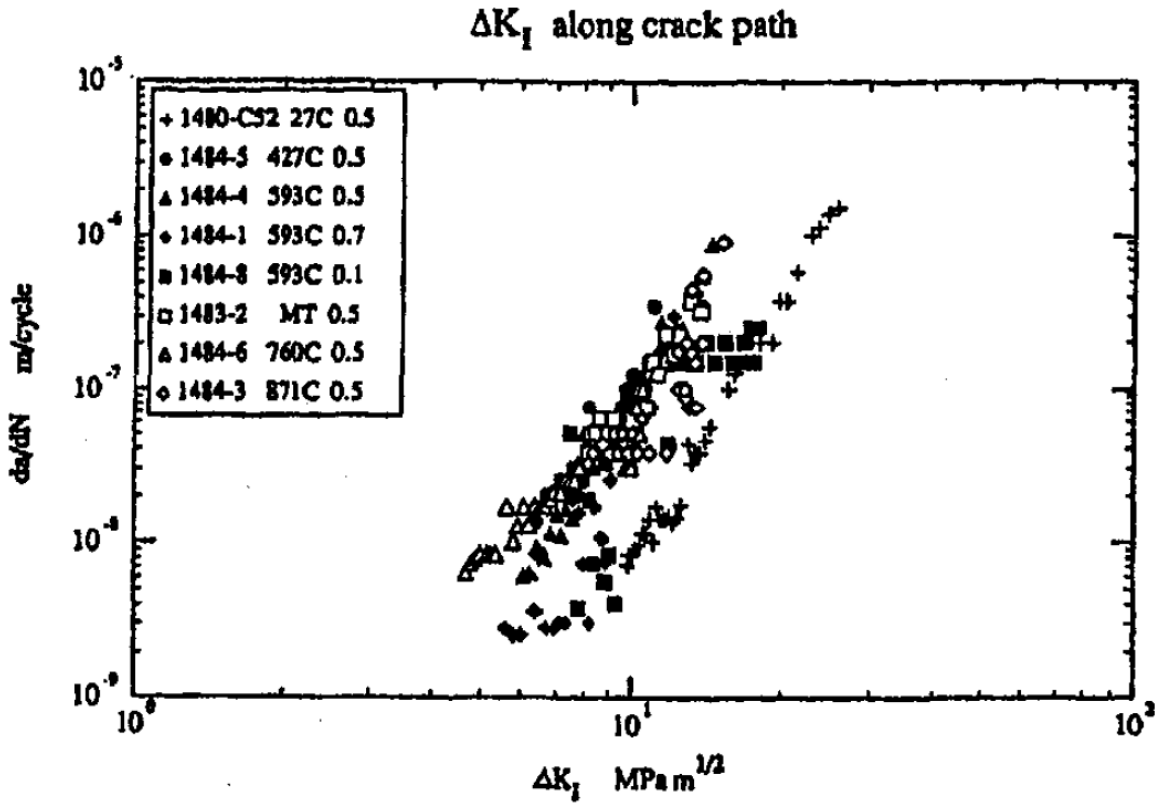

Figure 2.24: Fatigue Crack Growth Rates in PWA1484 at Temperature from 27°C to 871°C [87]

Numerous studies have shown that the environment, in particular the presence of oxygen at the crack tip increases the crack growth rate [121-123]. It is well known that turbine blades and disks operating in very hot corrosive environments have shorter lives than similar components running in hot only environments. Hancock [124] reasoned for the environment to have any effect on fatigue crack growth rates it has to have access to the crack tip and when environmental factors are present the effect is more pronounced on initiation life than propagation life. Earlier testing by Hoffelner [125] showed that the fatigue crack growth rate of IN738LC and IN939 was unaffected by synthetic flue ash in SO_2 and SO_3 when compared to the rates in air. The effect of environment was also considered by Hancock [124] on polished round bar Nimonic alloy 90 specimens. Testing performed by Hancock showed that Nimonic alloy 90 specimens tested at 850°C

had fatigue lives reduced by as much as 2x when tested in a sea salt environment. Hancock attributed these differences to initiation and propagation concluding that components with existing surface cracks would not be as affected by environment as components without preexisting cracks. Andrieu et al. [126] leveraging off extensive work showing that environmental crack growth rate increase is the result of oxygen at the crack tip, worked with Inconel 718 to show the role that oxygen plays on the crack growth rate. Andieu work with compact specimens at 0.05 Hz, R = 0.1 and 650°C showed that it took 5000 cycles in air while it took 65,000 cycles to grow the same crack length in a vacuum. Also looked at was the effect of adding a 600 second hold time at minimum load showed increased crack growth over the continuous 0.05 Hz test in air.

The environmental fatigue crack propagation behavior of single crystal CMSX-2 was investigated by Antolovich et al. [79] in air and vacuum at room temperature and 700°C. It was found that when using the Mode I stress intensity factor the fatigue crack growth rates were rather independent of the crystallographic orientation, temperature and environment. In addition the fracture surfaces at RT and 700°C were characterized by what resembled cleavage along {111} planes and at 700°C only a rough surface that propagated normal to the loading axis. It was determined that the morphology of the crack surface was either ‘‘shearing” or undergoing ‘‘precipitate avoidance” due to the ratio of normal stresses to shear stresses at the crack tip depending on the particular environment. The validity of the Mode I stress intensity solution for crack growth in single crystals was also brought into question.

2.7.5: Effect of Operating Conditions on Propagation Rates

It has been shown that changing frequency is of little significance at room temperatures and under vacuum, clearly showing frequency is a magnifier of the previously mentioned effects of temperature and environment. Larsen's and Adair's [115, 127] work with IN100 along with many others have shown that frequency has an inverse relationship with FCGR, where with decreasing frequency comes an increased crack growth rate. At lower frequencies the crack tip is open longer allowing the environment to influence the FCGR.

The role of R ratio on FCGR is not entirely clear with some studies showing stress ratio is dominated by crack closure at lower ratios. Crack closure has been shown to be greatly dependent on temperature, environment, microstructure etc. At R ratios of -0.25, 0.05, 0.25 and 0.5 Gabb et al. [110] work with René 104 revealed for the most part that the FCGR tended to increase with decreasing R ratio but this trend was not very clear. Conversely, Larsen et al. [115] testing of IN100 demonstrated that increasing the R ratio led to a direct increase in the fatigue crack growth rate. This relationship became more apparent with increasing R ratio showing the dominance of crack closure at lower ratios. Mercer, Shademan and Soboyejo [128] looked at the effects of R ratio for Inconel 718 with the same result as Larsens' study where increased crack growth rate follows an increasing R ratio. Work performed by Telesman and Ghosn [87] with PWA1484 show a weak correlation between increasing R ratio and increasing crack growth rate at 593°C as seen in Figure 2.25. Their results show that the crack growth rate at R=0.5 is faster than R=0.1 but on the other hand the crack growth rates at R=0.5 and R=0.7 are very similar. Work by Krueger et al. [129] looking at the effect of grain size and precipitate size on the

fatigue crack growth rates for four different microstructures showed that closure was not responsible for microstructural effects. For an R Ratio of 0.75, the effects of grain size and γ'' size were indistinguishable from those observed at an R Ratio of 0.05. This demonstrated that roughness-induced closure had a minimal influence on fatigue crack growth rates. These results demonstrate the ambiguity present when determining the effect of R ratio and closure on the fatigue crack growth rate in superalloys.

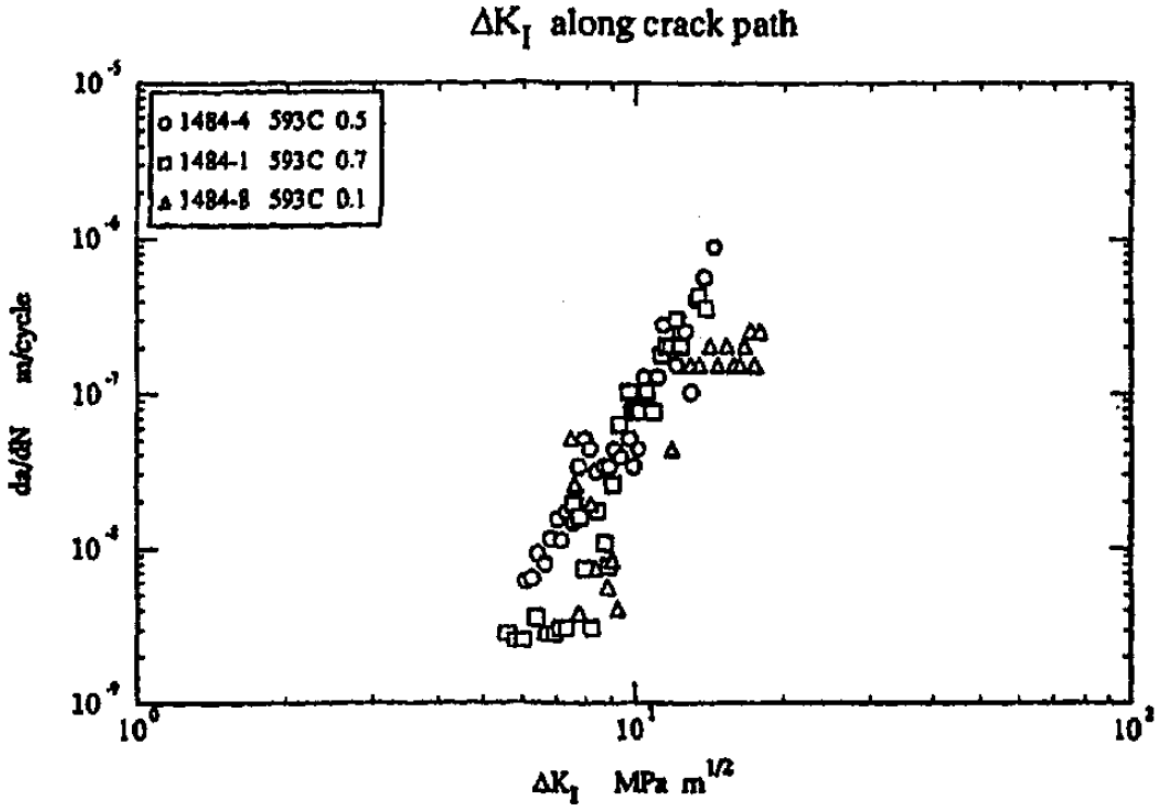

Figure 2.25: Fatigue Crack Growth Rates in PWA1484 at R=0.1, R=0.5 and R=0.7 [87]

The influence of overloads on nickel based superalloys is not widely reported in the literature. Overloads, common in flight loading spectrums, create a large overload plastic yield zone that has to be grown through creating a period of retarded crack growth. Larsen et al. [115] have looked into the effect of overload size and cycles between

overloads on powdered metallurgy IN100. All testing was performed at 649°C at an R ratio of 0.5 and frequency of 0.167 Hz using compact tension specimens to ASTM standards. The effect of 1.25 and 1.5 overloads with 40 1.0x cycles between were also examined, with increasing overloads leading to a decrease in the crack growth rate. This trend can be seen in Figure 2.26. It was also shown that the smaller number of cycles between overloads (CBO) led to an increase in the crack growth rate. This trend can be seen in Figure 2.27.

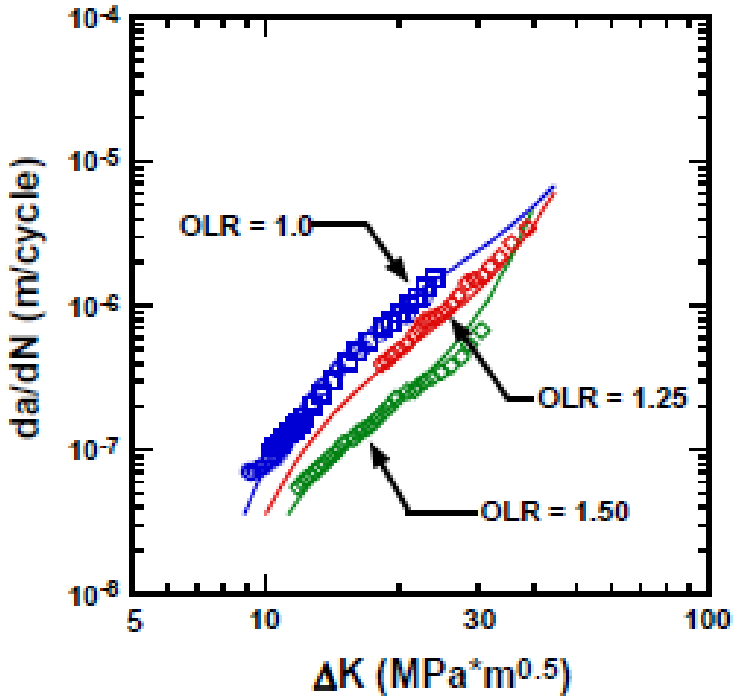

Figure 2.26: Effect of Overload Ratio (OLR) on Crack Growth in IN100; T = 649°C, R = 0.5, Freq = 0.167 Hz, CBO = 40 [115]

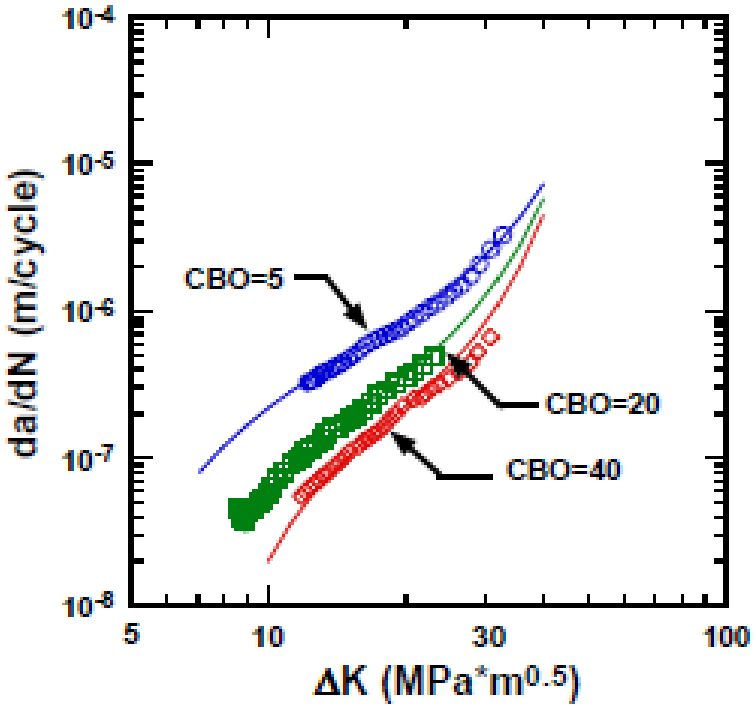

Figure 2.27: Effect of Number of Cycles Between Overloads (CBO) on Crack Growth in IN100; T = 649°C, R = 0.5, Freq = 0.167 Hz, OLR = 1.5 [115]

Numerous fatigue crack growth studies on a variety of materials have reported on the underlying mechanisms responsible for load interaction effects, as illustrated in extensive literature reviews [130-132]. In particular there have been several studies on the effect of overloads on the fatigue crack growth rate in superalloys [115, 133-136]. When it comes to temperature interaction effects most work has been concerned with using two types of idealized TMF cycles: in-phase (IP) and out-of-phase (OP) [137-141]. Studies utilizing nontraditional types of TMF cycles are of particular interest to this research. For example Cailletaud and Chaboche [142] used block temperature changes to look at the cyclic viscoplastic behavior of IN100. Work by Adair et al. [143] took this block temperature idea one step further by looking at the effect on fatigue crack growth rate in IN100. Barker and Johnson [144] created a multi-parameter yield zone model that takes

into account temperature interaction and load interactions based of the work by Adair. Presently there is no known published literature that investigates the interaction effect of alternating temperature blocks on fatigue crack propagation in superalloys outside of the work by Adair et al.

2.7.6: Effect of Crystal Orientation on Propagation Rates

An investigation by Kiyak et al. [145] looking at the influence of crystal orientation on the crack growth behavior found that in the Paris regime and in the (001) plane cracks grew approximately two times faster in the [100] direction than in the [110] direction. Similar results were obtained by Anton [146] who discovered that in the (001) plane crack growth rate was largest in the [010] direction and smallest in the [011] direction. Kiyak et al. [145] also revealed that there was no noticeable crack growth rate difference between growth in the [110] direction in the (001) plane and growth in the [-1-12] direction in the (111) plane. Chan et al. [147] looked at the fatigue crack growth behavior of PWA1484 under mixed loading and found that the Mode I threshold was highly dependent on the crack growth plane and crack growth direction. Figure 2.28 shows transprecipitate, non-crystallographic (TPNC) fatigue crack results obtained by Chan et al. Notice the variability in crack growth rate even when all testing was performed under the same loading conditions due to slight differences in the secondary orientation.

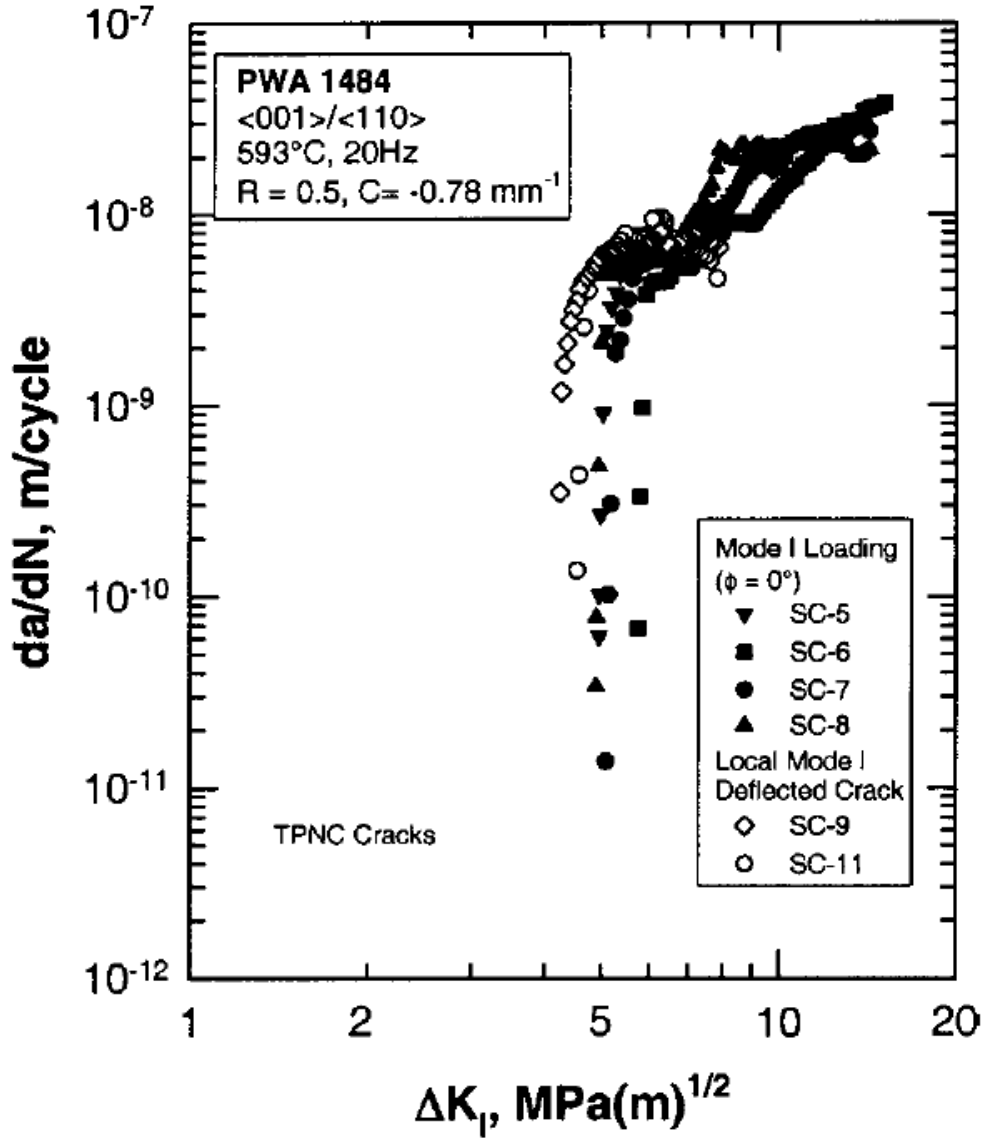

Figure 2.28: PWA1484 Fatigue Crack Growth Rates for <001>/<110> Loaded Specimens at 593°C, R=0.5 and 20Hz [147]

CHAPTER 3: EXPERIMENTAL METHODS

3.1: Material

Rectangular bars (204 mm x 49 mm x 13 mm) of single crystal PWA1484 were cast by Pratt & Whitney at their in house Rapid Prototype Casting Laboratory. The chemical composition for PWA1484 can be seen in Table 2.3. Each slab was verified to be single crystal with a primary (loading) orientation of <001> with a deviation of 11° or less by Laue X-ray diffraction. Twenty four specimens were manufactured without using seed crystals, so secondary orientations were random. An additional thirty specimens were cast with seed crystals ensuring a primary orientation of <001> and secondary orientation of <010>. In addition to the fifty four fatigue crack growth specimens a total of twenty six tensile round bar specimens were manufactured for this research. The specimen orientation details for all specimens can be seen in Table 3.1 through Table 3.3. Figure 3.1 and Figure 3.2 show the Euler angle definitions and analysis setup for the Laue back reflection method. In Table 3.3 the Alpha angle is the misorientation from [001] direction in the primary (loading) direction while the Beta is the misorientation from [001] direction in the secondary (crack growth) direction. For all of these specimens the standard heat treatment of solution annealing at 1316°C for two hours in vacuum, coating diffusion heat treatment at 1080°C for 4 hours in a controlled atmosphere and precipitation heat treatment at 704°C for 24 hours in air was followed [28, 148].

Table 3.1: Material Orientation Details for 24 Fatigue Crack Growth Specimens and 12 Tensile Specimens

Item	Qty	Material	Specimen No:	Dim's as shipped	Orientation	Deviation(deg)
1	1	PWA 1484	023831	~1/2" x 1-15/16" x 8"	<001>	2.6
2	1	PWA 1484	023832	~1/2" x 1-15/16" x 8"	<001>	10.5
3	1	PWA 1484	023833	~1/2" x 1-15/16" x 8"	<001>	7.7
4	1	PWA 1484	023834	~1/2" x 1-15/16" x 8"	<001>	1.7
5	1	PWA 1484	023835	~1/2" x 1-15/16" x 8"	<001>	7.4
6	1	PWA 1484	023836	~1/2" x 1-15/16" x 8"	<001>	5.2
7	1	PWA 1484	023837	~1/2" x 1-15/16" x 8"	<001>	4.2
8	1	PWA 1484	023838	~1/2" x 1-15/16" x 8"	<001>	5
9	1	PWA 1484	023841	~1/2" x 1-15/16" x 7-7/8"	<001>	0.5
10	1	PWA 1484	023842	~1/2" x 1-15/16" x 8"	<001>	2.4
11	1	PWA 1484	023843	~1/2" x 1-15/16" x 8"	<001>	5
12	1	PWA 1484	023844	~1/2" x 1-15/16" x 7-7/8"	<001>	4.1
13	1	PWA 1484	023845	~1/2" x 1-15/16" x 8"	<001>	2.2
14	1	PWA 1484	023846	~1/2" x 1-15/16" x 7-7/8"	<001>	6.1
15	1	PWA 1484	023847	~1/2" x 1-15/16" x 8"	<001>	6.2
16	1	PWA 1484	023848	~1/2" x 1-15/16" x 8"	<001>	7.2

Table 3.2: Material Orientation Details for 14 Tensile Specimens

Specimen #	Alloy & Heat #	Primary Orientation	Deviation, Alpha (degrees)
195003	PWA1484 (1115)	<001>	7.4
195010	PWA1484 (1115)	<001>	5.0
210902	PWA1484 (1115)	<001>	2.7
210907	PWA1484 (1115)	<001>	6.3
210912	PWA1484 (1115)	<001>	6.3
210905	PWA1484 (1115)	<001>	2.7
210910	PWA1484 (1115)	<001>	5.1
210908	PWA1484 (1115)	<001>	8.9
210906	PWA1484 (1115)	<001>	9.1
215007	PWA1484 (1115)	<001>	4.4
215012	PWA1484 (1115)	<001>	7.2
963804	PWA1484 (1082)	<001>	6.0
963307	PWA1484 (1082)	<001>	7.2
963803	PWA1484 (1082)	<001>	1.2

Table 3.3: Material Orientation Details for 30 Fatigue Crack Growth Specimens

Serial Number	MAG #	Orientation	Alpha	Beta	Gamma	Delta
Category B	MAG					
5111BA-1	14929	<001>	3	3	-3	0
5111BB-5	14929	<001>	6	3	5	-5
5111BA-9	14929	<001>	3	-2	-3	0
5111BB-12	14929	<001>	2	5	-1	-2
Category A						
5111BB-2	14929	<001>	7	-2	-6	3
5111BB-3	14929	<001>	2	-4	1	-1
5111BB-4	14929	<001>	1	4	-1	1
5111BB-7	14929	<001>	0	3	0	0
5111BB-8	14929	<001>	2	4	1	-2
5111BB-9	14929	<001>	4	3	-1	3
5111BB-10	14929	<001>	1	4	1	0

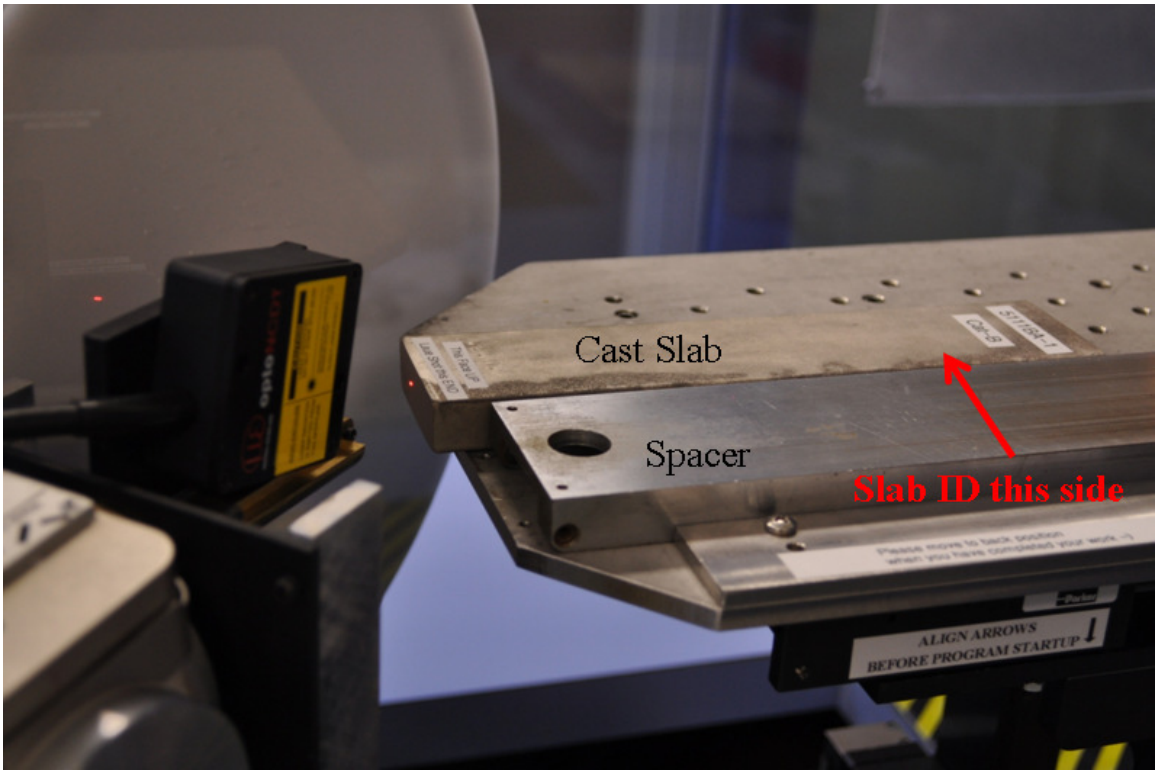

Figure 3.1: Cast Slabs for Single Edge Notch Specimen Laue Analysis, Showing Setup on Laue System

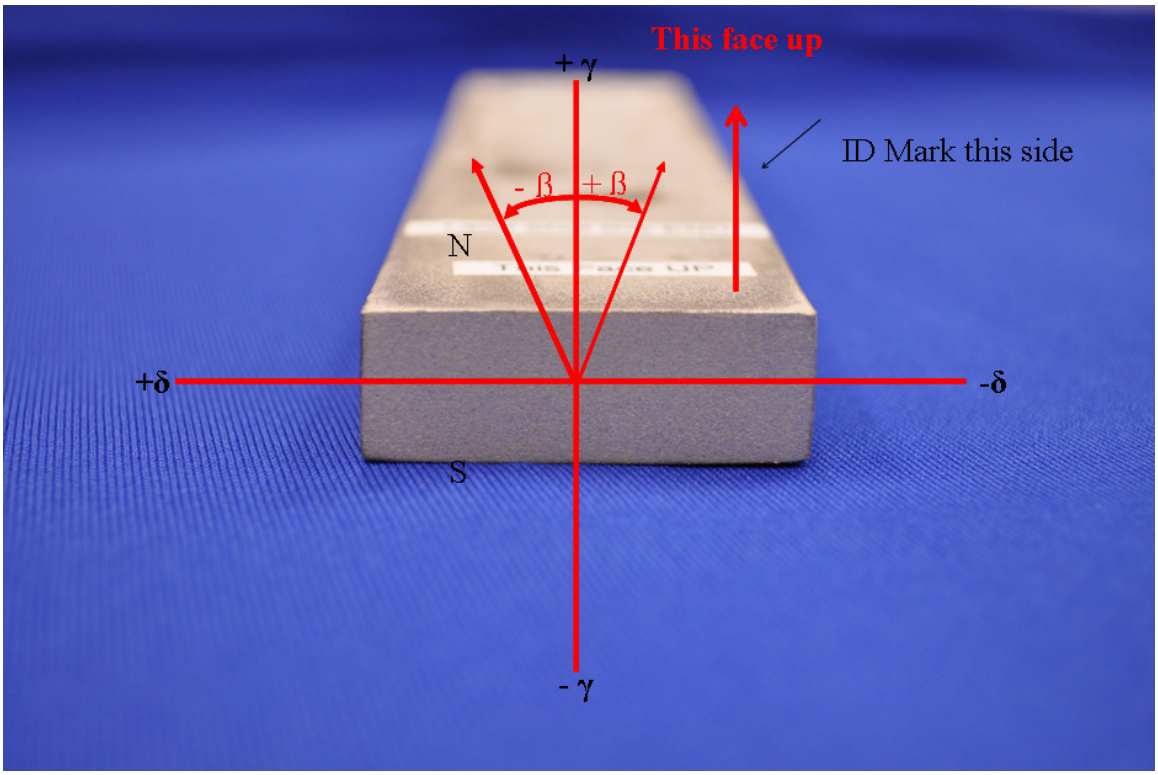

Figure 3.2: Cast Slabs for Single Edge Notch Specimen Laue Analysis, Showing Definitions of Beta, Delta, and Gamma

3.2: Specimens

3.2.1: Specimen Design

For this investigation the single edge notch tension (SENT) specimen configuration was chosen due to the ease of crack length measurement and ability to be gripped with water cooled hydraulic wedge grips. This water cooled gripping arrangement allowed for more rapid cooling than a pin loaded arrangement. The test specimens are 203.2 mm long, 38.1 mm wide and 2.54 mm thick as seen in Figure 3.3. The wall thickness of turbine engine blades are on the order of 0.3 to 2.5 mm with the thickest part of the blade located at the root which is right above the blade attachment [149]. This research program aimed to have as thin as possible specimens while still meeting plane strain testing requirements. Either two or three specimens were cut from each PWA1484 slab using

wire electro-discharge machining (EDM) and low stress grinding. Most fatigue crack growth data found in literature is for specimens 6.35 mm and thicker, with very little information available for specimens as thin as 2.54 mm [150]. To promote rapid fatigue crack initiation, wire EDM was used to create an 11.4 mm long notch with a 0.152 mm root radius.

For tensile and cyclic testing three round bar specimens were cut from each PWA1484 slab. These specimens have an overall length of 114.3 mm and a gauge length of 31.8 mm as is shown in Figure 3.4. The gauge diameter is 6.4 mm and the ends are 12.7 mm in diameter for placement in collet grips. The surface finish for these specimens was specified as 32 RMS.

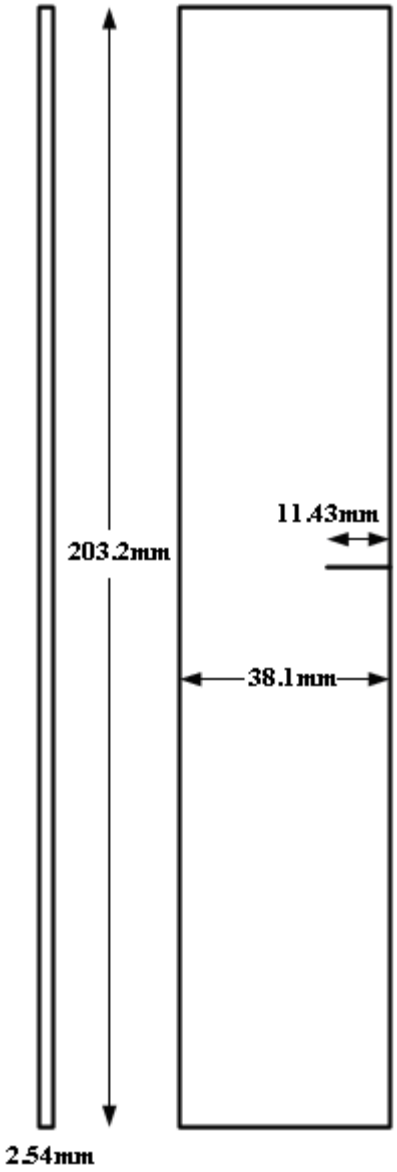

Figure 3.3: Single Edge Notch Tension Specimen with Dimensions

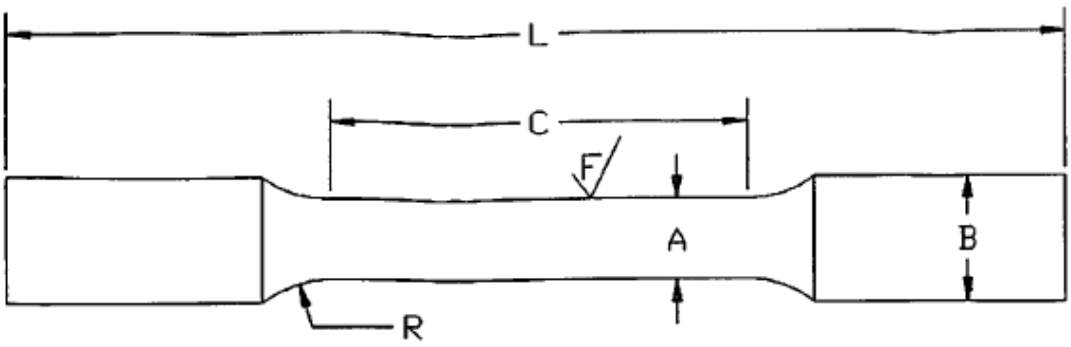

Feature	A	B	C	L	R	F
Size	.250 +/- .001	.499 +/- .001	1.250 +/- .02	4.500 +/- .002	.500 +/- .01	32 RMS

Figure 3.4: Round Bar Tensile Specimen with Dimensions

3.2.2: Specimen Uniform Stress vs. Uniform Displacement

ASTM standard E647-13 describes the eccentrically-loaded single edge crack tension specimen ESET. This is a pin loaded single edge notch tension specimen similar to the CT specimen. The use of pins allows the specimen to rotate creating a uniform stress loading state. For this research wedge grips were used to increase the rate of heat transfer during the cooling phase of thermo-mechanical temperature cycling. Gripping the SENT specimens with hydraulic wedge grips creates a uniform displacement boundary condition. It is well known that a uniform stress boundary condition yields a much different stress distribution than a uniform displacement boundary condition as seen in Figure 3.5. By performing a review of published stress intensity factor solutions it became apparent that most if not all solutions were for a uniform stress boundary condition. It was determined to use a finite element program to correctly model the boundary conditions of the SENT specimens. Knowing the applied far field stress and the stress at the crack tip, it would be possible to back calculate a stress intensity factor solution.

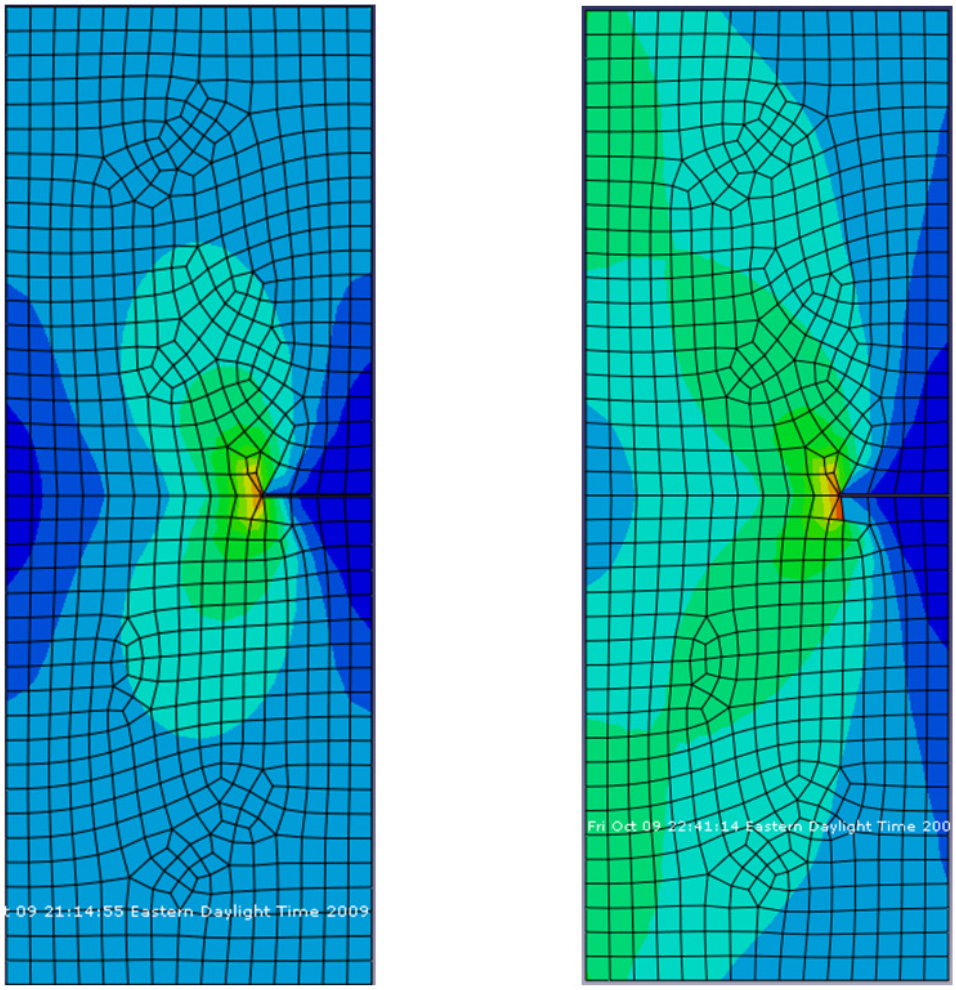

Figure 3.5: ABAQUS FEM For Uniform Stress (Left) and Uniform Displacement (Right)

FRANC2D is a finite element program maintained by the Cornell Fracture Group for predicting crack propagation through plane strain and plane stress two dimensional structures. The SENT specimen was modeled and meshed using a simple pre-processor that is included with FRANC2D called CASCA. The crack tip mesh can be seen in Figure 3.6. Using FRANC2D the appropriate boundary conditions were applied to mimic the uniform displacement conditions imposed by the hydraulic wedge grips. The notch was then allowed to propagate through the specimen yielding stress intensity factors as a function of crack length as seen in Figure 3.7.

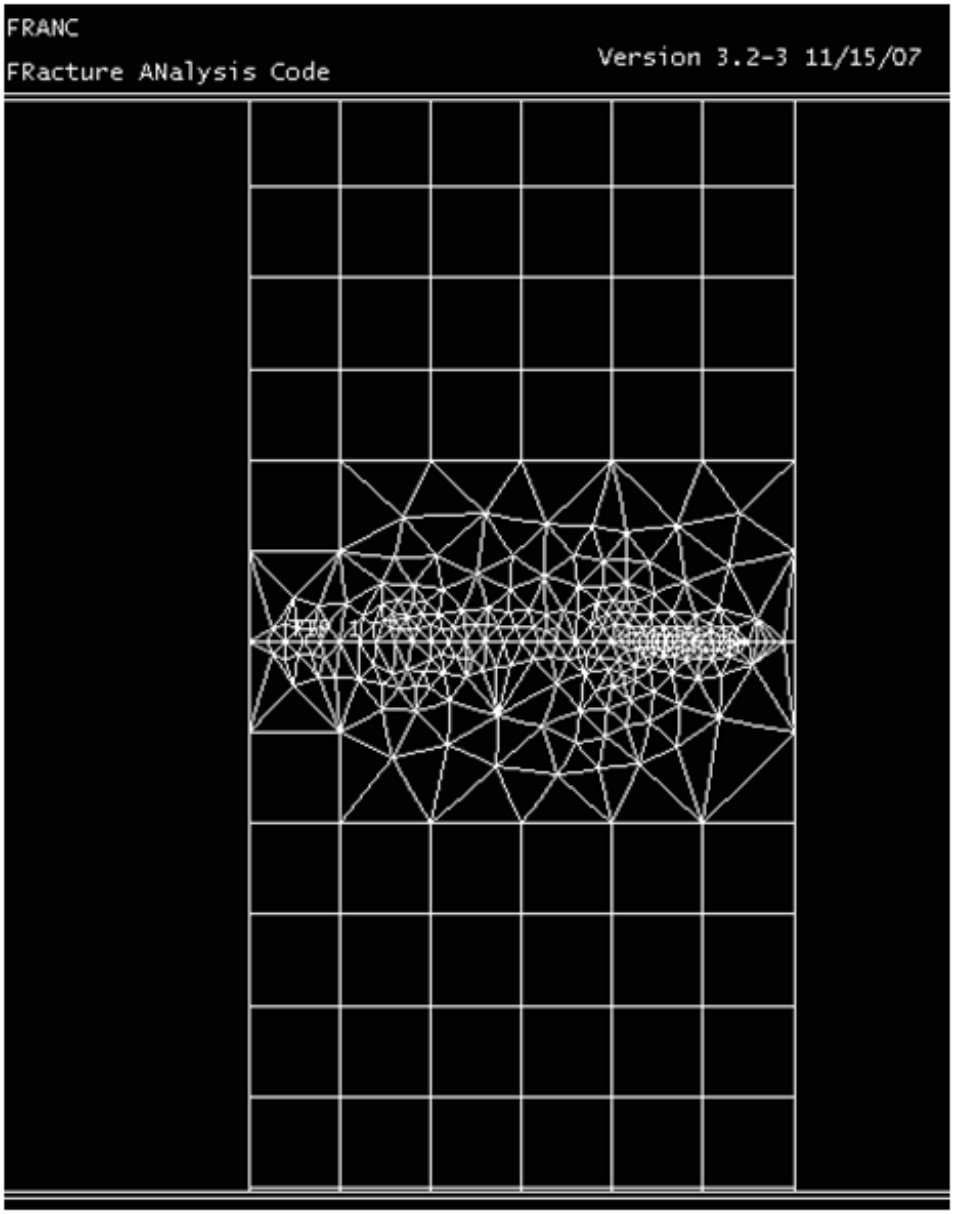

Figure 3.6: FRANC2D SENT Specimen Crack Tip Mesh

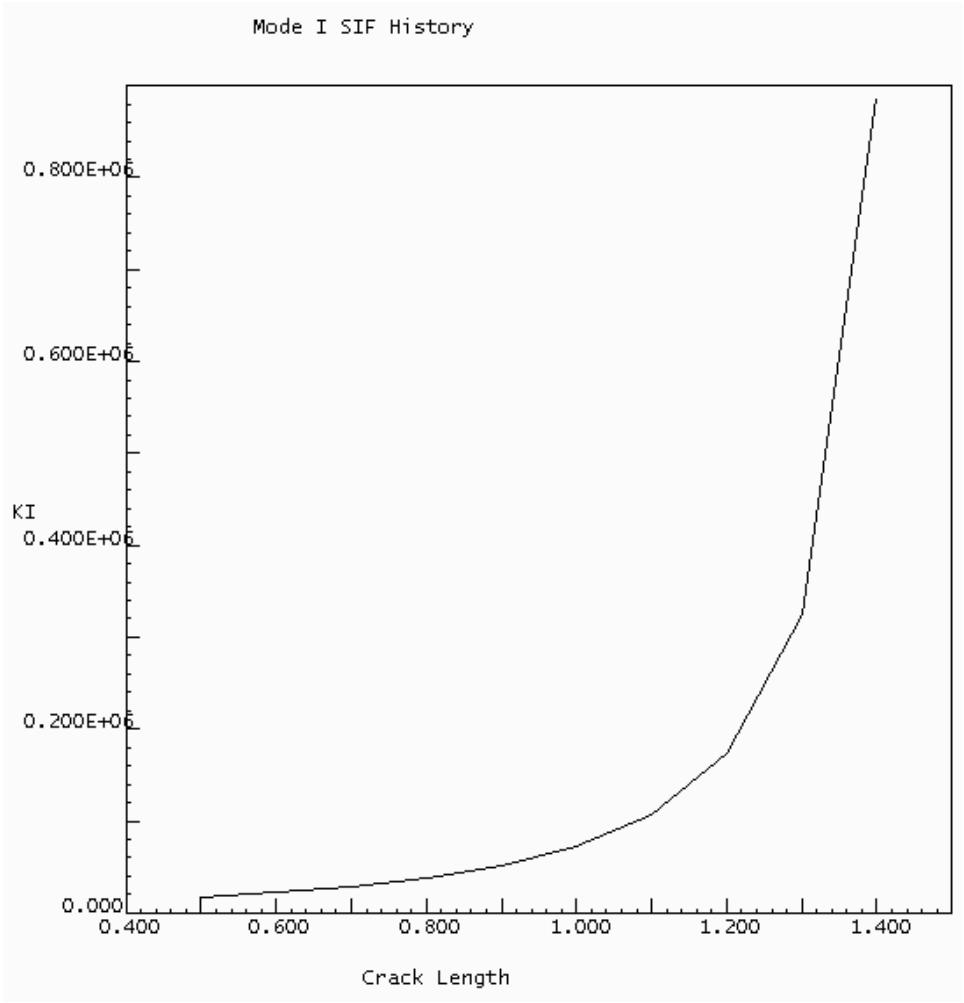

Figure 3.7: FRANC2D Stress Intensity Factor as a Function of Crack Length

For comparison purposes the correction factor, f(a/b), was also calculated using the Gross/Brown and Tada formulas, respectively Equations 3.1 and 3.2, both found in The Stress Analysis of Cracks Handbook [55].

$$f(a/b) = 1.122 - 0.231\left(\frac{a}{b}\right) + 10.550\left(\frac{a}{b}\right)^2 - 21.710\left(\frac{a}{b}\right)^3 + 30.882\left(\frac{a}{b}\right)^4 \quad \textbf{(3.1)}$$

$$f(a/b) = \sqrt{\frac{2b}{\pi a}\tan\frac{\pi a}{2b}}\,\frac{0.752 + 2.02(a/b) + 0.37\left(1-\sin\frac{\pi a}{2b}\right)^3}{\cos\frac{\pi a}{2b}} \qquad \textbf{(3.2)}$$

As can be seen in Table 3.4 the FRANC2D correction factors are very close to the uniform stress formulas from The Stress Analysis of Cracks Handbook up until a crack length over specimen width of 0.87. Realizing there might have been an error with how the boundary conditions were applied in FRANC2D, Mark James was contacted. James is one of the originators of the FRANC2D code. In discussions with him it became apparent that FRANC2D was designed to be used for uniform stress boundary conditions not uniform displacement.

Table 3.4: Comparison of Sent Specimen Correction Factors

Crack Length/ Specimen Width	The Stress Analysis of Cracks Handbook		FRANC2D
a/b	F(a/b) Gross/Brown	F(a/b) Tada	F(a/b)
0.33	1.79	1.78	1.79
0.40	2.11	2.11	2.11
0.47	2.55	2.55	2.54
0.53	3.16	3.16	3.09
0.60	4.03	4.04	4.03
0.67	5.23	5.40	5.32
0.73	6.85	7.67	7.63
0.80	9.02	11.99	11.79
0.87	11.85	22.38	21.17
0.93	15.50	64.27	55.71

An evaluation showing stress intensity factors for full rotation, partial rotation and no rotation boundary conditions provided by James is shown in Figure 3.8. The rotating

SENT specimen SIF increases faster as a function of crack length than the no rotation specimen. The partial rotation SIF in turn increases at a rate between the no rotation specimen and full rotation specimen. Work by Wu et al. [151] looking at the stress intensity factors for through-cracks emanating from notches in SENT specimens demonstrated a similar relationship between uniform stress and uniform displacement boundary conditions. This relationship can be seen in Figure 3.9. Their analysis using the boundary force method confirmed that the uniform stress SIF increases faster than the uniform displacement SIF as a function of crack length [152].

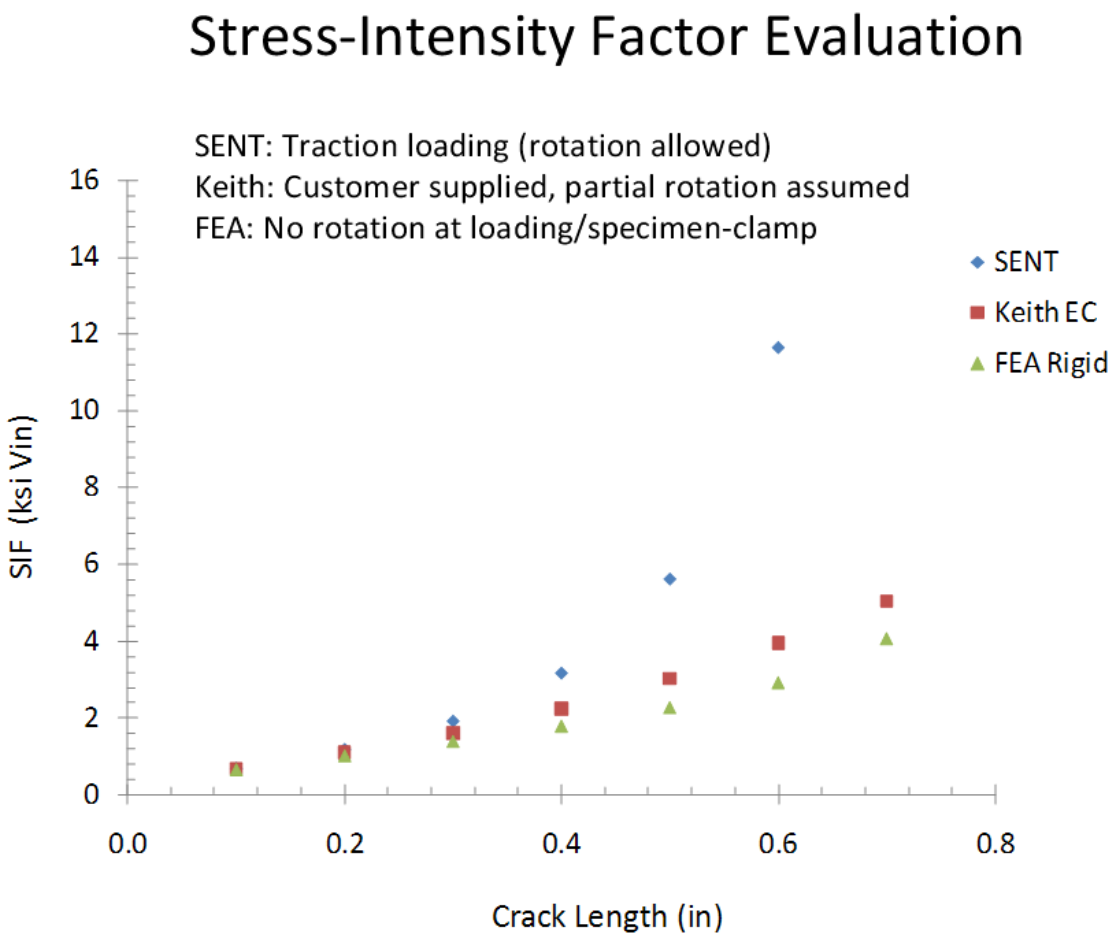

Figure 3.8: Comparison of Stress Intensity Factors for Uniform Stress and Uniform Displacement Conditions

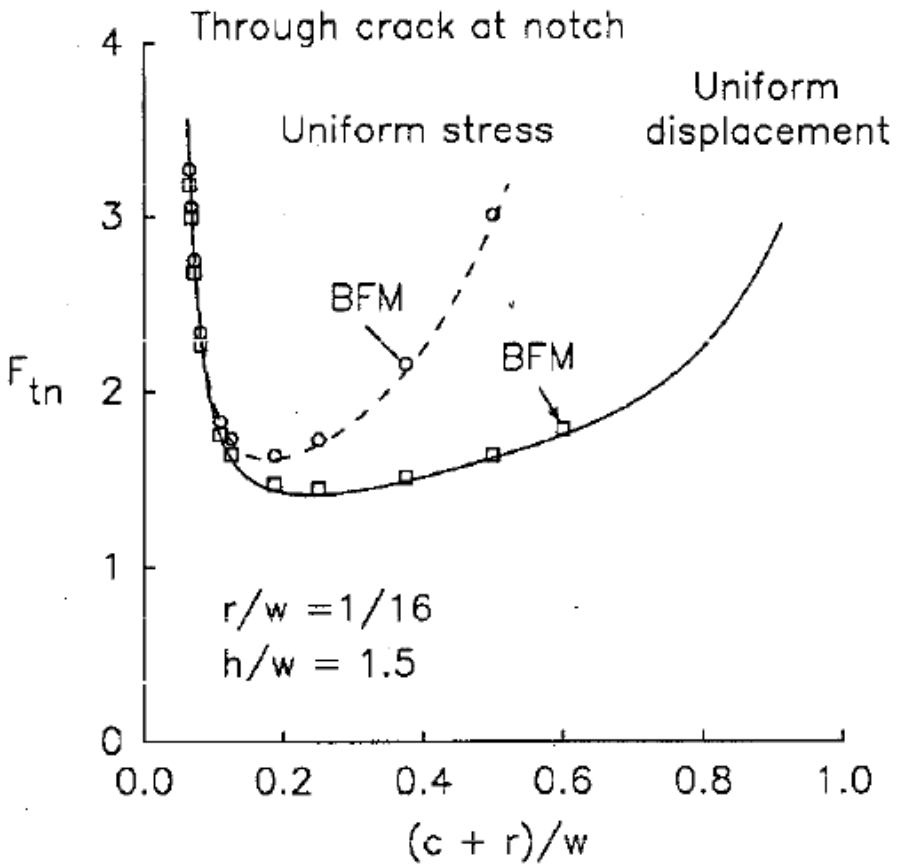

Figure 3.9: Comparison of Correction Factors Calculated Using the Boundary Force Method [151]

Jim Newman Jr. at Mississippi State University was able to use his FADD2D boundary element code to plot the SIF as a function of dimensionless crack length (a/b) for this study's SENT specimen. In similar fashion to how Telesman et al. [87] used a boundary integral equation and fitted a four-order equation to yield a solution a sixth-order equation was fitted to the FADD2D boundary element result. The uniform displacement stress intensity factor used for this study plotted against the uniform stress SIF can be seen in Figure 3.10. These results are expected since the mechanical advantage for rotation is enhanced with increasing crack length. Other methods that use FEA, weight functions and experimental data to determine the SIF for uniform displacement SENT

specimens can be found in published literature [153-156]. The correction factor solution for a specimen with fixed ends is as follows:

$$f(a/b) = 1.126 - 0.504\left(\frac{a}{b}\right) + 10.473\left(\frac{a}{b}\right)^2 - 48.17\left(\frac{a}{b}\right)^3 + 112.87\left(\frac{a}{b}\right)^4 - 124.63\left(\frac{a}{b}\right)^5 + 53.327\left(\frac{a}{b}\right)^6 \quad \textbf{(3.3)}$$

Where 'a' is the crack length and 'b' is the specimen width. This solution was implemented for a specimen height to width ratio of 1.33.

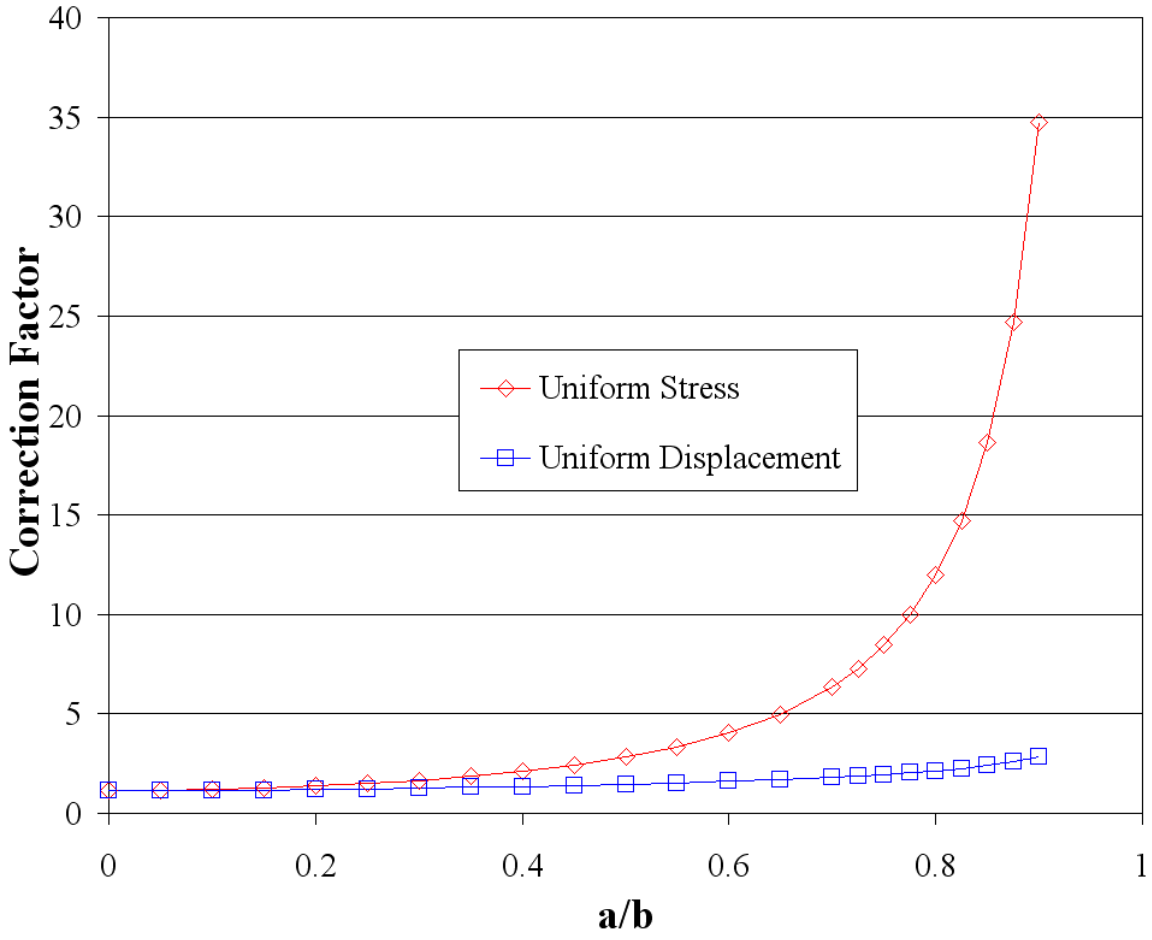

Figure 3.10: Comparison of Uniform Stress and Uniform Displacement Correction Factors for a SENT Specimen

In order to verify a correct SIF for the SENT specimen, fatigue crack growth was also performed on a compact tension specimen at room temperature. The commonly accepted uniform stress solution for a compact tension specimen is as follows [56]:

$$K = \frac{P}{b\sqrt{W}} \left(\frac{2+\left(\frac{a}{W}\right)}{\left(1-\left(\frac{a}{W}\right)\right)^{\frac{3}{2}}} \right) (0.886 + 4.64\left(\frac{a}{W}\right) - 13.32\left(\frac{a}{W}\right)^2 + 14.72\left(\frac{a}{W}\right)^3 - 5.6\left(\frac{a}{W}\right)^4 \quad \textbf{(3.4)}$$

Where P is the load, b is the specimen thickness and W is the specimen width. During testing of IN100 it was shown that there was excellent correlation between SENT and CT room temperature FCGR data [127, 157].

3.2.2: Specimen Preparation

Specimens were machined by Element Cincinnati (formerly known as MAR-TEST Inc.). A total of 54 PWA1484 single edge notch tension specimens and 26 round bar specimens were produced for fatigue testing. Low stress grinding was utilized during the production process to ensure that residual surface stresses were kept to a minimum.

For optimal viewing of the crack tip specimens were ground and polished in front of the EDM notch on the side of the specimen that was to be observed by the optical microscope. Specimens were first ground with 320 grit silicon carbide paper followed by 600 and 2400 grit silicon carbide paper. This was followed up with 4000 grit silicon carbide paper and lastly specimens were then polished using 6 and ½ micron diamond

lapping paste. Polishing was aided with a Dremel tool and a felt polishing wheel. Extra care was used between each step to make sure that the specimen was fully clean using acetone and isopropyl alcohol so as to not contaminate the next step.

High temperature glass insulated “K” type thermocouples were then precisely welded in the center of the specimens just below the crack path for optimal temperature control. The thermocouple position can be seen in Figure 3.11.

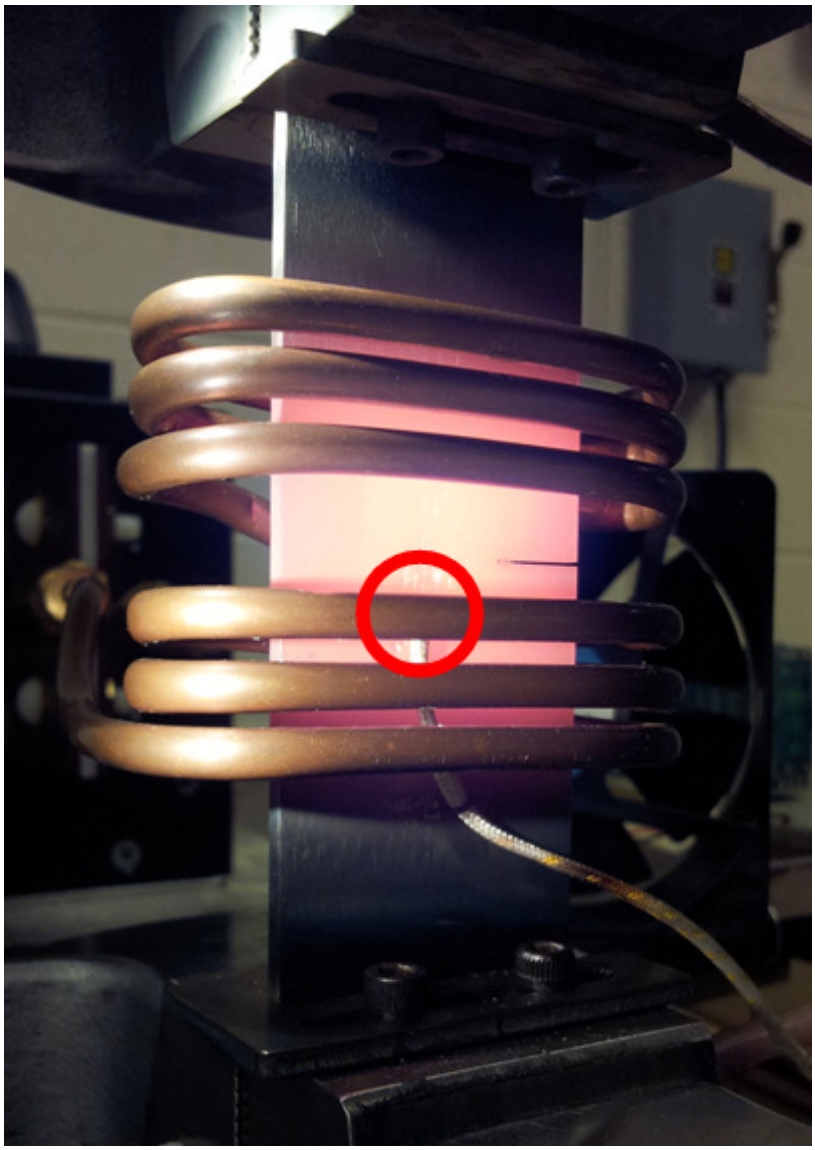

Figure 3.11: Thermocouple Placement in the Center of the Specimen Just Below the Crack Path

3.3: TMF and Monotonic Testing

The nickel based components in gas turbine engines are subjected to extreme fluctuations in both stress and temperature as can be seen in Figure 3.12. This combination of mechanical and thermal strains has been shown to be responsible for great damage in many engineering systems especially the gas turbine industry [141]. This combination of cyclic stress and temperature variation is known as thermo-mechanical fatigue. The

understanding of the TMF crack behavior of hot section superalloys is crucial for the development of sophisticated life prediction methods. TMF testing procedures for startup, setup and shutdown can be found in Appendices A.2 through A.4, respectively.

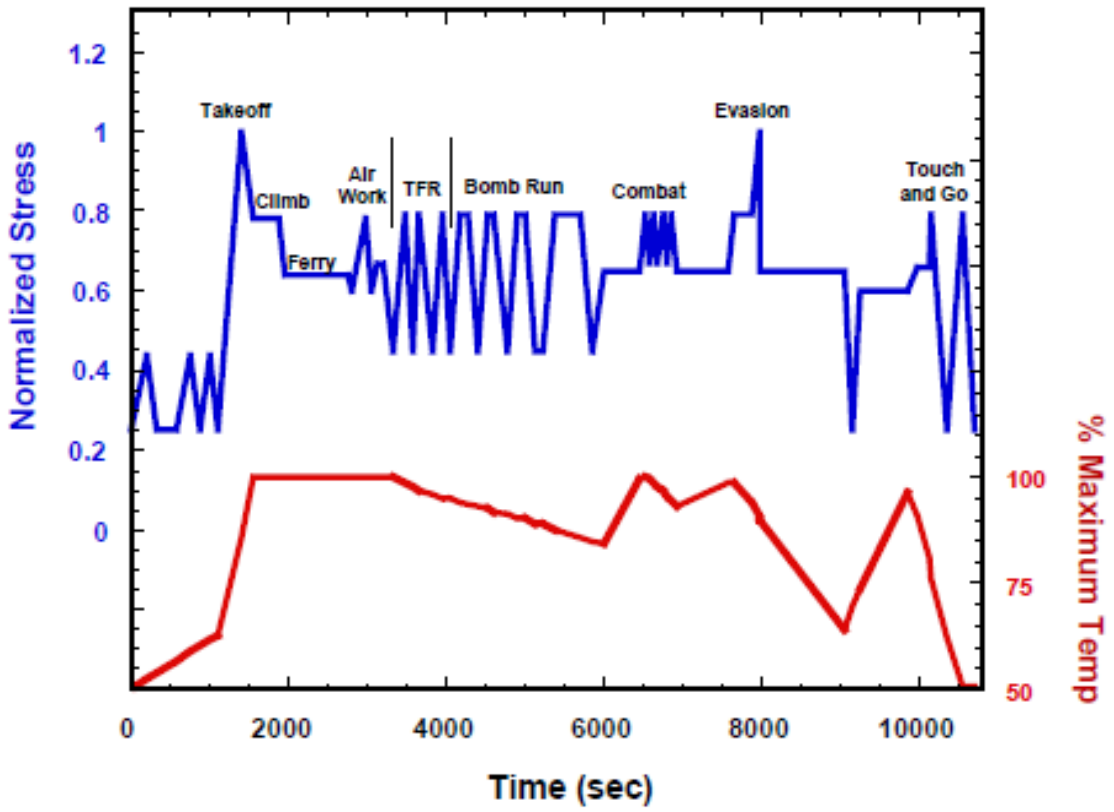

Figure 3.12: Semi-Realistic Fighter Jet Flight Spectrum Showing Cyclic Mechanical and Thermal Loading [115]

3.3.1: Thermo-Mechanical Fatigue Crack Growth Test Equipment

Shown in Figure 3.13 a 100 kN MTS servo-hydraulic load frame paired with a MTS TestStar IIs control system was used for testing of the SENT specimens. Specimens were gripped approximately 50.8mm on each end by pyramid teeth wedge grips 44.45mm wide as seen in Figure 3.14. Nominal grip pressure was set at 16,550 kPa. Specimens are pre-cracked at 10 Hz at the lowest temperature at which they were tested. MTS

TestStar IIs software allows for the creation of elaborate test programs featuring cyclic loading and temperature. Water cooled hydraulic wedge grips were used for rapid heat dissipation during temperature cycling. The use of a laser level along with aligning guides ensured that specimens were positioned in a repeatable fashion and placed squarely in the grips.

Crack length measurement was accomplished through the use of a QM-100, Questar Microscope mounted on a three-axis Remote Measurement System platform with linear encoders. This microscope has the ability to magnify the crack tip between 50x and 300x for optimal crack length measurement. Attached to this microscope is an Edmund Optics USB 2.0 CCD camera with the ability to take still images and record video. A screen capture program was utilized to record images every five minutes so the crack length could be recorded 24 hours a day.

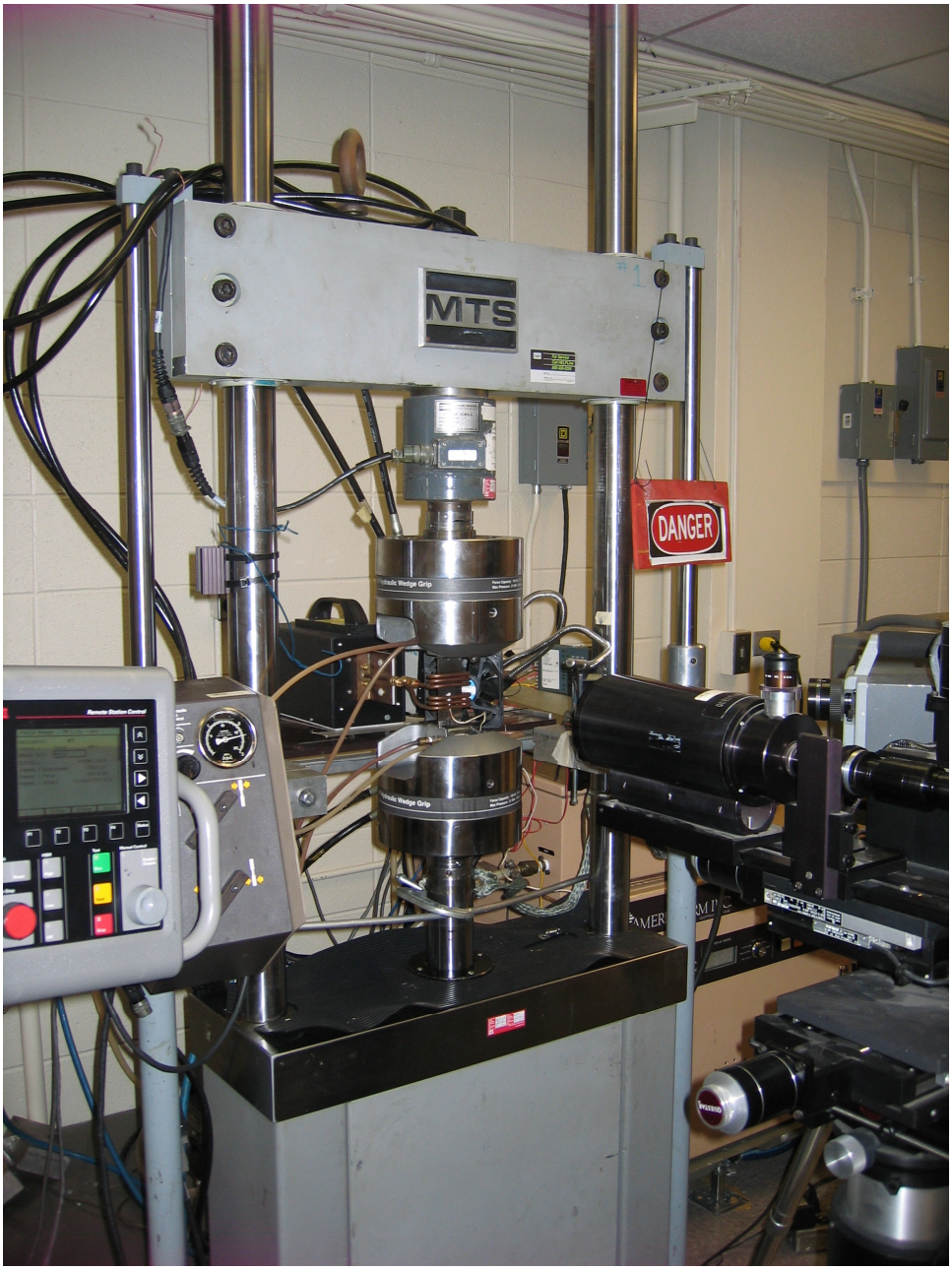

Figure 3.13: MTS Load Frame Used for Thermo-Mechanical Fatigue Testing

Figure 3.14: Water Cooled Pyramid Teeth Wedges

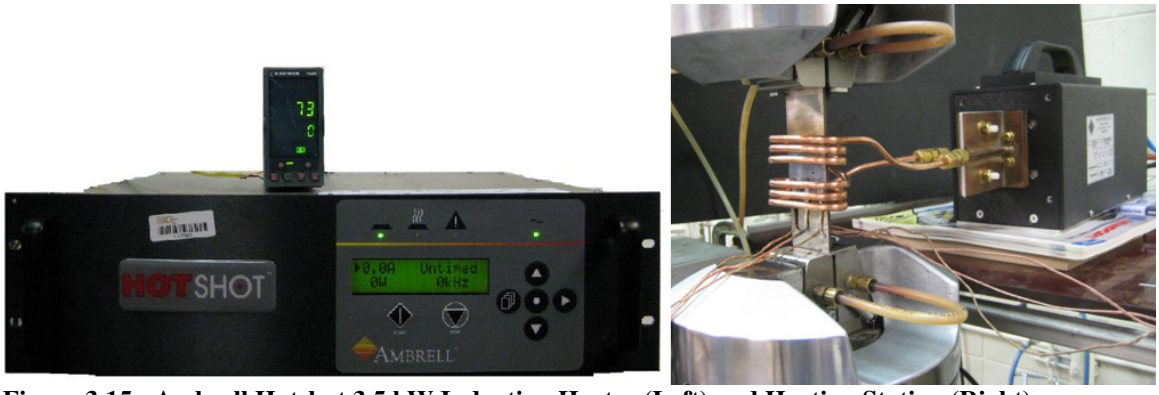

Figure 3.15: Ambrell Hotshot 3.5 kW Induction Heater (Left) and Heating Station (Right)

An Ambrell Hotshot 3.5 kW induction heater and heating station seen in Figure 3.15, along with high temperature glass insulated "K" type thermocouple wire were used to maintain temperatures ranging from 482°C to 982°C. An unique coil design made out of

4.76mm copper tubing was created with a 11.43mm crack viewing window with 3 turns above and below to provide uniform heat distribution. Twin fans controlled by the EuroTherm temperature controller were mounted on either side of the specimen to achieve rapid cooling. These cooling fans along with the copper induction coil can be seen in Figure 3.16. Temperature inspection using an optical pyrometer showed a small temperature variation of +/- 5°C across the crack plane.

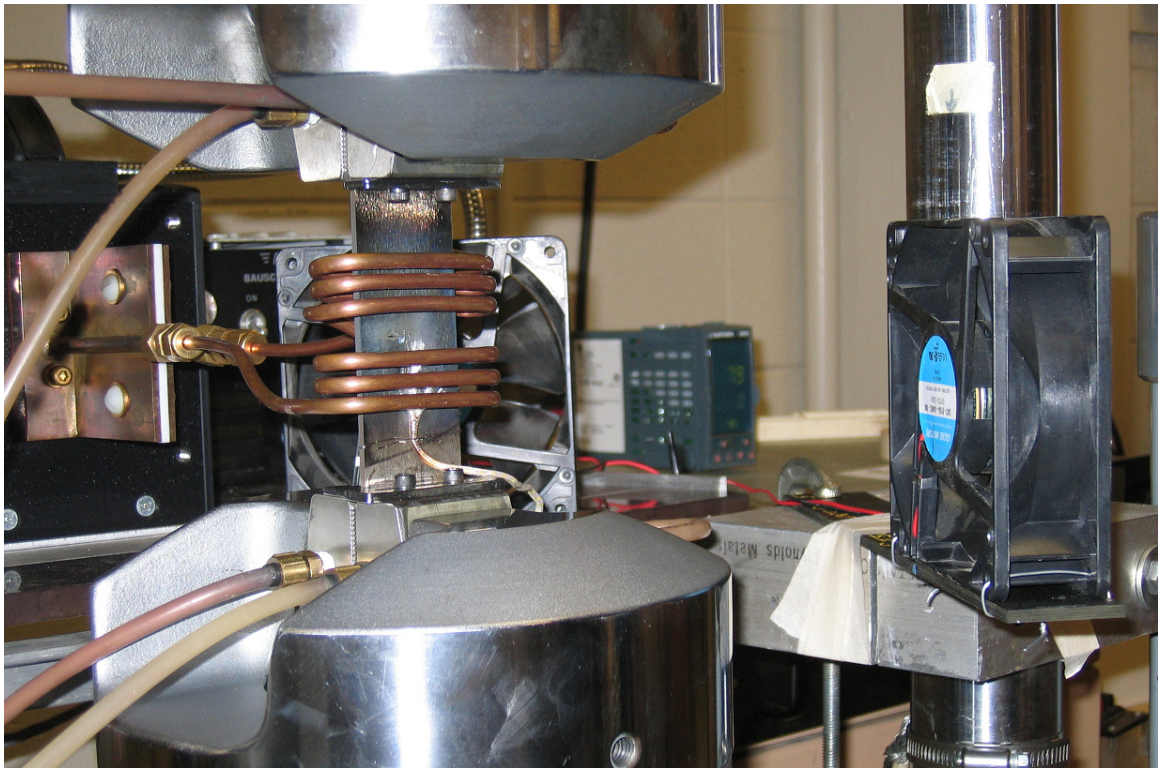

Figure 3.16: Specimen in Test Rig Showing Unique Coil Design and Twin Cooling Fans

For safety the TestStar IIs control system was set up to interlock the hydraulic pump when the applied load deviated outside of controlled limits. In the event of a specimen fast fracture failure there were also interlocks set for when the displacement deviated

outside an upper and lower limit. Improving the safety of the system a relay was added to disable the induction heater when the hydraulic interlock system was tripped.

3.3.2: Monotonic and Cyclic Round Bar Test Equipment

Monotonic and cyclic round bar specimens were tested using hydraulic collet water cooled grips that ensure precision specimen alignment and are ideal for fatigue testing. Strain rate was controlled using a MTS 632 series high-temperature axial extensometer. A heating coil was again made out of 4.76mm copper tubing with proper spacing for the high temperature extensometer while still ensuring an optimal heating distribution. The testing setup can be seen in Figure 3.17,

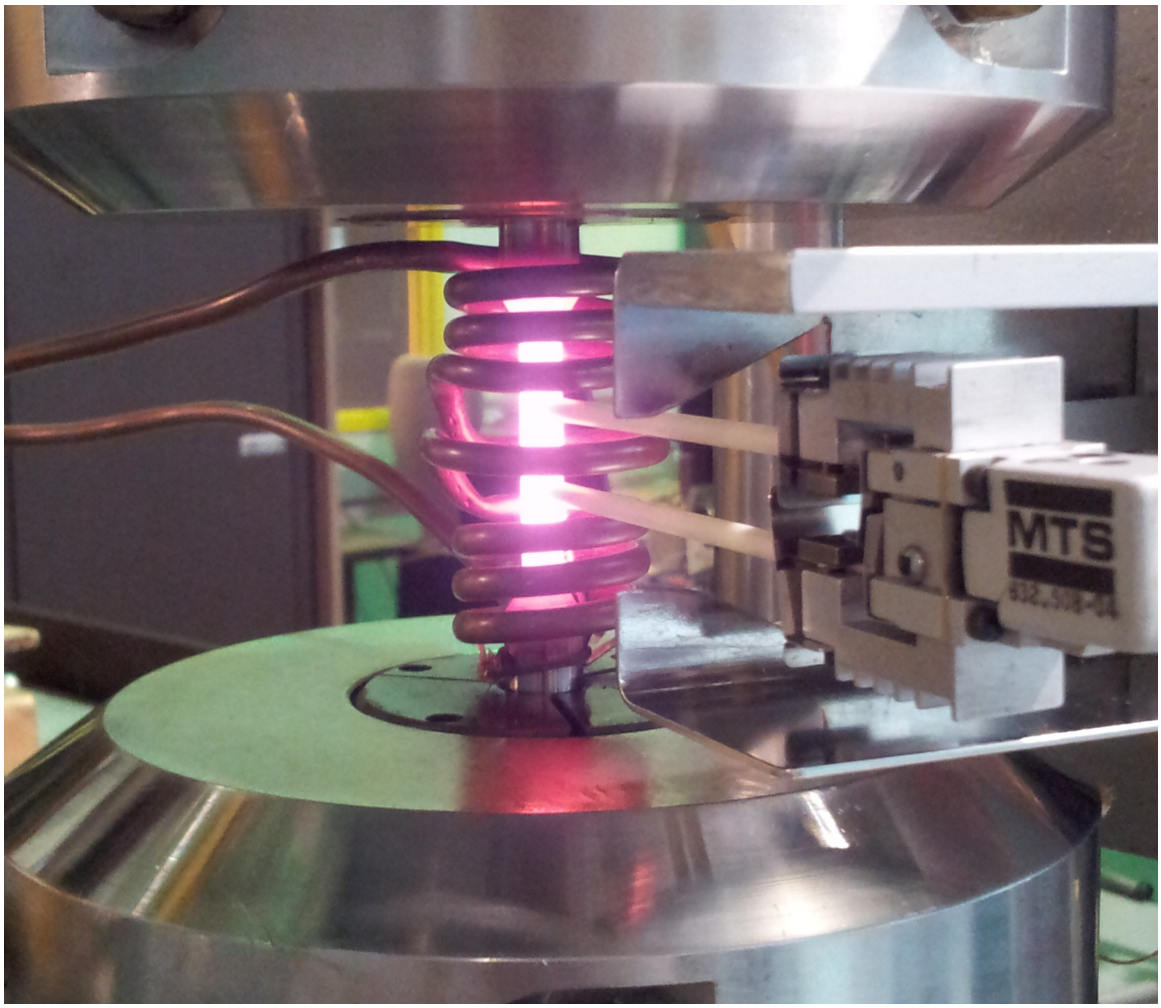

Figure 3.17: Monotonic Tensile Specimen in Test Rig Showing Coil Design and High-Temperature Axial Extensometer Placement

3.3.3: Inert Environment Test Equipment

Inert environment testing was performed on the 100 kN MTS servo-hydraulic load frame by using a chamber fashioned out of 1.5mm thick acrylic and silicone. The acrylic was easily shaped to fit around the hydraulic wedge grips using a heat gun. Silicone gaskets were then glued to the acrylic to create an airtight fit around the grips. Hose clamps were used to hold the chamber in place. The chamber can be seen in Figure 3.18.

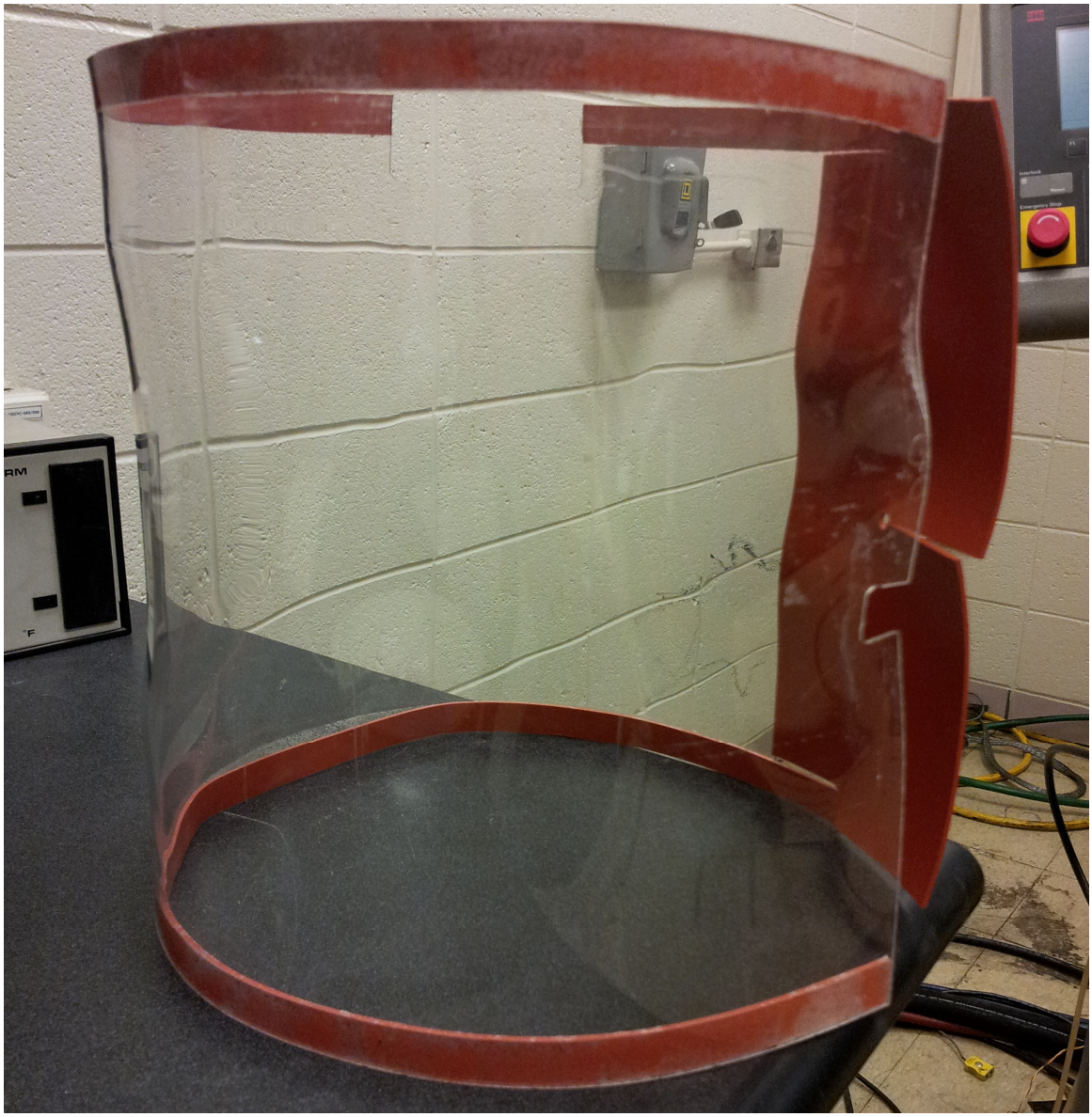

Figure 3.18: Acrylic and Silicone Inert Environment Chamber

The inert environment test chamber was flooded with ultra high purity (99.999%) argon gas. The flow rate was controlled with a high precision low flow regulator as shown in Figure 3.19.

Figure 3.19: Ultra High Purity Argon Tanks with High Precision Low Flow Regulator

The successful displacement of oxygen was measured with an OXIGRAF Fast Oxygen Analyzer as shown in Figure 3.20. The Model O2L Analyzer is designed to measure oxygen from 0-100% with resolution of 0.01% from 0-10% and 0.1% from 10-100%. A ceramic tube was fitted to the oxygen analyzers intake hose with the tip of the tube placed at the center of the specimen in line with the crack. The oxygen analyzer ran throughout inert environment tests making sure that oxygen detected was 0.0%. Review of the specifications revealed that as much as 0.04% oxygen can still be present when the analyzer is reading 0.0%.

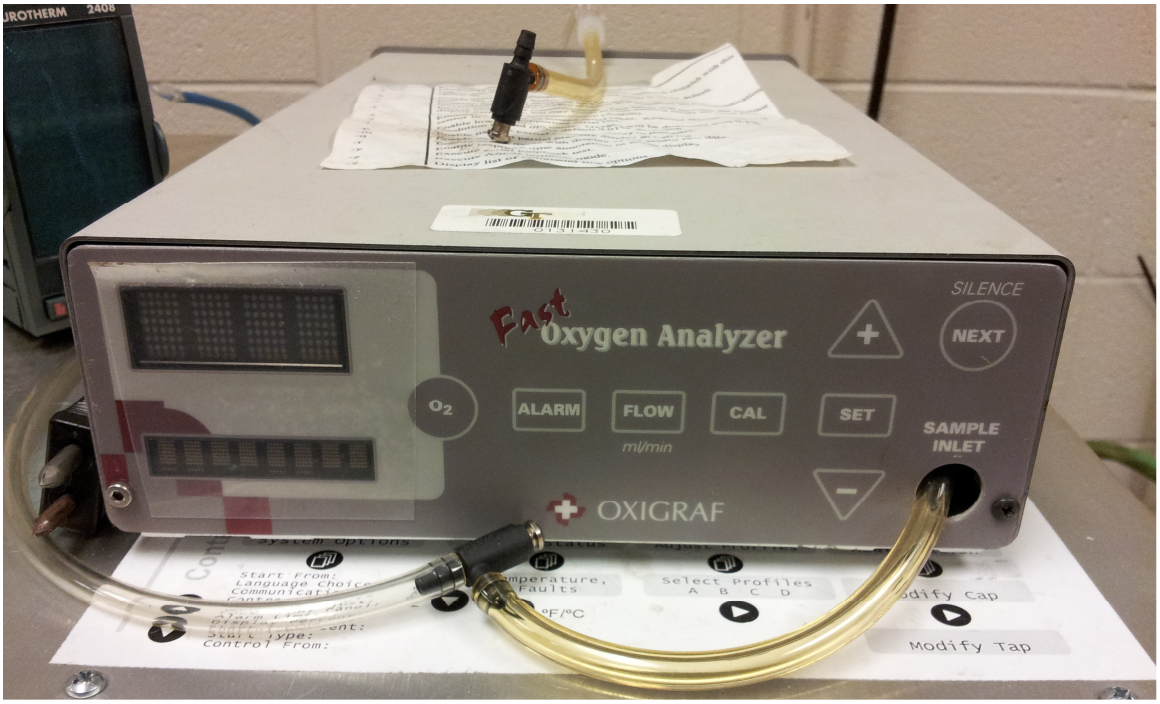

Figure 3.20: OXIGRAF Fast Oxygen Analyzer

The overall inert environment test set-up can be seen in Figure 3.21. Argon is 38% denser than air and was continually allowed to flow into the top while the bottom and sides of the chamber were completely sealed. This provided excellent displacement of air in the test chamber. The Questar optical microscope was used to measure the crack

length as a function of applied loading cycles. As seen on the right the oxygen analyzer ran continuously to insure a successful test. When dealing with argon, extra care was used to make sure that there was plenty of ventilation in the lab area due to the danger of asphyxiation.

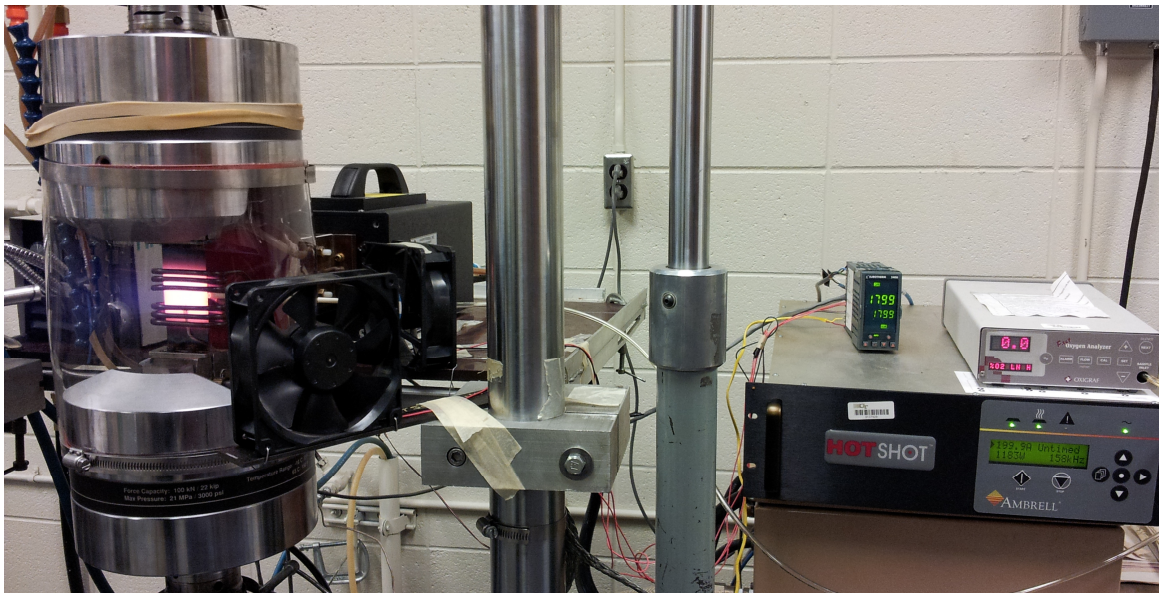

Figure 3.21: Inert Environment TMF Test Set-Up

3.3.4: Testing Standards

Fatigue crack growth testing was done in accordance with the ASTM Standard Test Method for Measurement of Fatigue Crack Growth Rates, E647-13 [158]. Below is a summary of this test method according to the ASTM standard:

> *This test method involves cycle loading of notched specimens which have been acceptably precracked in fatigue. Crack size is measured, either visually or by an equivalent method, as a function of elapsed fatigue cycles and these data are subjected to numerical analysis to establish the rate of crack growth. Crack growth rates are expressed as a function of*

the stress-intensity factor range, ΔK, which is calculated from expressions based on linear elastic stress analysis. [158]

This standard lists many requirements that need to be met in order for the test to be considered a success. Several of requirements applicable to this study are as follows:

Requirement #1: Precracking must be performed on a specimen fully heat treated to the condition it is to be tested and may be executed at any convenient frequency. The fatigue precrack must be at least $1/10^{th}$ the specimen thickness, the notch height, or 1.016mm, whichever is greater. Fatigue Precracking was also performed in accordance with ASTM Standard Test Method of Linear-Elastic Plane-Strain Fracture Toughness K_{IC} of Metallic Materials, E399-09 [159].

Requirement #2: Crack measurement equipment should be capable of resolving 0.1016mm or $1/500^{th}$ the specimen width, whichever is greater. Applying reference grids to the surface of the polished specimen decreases the chance of measurement area. It is preferred that crack length measurements are taken without test interruption.

Requirement #3: Crack measurements should be taken with a minimum crack length interval of 0.254mm. In situations where Δa must be smaller, such as near threshold, the minimum shall be ten times the crack size measurement precision.

Requirement #4: If the crack deviates more than 20° from the notch plane over a distance of $1/10^{th}$ the specimen width the data is invalid. If the crack deviates between 10° and 20°, this deviation must be reported along with the data.

Requirement #5: If crack tip tunneling is present and a crack curvature correction results in a 5% or greater change in stress intensity factor, then this correction should be applied when analyzing the test data.

3.4: Secondary Orientation Using Metallography

Each of the twelve slabs that the 24 uncontrolled secondary orientation SENT specimens had sections cut, mounted, ground, polished and etched. From each slab small specimens with X, Y and Z faces were cut and mounted so the full crystallographic orientation could be verified through the use of dendrite observation. These X, Y and Z faces can be seen in Figure 3.22.

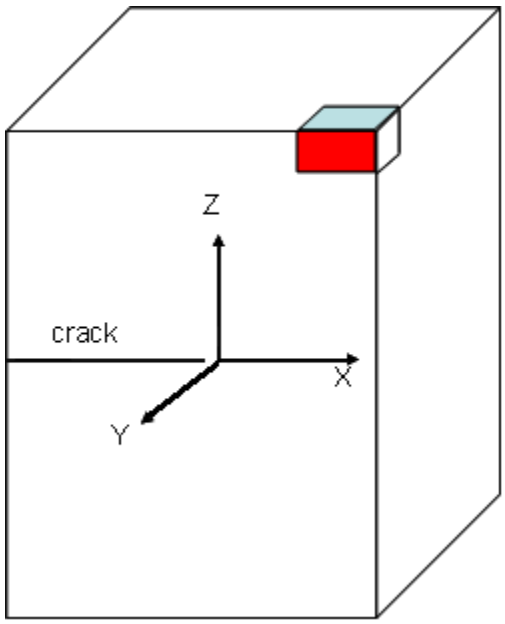

Figure 3.22: X, Y and Z Faces of Single Edge Notch Tension Specimen for Metallographic Inspection

The metallographic preparation procedure can be found in Appendix A.1. Nine of the slab specimens can be seen in Figure 3.23. An optical microscope was then used to take pictures that could then be analyzed to determine the secondary orientation deviations from pure cubic directions.

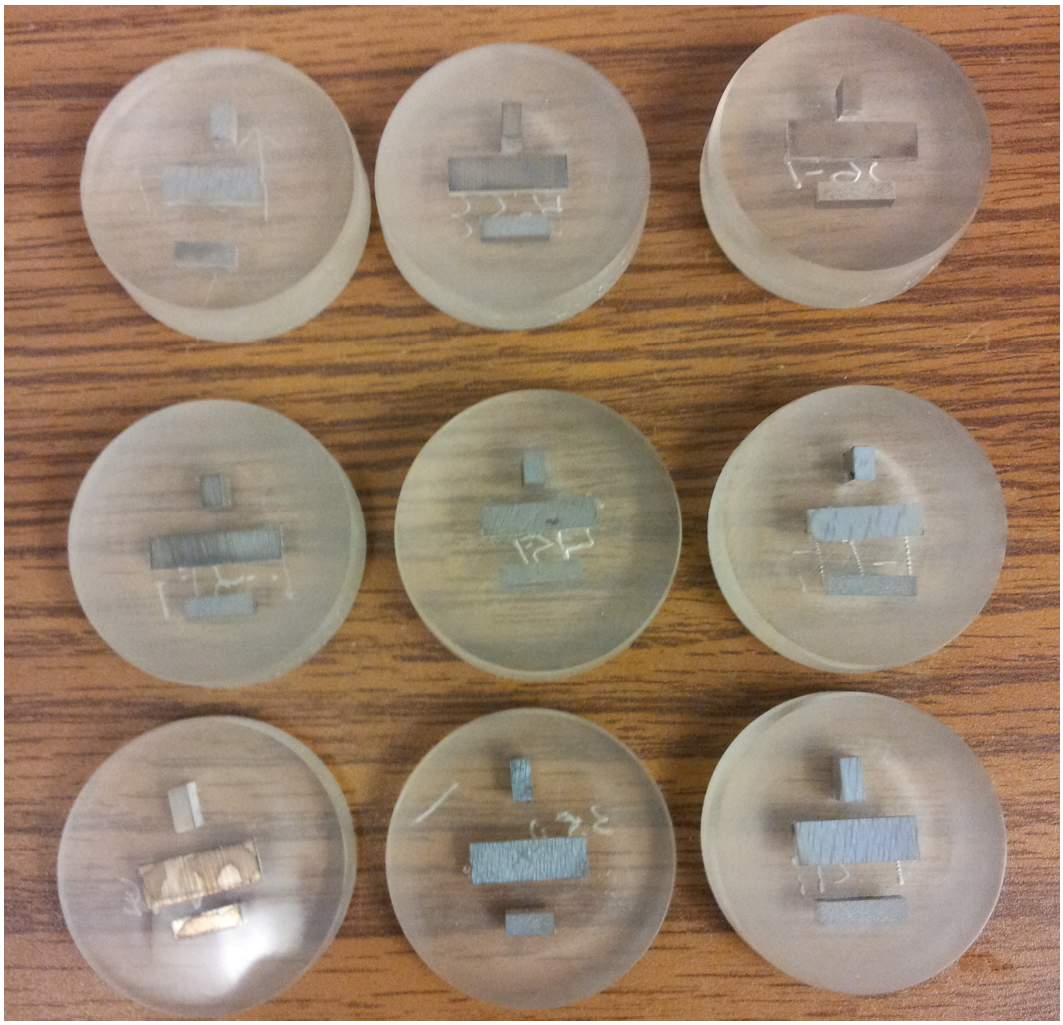

Figure 3.23: Mounted Specimens after Grinding, Polishing and Etching

3.5: SEM Crystallographic Plane Measurement Technique

When crystallographic cracking is present the planes are verified through the use of precision SEM. The stage positioning in scanning electron microscopes is very accurate and allows for the precise measuring of coordinates. Two independent vectors on the surface of the facet can be obtained by measuring the (x, y, z) coordinates of three points on the crystallographic facet. The cross product can then be performed to get a normal vector to the surface of the facet. This normal vector can then be compared to the known

loading/crystallographic direction. With this information the orientation of the crystallographic fracture plane is now known. This process can be seen in Figure 3.24.

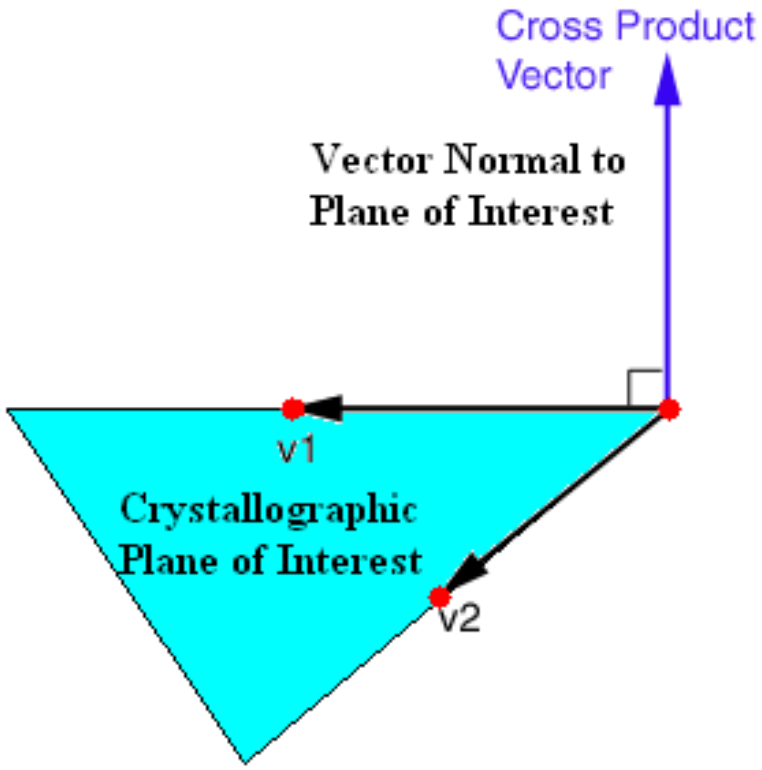

Figure 3.24: SEM and Cross Product Approach to Determining Crystallographic Fracture Planes

3.6: Crack Growth Non-Interaction Modeling

A model, using the isothermal constant amplitude test data obtained in this study, was created to calculate crack growth cycle by cycle and was used as a baseline for subsequent fatigue crack growth interaction testing. Generating a model based on the Paris equation and using Paris constants from multiple sets of test data, allows the ability to calculate non-interaction crack growth for TMF profiles with overloads and cycling temperature and even semi-realistic flight spectrums. Comparing the crack growth

predicted with the non-interaction model to actual experimental data will show growth or retardation that can be attributed to load and temperature interactions.

Due to ease of programming, MATLAB was chosen as the numerical computing environment for modeling. Crack length calculation was done through the use of a forward iterative loop. Starting with an initial crack length the stress intensity factor was calculated. Knowing the maximum and minimum cyclic loading and using the initial crack length and previously calculated SIF, ΔK can then be calculated. Using the Paris equation (Equation 2.6), Paris constants and ΔK an increment in new crack growth can then be calculated. The Paris constants were obtained in Excel using power law curve fitting as seen in Figure 3.25. This increment is then added to the initial crack length and a new SIF can then be calculated based on the current crack length. This process is repeated until a critical crack length is reached for the specimen being modeled. As the modeling is done cycle by cycle at anytime the maximum and minimum cyclic loads and Paris constants can be changed to represent underloads, overloads or a change in temperature.

Non-interaction modeling provides a good baseline from which to compare experimentally determined load and temperature interactions. Interaction effects such as overload plastic zones, crack tip embrittlement and microstructural changes due to environmental exposure can then be quantified in terms of the differences between the non-interaction modeling and the interaction testing. This along with the non-interaction

predictions alongside the experimental results will be discussed further in the experimental results and conclusions.

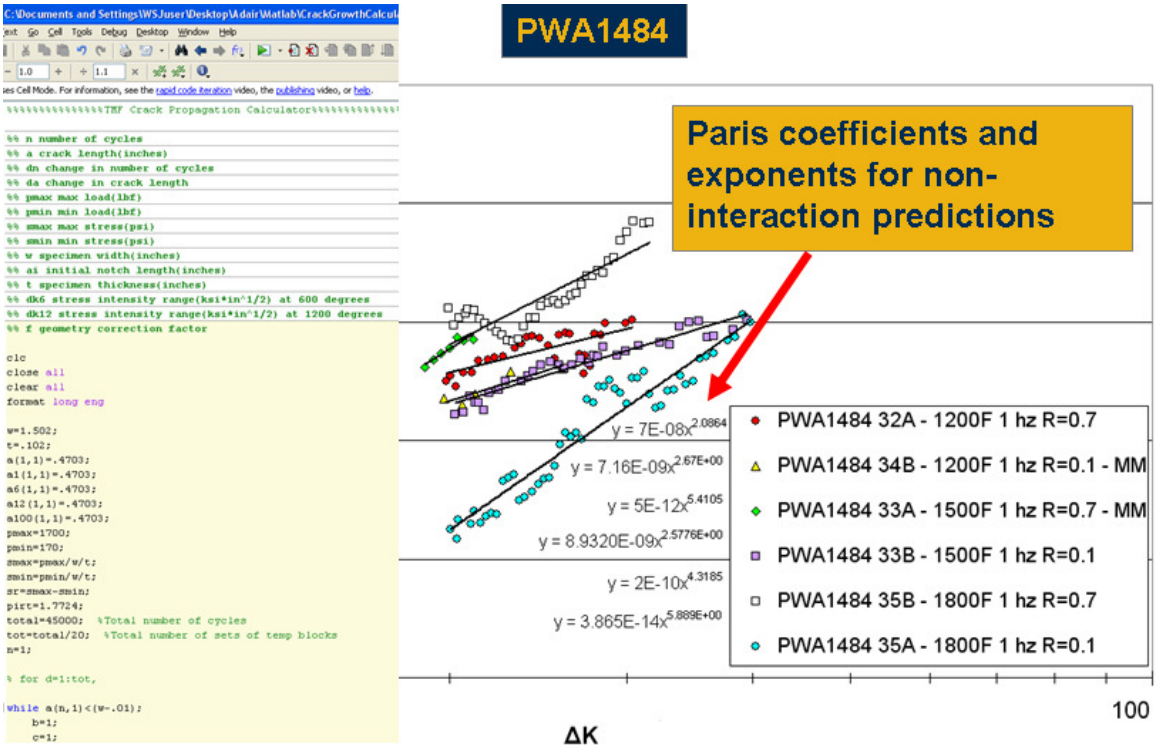

Figure 3.25: MATLAB Code and Paris Coefficients and Exponents used for Non-Interaction Fatigue Crack Growth Modeling

CHAPTER 4: EXPERIMENTAL RESULTS

This section begins by presenting the results of a material analysis on the PWA1484 single crystal material. Next the secondary orientation determination for the uncontrolled slabs will be discussed. The results of PWA1484 monotonic and cyclic property determination will be presented. A discussion on the fatigue crack growth rate data for constant amplitude isothermal testing for different temperatures, R Ratios and secondary orientations will follow the monotonic and cyclic properties. Next the effect of environment and aged microstructure on the FCGR will be shown. Following this crack growth data for load and temperature interaction tests will be presented. A study looking into the effect of relative load levels and dwell times on specimens tested under semi-realistic spectrums will reveal some interesting results.

4.1: Material Analysis

PWA1484 is composed of 59.7% nickel by weight with the rest of the chemical composition shown in Table 4.1.

Table 4.1: PWA1484 Nominal Chemical Composition in Weight Percent

Co	Cr	Al	Ta	W	Mo	Re	Ni
10	5	5.6	8.7	6	2	3	59.7

The PWA1484 γ' precipitate is cuboidal in shape, on the order of 0.3 to 0.5 μm in size, creating a blocky morphology as can be seen in Figure 4.1 and Figure 4.2. In addition a distribution of fine (30 nm) spherical γ' precipitates reside between the cuboidal precipitates in the γ matrix channels. The γ' precipitate volume fraction is approximately 0.6. These figures were obtained while in BSE (back scattered electrons) mode which

enhances the contrast and provides sharp distinction between phase due to differences in the atomic number, Z.

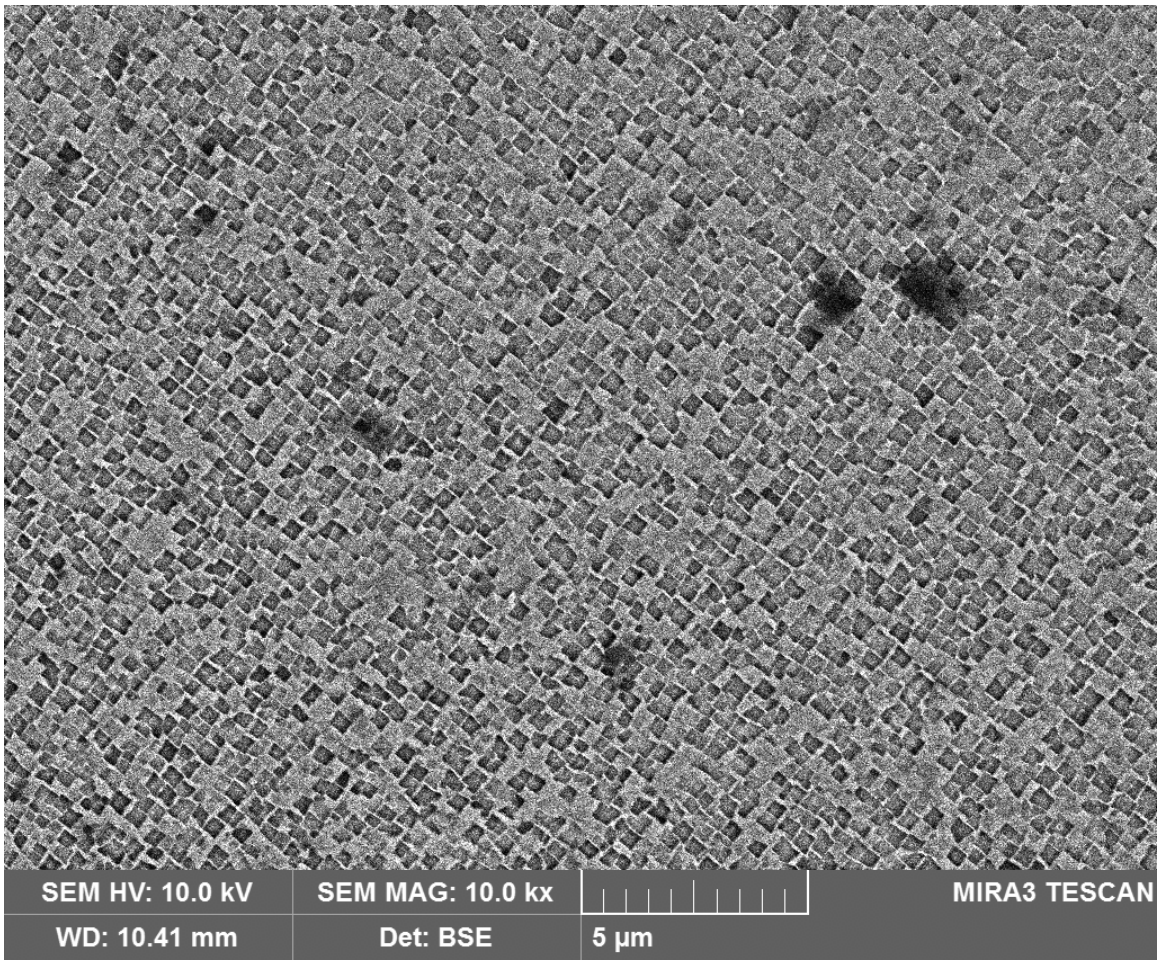

Figure 4.1: Fully Heat Treated PWA1484 Microstructure Showing Cuboidal γ' Precipitates on the Order of 0.4 µm

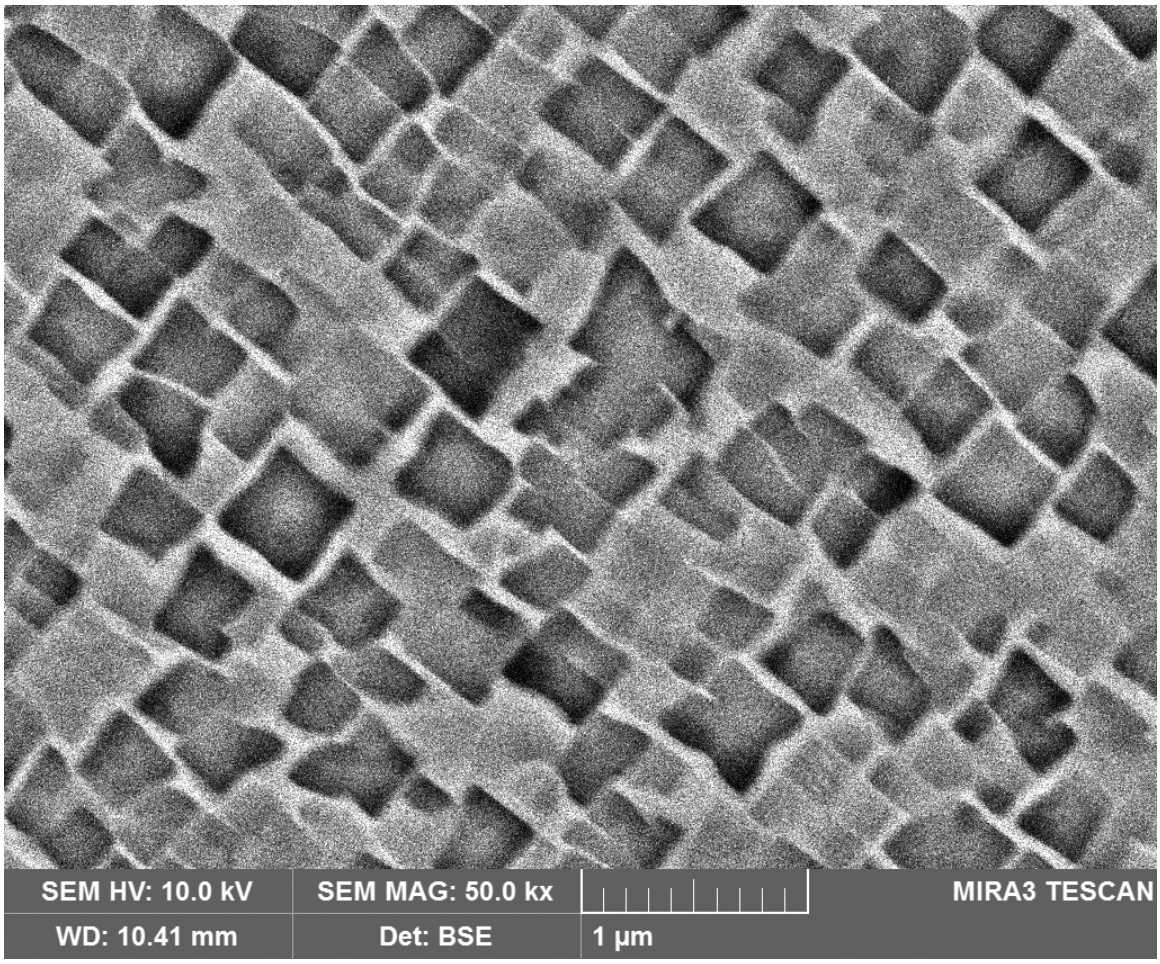

Figure 4.2: Fully Heat Treated PWA1484 Microstructure Showing High Volume (>0.60) Fraction of Precipitate

4.2: Secondary Orientation Determination

The secondary orientation deviations from cubic directions can be determined through inspection of the dendrites formed during the casting process. Following the specimen preparation process outlined in Appendix A.1 an optical microscope was used to take pictures of all twelve uncontrolled secondary orientation PWA1484 slabs. These pictures can be seen in Figure 4.3 through Figure 4.14. In all of these pictures the view is looking down on the loading axis.

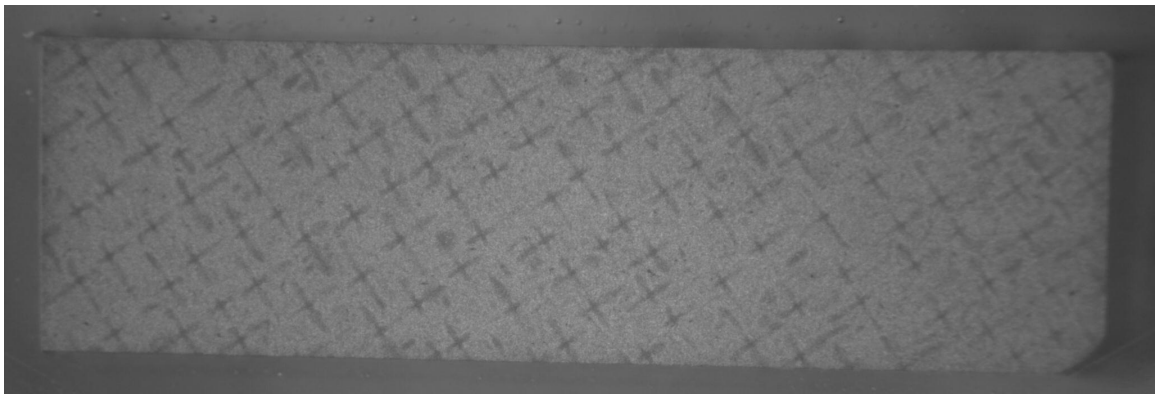

Figure 4.3: PWA1484 Slab 23831 Secondary Dendritic Orientation

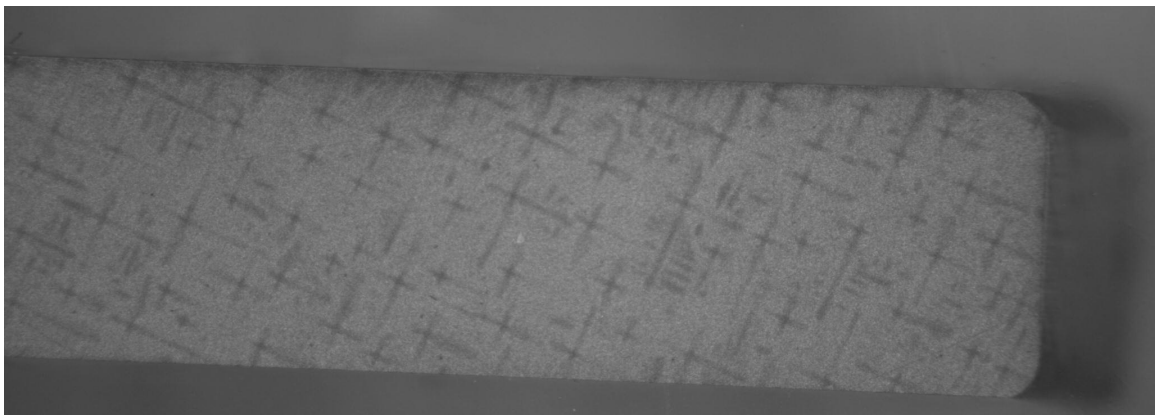

Figure 4.4: PWA1484 Slab 23832 Secondary Dendritic Orientation

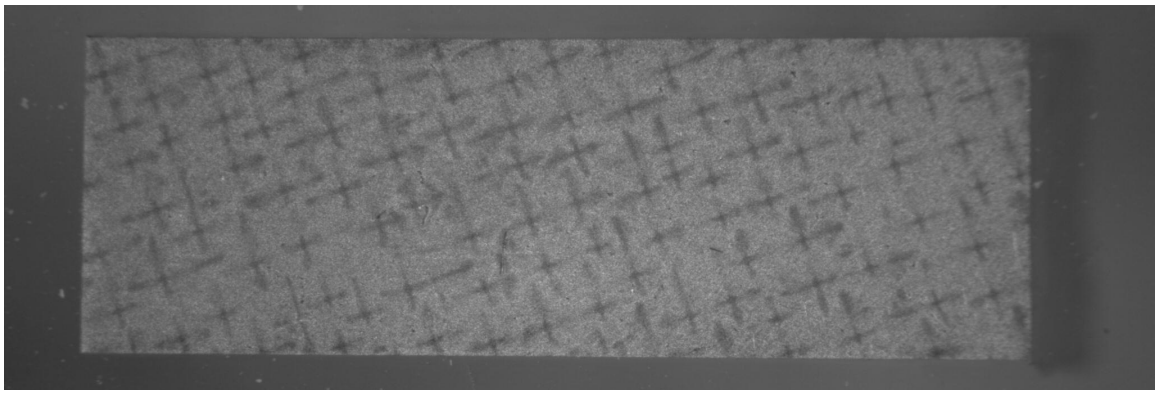

Figure 4.5: PWA1484 Slab 23833 Secondary Dendritic Orientation

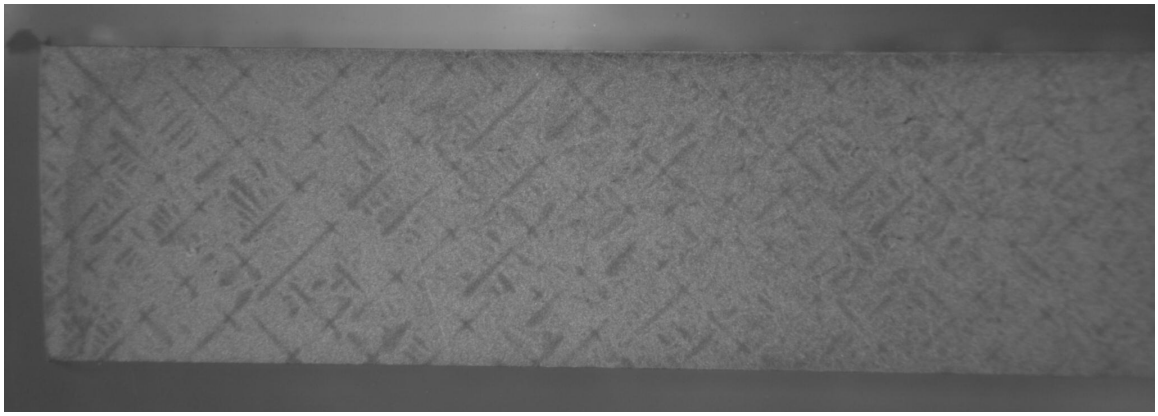

Figure 4.6: PWA1484 Slab 23834 Secondary Dendritic Orientation

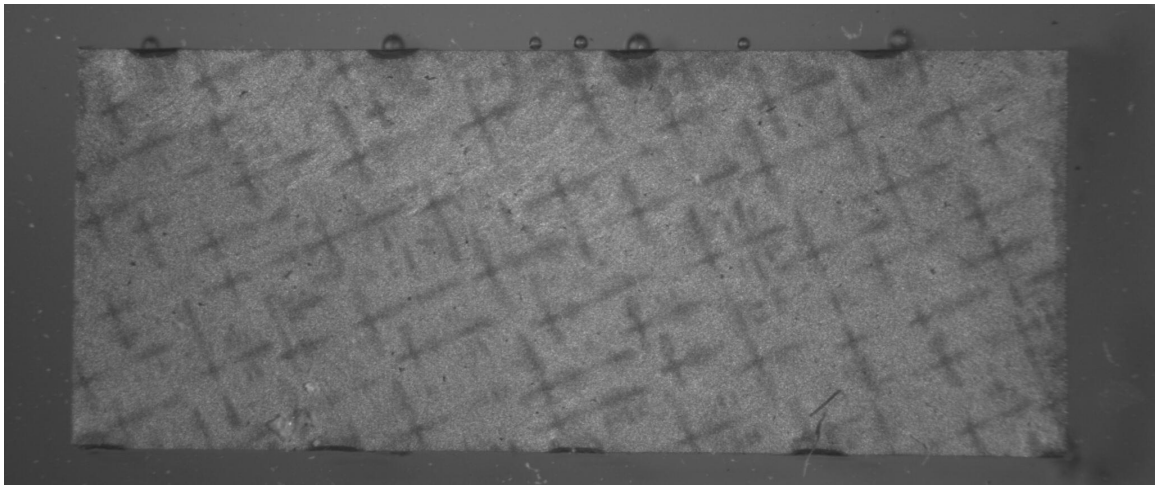

Figure 4.7: PWA1484 Slab 23835 Secondary Dendritic Orientation

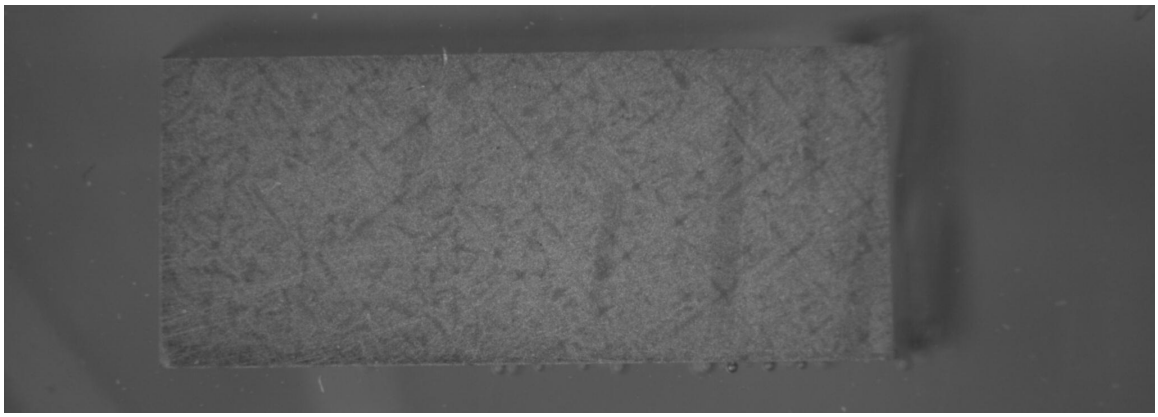

Figure 4.8: PWA1484 Slab 23836 Secondary Dendritic Orientation

Figure 4.9: PWA1484 Slab 23838 Secondary Dendritic Orientation

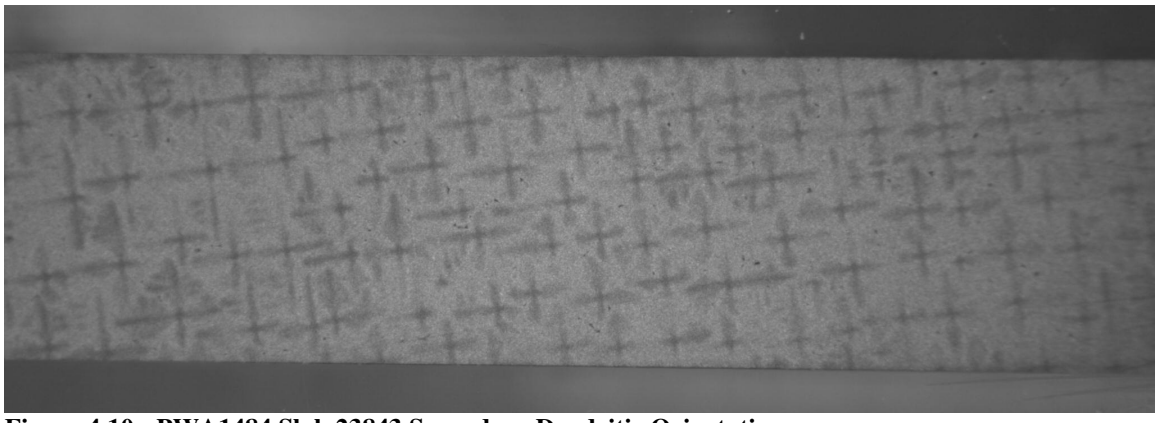

Figure 4.10: PWA1484 Slab 23843 Secondary Dendritic Orientation

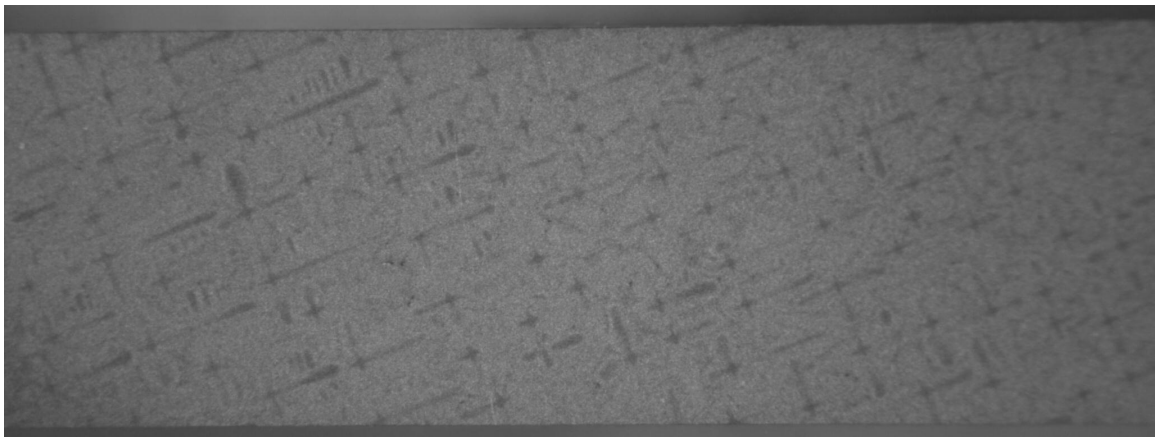

Figure 4.11: PWA1484 Slab 23844 Secondary Dendritic Orientation

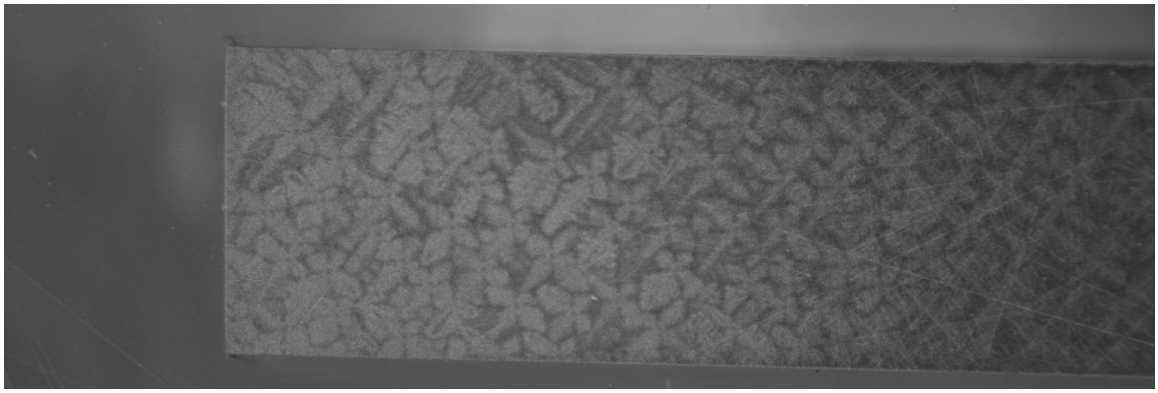

Figure 4.12: PWA1484 Slab 23845 Secondary Dendritic Orientation

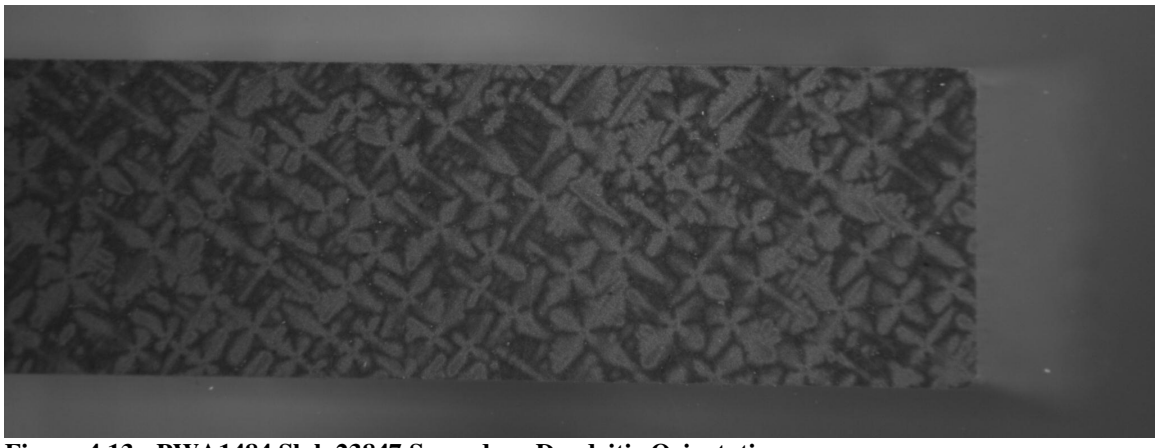

Figure 4.13: PWA1484 Slab 23847 Secondary Dendritic Orientation

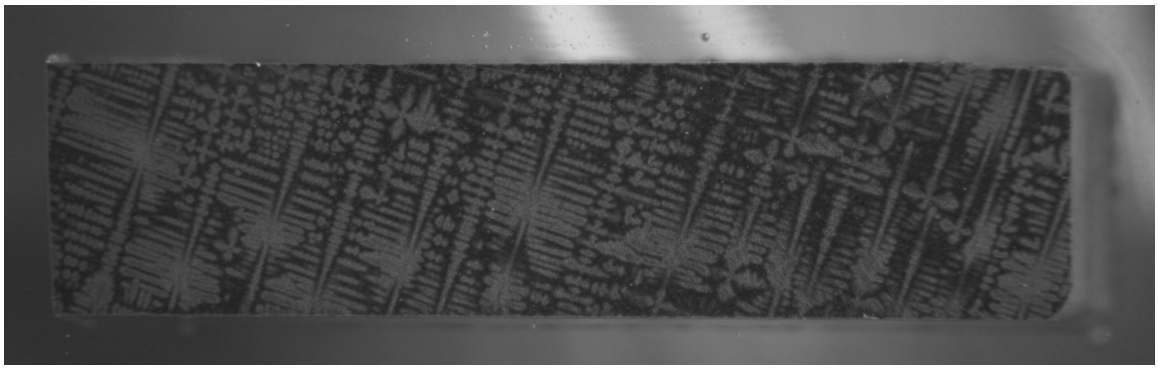

Figure 4.14: PWA1484 Slab 23848 Secondary Dendritic Orientation

The results of the dendritic inspection can be seen in Table 4.2. The cross sign formed by the dendrites has arms pointing in the [100] and [010] directions as the primary orientation is [001]. The deviation for each of these slabs from either of these cubic directions is between 16 and 44 degrees for all twelve slabs. Secondary orientations deviations from [110] are between 1 and 25 degrees as shown in Table 4.2.

Table 4.2: PWA1484 Uncontrolled Slab Primary and Secondary Orientations

Material	Slab ID	Primary Orientation	Deviation (degrees)	Secondary Orientation	Deviation (degrees)
PWA1484	23831	<001>	2.6	<110>	17
PWA1484	23832	<001>	10.5	<110>	25
PWA1484	23833	<001>	7.7	<110>	1
PWA1484	23834	<001>	1.7	<110>	19
PWA1484	23835	<001>	7.4	<110>	5
PWA1484	23836	<001>	5.2	<110>	1
PWA1484	23838	<001>	5.0	<110>	1
PWA1484	23843	<001>	5.0	<110>	23
PWA1484	23844	<001>	4.1	<110>	1
PWA1484	23845	<001>	2.2	<110>	25
PWA1484	23847	<001>	6.2	<110>	29
PWA1484	23848	<001>	7.2	<110>	9

4.3: Monotonic and Cyclic Property Determination

To better understand the monotonic and cyclic properties of PWA1484 in the <001> loading direction a series of tests ranging from 316°C to 982°C were run at two different strain rates. 2.5E-05 1/s and 2.5E-03 1/s were the strain rates chosen for all sets of tests. These two strain rates differ by two orders of magnitude and allow for a wide strain rate characterization of PWA1484. All test conditions can be seen in Table 4.3.

Table 4.3: Temperature, Strain Rate and Strain Range for Monotonic and Cyclic Testing

Monotonic at Constant Temperature

Specimen	Temperature (°C)	Strain Rate (s^{-1})
1	316	2.50E-05
2	316	2.50E-03
3	482	2.50E-05
4	482	2.50E-03
5	649	2.50E-05
6	649	2.50E-03
7	816	2.50E-05
8	816	2.50E-03
9	982	2.50E-05
10	982	2.50E-03

Cyclic at Constant Temperature

Specimen	Temperature (°C)	Strain Rate (s^{-1})	Strain Range (%)
11	649	2.50E-03	+/- 0.5 & +/- 0.66
12	649	2.50E-03	+/- 0.83
13	649	2.50E-03	+/- 1.0
14	649	2.50E-03	+/- 1.33
15	816	2.50E-03	+/- 0.5 & +/- 1.0
16	816	2.50E-03	+/- 1.16
17	816	2.50E-03	+/- 1.33
18	982	2.50E-03	+/- 0.5 & +/- 0.66
19	982	2.50E-03	+/- 0.83
20	982	2.50E-03	+/- 1.0
21	982	2.50E-03	+/- 1.33

All monotonic stress strain curves are shown in Figure 4.15. Monotonic testing was performed at 316°C, 482°C, 649°C, 816°C and 982°C and carried out to an engineering strain of 8.0%. In nearly all cases the PWA1484 demonstrated almost pure elastic

perfectly plastic behavior. Notable exceptions are the 816°C fast, 816°C slow and 982°C slow tests.

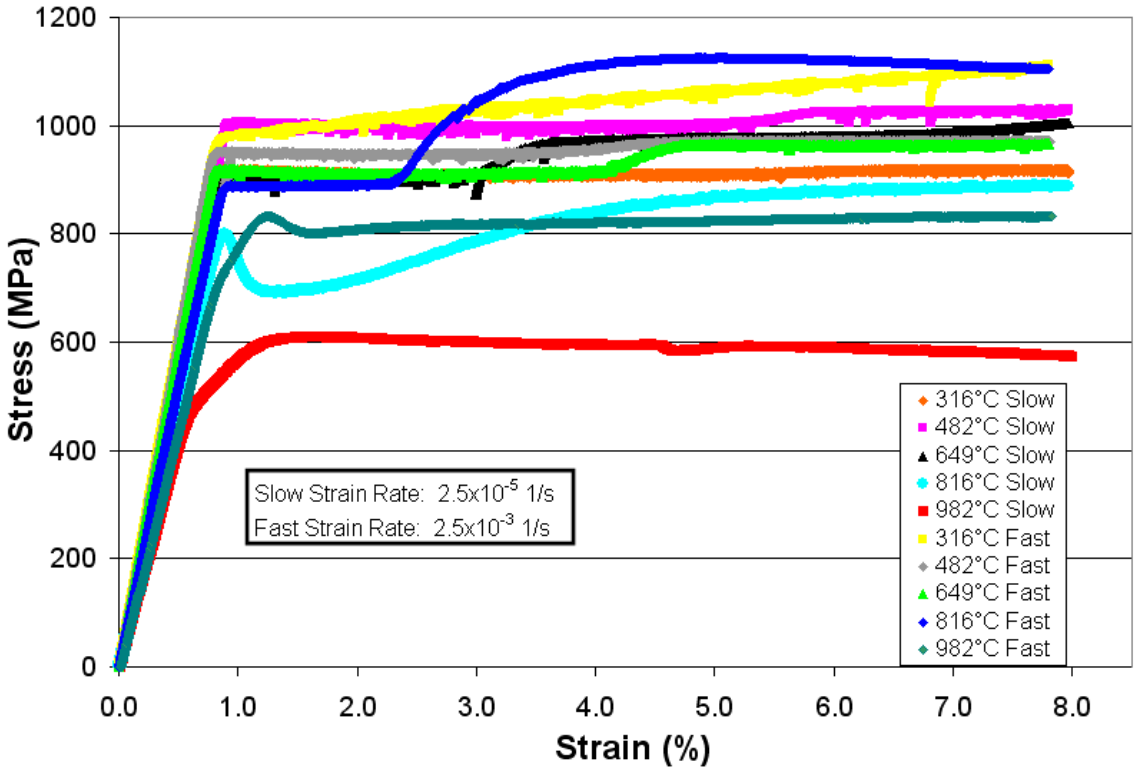

Figure 4.15: Stress Strain Curves under Slow and Fast Strain Rates for PWA1484

The 2.5E-03 1/s strain rate stress strain results are shown in Figure 4.16. As would be expected at a faster strain rate the yield stress decreases with increasing temperature with the most notable drop at 982°C. Also interesting to note is the modulus of elasticity also tends to decrease slightly with increasing temperature. The 816°C fast stress strain curve demonstrates some hardening behavior around 2.5% strain. In addition the 316°C fast stress strain curve exhibits clear serrated flow also known as the Portevin–Le Chatelier (PLC) effect [160]. The PLC effect can lead to inhomogeneous deformation due to strain concentrations. This phenomenon occurs at certain combinations of temperature and strain rate and arises from a dynamic interaction between dislocations and solute atoms.

This occurrence has been shown to occur in precipitate systems and in particular for Ni-base superalloys [161-163].

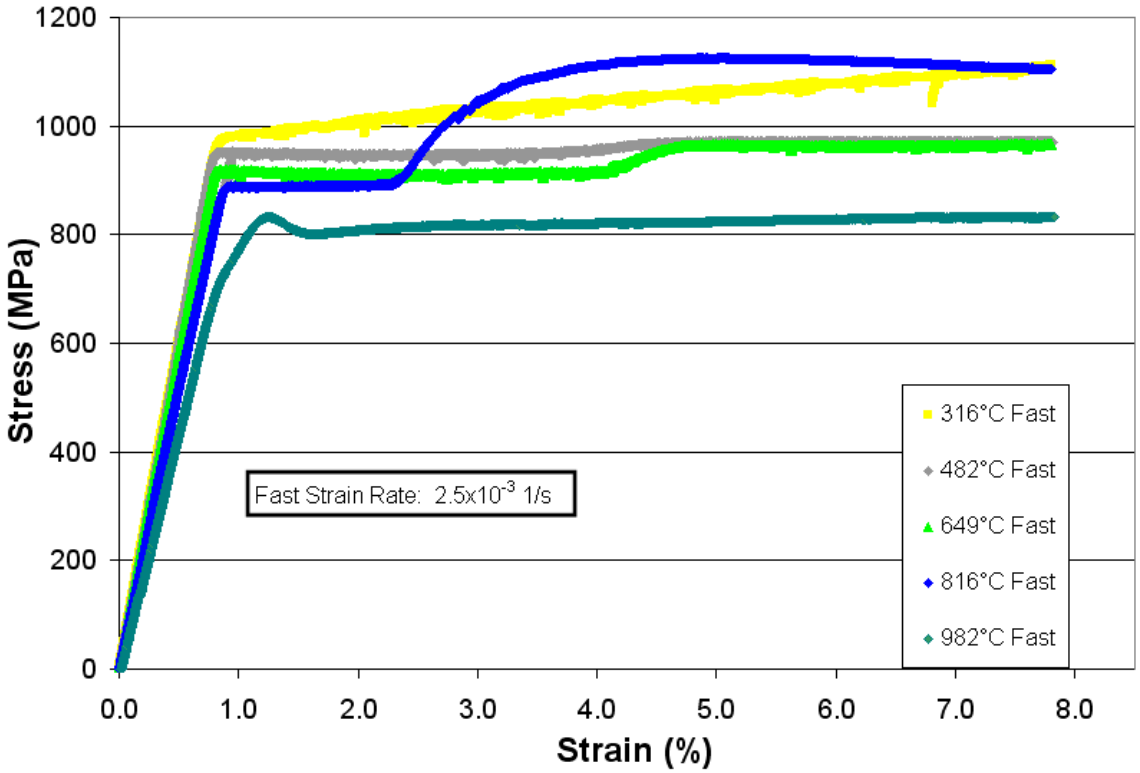

Figure 4.16: Stress Strain Curves Under Fast Strain Rates for PWA1484

The 2.5E-05 1/s strain rate stress strain results are shown in Figure 4.17. The 482°C stress strain curve has the highest yield stress and again the modulus of elasticity tends to decrease slightly with increasing temperature. The 816°C stress strain curve has an interesting double yield point as is seen in low carbon steels. The 482°C and 649° stress strain curves demonstrate very strongly the PLC effect. A trend can now be seen with the PLC effect present at lower temperature under faster strain rates and intermediate temperatures at the slower strain rate. It could be reasoned that the PLC effect would be present at higher temperature under an even slower strain rate than 2.5E-05 1/s.

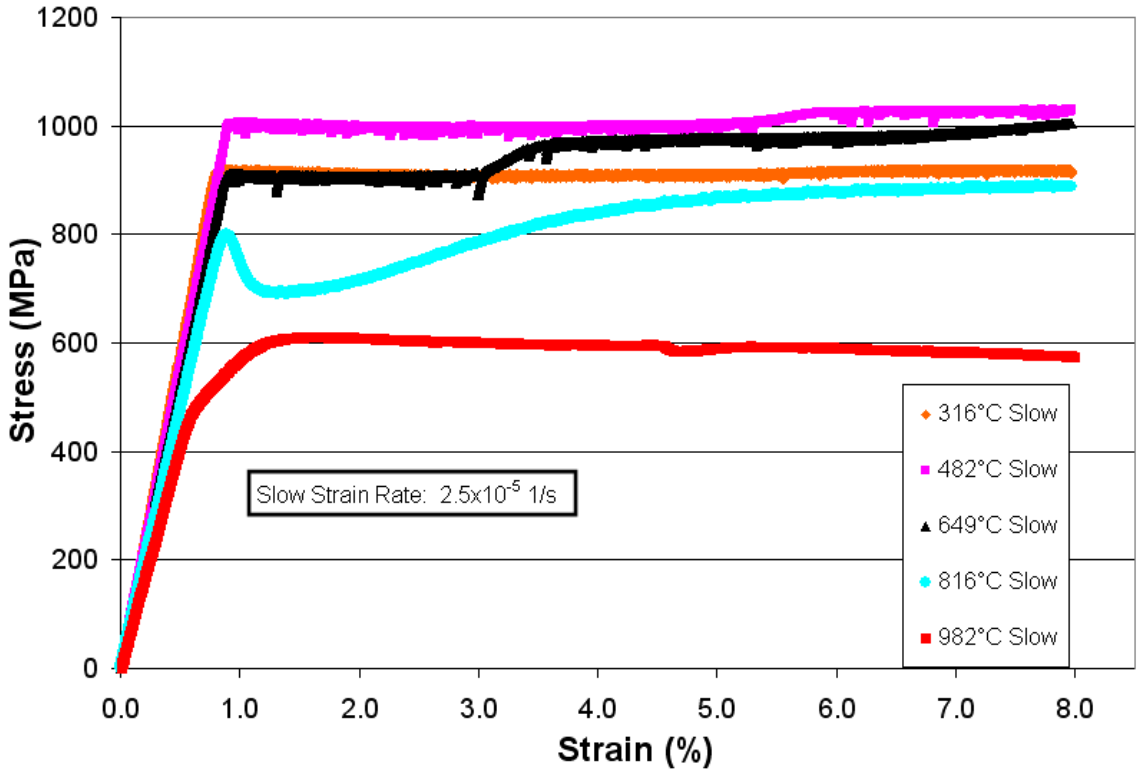

Figure 4.17: Stress Strain Curves Under Slow Strain Rates for PWA1484

The yield strength for each of the monotonic tensile tests was determined using a 0.2% strain offset. These results can be seen graphically in Figure 4.18. In addition data points from the Nickel Development Institute are also plotted [164]. The strain rate used to obtain the Nickel Development Institute data was not given but conventional wisdom is that yield strength data is taken at slower strain rates very similar to our slow strain rate of 2.5E-05 1/s. Overall there is very good correlation between the data points except for a slight discrepancy in the temperatures corresponding to the maximum yield strengths. For the slow strain rate data the peak is at around 482°C while the Nickel Development Institute data peaks between 649°C and 760°C.

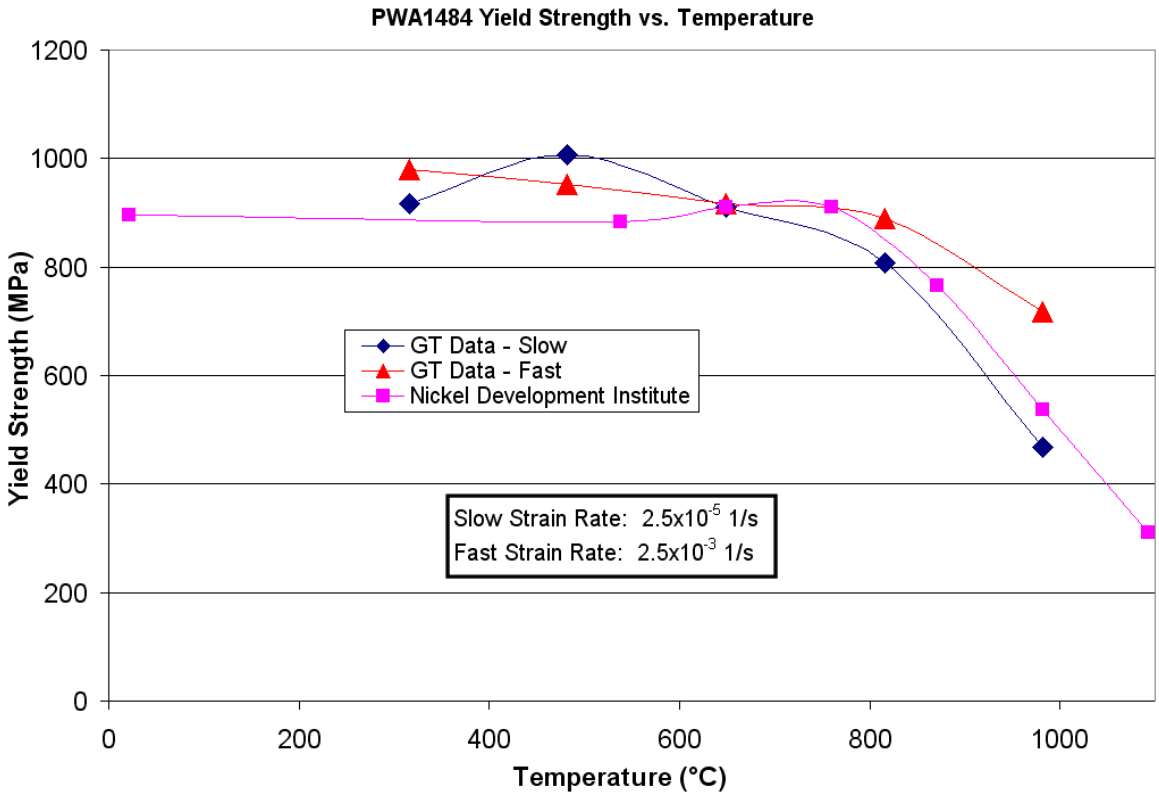

Figure 4.18: PWA1484 Yield Strength as a Function of Temperature [164]

The modulus for each of the monotonic tensile tests is shown graphically in Figure 4.19. Again there is excellent correlation between the slow strain rate data and the data from the Nickel Development Institute. At all temperatures the fast strain rate data is slightly higher than the slow strain rate data. Elastic modulus strain rate sensitivity of superalloys is not a phenomenon discussed in currently published literature. The fast strain rate tests took 32 seconds to run and the slight increase in modulus could be due inertia of the test system. What is common for single crystal superalloys is a difference in modulus due to orientation effects [165, 166]. In this case all tensile specimens had a maximum deviation of 10.5° from the <001> orientation so this slight increase in modulus is most likely due to an artifact of the high strain rate and the test system. The yield strength and

modulus PWA1484 are presented in tabular form in Table 4.4 and Table 4.5, respectively.

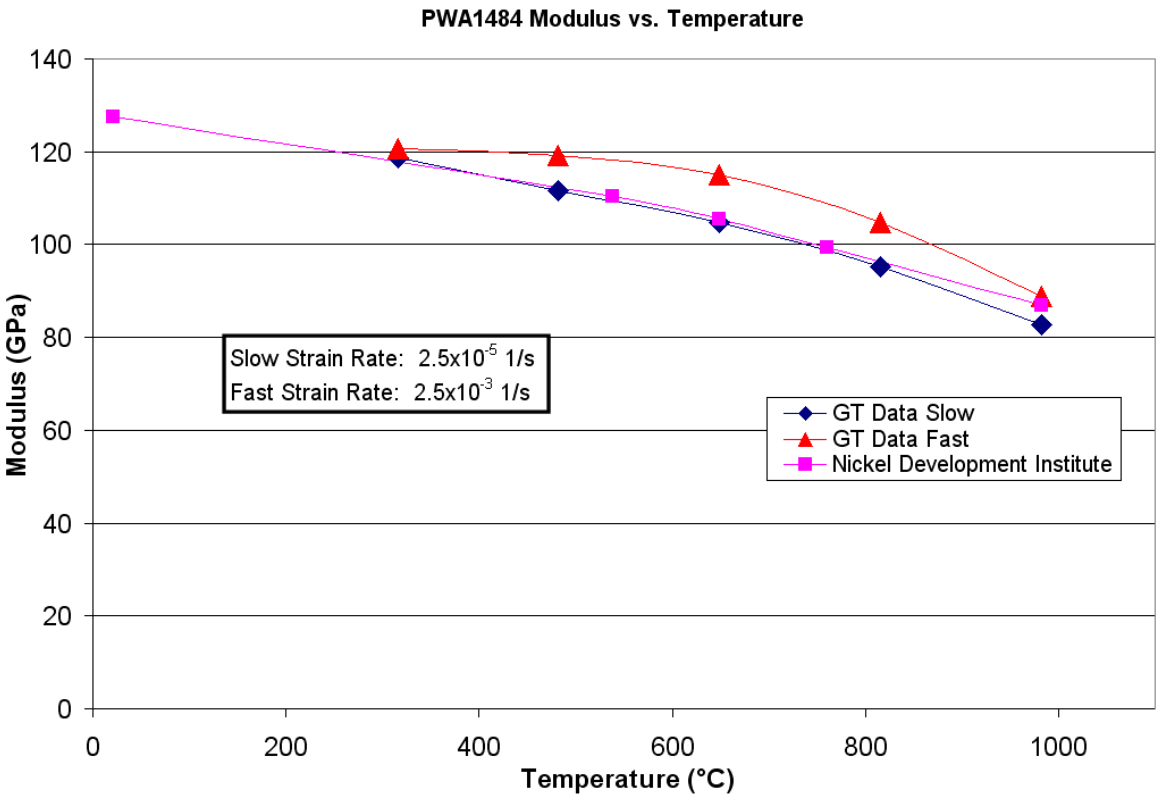

Figure 4.19: PWA1484 Modulus as a Function of Temperature [164]

Table 4.4: PWA1484 Slow and Fast Yield Strength Values

Temp (°C)	Slow Yield Strength (MPa)	Fast Yield Strength (MPa)
316	917.0	979.1
482	1006.6	951.5
649	910.1	917.0
816	806.7	889.4
982	468.8	717.1

Table 4.5: PWA1484 Slow and Fast Modulus Values

Temp (°C)	Slow Modulus (GPa)	Fast Modulus (GPa)
316	118.6	120.7
482	111.7	119.3
649	104.8	115.1
816	95.1	104.8
982	82.7	88.9

A strain rate of 2.5E-03 1/s was used for all cyclic stress strain tests. This faster rate was determined to be more representative of the conditions seen at the crack tip during fatigue crack growth rate testing. Hysteresis stress strain loops for tests performed at 649°C, 816°C and 982°C are shown in Figure 4.20 through Figure 4.22. Strain amplitudes of 0.5%, 1.0% and 1.33% are shown for each of the temperatures. For all 3 temperatures a 0.5% cyclic strain amplitude was shown to be purely elastic. At a 1.0% cyclic strain amplitude the 649°C and 982°C curves showed a slight amount of plasticity while at 816°C the specimen cycled elastically. This is to be expected due to the increasing yield strength phenomenon at intermediate temperatures. 816°C also demonstrated the least bit of plasticity at a strain amplitude of 1.33%. At 649°C and 816°C there was a decent amount of cyclic strain hardening throughout the life of the specimen while at 982°C there was only a slight bit of cyclic strain that stabilized after only a few cycles.

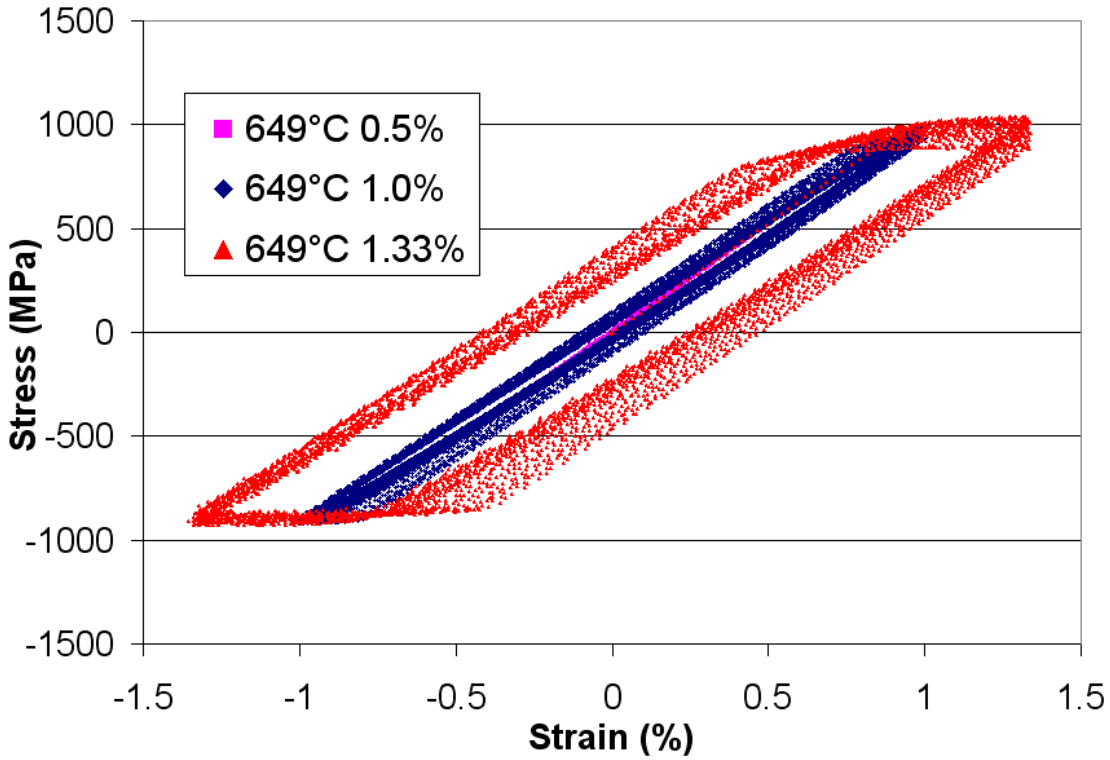

Figure 4.20: PWA1484 Cyclic Stress Strain Curves at 649°C

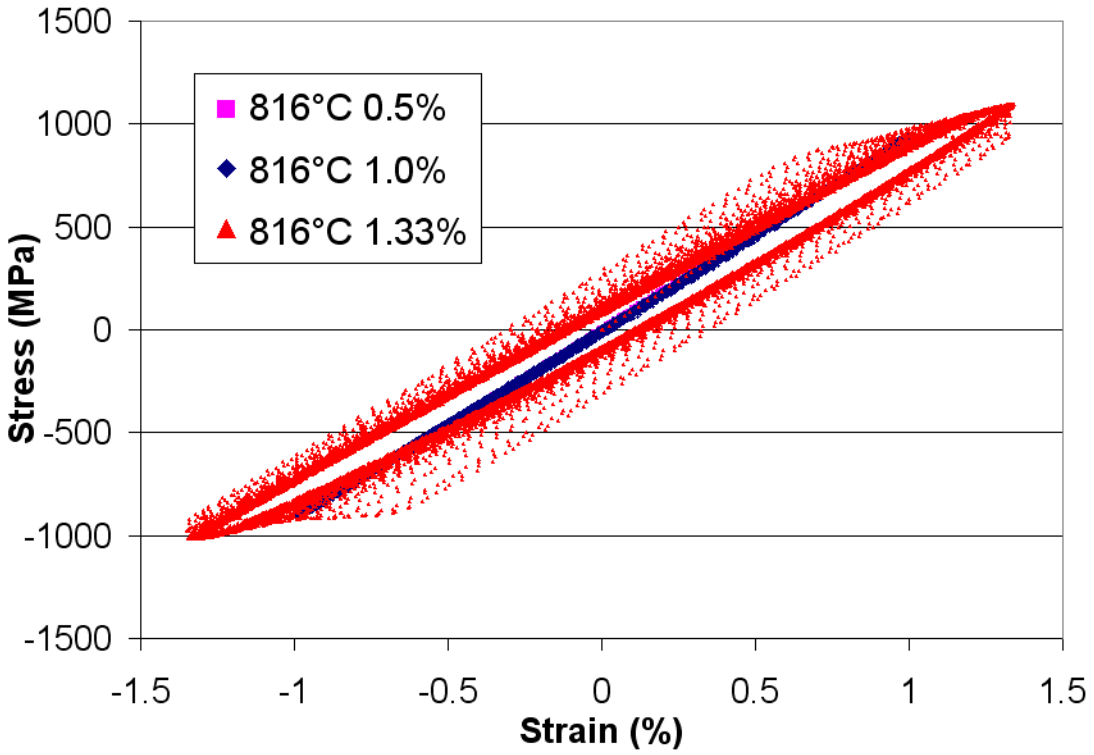

Figure 4.21: PWA1484 Cyclic Stress Strain Curves at 816°C

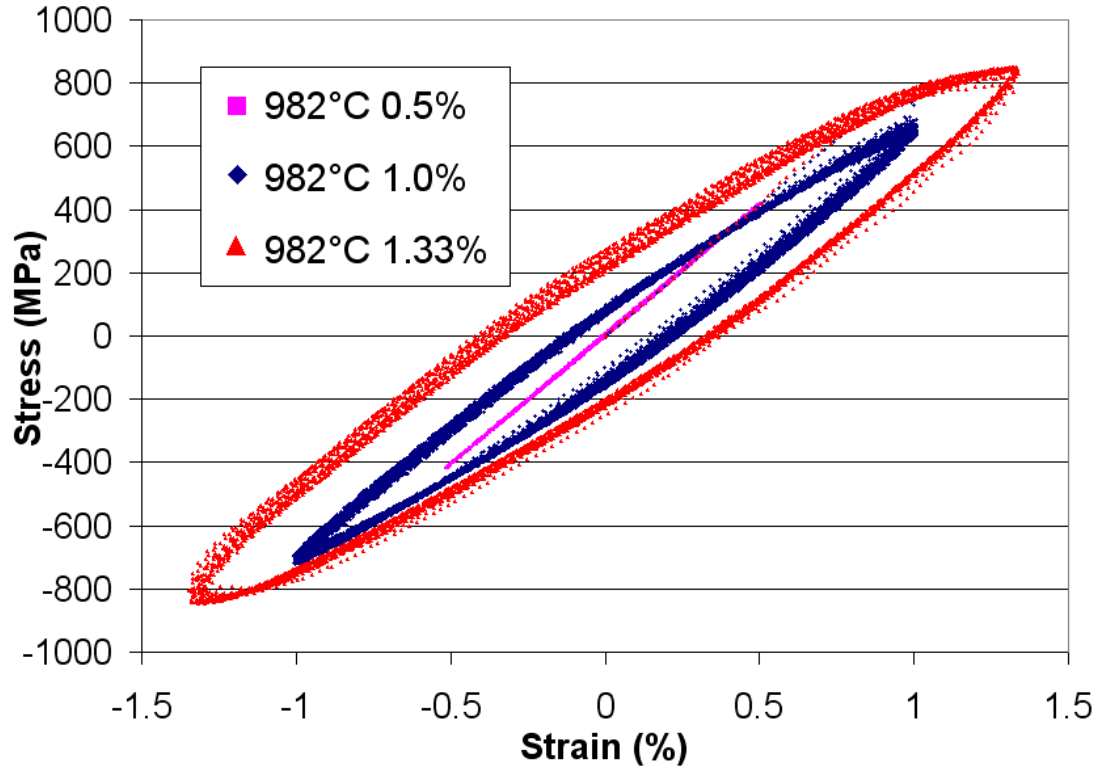

Figure 4.22: PWA1484 Cyclic Stress Strain Curves at 982°C

The strain life at all three temperatures and strain amplitudes between 0.66% and 1.33% is shown in Figure 4.23. The lives at 649°C and 982°C are very similar with the life at 816°C being longer on average. 982°C and 649°C tests at a strain amplitude of 0.66% were stopped at 1200 cycles due to time constraints on the testing machine. This is the reason for the run-out arrows on the figure.

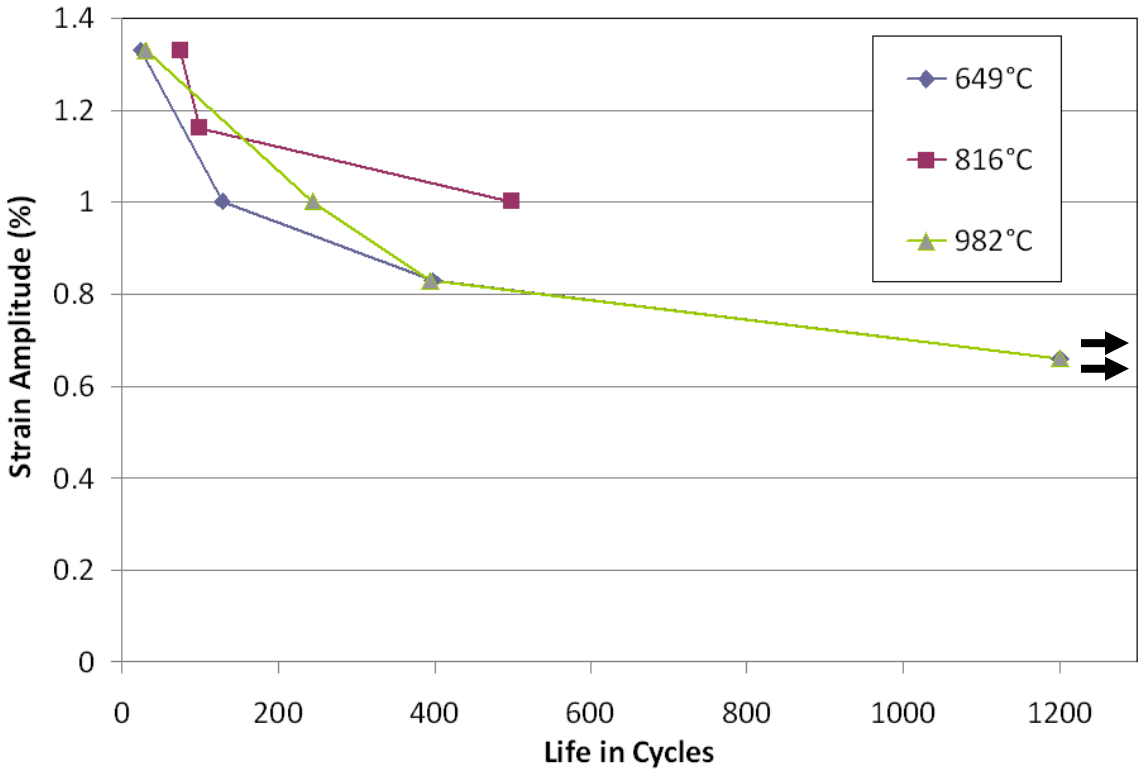

Figure 4.23: PWA1484 Strain Life Results for 649°C, 816°C and 982°C

4.4: Isothermal Constant Amplitude Testing

The fatigue crack growth rates for isothermal constant amplitude will be presented in this section. Within isothermal constant amplitude testing the effect of secondary orientation, temperature, R Ratio and inert environment will be discussed. All twelve isothermal constant amplitude results are shown in Figure 4.24. These tests were performed at 649°C, 816°C, 982°C and R Ratios of 0.1 and 0.7. All testing was performed at a frequency of 1 Hz. Of these twelve specimens tested six specimens had uncontrolled secondary orientations and six specimens had controlled secondary orientations. All fatigue crack growth rate data was processed using the seven point incremental polynomial technique as described by Hudak et al. [167] and is in accordance with ASTM E647-13, "Standard Test Method for Measurement of Fatigue Crack Growth Rates" [158].

Standard Mode I ΔK was used for most of the fatigue crack growth rate data. Chan and Cruse [92] have shown that isotropic stress intensity factors are valid for cracking that is inclined 30° or less from the plane perpendicular to loading in single crystal superalloys. They found that the boundary-correction factors for both 0° and 30° cracks were almost identical and do not become greatly dependent until angles of 45° and larger. Their results demonstrated that the stress intensity factors did not depend on the elastic anisotropy for single crystal Mar-M200 CT specimens. For this research the few specimens where the cracking was larger than 30° Mode I and Mode II stress intensity factors were combined through the energy release rate, G, as shown in Equation 4.1. This equation is for plane strain conditions. Even though ΔK is not the ideal crack

driving force in single crystal materials it still scales appropriately for relative comparisons.

$$G = \frac{K_I^2\left(1-v^2\right)}{E} + \frac{K_{II}^2\left(1-v^2\right)}{E} = \frac{K^2\left(1-v^2\right)}{E} \tag{4.1}$$

4.4.1: Effect of Secondary Orientation

All uncontrolled secondary orientation fatigue crack growth rate data is shown in Figure 4.25 while the controlled secondary orientation FCGR data is shown in Figure 4.26. The controlled orientation crack growth data has less rate variance among the three temperatures and two R Ratios. Most uncontrolled specimens ended up having a secondary orientation within several degrees of <110>. A couple specimens had deviations as large as 25° from <110>. Figure 2.25 clearly shows that the controlled specimens which have a cubic secondary orientation, (<100>) exhibit faster crack growth than the uncontrolled secondary orientation, (<110>) specimens. This correlates very well with published literature where it is often found that <100> crack growth is roughly 2x faster than <110> crack growth.

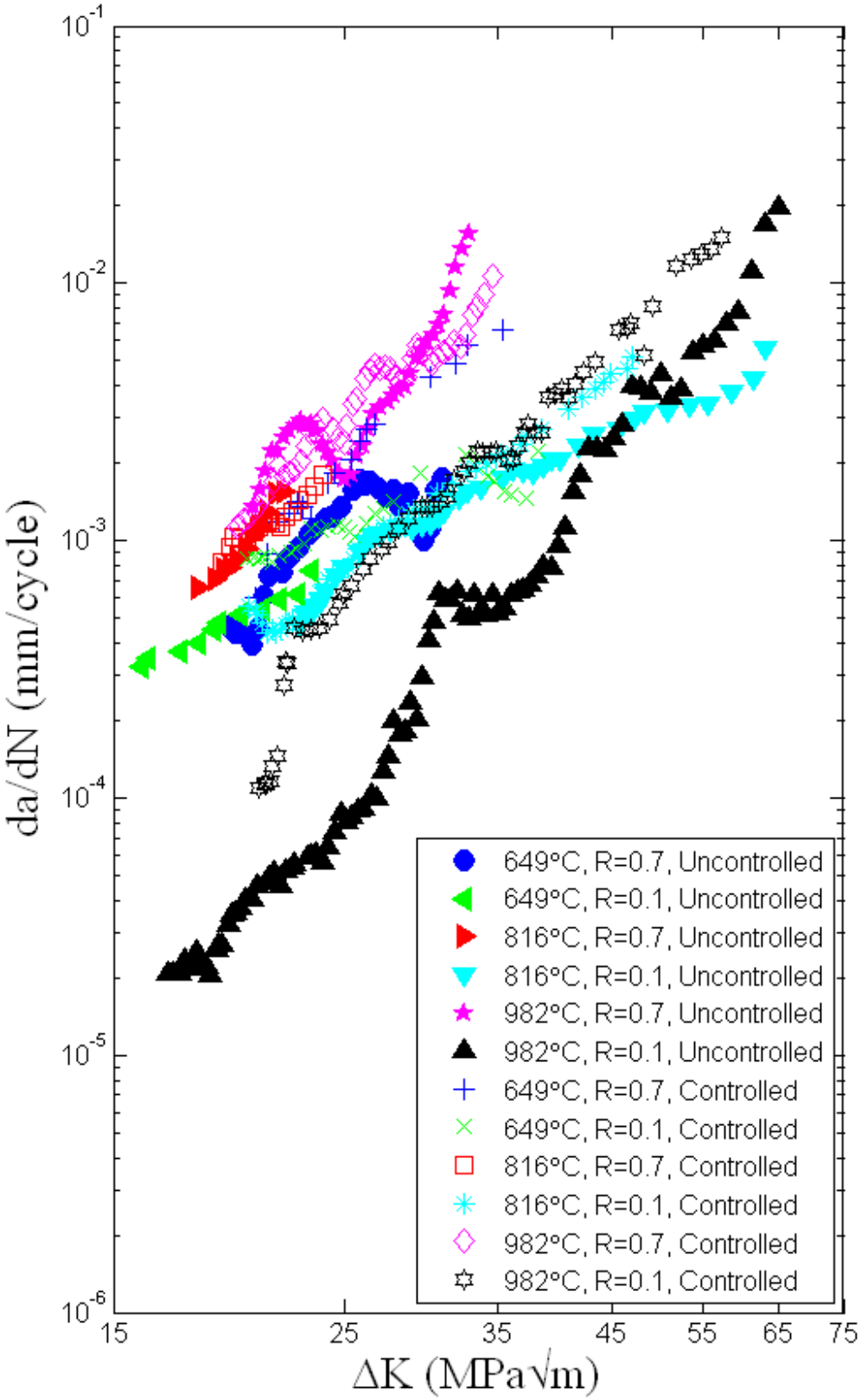

Figure 4.24: PWA1484 Fatigue Crack Growth Rates for All Isothermal Constant Amplitude Tests

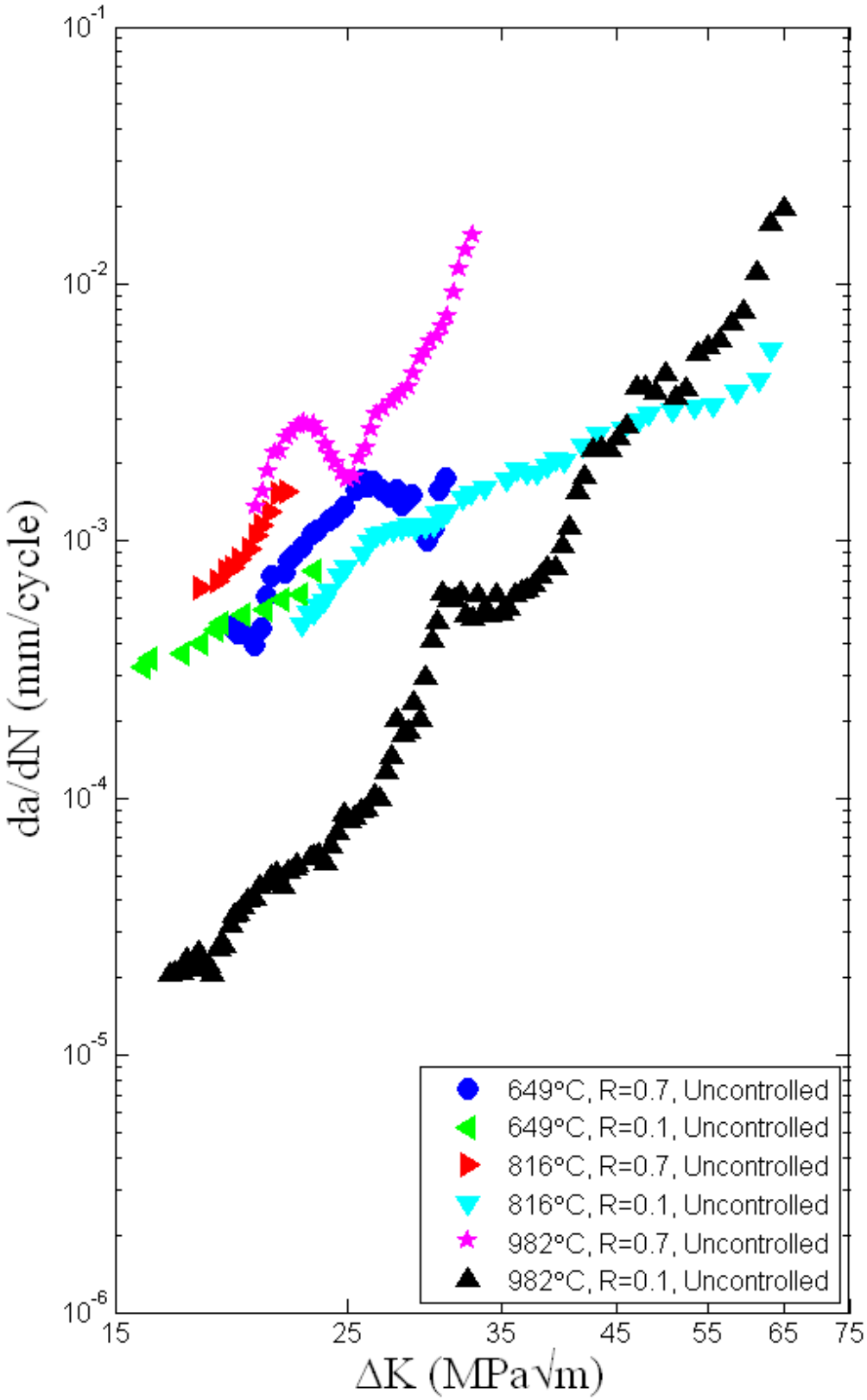

Figure 4.25: PWA1484 Fatigue Crack Growth Rates for Uncontrolled Secondary Orientation Isothermal Constant Amplitude Tests

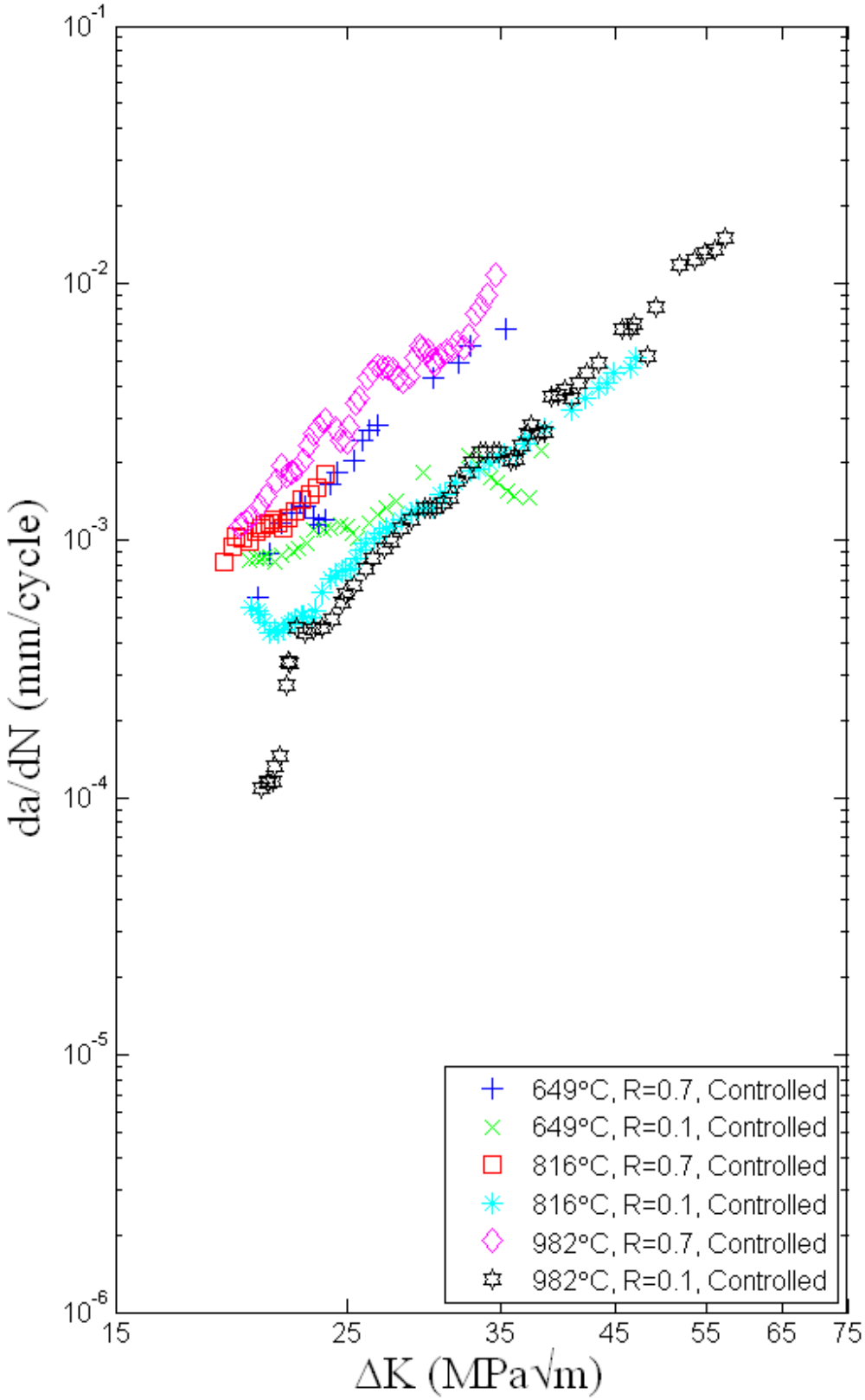

Figure 4.26: PWA1484 Fatigue Crack Growth Rates for Controlled Secondary Orientation Isothermal Constant Amplitude Tests

4.4.2: Effect of Temperature

The effect of temperature at both R Ratios can clearly be seen in Figure 4.27 and Figure 4.28. At R=0.7 (Figure 4.27) the crack growth rate increases with increasing temperature for both the controlled and uncontrolled specimens as shown in Figure 4.27. By looking at the figure one could call into question the use of ΔK as the crack driving force in single crystal materials. There are situations where the trans-precipitate non crystallographic cracking transitions to crystallographic cracking which creates a decrease in the crack growth rate that ΔK can not properly account for. As discussed in the previous section at all three temperatures (649°, 816° and 982°) the controlled specimens have slightly faster crack growth rates when compared to the uncontrolled specimens.

In Figure 4.28 the R=0.1 data shows a little bigger crack growth rate variance than at R=0.7. This is mostly due to the slow growth rate at low ΔK values for the 982°C uncontrolled specimen. At this R Ratio and low values of ΔK the crack growth rate decreases with increasing temperature. This is rather unusual and is most likely caused by crack closure as a result of increased plasticity and oxidation at the higher temperatures. As ΔK increases the crack growth rates return to what is expected with the crack growth rate increasing with increasing temperature at R=0.1. This phenomenon has not been seen in any published literature but in talking with Pratt & Whitney this is something that has been documented before in PWA1484.

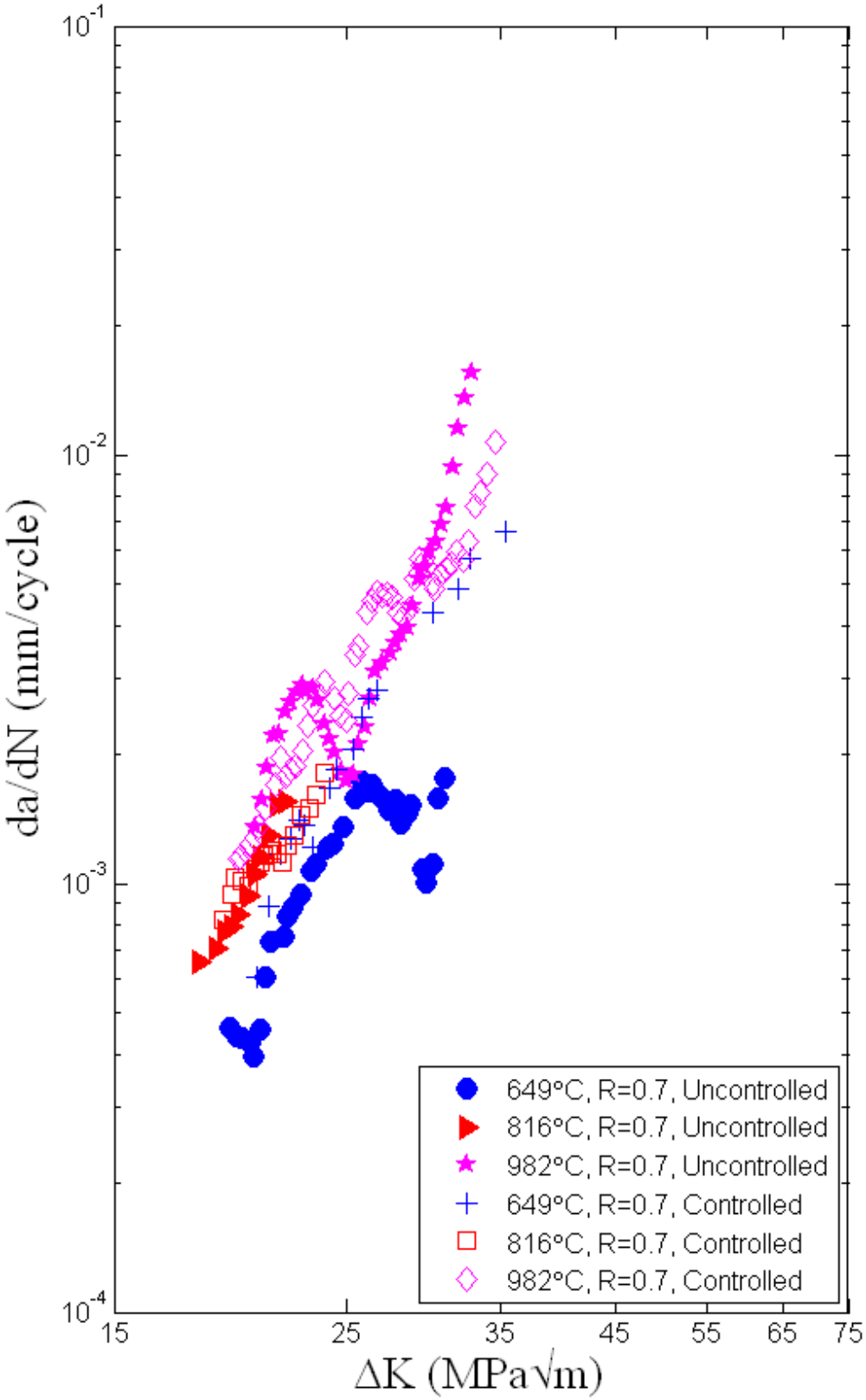

Figure 4.27: PWA1484 Fatigue Crack Growth Rates for R Ratio=0.7 Constant Amplitude Tests

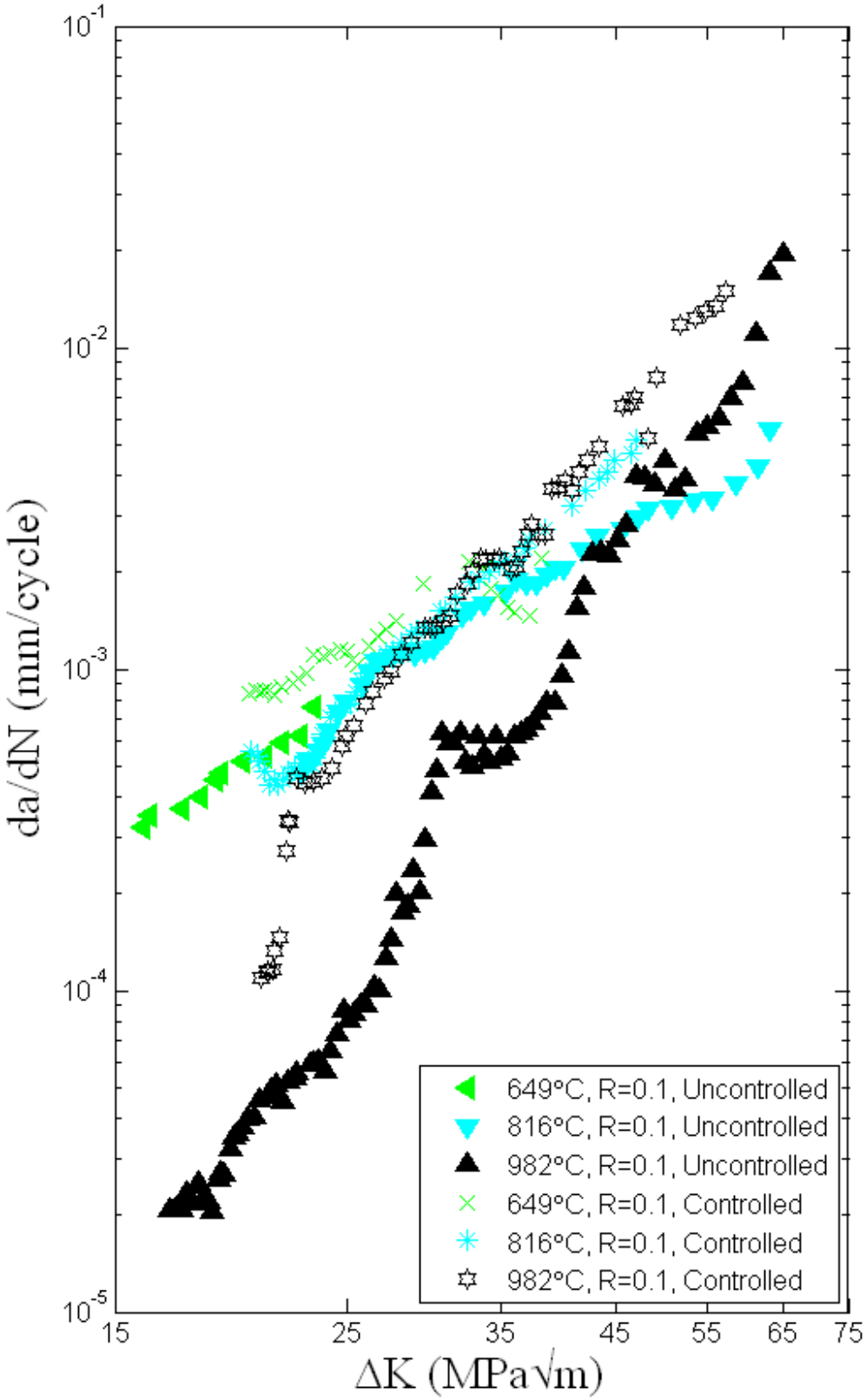

Figure 4.28: PWA1484 Fatigue Crack Growth Rates for R Ratio=0.1 Constant Amplitude Tests

4.4.3: Effect of R-Ratio

Figures 29-31 display the fatigue crack growth rates at 649°C, 816°C and 982°C respectively. At 649°C the effect of R Ratio is very minimal as seen in Figure 4.29. The R=0.7 tests show a slightly faster crack growth rate for both the controlled and uncontrolled specimens at 649°C.

At 816°C in Figure 4.30 the effect of R Ratio is very clearly seen with the R=0.7 test data being faster than the R=0.1 data. There is also very good correlation between the controlled and uncontrolled specimens. The uncontrolled specimens have a secondary orientation of 1° off <110> while the controlled specimens have a secondary orientation of a couple degrees within <010>. At 816°C the effect of secondary orientation appears to be very slight or non-existent.

The effect of R Ratio is most evident at 982°C as seen in Figure 4.31. The R=0.7 fatigue crack growth rate is faster than the R=0.1 data with the amount depending on the secondary orientation. For these tests the uncontrolled specimens have a secondary orientation of 5° of <110> while the controlled specimens have a secondary orientation of a couple degrees within <010>.

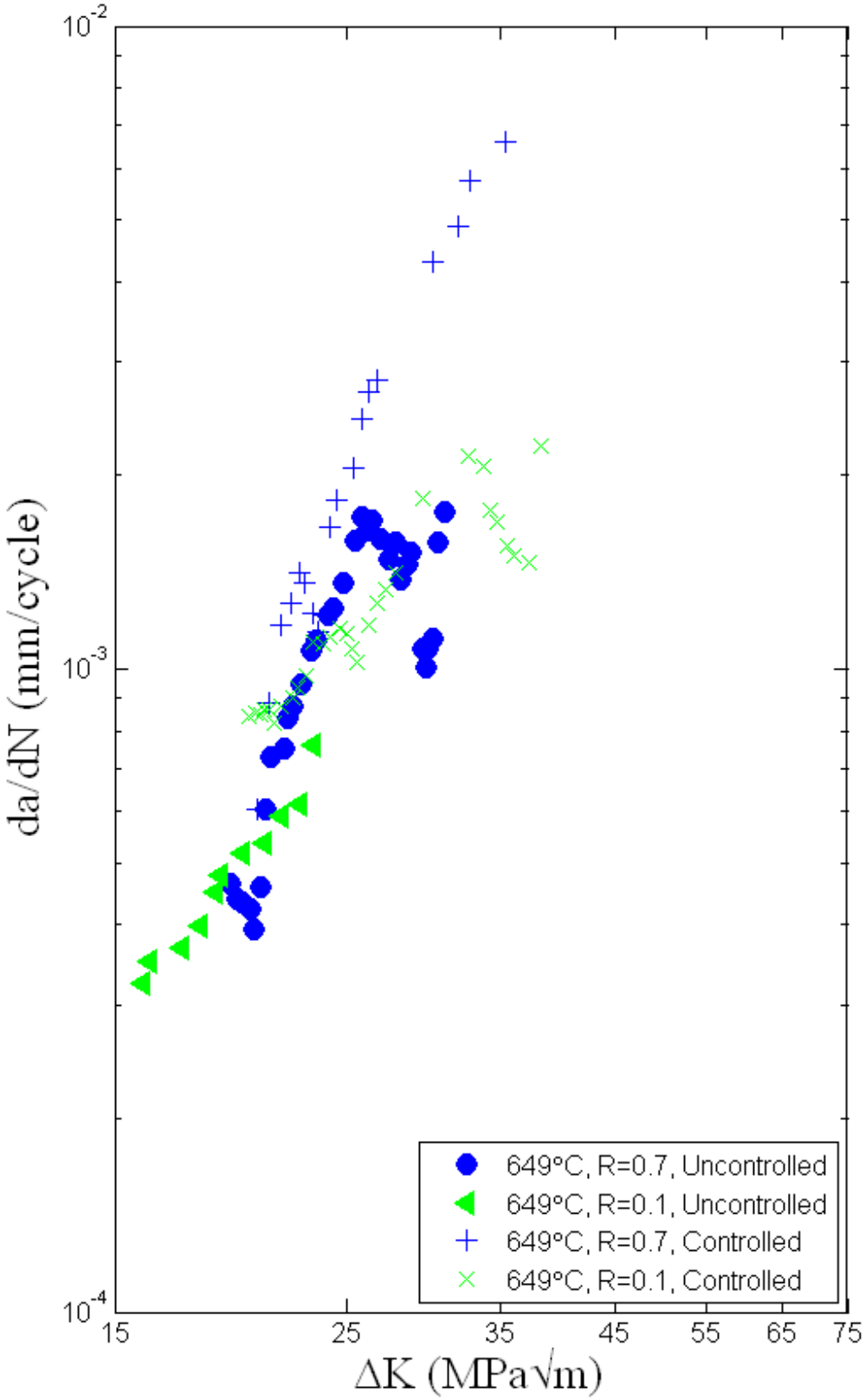

Figure 4.29: PWA1484 Fatigue Crack Growth Rates for 649°C Constant Amplitude Tests

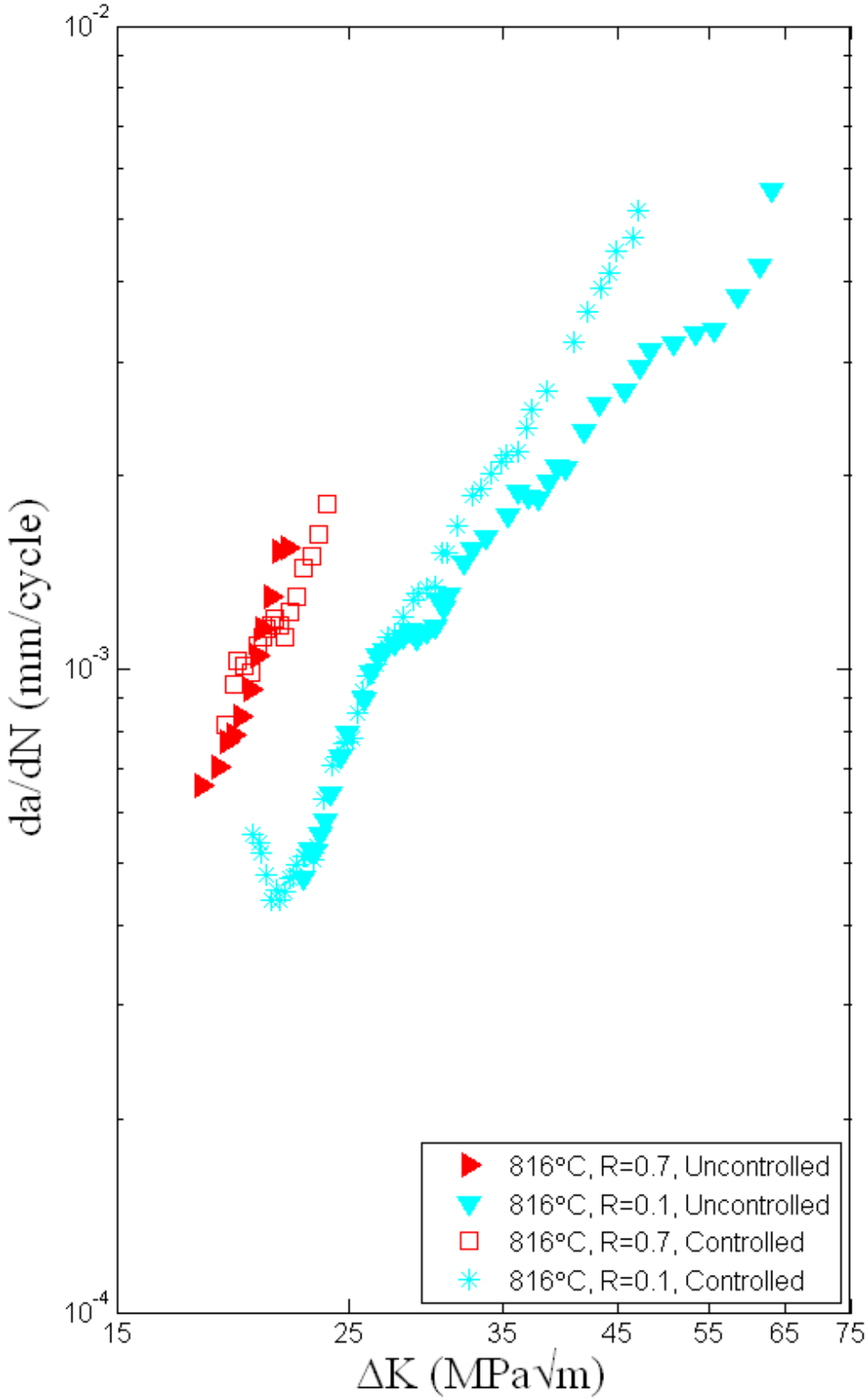

Figure 4.30: PWA1484 Fatigue Crack Growth Rates for 816°C Constant Amplitude Tests

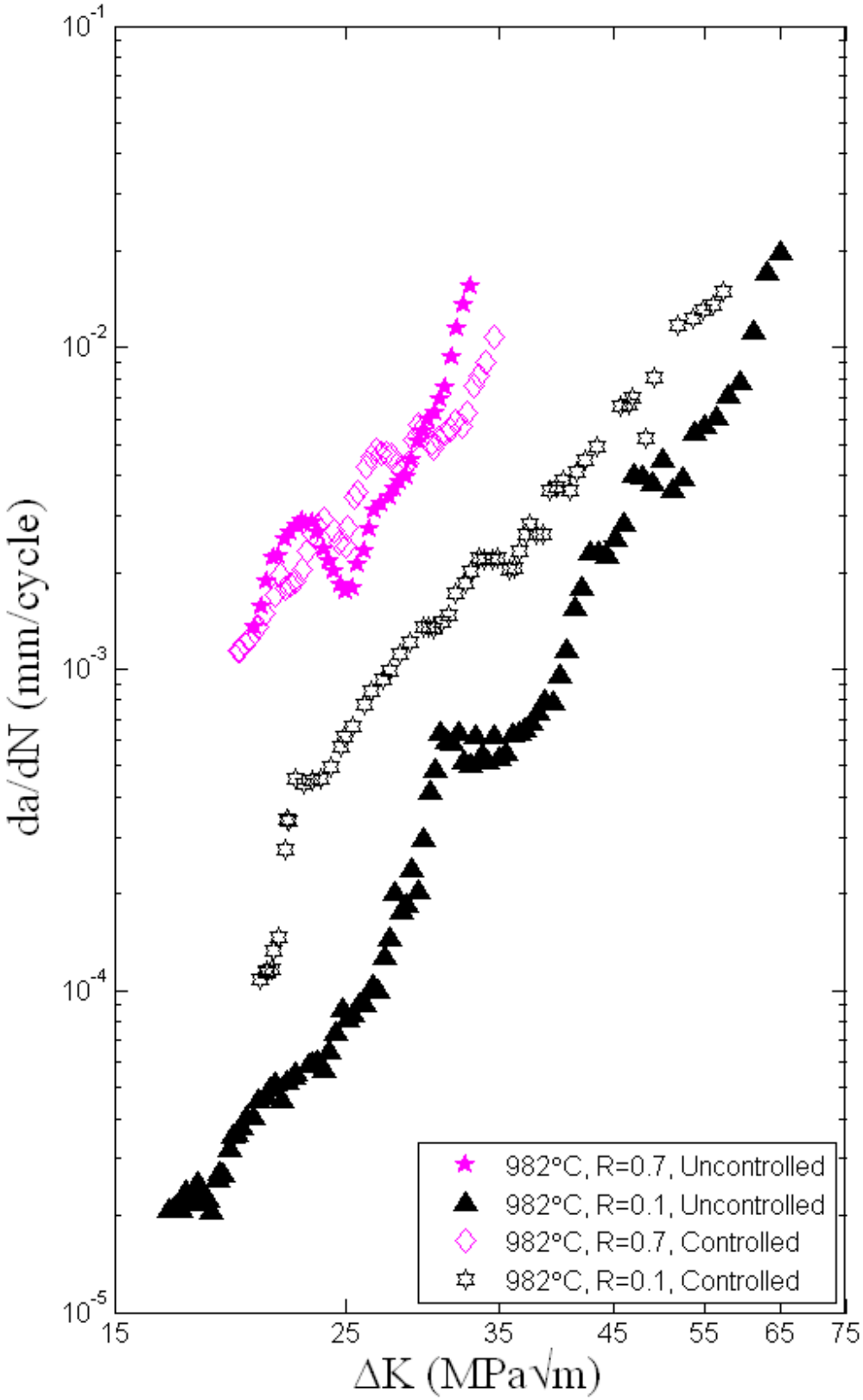

Figure 4.31: PWA1484 Fatigue Crack Growth Rates for 982°C Constant Amplitude Tests

4.4.4: Effect of Environment

One PWA1484 SENT specimen was tested in an argon purged environment to determine the effect oxygen has on the fatigue crack growth rate. This specimen was tested at 982°C and an R Ratio of 0.1. Throughout the test the percentage of oxygen in the chamber was measured to be 0.0%. This was as low as the oxygen analyzer would read. This FCGR data was then compared to 982°C, R=0.1 data tested in air. The argon tested specimen was chosen so that it had the same secondary orientation so the effect of environment on the crack growth rate was isolated. The results can be seen in Figure 4.32. Around a ΔK of 22 MPA$\sqrt{m}$ the argon crack growth rate falls on top of the air rate. The load was then increased to a ΔK of 33 MPA$\sqrt{m}$. These results show a faster crack growth rate than the air rate. The argon was then removed from the test chamber and the test was finished with laboratory air. The fatigue crack growth rate slowed matching with the original air test.

Even though the analyzer was reading 0.0% oxygen throughout the test there could still be 0.04% of oxygen present. This results in an oxygen partial pressure of .304 Torr which is still quite large when compared to the pressure of a high vacuum, 10^{-8} Torr. To better understand the results the partial pressure of oxygen would need to be analyzed. It is well known that gases diffuse and react relative to their partial pressures and not their mixture concentrations [168, 169]. The addition of argon could have potentially increased the amount of oxygen diffusion. To truly determine the effect of oxygen it is advised that additional testing be performed in a vacuum chamber. The use of a vacuum chamber for this research project was determined to be cost prohibitive.

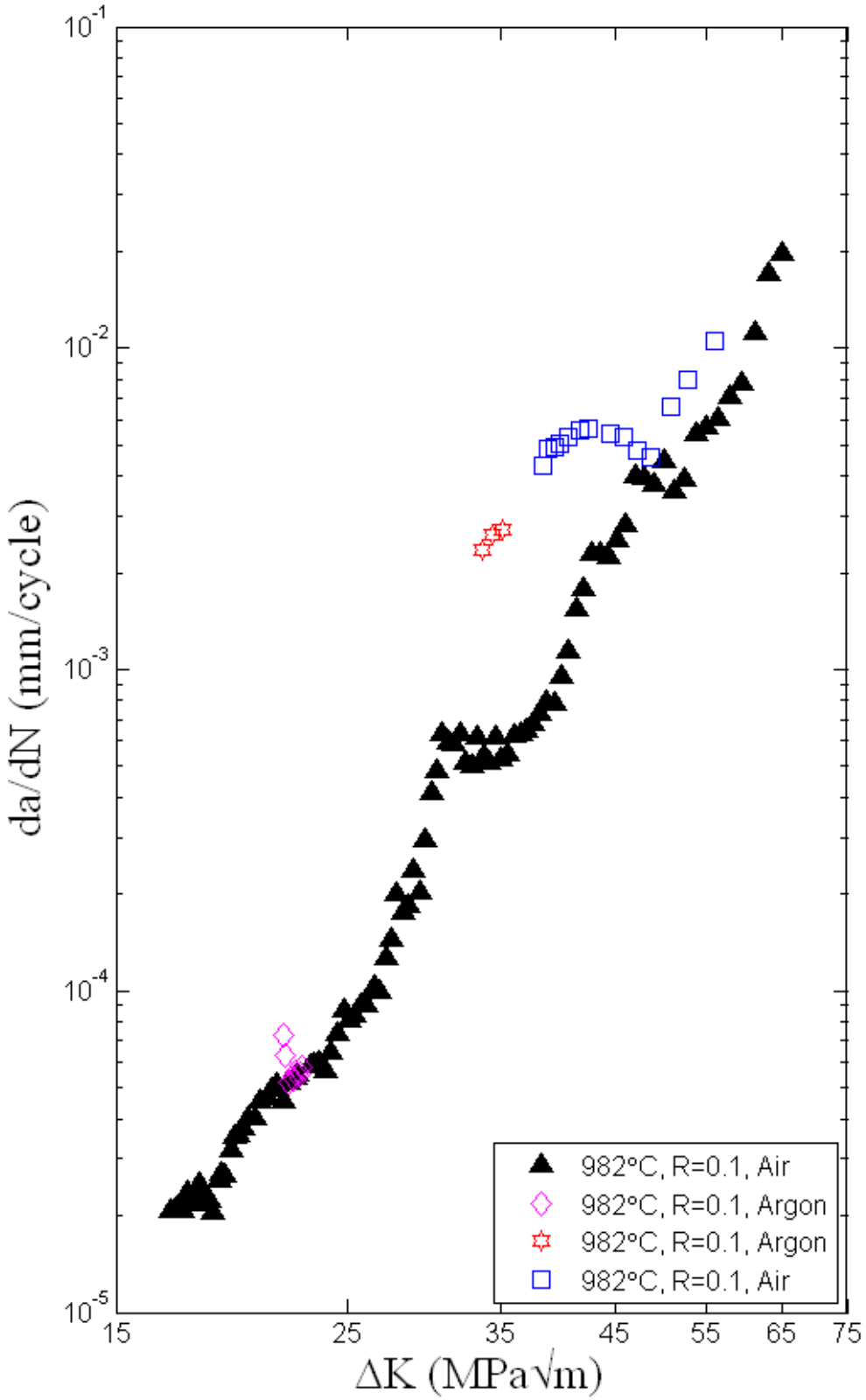

Figure 4.32: PWA1484 Fatigue Crack Growth Rates for 982°C Argon Constant Amplitude Tests

In summary the fatigue crack growth rate increases with increasing temperature except at low crack driving forces and low R Ratios at 982°C. This is possibly due to large levels of plasticity at 982°C creating crack closure that is not present at high R Ratios. As one would expect R = 0.7 displays faster crack growth when compared to R = 0.1. The effect of temperature on the FCGR becomes more pronounced as the crack driving force increases and secondary orientation and R Ratio effects increase on the FCGR with increasing temperature. Even in low oxygen environments the partial pressure of oxygen and the diffusion process most likely still plays a large role in determining fatigue crack growth rates.

4.5: Aged Microstructure Testing

Four PWA1484 SENT specimens were aged for two weeks at 982°C. Two of these specimens were held under tension during these two weeks at 20% of their 982°C yield stress. The other two specimens were placed in a tube furnace for the two weeks. All four specimens were then subjected to isothermal constant amplitude fatigue crack growth tests at 649°C and 1 Hz. One set was tested at R=0.1 while the other set was tested at an R Ratio of 0.7.

These results were then plotted alongside 649°C "virgin" specimen crack growth rates. The R=0.1 results can be seen in Figure 4.33. In this plot the aged/stressed results have the slowest crack growth rates with the virgin results displaying the fastest crack growth rates. All of these specimens had matching secondary controlled orientations but even so the crack growth rates fall within typically accepted scatter. Without performing additional testing the three specimens appear to show very similar crack growth rates.

The R=0.7 results are shown in Figure 4.34. For these three specimens the fatigue crack growth rates all fall on top of one another. When looking at the PWA1484 heat treatment procedure the matching results are to be expected. The 1316°C solution heat treatment and controlled cooling to 1080°C creates the optimum γ' size and array distribution. During the third heat treatment step the ultra fine γ' (0.3nm) is precipitated at 704°C [28]. The 982°C two week aging the four specimens were subjected to is below the temperatures used to precipitate and organize the blocky cuboidal γ' microstructure responsible for giving strength to PWA1484. In addition the 20% yield strength load used for the aged/stressed must be below the critical load where rafting is present. Both the aging temperature and applied load would leave the microstructure most responsible for fatigue crack growth rates wholly intact.

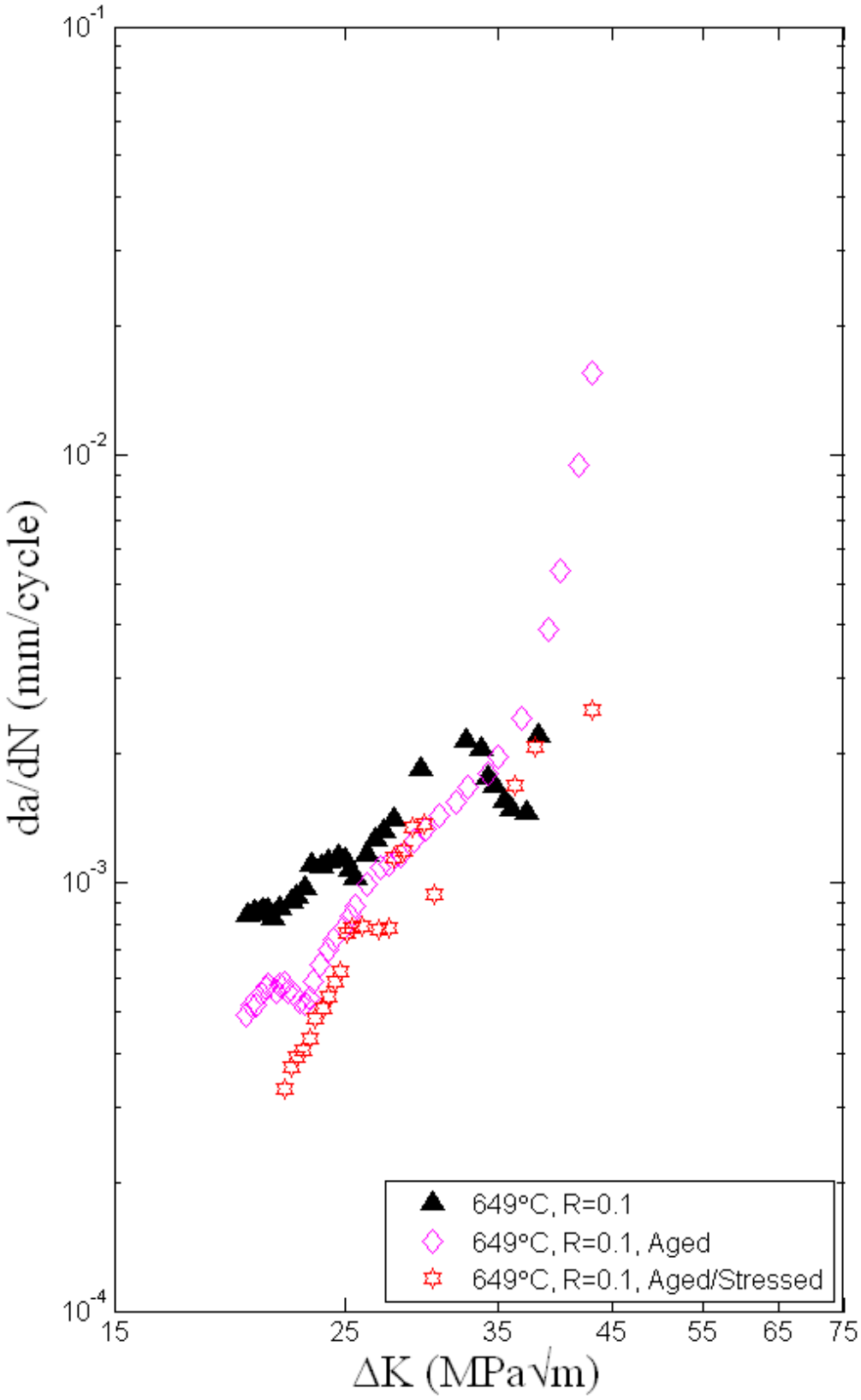

Figure 4.33: PWA1484 Fatigue Crack Growth Rates for 649°C, R=0.1 Aged Microstructure Constant Amplitude Tests

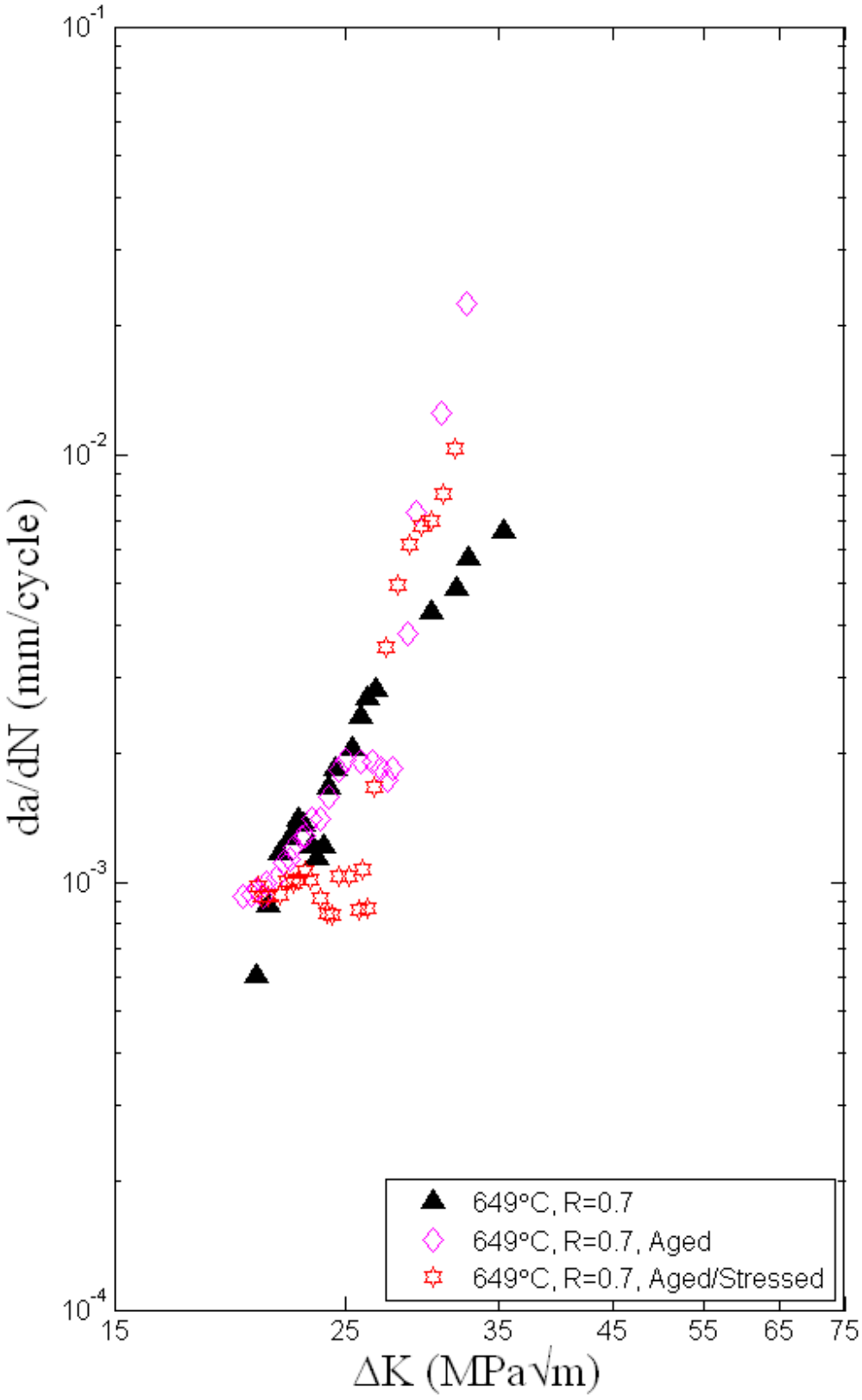

Figure 4.34: PWA1484 Fatigue Crack Growth Rates for 649°C, R=0.7 Aged Microstructure Constant Amplitude Tests

4.6: Temperature Interaction Testing

Temperature interaction testing was performed by cycling between 649°C and 982°C in blocks of 1, 10, 20, 50 and 100 cycles at R Ratios of 0.1 and 0.7. For each test the number of cycles in each temperature block was the same. Loading cycles were constant amplitude and applied at 1 Hz as seen in Figure 4.35. During heating and cooling the specimen dwelled at minimum load to avoid creep effects. Acceleration and retardation due to temperature interactions was determined by comparing the experimental results to the non-interaction crack growth predictions.

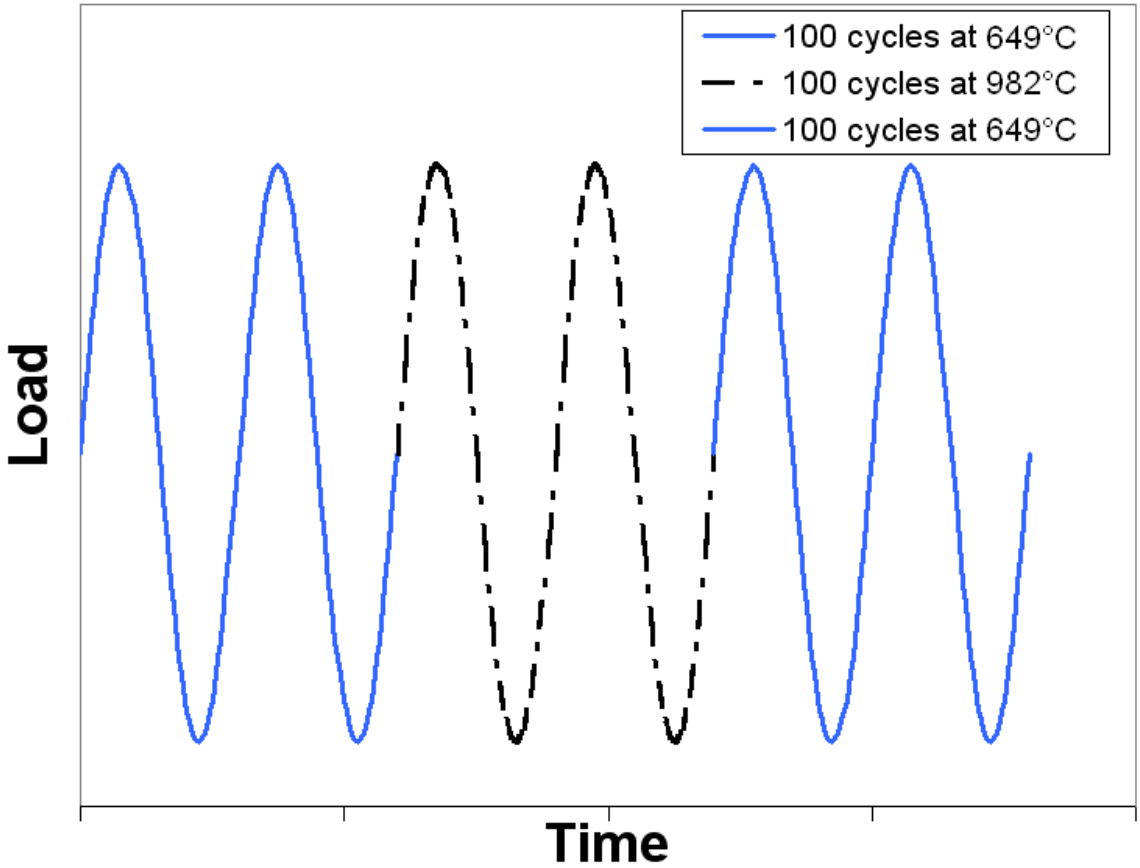

Figure 4.35: Temperature Interaction Testing Between 649°C and 982°C Schematic

The non-interaction predictions along with the experimental results for blocks of 1, 10 and 100 alternating temperature cycles is shown in Figure 4.36 for R=0.1 testing. As one would expect all three predictions fell on top of each other. Alternating the temperature every one cycle between temperatures caused the fatigue crack growth rate to be substantially faster than the non-interaction prediction. Ten block alternating temperature interaction testing also grew faster than the non-interaction prediction but not to the same extent as the one block alternating test. On the other hand one hundred block alternating testing grew slower than the non-interaction prediction. It was found that as the number of alternating temperature cycles increased, changes in the morphology (and hence deformation mode) caused changes in the environmental interactions thus demonstrating the sensitivity of the environmental interaction on the details of the deformation mode.

With the aid of SEM fractography discussed later on it was shown that at low alternating cycles, 649°C crack growth was accelerated due to crack tip embrittlement caused by 982°C cycling. At higher alternating cycles the 649°C cycling quickly grew through the embrittled crack tip but then grew slower than expected due to microstructural evolution such as γ' strengthening at 982°C and possibly the formation of Kear-Wilsdorf locks.

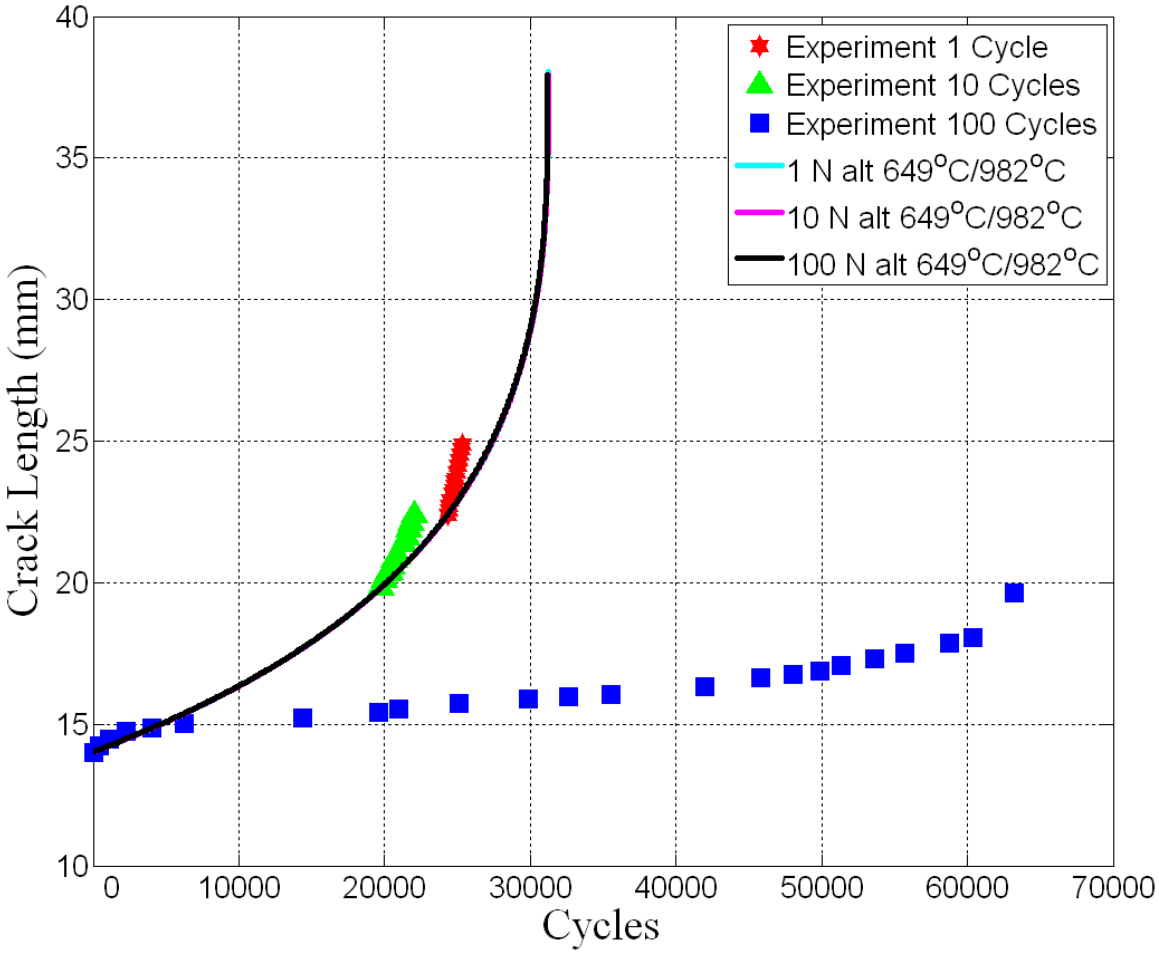

Figure 4.36: Temperature Interaction Testing Between 649°C and 982°C for 1, 10 and 100 Alternating Cycles at R=0.1 Along with Non-Interaction Predictions

To get a better understanding of the number of alternating cycles where the transition between crack growth acceleration and retardation takes place 20 and 50 alternating testing was performed. This testing was performed on controlled secondary orientation specimens and as such had a different non-interaction prediction curve. These results are seen in Figure 4.37. Both the 20 and 50 alternating cycle blocks resulted in crack growth retardation demonstrating that the transition occurs between 10 and 20 alternating cycles.

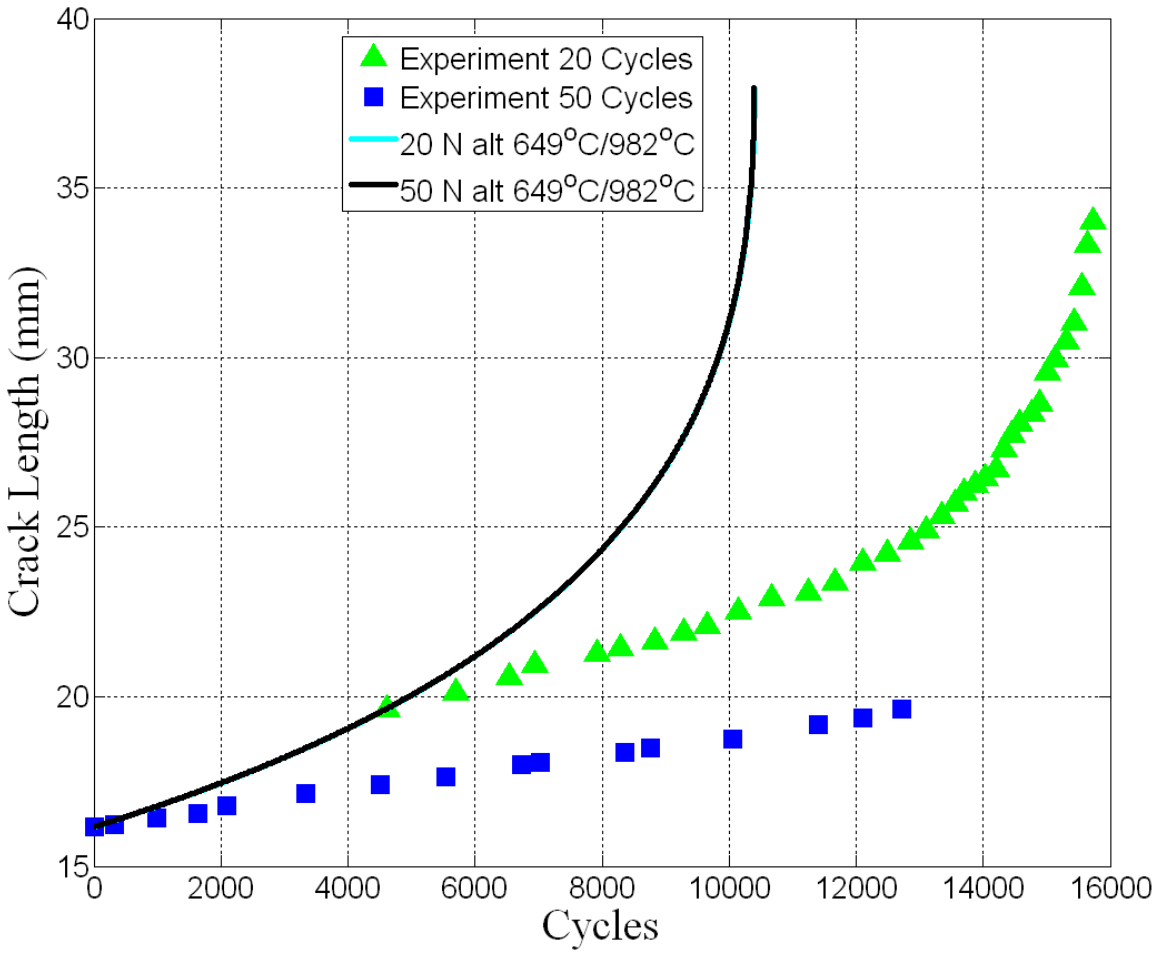

Figure 4.37: Temperature Interaction Testing Between 649°C and 982°C for 20 and 50 Alternating Cycles at R=0.1 Along with Non-Interaction Predictions

To rule out the possibility of plasticity or oxide induced crack closure additional temperature interaction specimens were tested at an R Ratio of 0.7. The results along with the non-interaction predictions for 1, 10 and 100 alternating cycles can be seen in Figure 4.38. Again like at R=0.1 there is acceleration present at 1 and 10 alternating cycles and overall retardation for 100 alternating cycles.

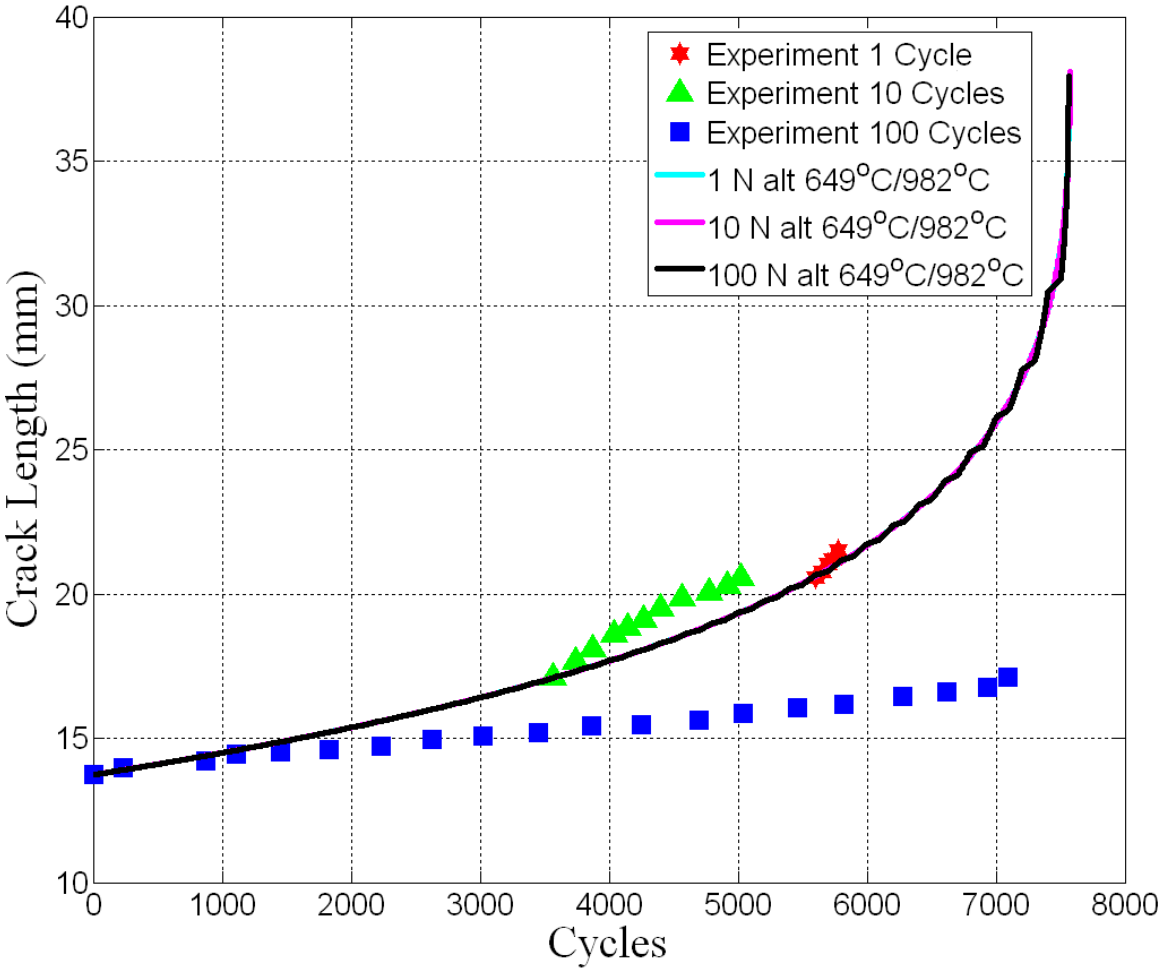

Figure 4.38: Temperature Interaction Testing Between 649°C and 982°C for 1, 10 and 100 Alternating Cycles at R=0.7 Along with Non-Interaction Predictions

Temperature interaction testing was also performing for 20 and 50 alternating cycles at R=0.7 on a controlled secondary orientation specimen. These results are shown in Figure 4.39. The 50 alternating cycles grew just slightly slower than the non-interaction prediction while the 20 alternating cycles grew at the same rate showing neither retardation nor acceleration.

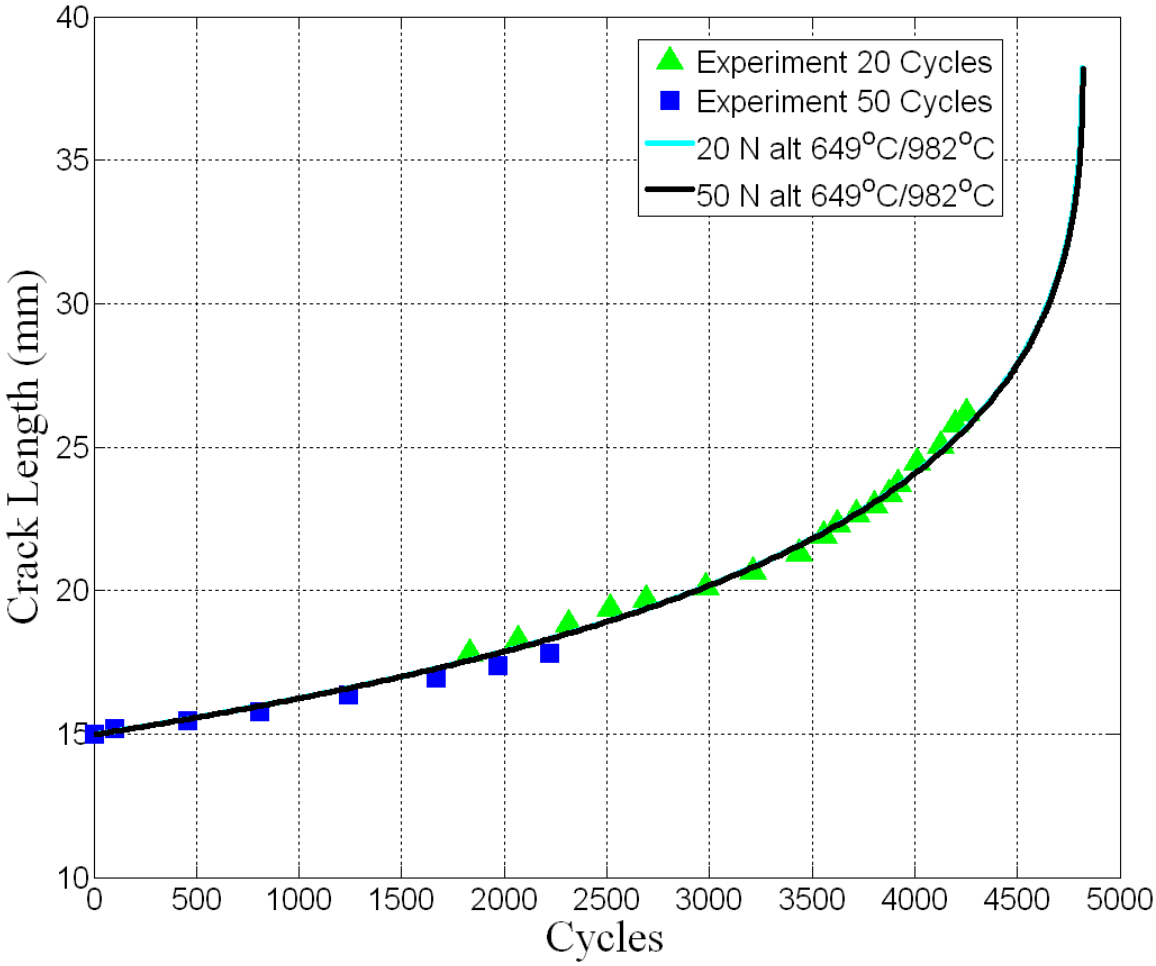

Figure 4.39: Temperature Interaction Testing Between 649°C and 982°C for 20 and 50 Alternating Cycles at R=0.7 Along with Non-Interaction Predictions

In summary for both R=0.1 and 0.7, alternating between 649°C and 982°C demonstrates that retardation is present at the higher alternating cycles and acceleration is present the lower alternating cycles. At low alternating cycles, 649°C crack growth is accelerated due to crack tip embrittlement caused by 982°C cycling. At higher alternating cycles the 649°C cycling quickly grows through the embrittled crack tip but then grows slower than expected due to microstructural evolution such as γ' strengthening at 982°C. The transition between acceleration and retardation for R=0.1 occurs between 10 and 20 alternating cycles while the transition for R=0.7 occurs around 20 alternating cycles. The higher cycle transition for R=0.7 can possibly be explained by the much larger crack tip

stresses present at the high R Ratio. This would tend to promote more γ' coarsening allowing the 649°C cycles to growing even faster than just the 982°C crack tip embrittlement that was seen at the lower R Ratio of 0.1. Additional testing would have to be performed to make sure that the acceleration/retardation cycle transition difference between R=0.1 and 0.7 is a real phenomenon.

4.7: Load Interaction Testing

Load interaction testing was performed at 649°C, 816°C and 982°C with 1.3x, 1.6x and 2.0x overloads applied. Testing was performed at a frequency of 1 Hz and an R Ratios of 0.1 for the 1.0x cycles. Repeated overloads were applied every 800 cycles as shown in Figure 4.40. Acceleration and retardation due to load interactions was determined by comparing the experimental results to the non-interaction crack growth predictions.

Yield zone calculations showed that it would take approximately 800 cycles for the crack to grow out of a 1.6x overload monotonic plastic zone. Using this calculation, overloads of 2.0x, 1.6x and 1.3x were applied every 800 cycles. It was anticipated that this would allow the observation of fully retarded crack growth for 2.0x overloads, crack growth that just exits the zone of influence for 1.6x overloads and crack growth that quickly exits the zone of influence for 1.3x overloads. Initially three specimens, one for each overload size, were used for overload testing. In order to minimize temperature interaction effects the specimens were started out at 649°C and the temperature was increased after obtaining enough crack growth to assess acceleration or retardation. Applying overloads in this order it was expected that there would be minimal interaction effects but due to a limited number of specimens this was unavoidable.

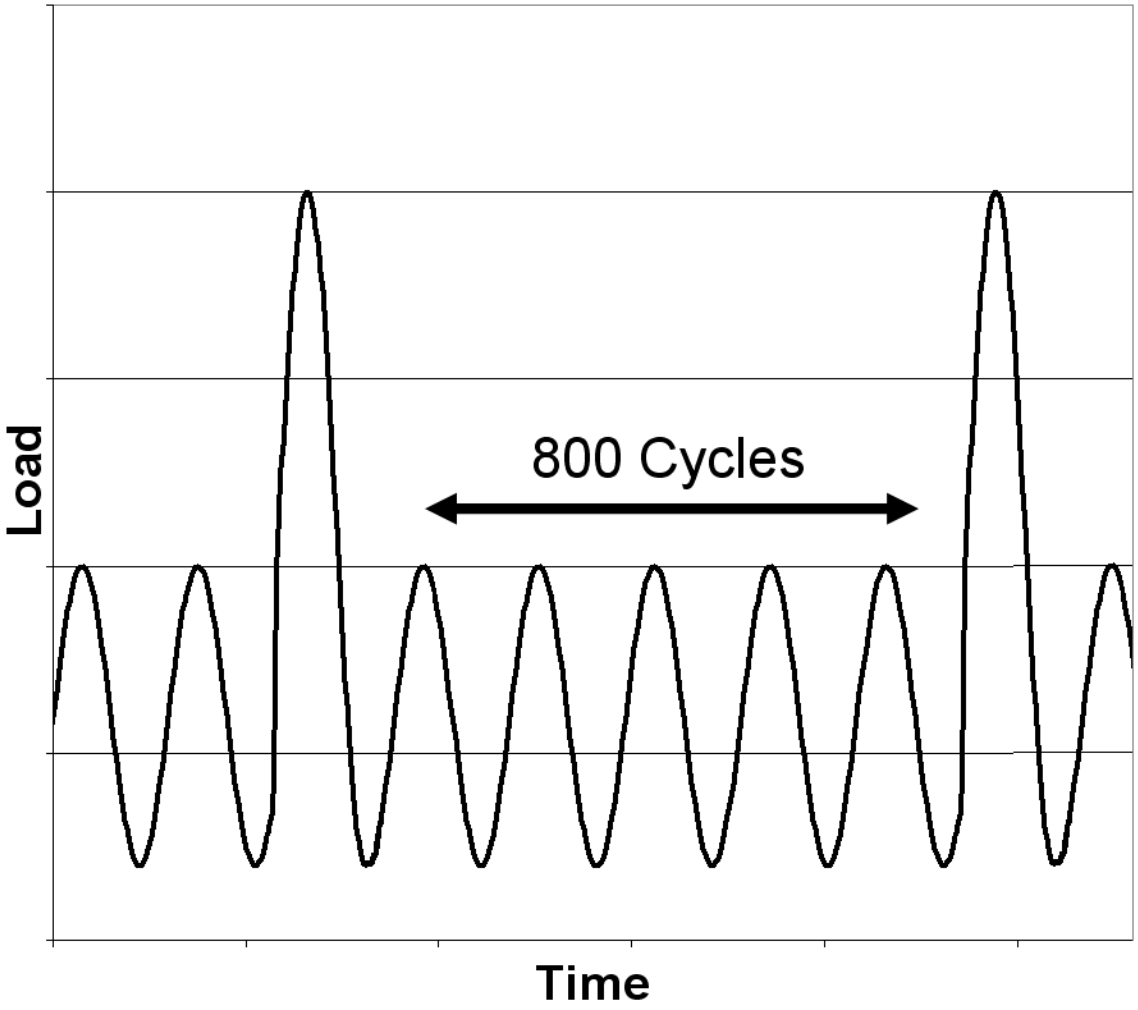

Figure 4.40: Overloads Were Applied Every 800 Cycles During Load Interaction Testing

The 1.3x overload results are shown in Figure 4.41. After precracking 1.3x overloads were applied every 800 cycles for 25,000 cycles at 649°C. The non-interaction model predicted only 10,000 cycles to reach the same crack length demonstrating that considerable crack growth retardation is present. Roughly the same amount of retardation was seen for 1.3x overloads at 816°C. At 982°C the 1.3x overloads displayed crack growth acceleration when compared to the non-interaction prediction.

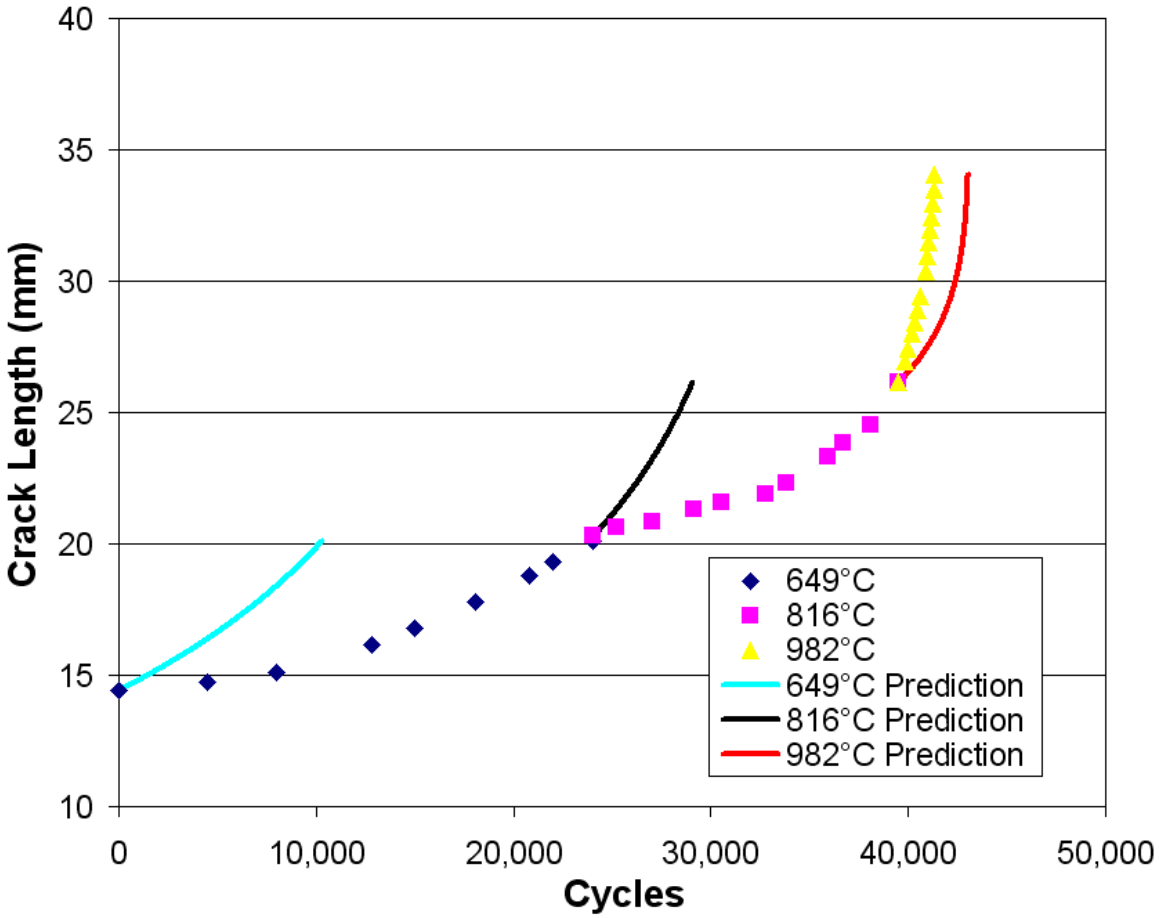

Figure 4.41: 1.3x Overload Testing at 649°C, 816°C and 982°C Along with Non-Interaction Predictions

The 1.6x overload results are shown in Figure 4.42. Retardation is seen at 649°C and 816°C for the 1.6x overload testing. In comparison to the 1.3x overloads the retardation is quite a bit more extensive. This suggests that the 1.0x cycles were fully retarded and the only crack growth accumulated is from the 1.6x overloads applied every 800 cycles. At 982°C the 1.6x overloads displayed neither crack growth acceleration nor retardation when compared to the non-interaction prediction.

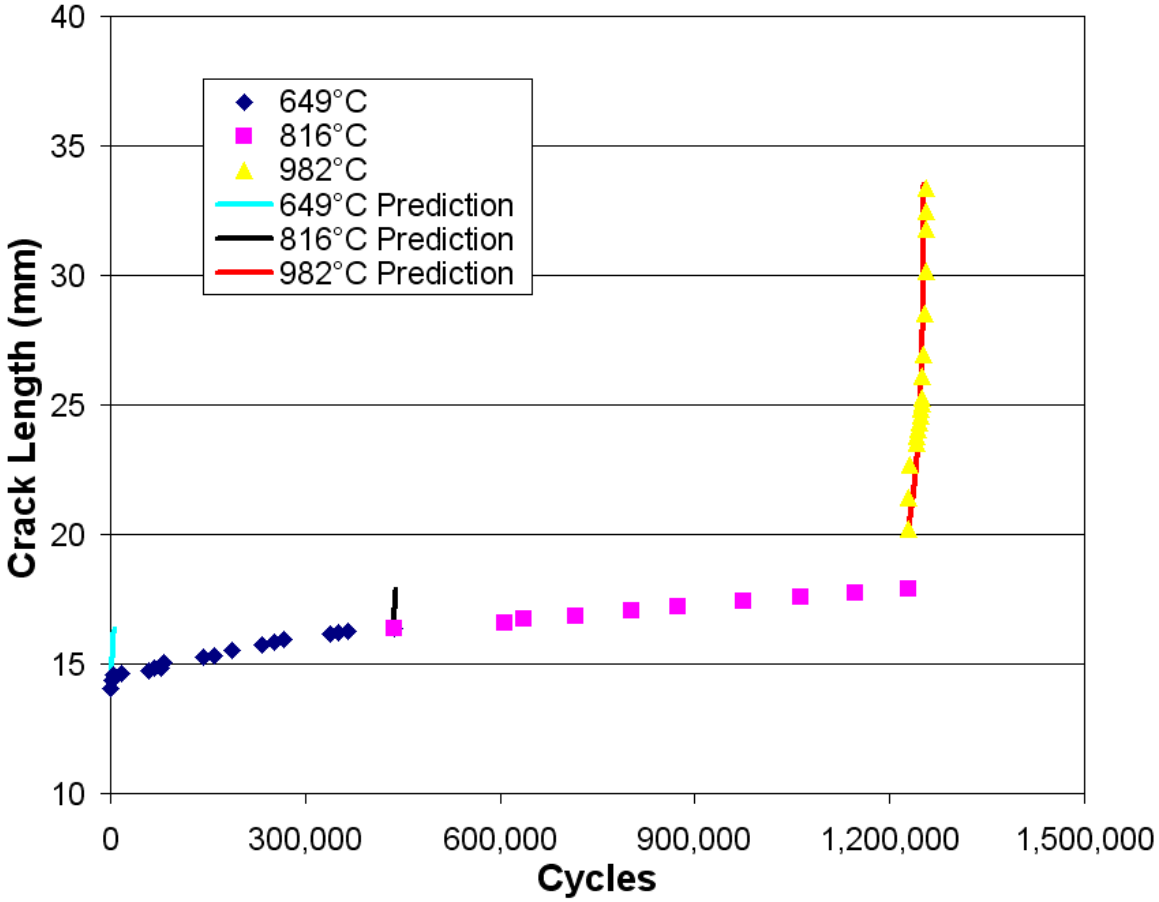

Figure 4.42: 1.6x Overload Testing at 649°C, 816°C and 982°C Along with Non-Interaction Predictions

The 2.0x overload results are shown in Figure 4.43. Retardation is seen at 649°C and 816°C for the 2.0x overload testing. In comparison to the 1.6x overloads the retardation is reduced. Even so it is likely that the 1.0x cycles were fully retarded and the only crack growth accumulated is from the 2.0x overloads applied every 800 cycles. At 982°C the 2.0x overloads displayed crack growth retardation when compared to the non-interaction prediction.

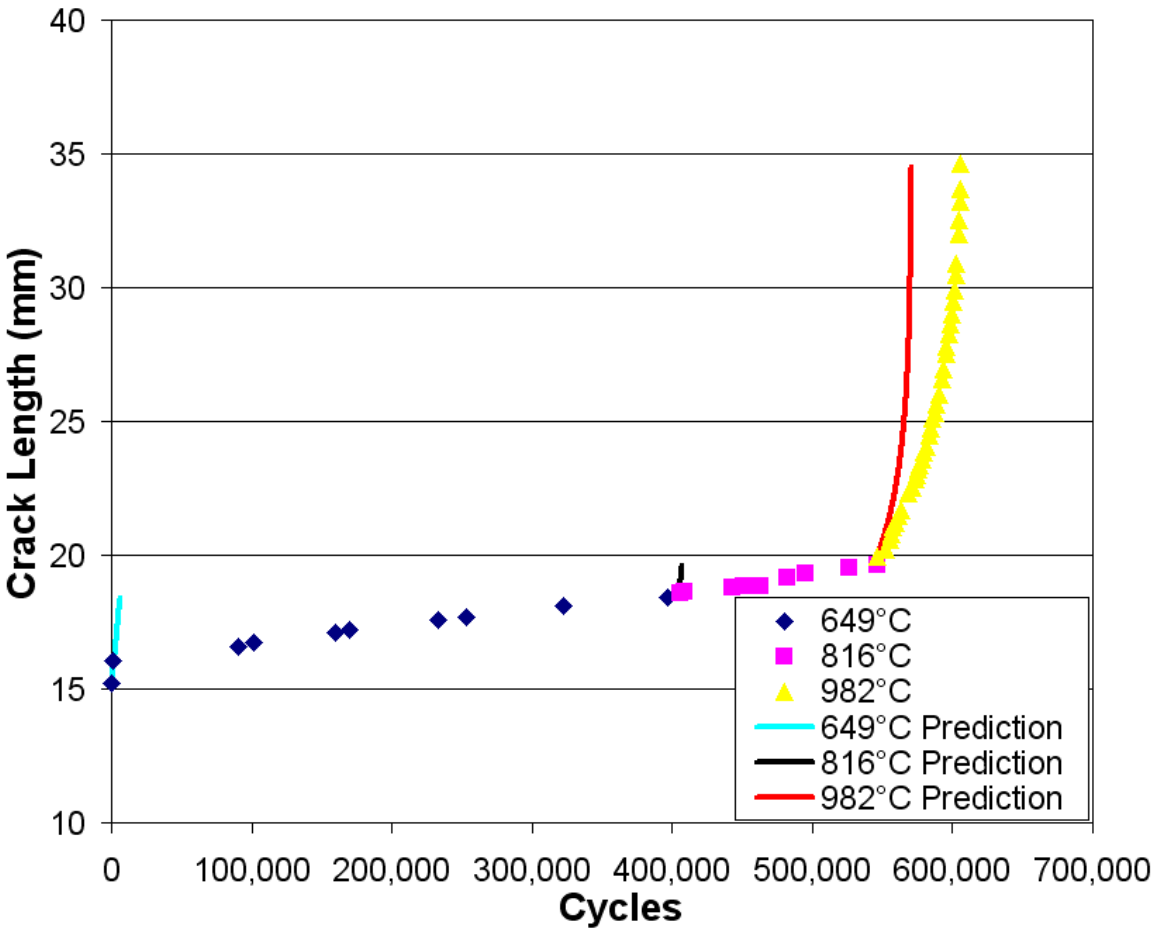

Figure 4.43: 2.0x Overload Testing at 649°C, 816°C and 982°C Along with Non-Interaction Predictions

The 1.3x, 1.6x and 2.0x overloads at 649°C and 816°C all displayed varying levels of retardation as would be expected. The overloads at 982°C tell a more interesting story. Initially with 1.3x overloads the crack growth was accelerated. Jumping up to 1.6x overloads the crack growth matched the non-interaction prediction and finally when increased to 2.0x overloads, retardation was seen. To better understand this phenomenon 3 full specimens were tested with 1.3x, 1.6x and 2.0x overloads at 982°C. The 1.3x results are shown in Figure 4.44. Initially the crack growth matches the non-interaction prediction but at a crack length of 17mm, retardation appears for the remainder of the

test. This retardation is in stark contrast to the acceleration seen on the shared temperature specimen.

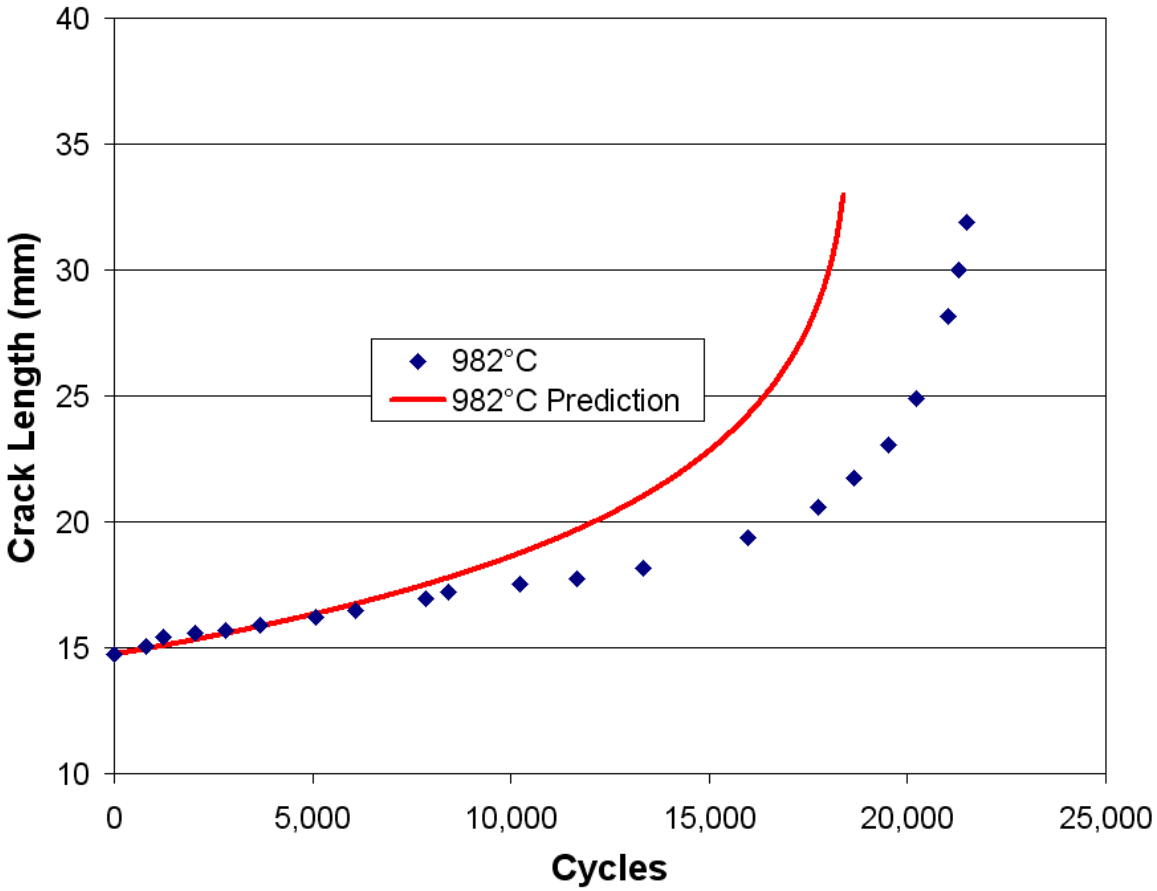

Figure 4.44: 1.3 x Overload Testing at 982°C Along with Non-Interaction Prediction

The full specimen 982°C 1.6x overload results can be seen in Figure 4.45. Right from the start this test shows signs of retardation which only increases throughout the remainder of the test. Again, this is in contrast to the shared specimen results in Figure 4.42 were the experimental data points fell on top of the non-interaction prediction.

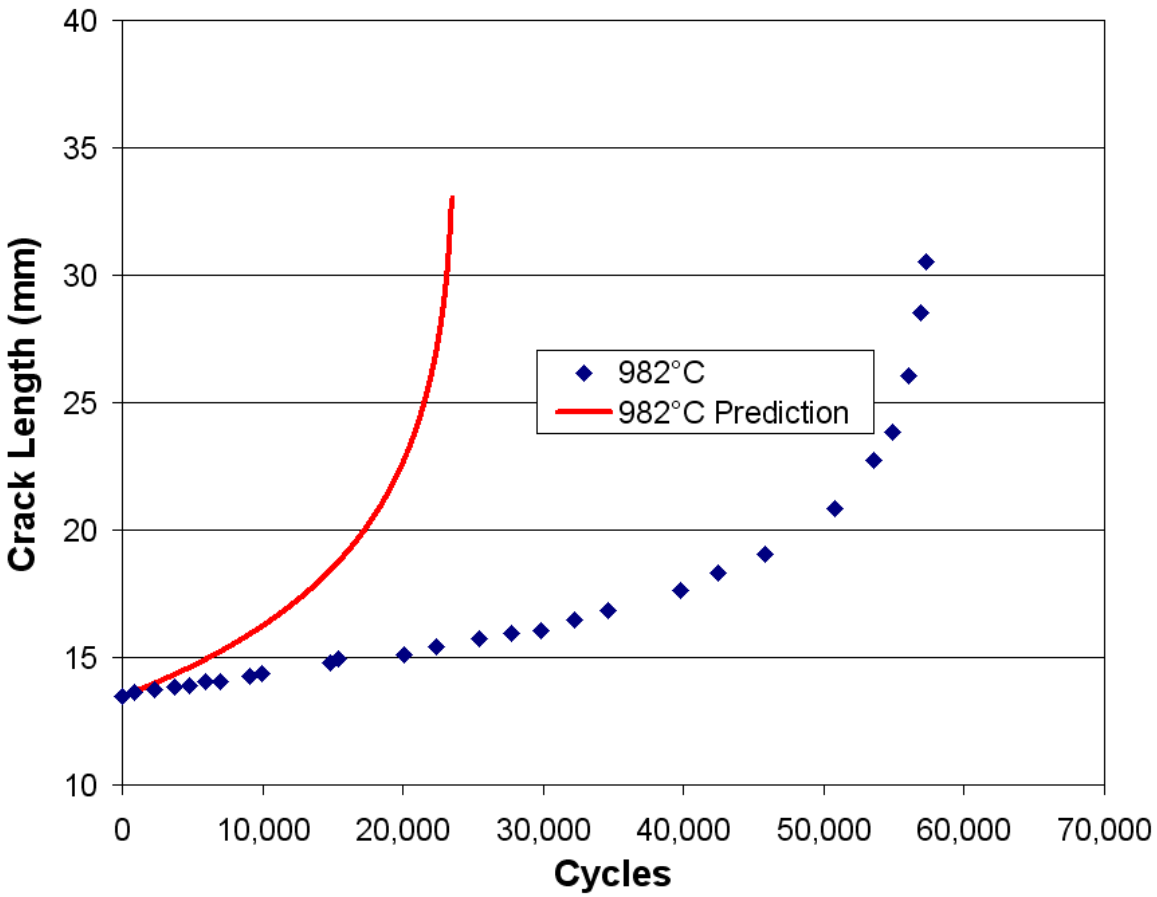

Figure 4.45: 1.6x Overload Testing at 982°C Along with Non-Interaction Prediction

Lastly the full specimen 982°C 2.0x overload results can be seen in Figure 4.46. Initially this test briefly shows acceleration but after 3,000 cycles switches to retardation. This retardation continues to increase throughout the remainder of the test. The three whole specimen 982°C overload tests demonstrated increasing retardation with increasing overload size. The predictions for the full specimen tests were shifted over to match the shared specimen crack lengths in an effort to understand what was happening at 982°C during the 1.3x, 1.6x and 2.0x overload tests.

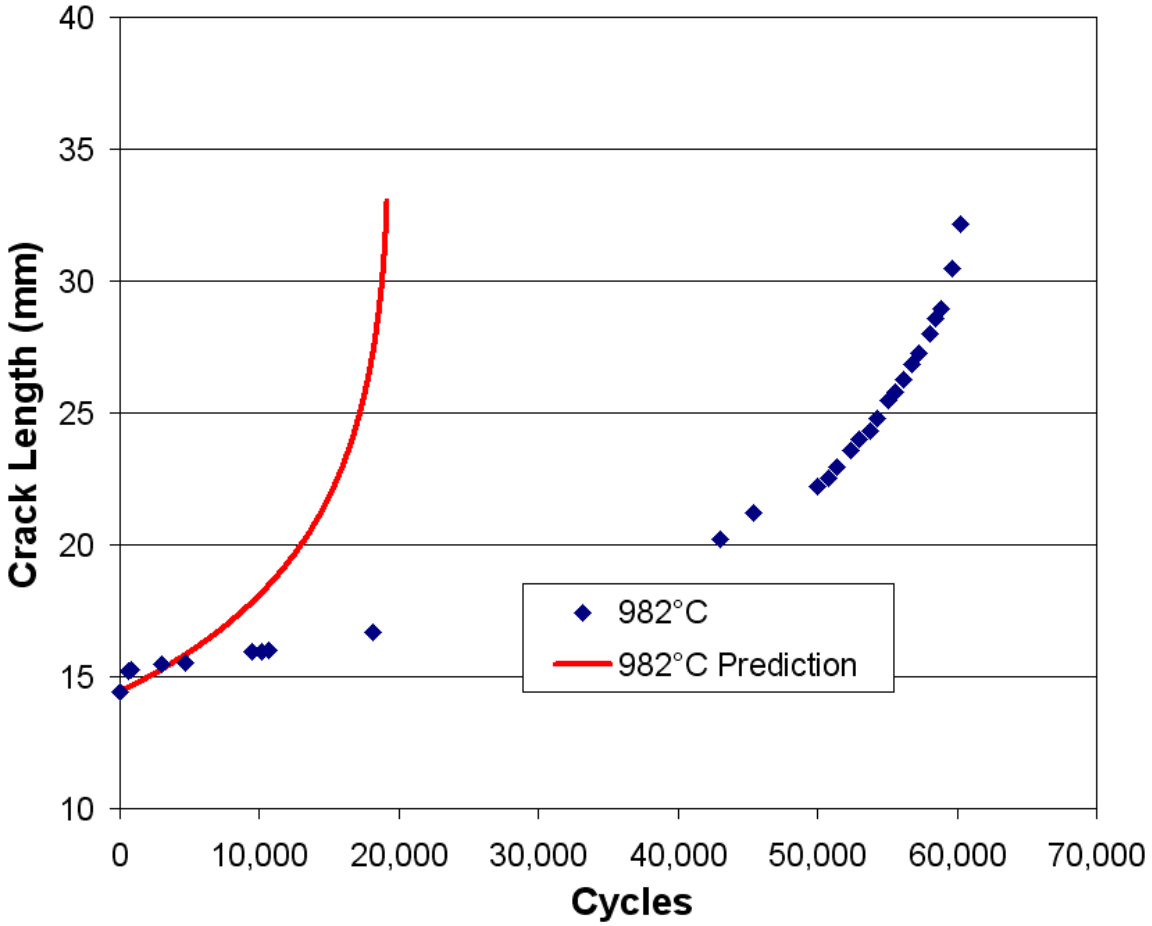

Figure 4.46: 2.0x Overload Testing at 982°C Along with Non-Interaction Prediction

Figure 4.47 is the full specimen 1.3x overload testing at 982° results with the prediction moved over to match the shared temperature specimen crack length. Very clearly crack growth acceleration is seen just like in the shared temperature specimen results.

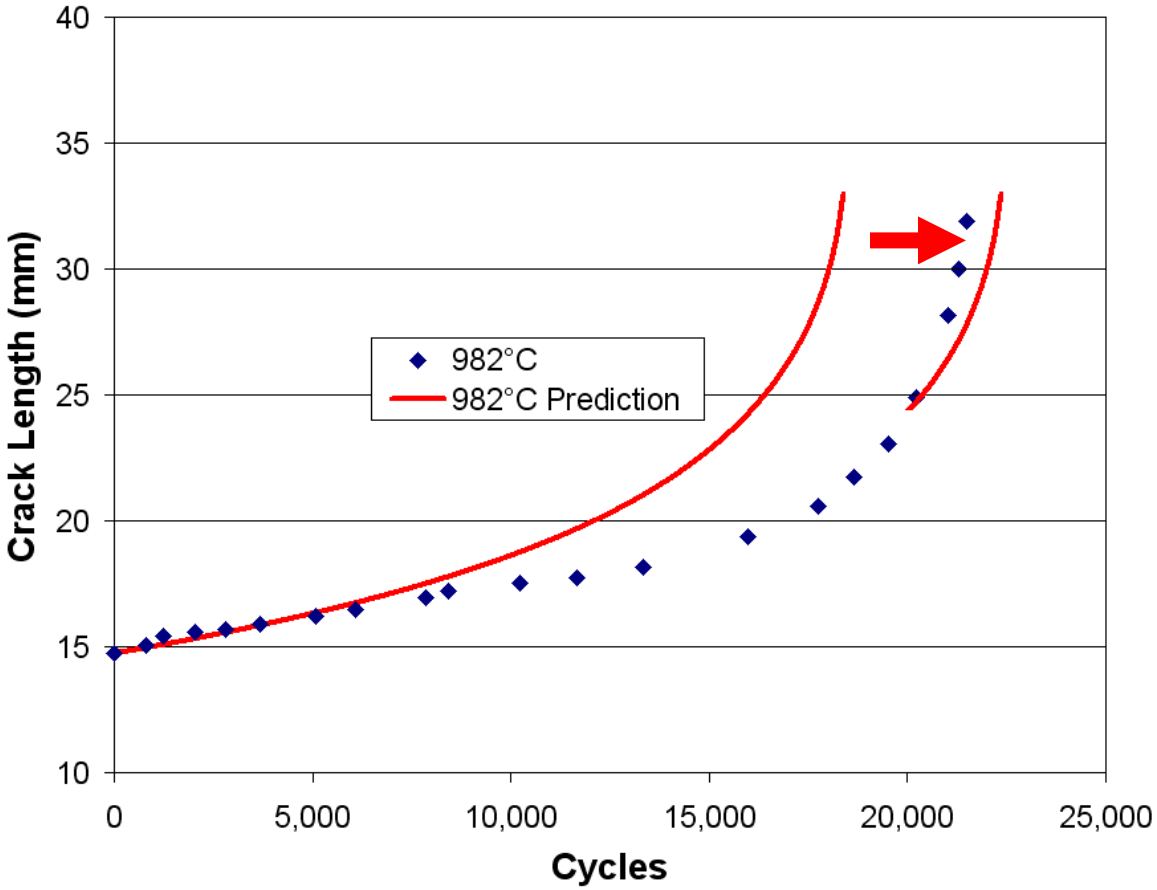

Figure 4.47: 1.3x Overload Testing at 982°C Along with Non-Interaction Prediction Shifted Over

Figure 4.48 is the full specimen 1.6x overload testing at 982° results with the prediction moved over to match the shared temperature specimen crack length. As before the crack growth displays neither acceleration nor retardation.

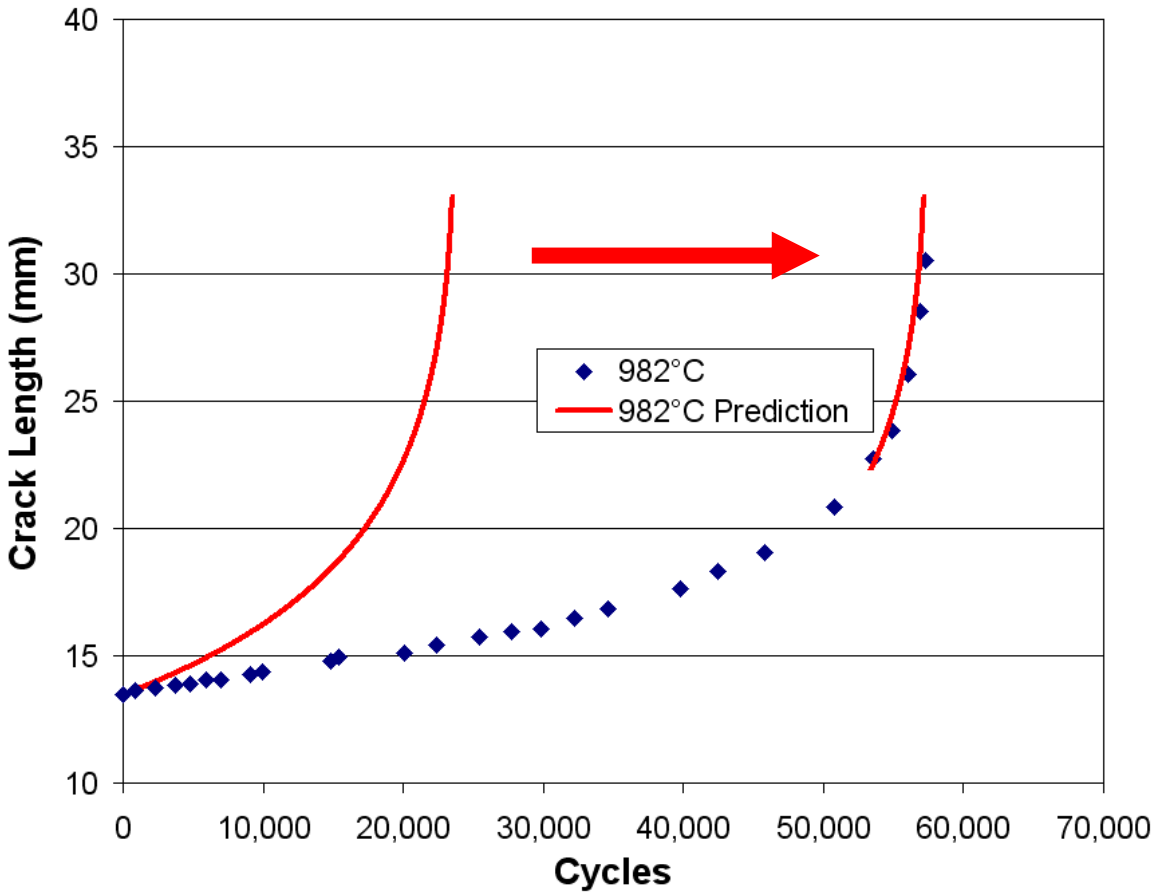

Figure 4.48: 1.6x Overload Testing at 982°C Along with Non-Interaction Prediction Shifted Over

Figure 4.49 is the full specimen 2.0x overload testing at 982° results with the prediction moved over to match the shared temperature specimen crack length. Matching the shared temperature specimen results crack growth retardation is seen. Load interaction testing showed that when the crack driving force is near K_{IC} the overload size greatly influences whether acceleration or retardation will occur at 982°C.

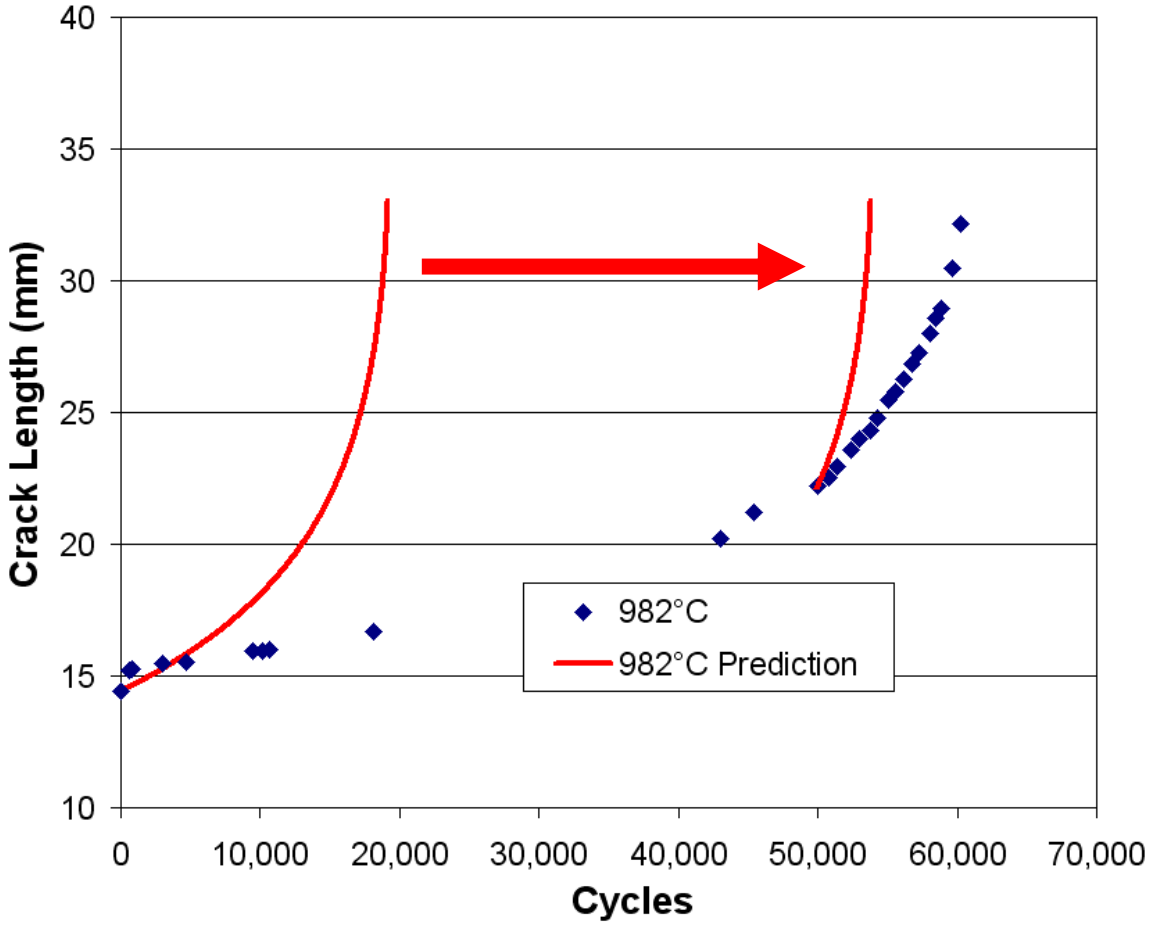

Figure 4.49: 2.0x Overload Testing at 982°C Along with Non-Interaction Prediction Shifted Over

4.8: Semi-Realistic Spectrum Testing

Realistic spectrum fatigue crack growth testing is a really difficult undertaking for several reasons. It is very hard if not impossible to obtain a publishable flight spectrum that contains the stresses and temperature that turbine blades are exposed to during either commercial or defense flights. There are so many load and temperature interactions that occur during spectrum tests that it is very difficult to come away with a basic understanding of the physics involved and what mechanisms are responsible for the observed retardations and accelerations. Spectrum tests are very time consuming due to the extremely long cycles that are involved and the relatively few loading cycles present in a flight spectrum. With this being said three different semi-realistic spectrums were created for this research based off a simplified fighter jet spectrum published by Larsen et al. [115] and shown in Figure 4.50.

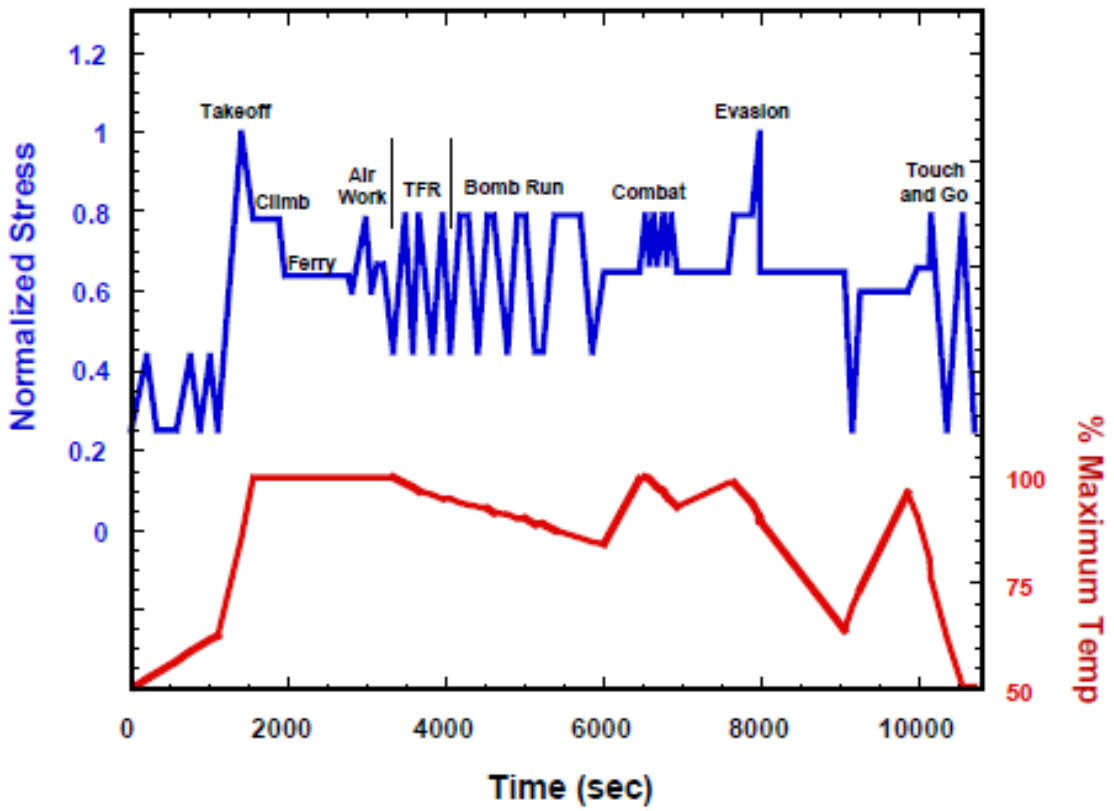

Figure 4.50: Fighter Jet Flight Spectrum Showing Cyclic Mechanical and Thermal Loading [115]

A frequency of 1 Hz was chosen for all three spectrums due to all isothermal constant amplitude test data being obtained at that frequency. The first spectrum shown in Figure 4.51 had constant load cycling throughout the test. The loads and temperatures for this spectrum can be found in Appendix A.5. Having continual loading present throughout the test allows non-interaction predictions to be made without having to take into account the effect of dwell times. This spectrum was used to address the life variability/scatter in spectrum tests and also the life sensitivity to changing the relative loading level.

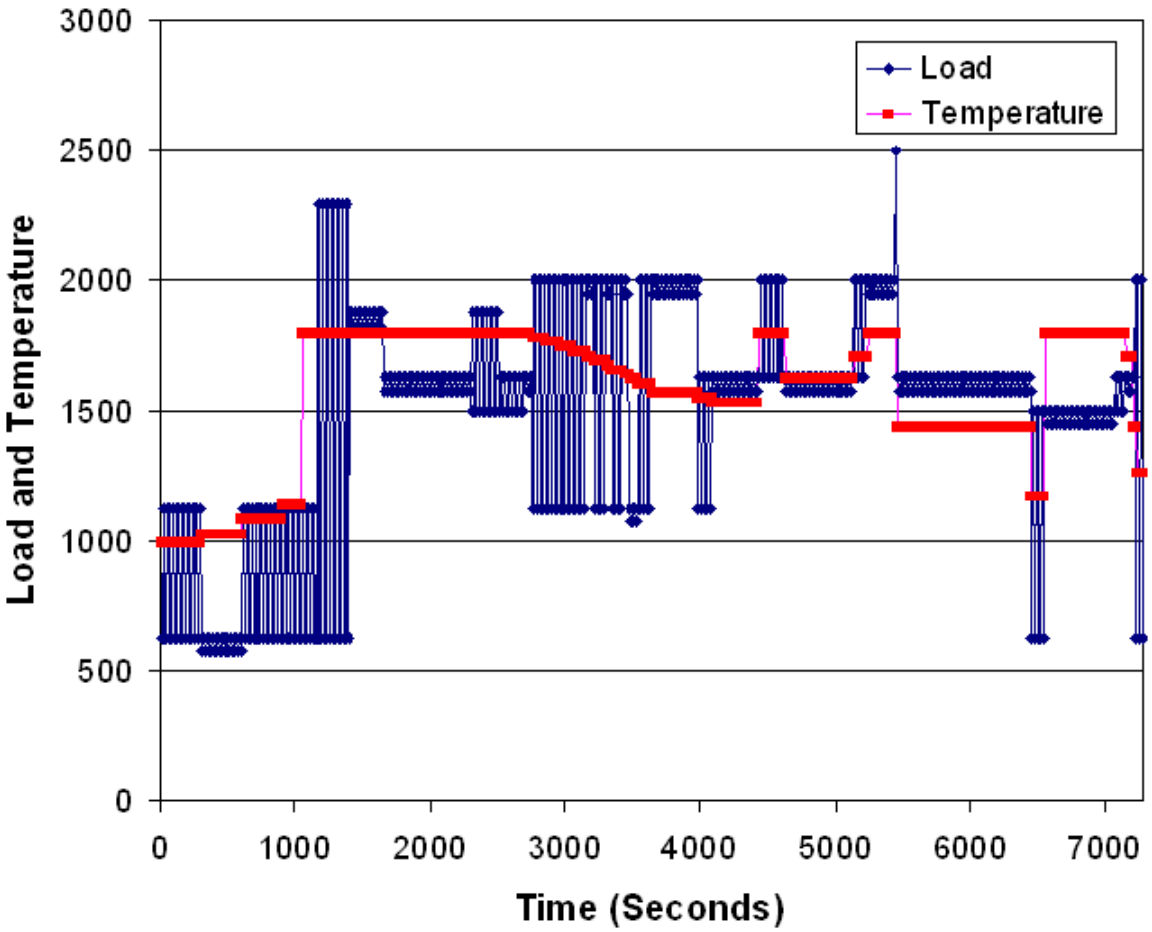

Figure 4.51: Two Hour Semi-Realistic Spectrum with Constant 1 Hz Cycling

The non-interaction prediction is shown in Figure 4.52 where the specimen is shown to last 12 flights. This is relatively short due to the fact the specimen starts with an 11.43mm notch and a 2.54mm precrack for an initial flaw size of 13.97mm. This is much larger than the nondestructive inspection (NDI) limit that is usually assumed to be present in jet engine components. As such this specimen is expected to have a life much less, even orders of magnitude less than is seen in aircraft single crystal turbine blades.

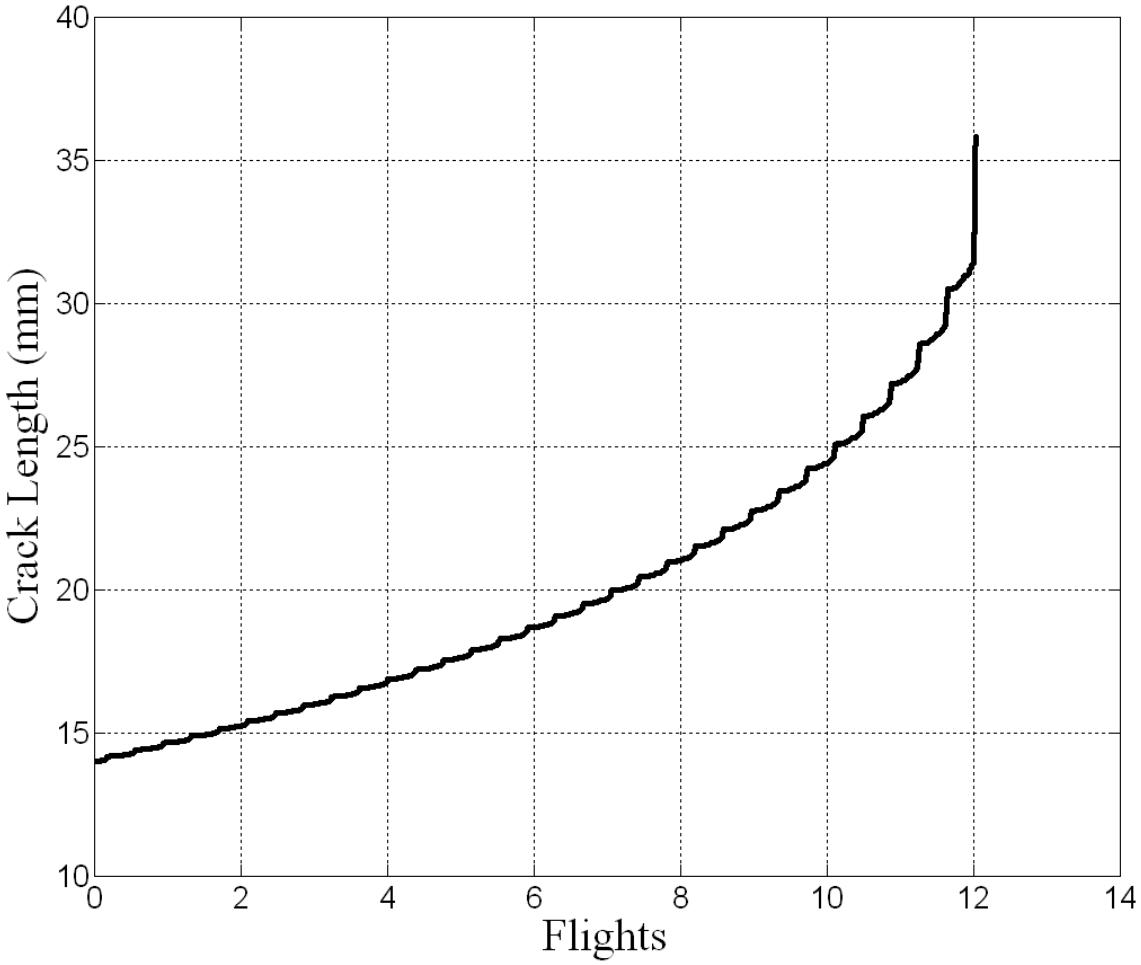

Figure 4.52: Non-Interaction Prediction for Two Hour Semi-Realistic Spectrum with Constant 1 Hz Cycling

As expected due to load interactions the specimen had a life longer than 12 flights as seen in Figure 4.53. The first specimen tested under the two hour semi-realistic spectrum with constant 1 Hz cycling had a life of 55 flights. The same exact test was performed again on a specimen that had an identical secondary orientation. The second time the specimen lasted 40% longer with a life of 77 flights. This goes to show the scatter that is present when performing these types of tests even when the exact same loading conditions and specimen orientation were used.

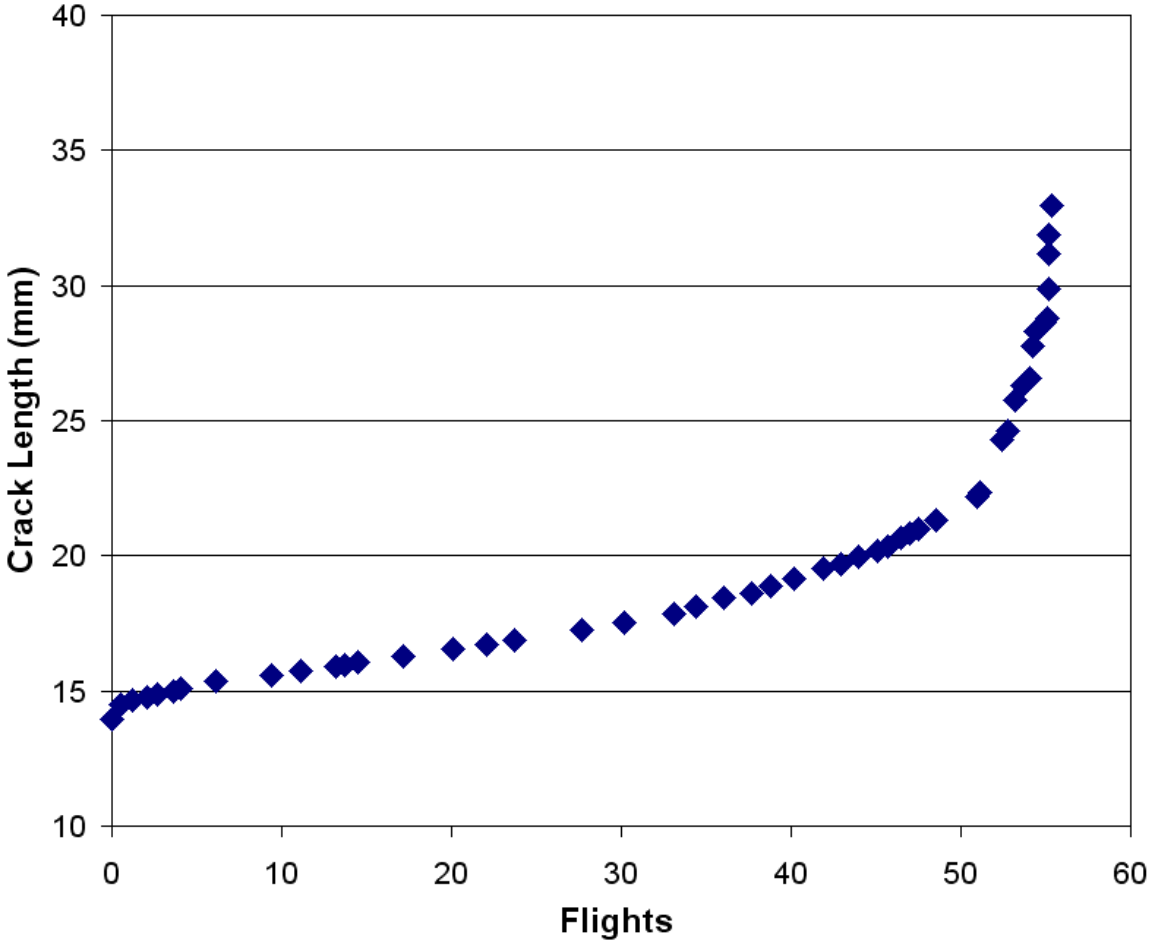

Figure 4.53: Two Hour Semi-Realistic Spectrum with Constant 1 Hz Cycling Test #1

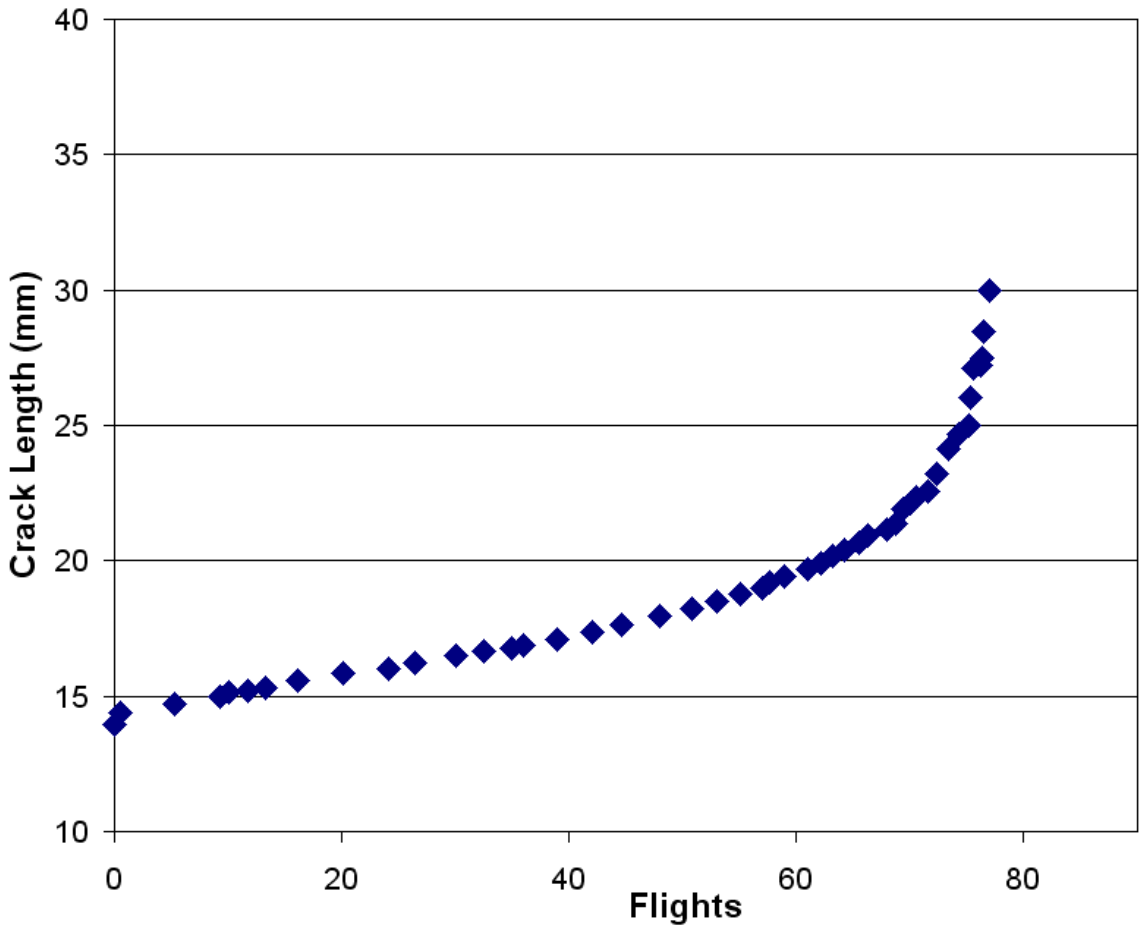

Figure 4.54: Two Hour Semi-Realistic Spectrum with Constant 1 Hz Cycling Test #2

For the third test with this spectrum the minimum and maximum loads were set to 80% of the values shown in Appendix A.5. Running a non-interaction prediction gave a life 0f 22 flights as seen in Figure 4.55. This is almost double the 12 flight life of the 100% loading prediction.

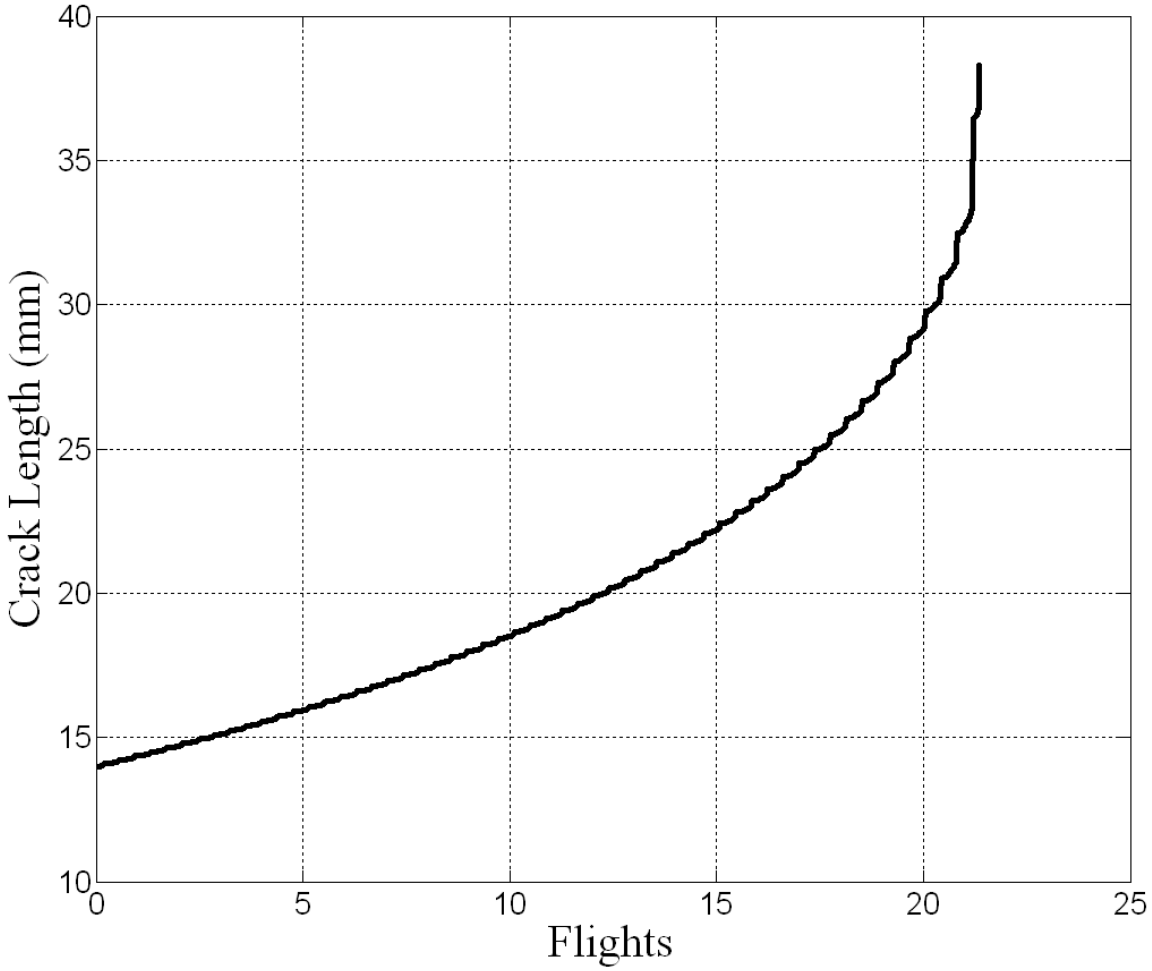

Figure 4.55: Non-Interaction Prediction for Two Hour Semi-Realistic Spectrum with Constant 1 Hz Cycling at 80% Load

The results for the third and final test performed under the first spectrum are shown in Figure 4.56. This third specimen lasted for 307 flights. The 20% drop in load resulted in roughly 5 times the life. On the other hand, the non-interaction model predicted an increase in life of approximately 2 times, demonstrating the extreme sensitivity that relative loading levels have on life in spectrum conditions.

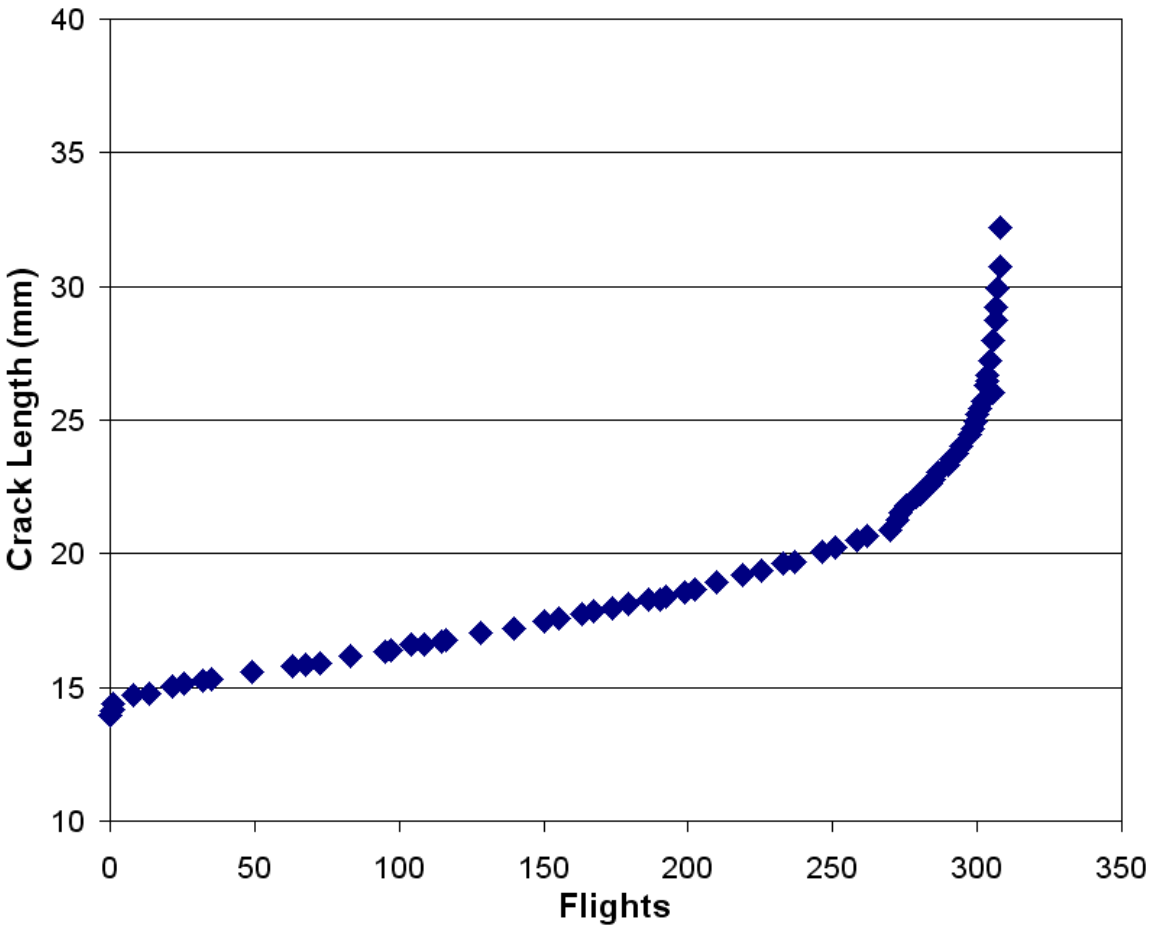

Figure 4.56: Two Hour Semi-Realistic Spectrum with Constant 1 Hz Cycling Test #3

The second spectrum is shown in Figure 4.57. This spectrum is more realistic in the fact that it only has twenty one 1 Hz loading cycles and utilizes dwell time to fill the full two hour run time. The load and temperature details for this spectrum can be found in Appendix A.6. Data points have been removed during the dwell times so the spectrum can fit in the appendix. The temperature behaves linearly during the removed data points. The third spectrum can be seen in Figure 4.58. This spectrum has the same number of loading cycles at the same temperatures as spectrum number two but has the dwell times removed so the entire spectrum lasts three and a half minutes. The details of this spectrum can be found in Appendix A.7. These two spectra were run to assess the effect of dwell times on the specimen life.

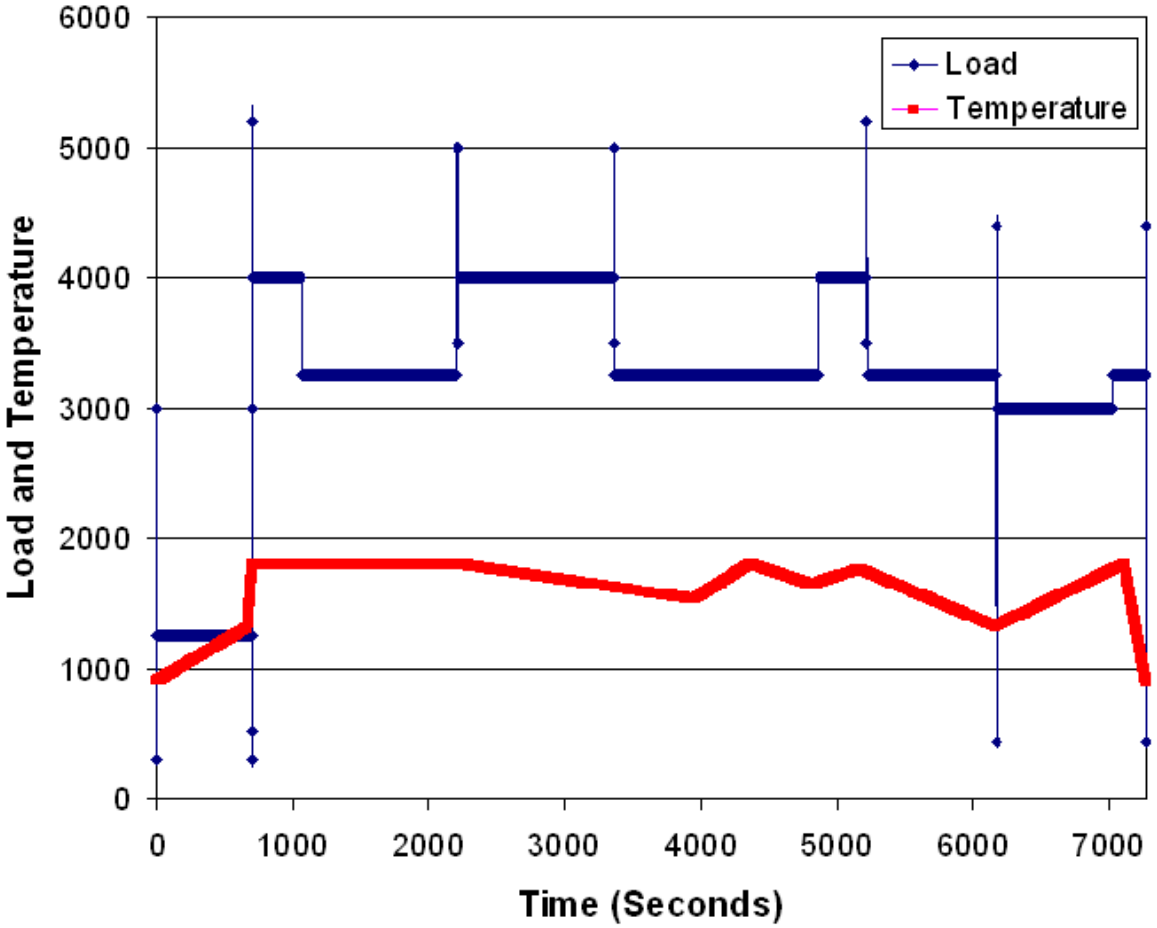

Figure 4.57: Two Hour Semi-Realistic Spectrum with Twenty One 1 Hz Loading Cycles and Dwell Time

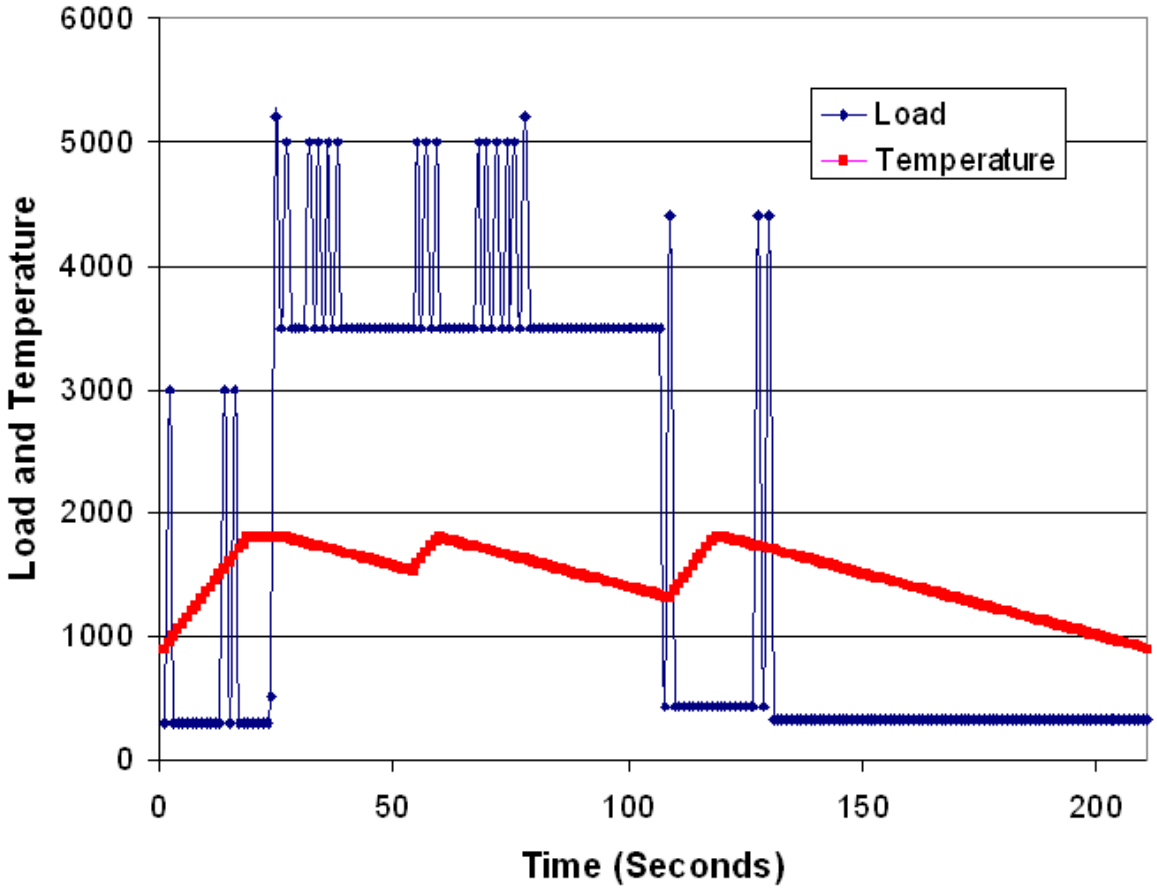

Figure 4.58: 3.5 Minute Semi-Realistic Spectrum with Twenty One 1 Hz Loading Cycles

The non-interaction life predictions for both spectra are shown in Figure 4.59. The non-interaction model does not take into account dwell times so both spectrums have a life of 29 flights. Due to the small number of loading cycles in both of these spectrums, the non-interaction prediction was iterated to make sure that the load levels were high enough so the spectrum tests would last less than 5 days.

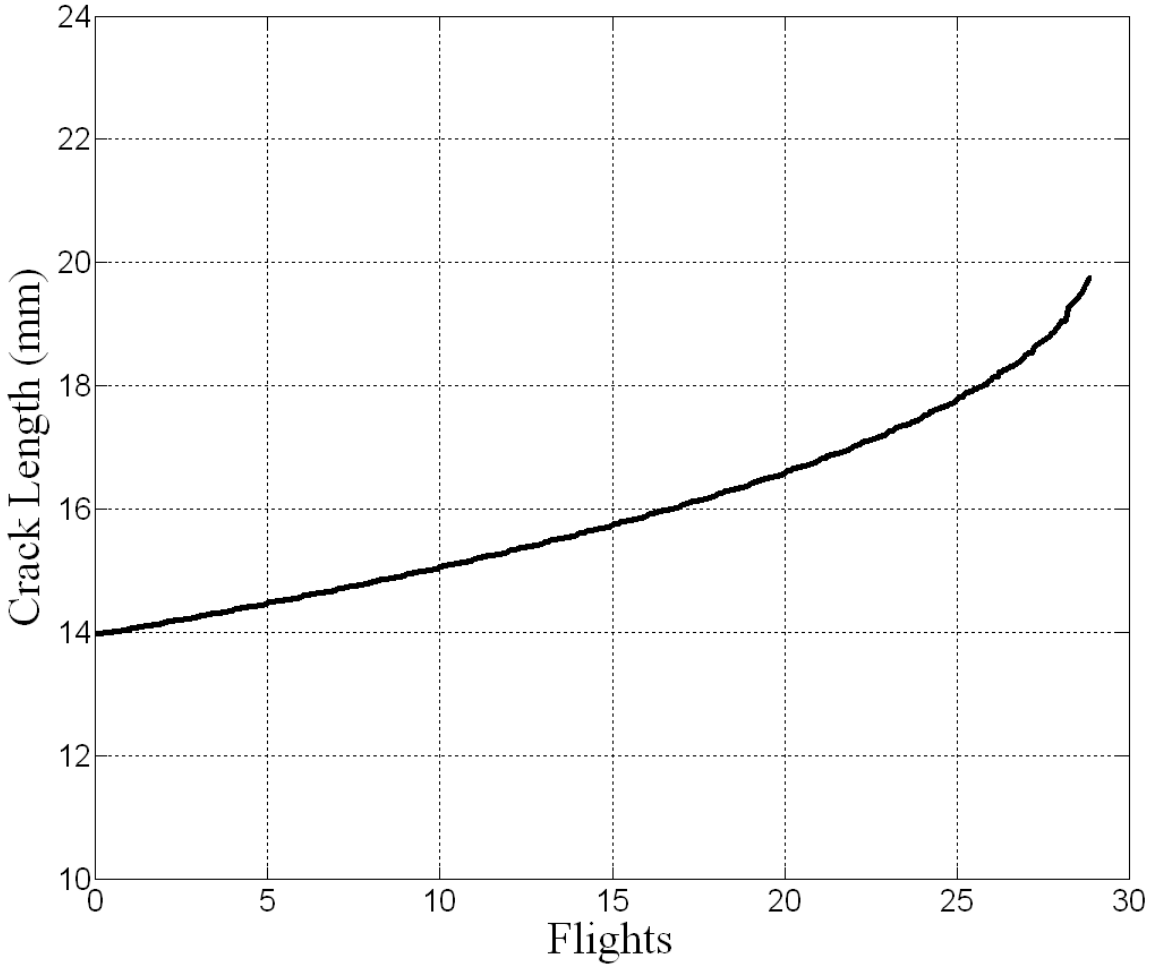

Figure 4.59: Non-Interaction Prediction for Spectrums with Twenty One Loading Cycles

The results for both spectrums can be seen in Figure 4.60 plotted as a function of time. As expected the spectrum test with dwell lasted quite a bit longer than the test without dwell times. The dwell test lasted a little less than 4 days, 27 times longer than the test without dwell. Figure 4.61 has both test results plotted as a function of flights. In this plot the crack growth curves are much closer together. The test with dwell times lasted for fewer flights but the difference is quite a bit smaller than expected. The dwell test lasted 46 flights while the test without dwell lasted for 58 flights. These results call into question the importance of including dwell times in flight spectra especially when taking into account the cost of overall time to perform spectrum tests with dwell times.

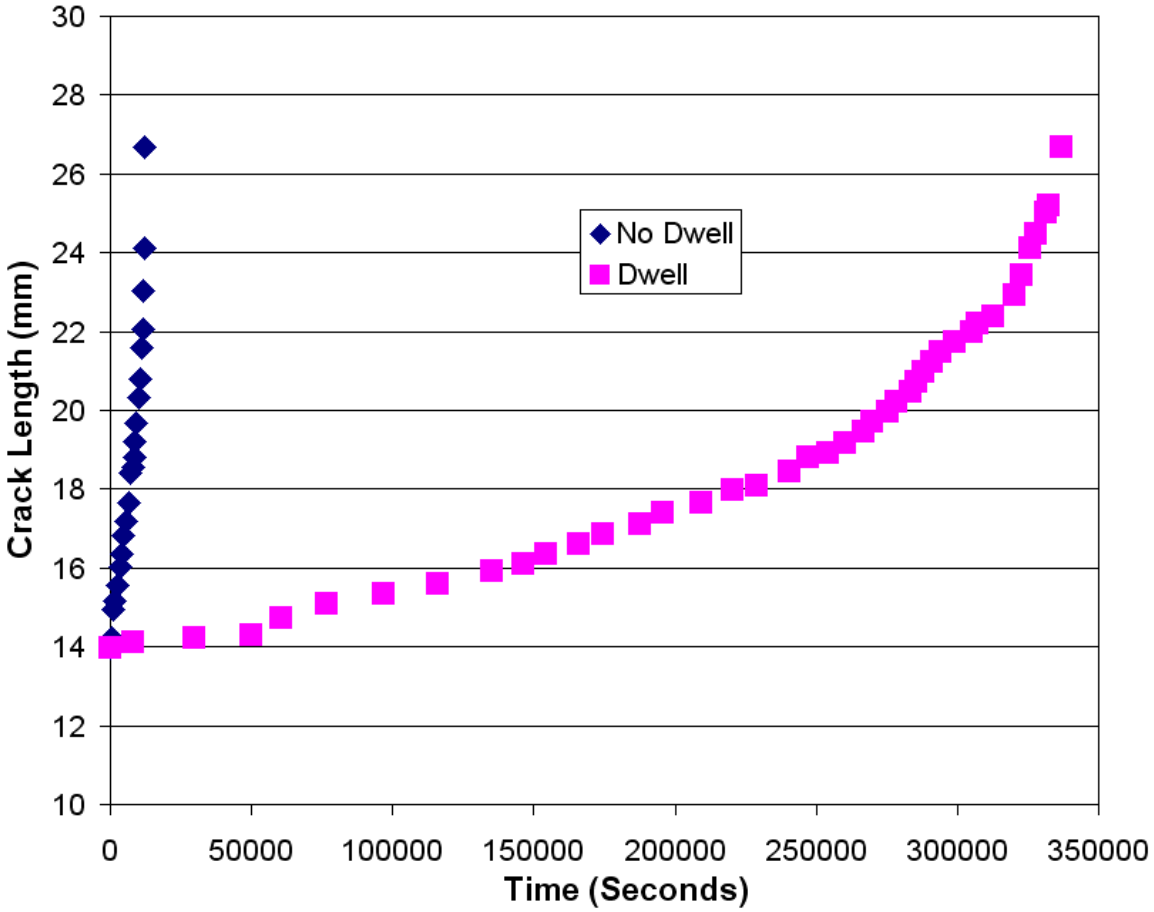

Figure 4.60: Results for Twenty One Loading Cycle Spectrums with Crack Length Plotted as a Function of Time

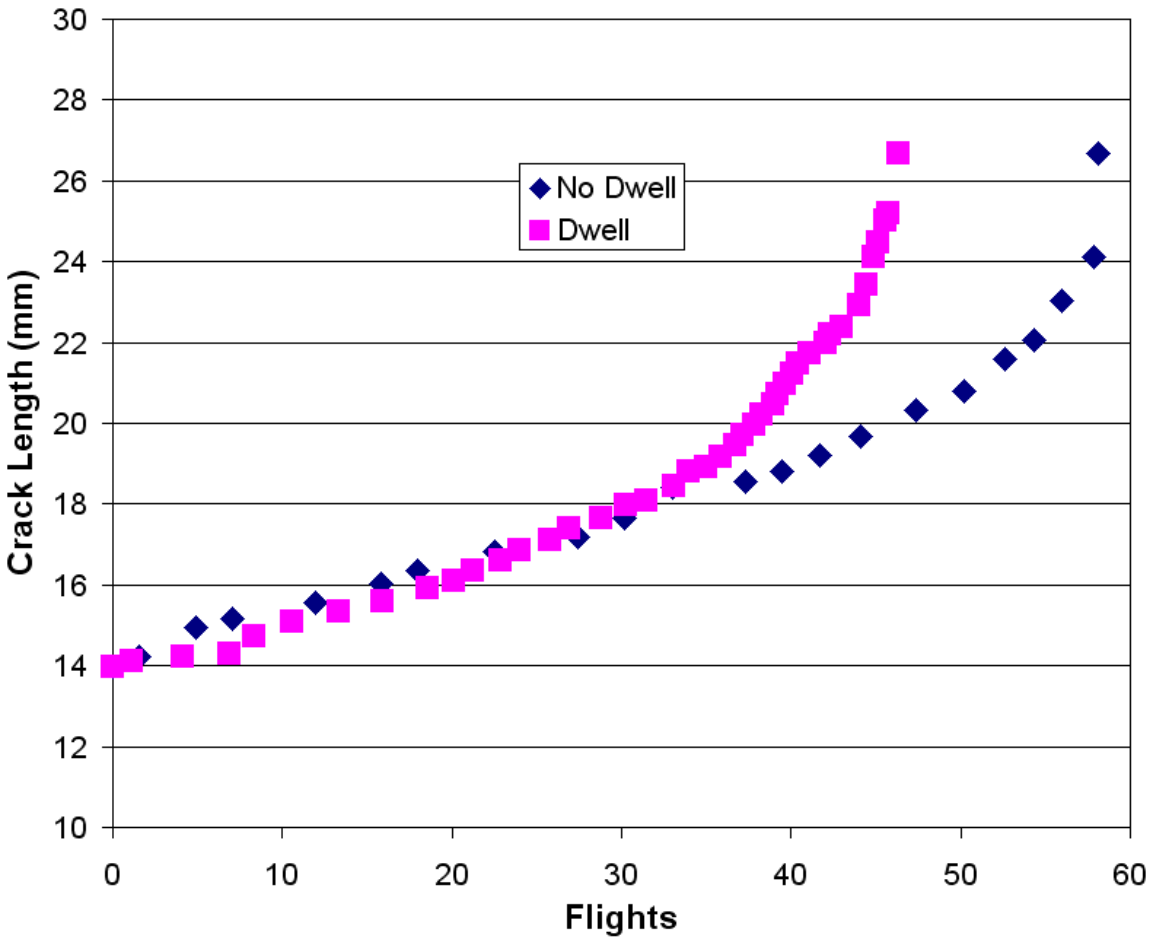

Figure 4.61: Results for 21 Loading Cycle Spectrums with Crack Length Plotted as a Function of Number of Flights

In summary semi-realistic spectrum testing demonstrated the extreme sensitivity that relative loading levels play on fatigue crack growth life. In addition 40% variability in life was seen, while also calling into question the importance of dwell times in spectrum testing.

CHAPTER 5: CRACK SURFACE MORPHOLOGY

A TESCAN SEM was used to obtain quality fractography images of the PWA1484 specimens. It was from these images that the failure modes and damage mechanism responsible for crack growth rates and TMF interactions were determined. In evaluating the PWA1484 fracture surfaces with the scanning electron microscope it became apparent that the surface can be divided into two main morphologies. The first is a precipitate avoidance morphology that is rolling but still predominantly flat. In <001> primary oriented specimens this fracture mode tends to shift from cubic plane to cubic plane and the interdendritic region while staying mostly normal to the applied loads. The second mode is a form of cleavage and occurs predominantly on octahedral crystallographic planes.

These two different morphologies result from two different underlying mechanisms; either γ' avoidance or γ' shearing. When a dislocation moves through the γ matrix material it will eventually encounter the γ' precipitate which will either be sheared or avoided by the dislocation. Avoidance is primarily observed at lower temperatures as glide looping but at higher temperatures dislocation climb may occur. The shearing mechanism happens when the dislocation passes through and "shears" the γ' as it travels through the γ matrix material. For various reasons when shearing is too difficult the avoidance mechanism occurs [170].

5.1: Isothermal Constant Amplitude Crack Surface Morphology

The influence of loading frequency on fracture surface morphology can clearly be seen in Figure 5.1. The right half of the fractograph is the starter notch created by the wire EDM process. Precracking is then performed at a frequency of 10 Hz and 982°C. Extensive octahedral crystallographic cracking can be seen occurring during this process until normal testing at 1 Hz is started and the morphology transitions to one of precipitate avoidance. The higher precracking frequency at elevated temperature minimized the effect of environment attack. A closer look at the crystallographic cleavage region confirms the shearing of the γ' precipitate as seen in Figure 5.2. The occurrence of γ' coarsening can be seen with average edge sizes of approximately 2 μm.

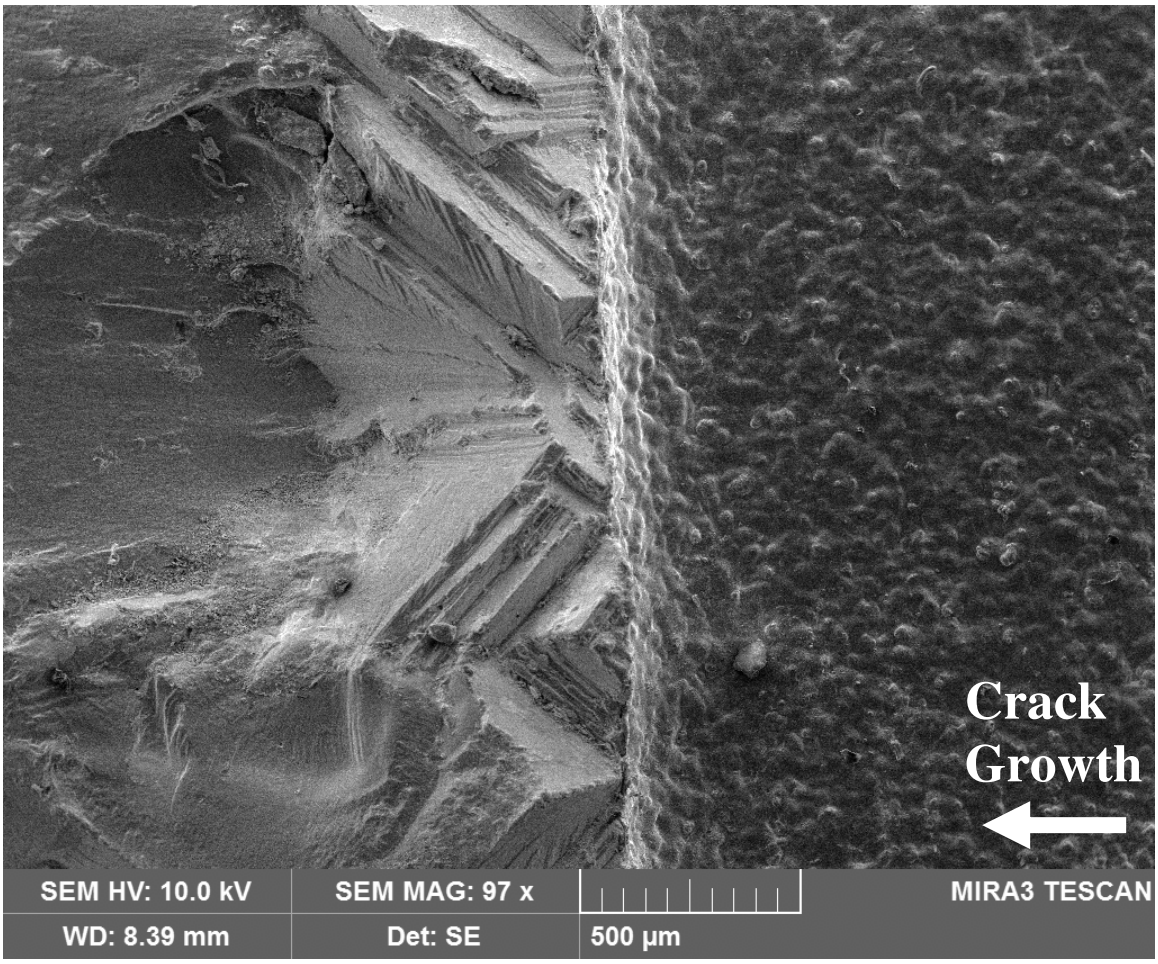

Figure 5.1: PWA1484 Fracture Surface Displaying Wire EDM Notch, Crystallographic Pre-Cracking and Flat Fracture at 1 Hz, 982°C and R=0.1

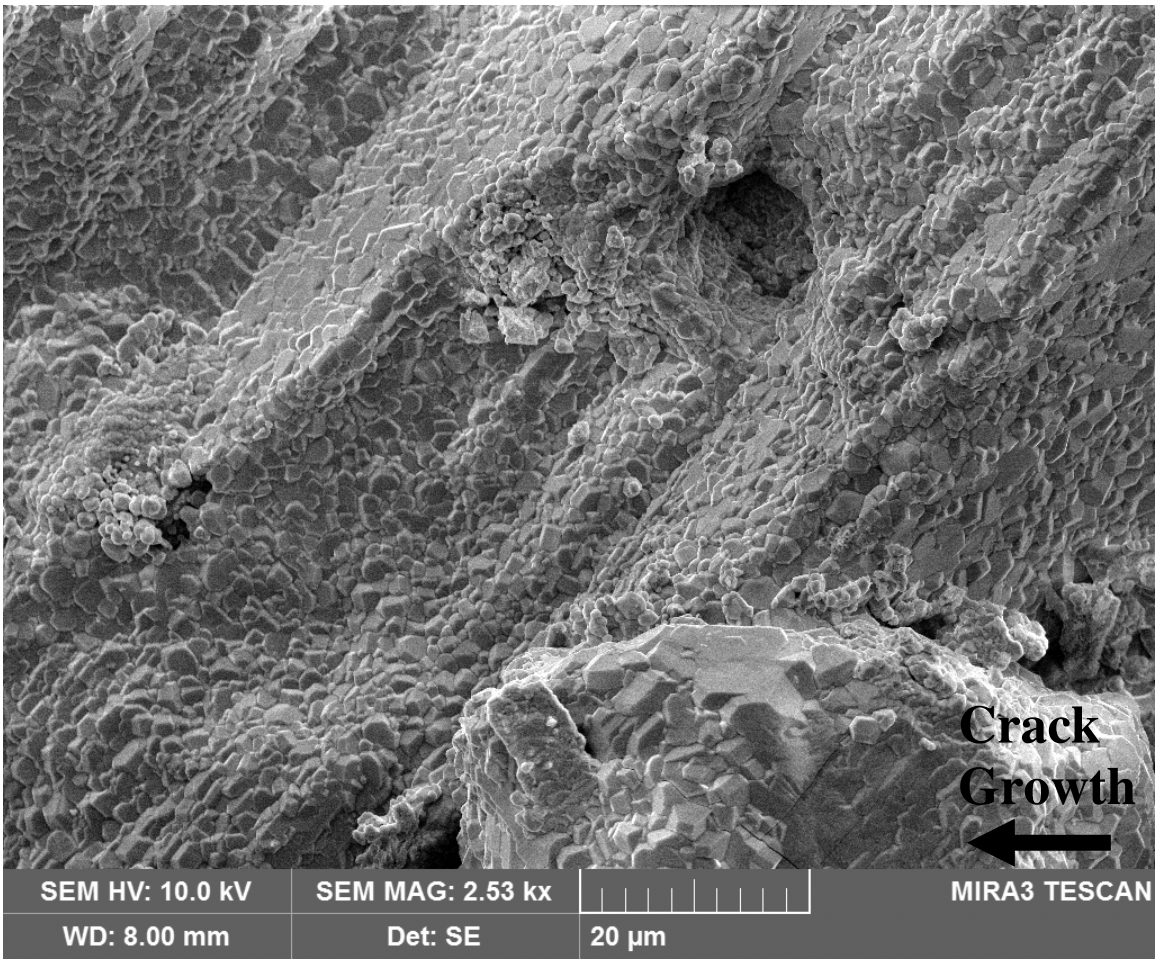

Figure 5.2: PWA1484 Fracture Surface Displaying Crystallographic Pre-Cracking Composed Predominantly of γ' Shearing at 1 Hz, 982°C and R=0.1

The precipitate avoidance morphology at 982°C, R=0.1 and 1 Hz is shown in Figure 5.3 and Figure 5.4. In Figure 5.3 the relatively flat fracture surface is seen undulating between the dendritic regions with γ' clustered on the dendritic arms. Taking a closer look at the fracture surface shows predominantly avoided precipitates with a mix of sheared precipitates as shown in Figure 5.3. Looking closely fatigue striations can be seen on some of the precipitates while the majority of precipitates were bypassed. This fatigue striation spacing was determined to correspond to the da/dN at the corresponding crack length. Again the γ' can be seen to have coarsened at 982°C.

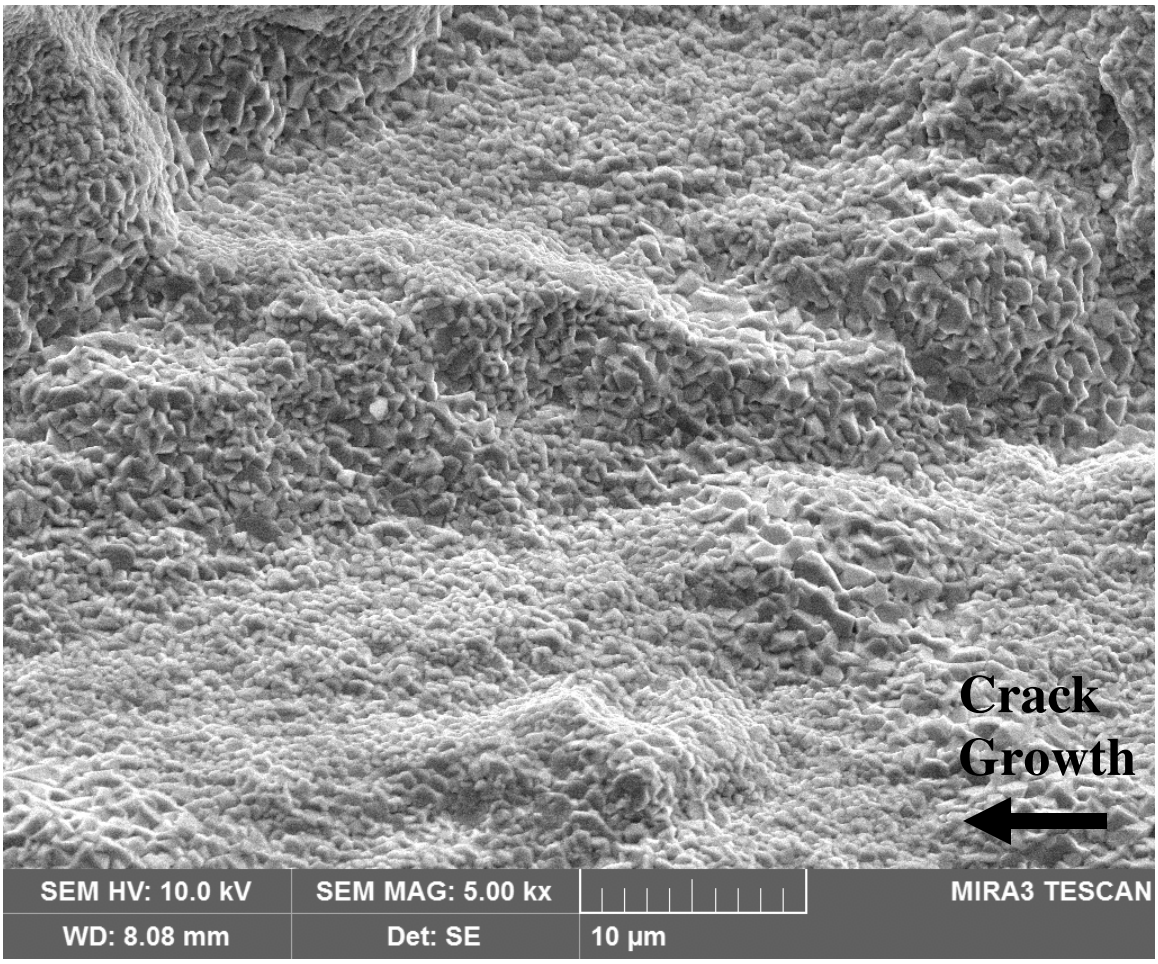

Figure 5.3: PWA1484 Fracture Surface Displaying Flat Fracture Composed Predominantly of γ' Avoidance at 1 Hz, 982°C and R=0.1

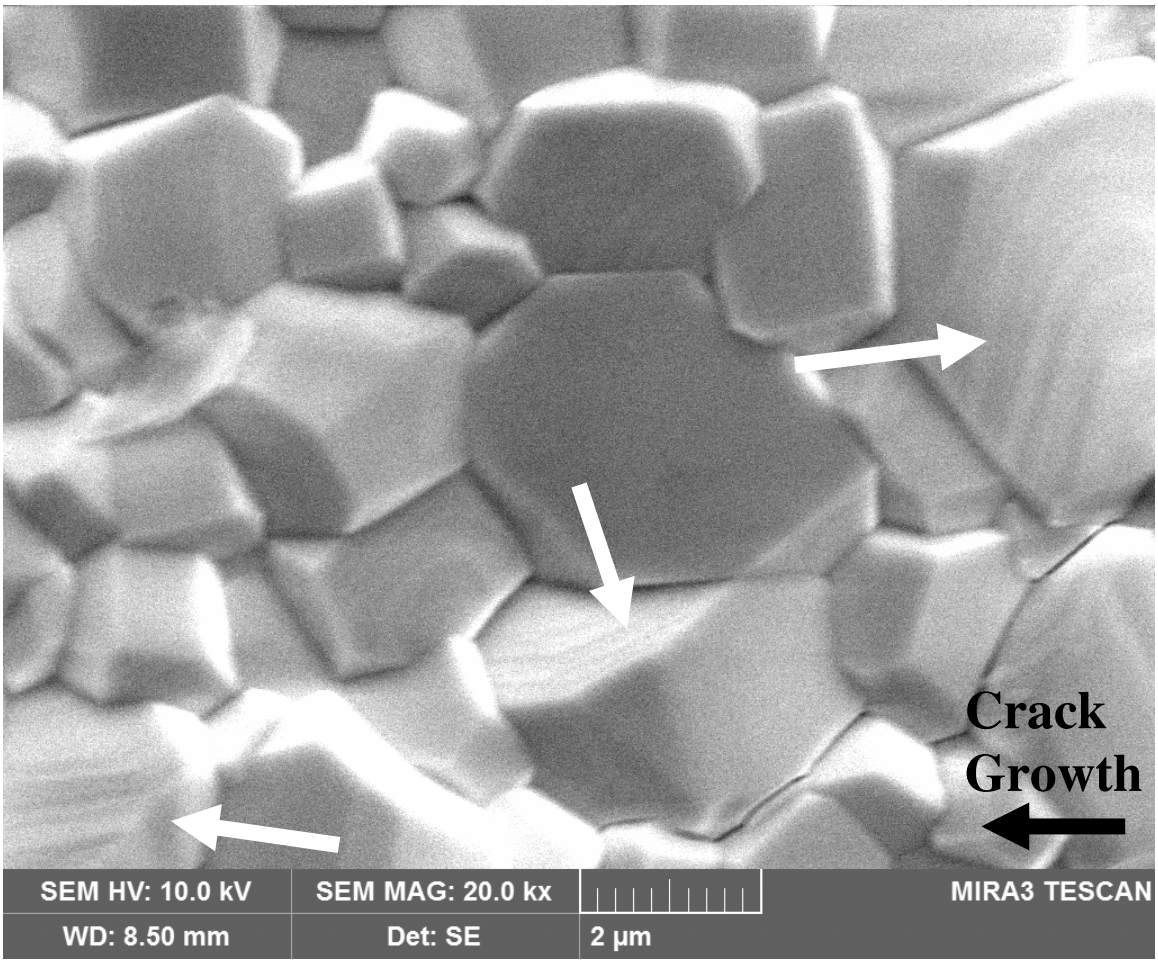

Figure 5.4: PWA1484 Fracture Surface Displaying Flat Fracture Composed of γ' Avoidance with Some γ' Shearing Visible (indicated with arrows) at 1 Hz, 982°C and R=0.1

Figure 5.5 details the fast fracture region of a test performed at 816°C, 1 Hz and an R Ratio of 0.1. In every single PWA1484 test there was a fast fracture region that was always crystallographic in nature with the size depending on the temperature and R Ratio. The higher the temperature the more ductile the PWA1484 leading to a smaller fast fracture region. The fracture region would decrease with increasing R Ratio due to K_{IC} being reached at shorter crack lengths.

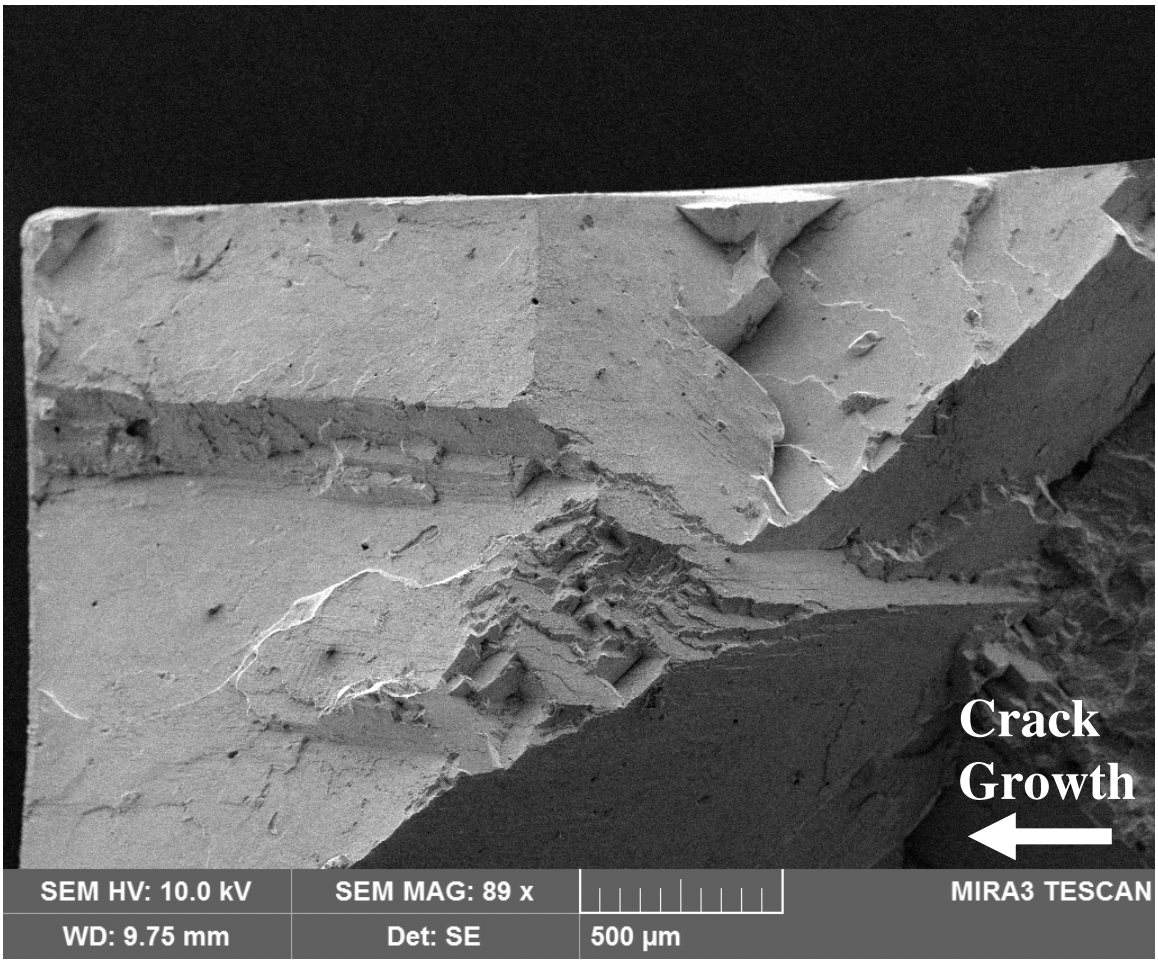

Figure 5.5: PWA1484 Fracture Surface Displaying Fast Fracture Region Composed of Crystallographic Cracking at 1 Hz, 816°C and R=0.1

The flat fracture morphology seen at 649°C, R=0.7 and 1 Hz is shown in Figure 5.6. In the upper right quadrant of this fractograph fatigue striations can clearly be seen. While a majority of the surface is composed of γ' avoidance some crystallographic cleavage can be seen in the bottom right quadrant. This was fairly common and would always happen at the free surface just as shear lips form in polycrystalline materials under plane stress conditions.

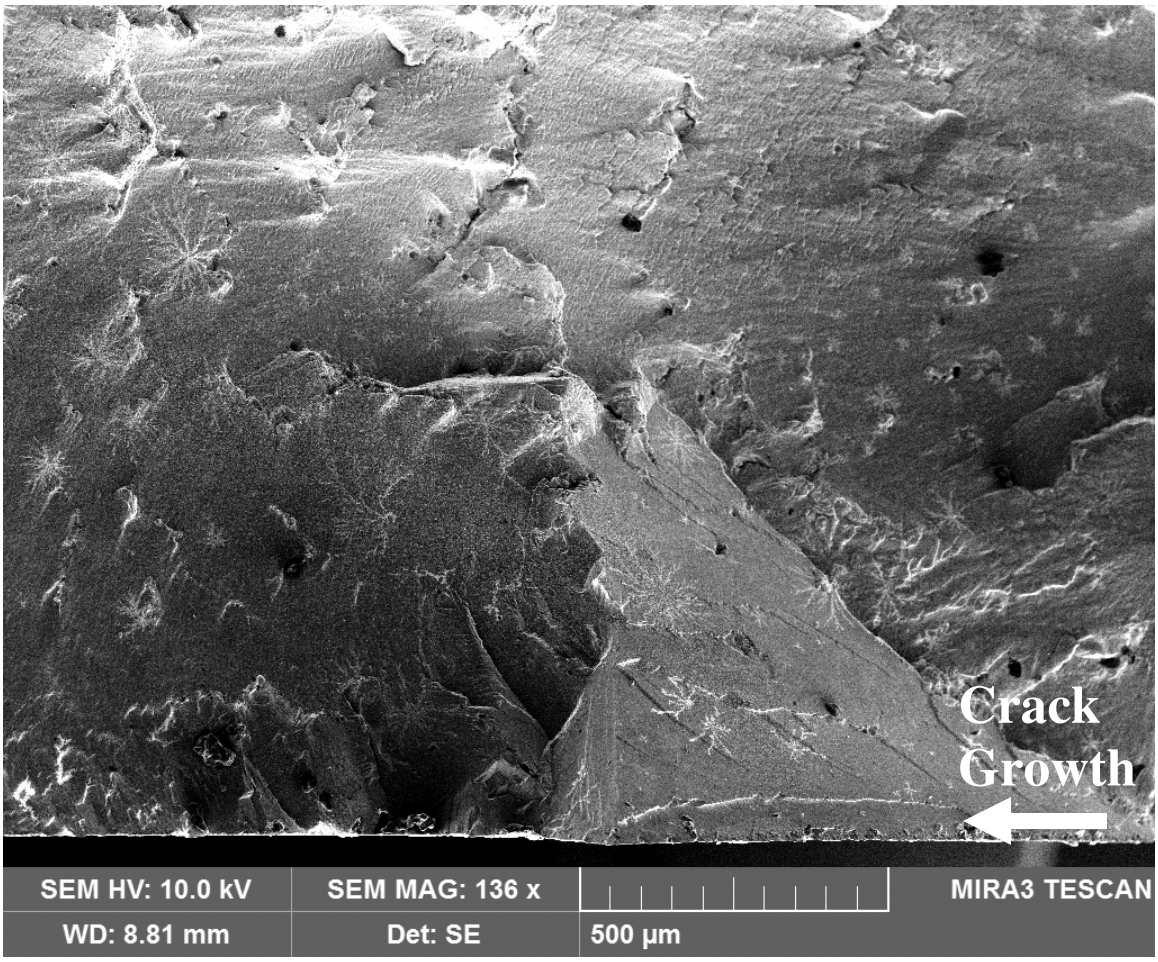

Figure 5.6: PWA1484 Fracture Surface Displaying Flat Fracture Comprised of Fatigue Striations along with Crystallographic Cracking at 1 Hz, 649°C and R=0.7

In Figure 5.6 an interesting "snowflake" phenomenon can faintly be seen. Upon closer inspection this "snowflake" could be a product of the casting process or was even created during fatigue crack growth cycling. This artifact is roughly 100 µm in diameter as seen in Figure 5.7. The high R Ratio (R=0.7) that this test was conducted at would tend to preserve the fracture surface.

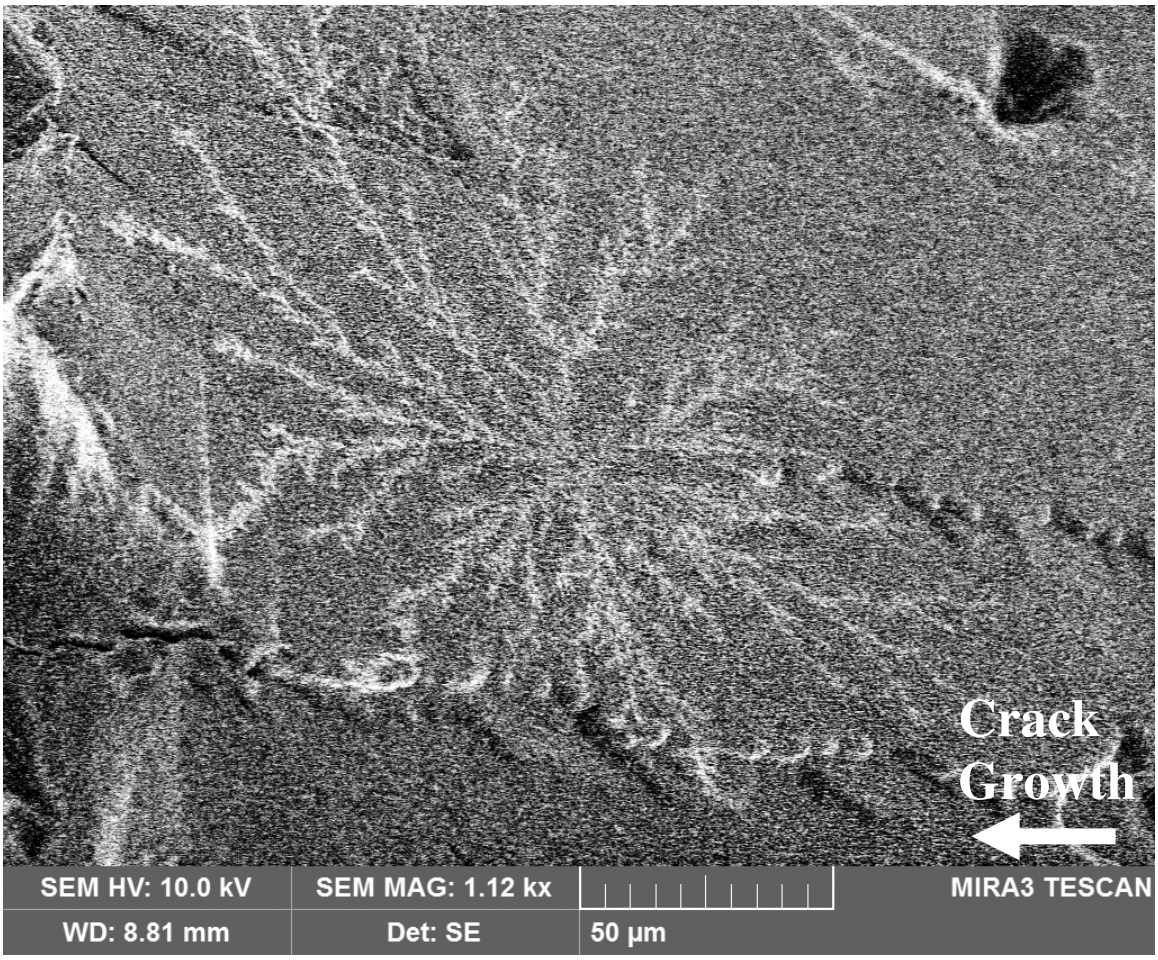

Figure 5.7: PWA1484 Fracture Surface Displaying Flat Fracture with Snowflake Pattern Possibly Formed During Casting at 1 Hz, 649°C and R=0.7

5.2: Temperature and Load Interaction Crack Surface Morphology

Very revealing temperature interacting fractography results can be seen in Figure 5.8 and Figure 5.9. The first figure clearly shows temperature striations created during 50 alternate cycle block testing between 649°C and 982°C. The smaller bands are the crack growth created during 649°C while the larger band is the crack growth created during the 982° cycles. The size ratios of the bands indicate that the 649°C crack growth was retarded by the 982°C cycling leading to overall crack growth retardation when compared to the non-interaction temperature prediction.

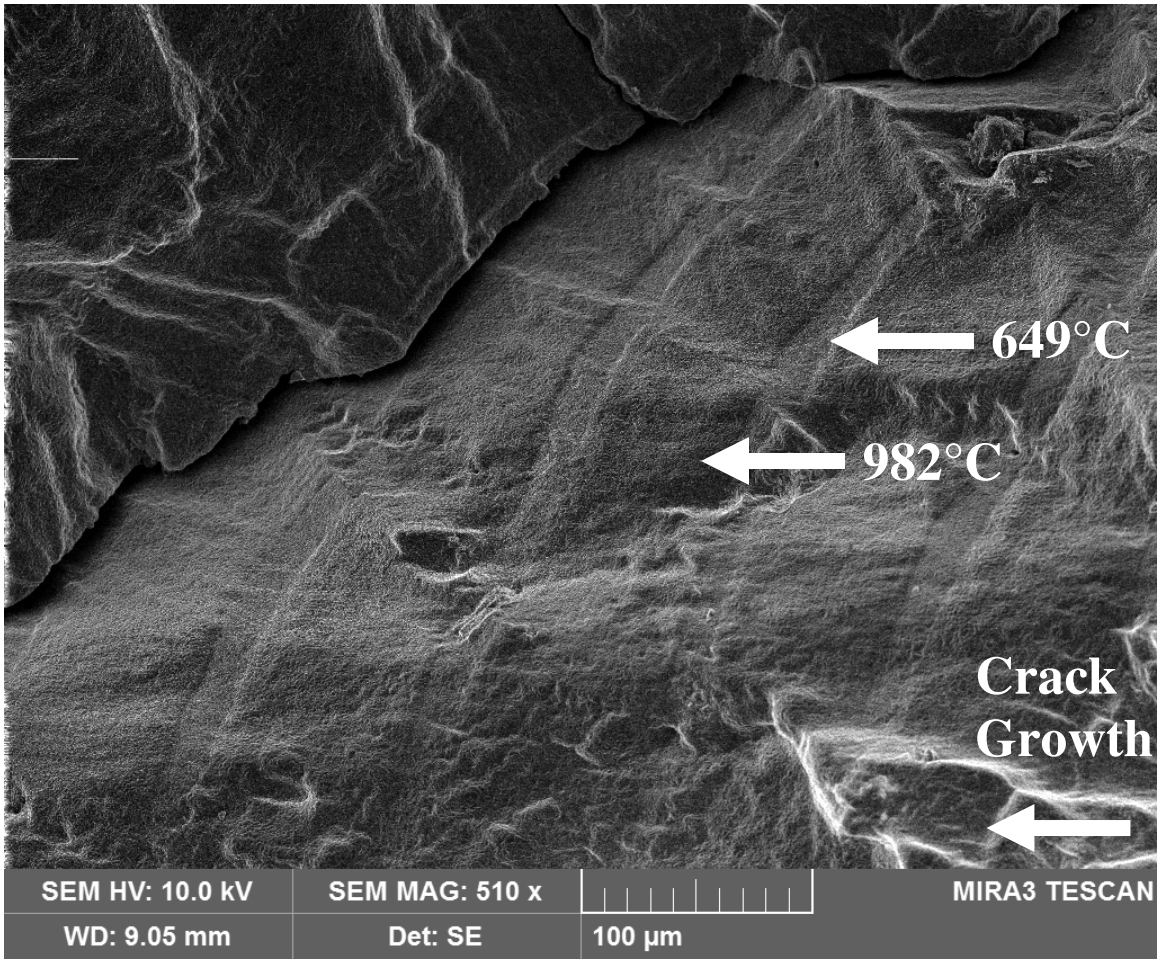

Figure 5.8: PWA1484 Fracture Surface Displaying Temperature Striations Created During 50 Alternating Cycle Block Testing at 1 Hz, 649°C/982°C and R=0.7

Looking more closely at the center of a 649°C temperature striation reveals even more information as seen in Figure 5.9. The 649°C striation is flanked on either side by coarsened γ' on the order of 2 to 3µm. These larger γ' were created under the high stress conditions at the crack tip during the high R Ratio 982°C cycles. Once the temperature decreased to 649°C the γ' coarsened as well but only to roughly 1µm in size.

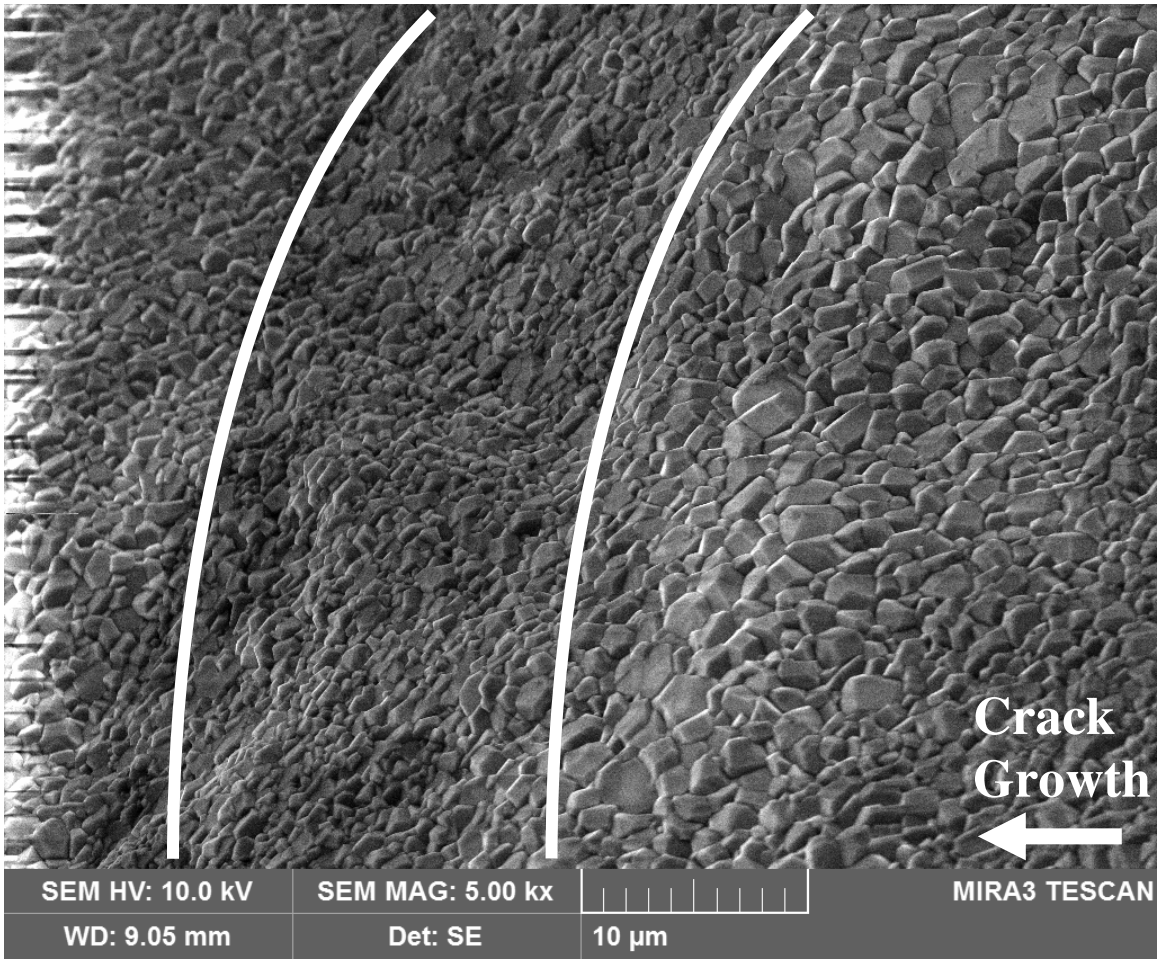

Figure 5.9: PWA1484 Fracture Surface Displaying Different Sized γ' Created During 50 Alternating Cycle Block Testing at 1 Hz, 649°C/982°C and R=0.7

As mentioned in the isothermal constant amplitude fatigue crack growth rate section, there is not much difference in the crack growth rates for the controlled orientation, R=0.7 specimens at 649°C, 816°C and 982°C. In Figure 5.10 temperature striations created during 20 alternate cycle block testing between 649°C and 982°C can be seen. The temperature striations appear to be approximately the same width, and neither acceleration nor retardation was observed when the experimental crack growth was compared to the non-interaction prediction. Therefore it is apparent that for 20 alternating cycles the retardation of the 649°C crack growth created by the γ' coarsening

at 982°C was negated by the acceleration on the 649°C crack growth caused by the increased crack tip embrittlement at 982°C.

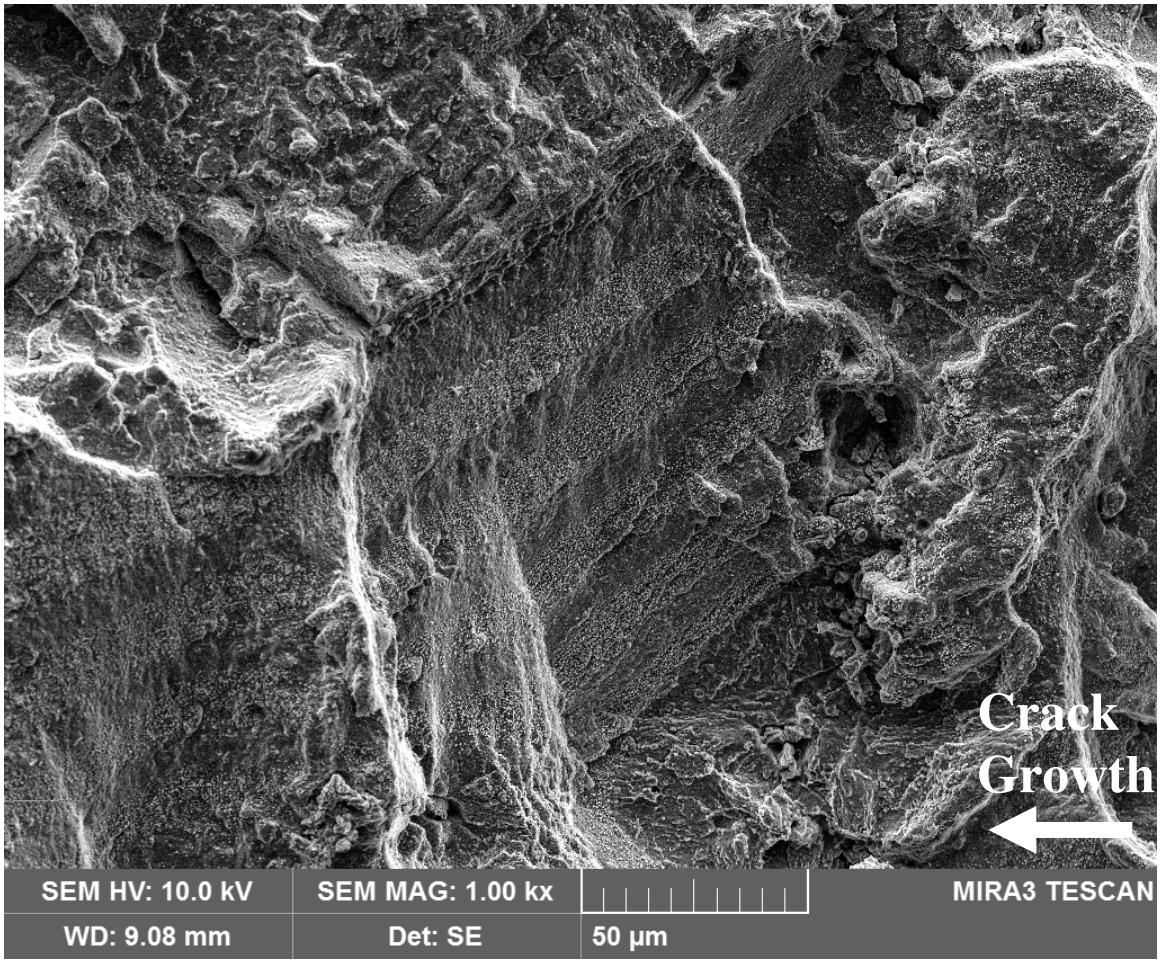

Figure 5.10: PWA1484 Fracture Surface Displaying Temperature Striations Created During 20 Alternating Cycle Block Testing at 1 Hz, 649°C/982°C and R=0.7

Crystallographic fracture from 2.0x overload cycling at 982°C can be seen in Figure 5.11. The overload cycle was large enough to promote precipitate shearing on the crystallographic octahedral planes. As can be seen in the figure the one overload cycle completely retarded the crack growth from the 800 1.0x cycles under 982°C conditions. This severe retardation of the 1.0x cycles led to very large overall retardation when compared to the non-interaction life prediction.

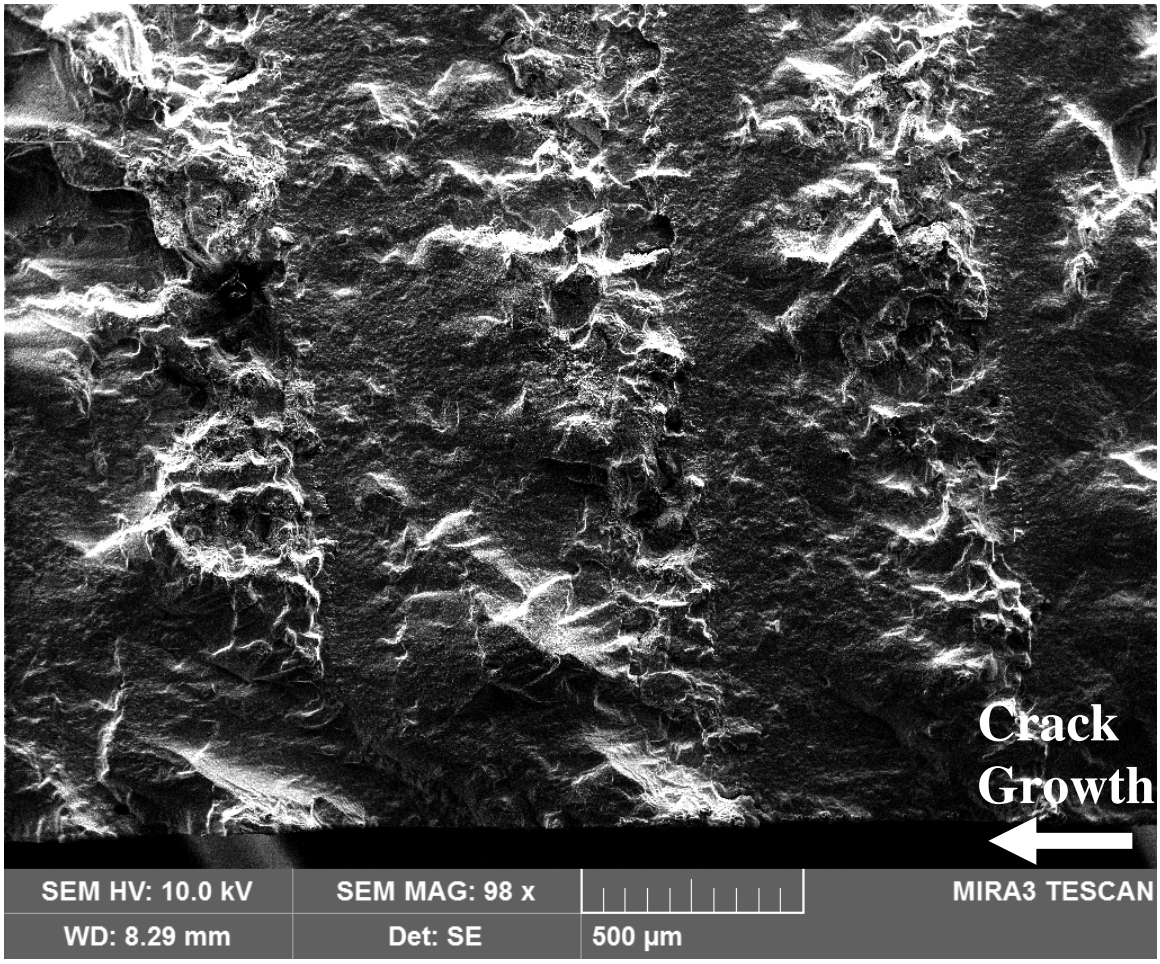

Figure 5.11: PWA1484 Fracture Surface Displaying Crystallographic Overload Regions Created During 2.0x Overload Testing at 1 Hz, 982°C and R=0.1

5.3: Crack Surface Morphology Mapping

The varied crystallographic fracture planes seen throughout the fractographs of PWA1484 can be understood by looking at Figure 5.12. The controlled specimens had a <010> cubic direction for secondary orientations while the uncontrolled specimens predominantly had <110> secondary orientations with the remaining uncontrolled specimens falling somewhere in between.

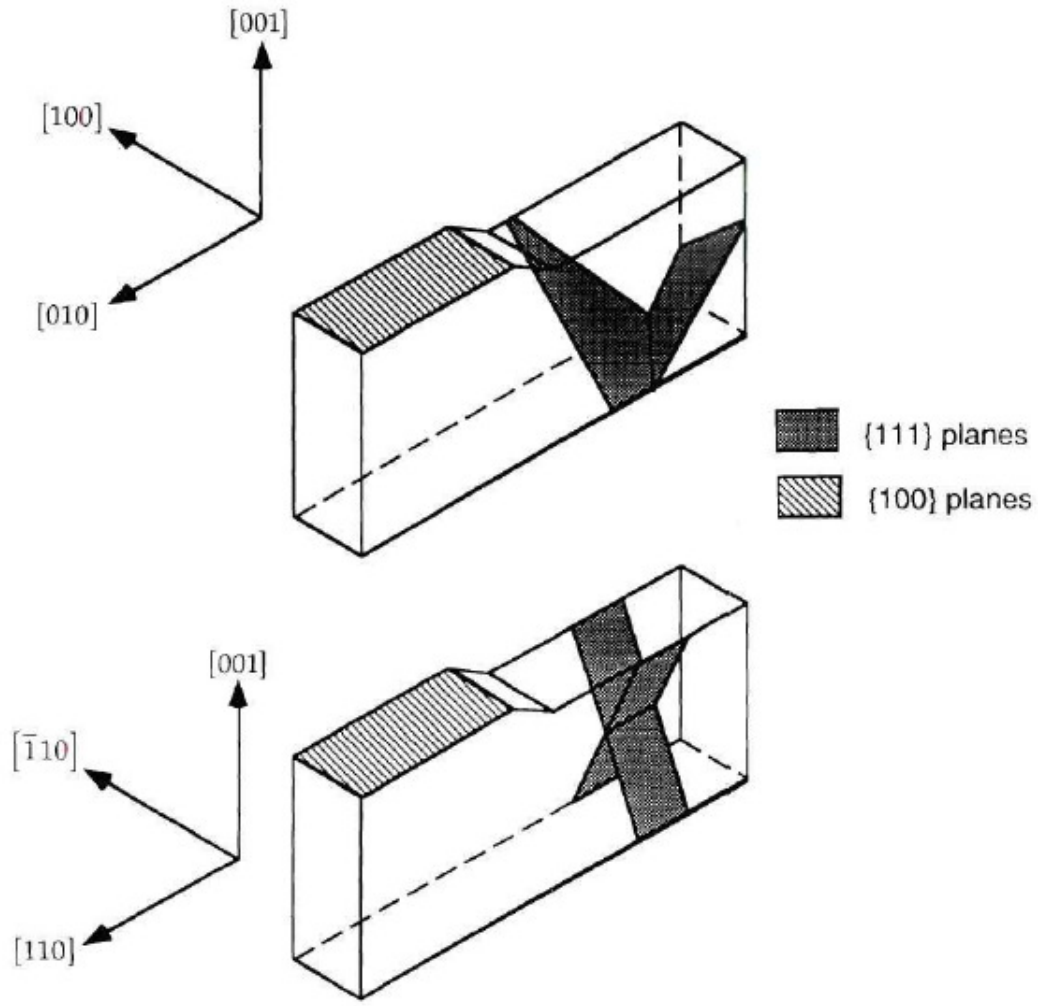

Figure 5.12: Octahedral and Cubic Planes Relative to Specimen Primary and Secondary Crystallographic Orientations [170]

The typical fracture surface morphology for all fatigue crack growth tests is shown in Figure 5.13. While all fracture surfaces looked similar to this figure the relative morphology ratios varied depending on temperature and R Ratio. During precracking there was always crystallographic morphology created due to the high frequency cycling negating the effect of environment. When the actual 1 Hz testing began, this transitioned to a precipitate avoidance morphology which persisted for a certain crack length depending on temperature and R Ratio. At higher R Ratios this region was shorter and became longer with increasing temperature. The precipitate avoidance morphology

would then transition to a precipitate shearing crystallographic morphology until fast crystallographic fracture was reached.

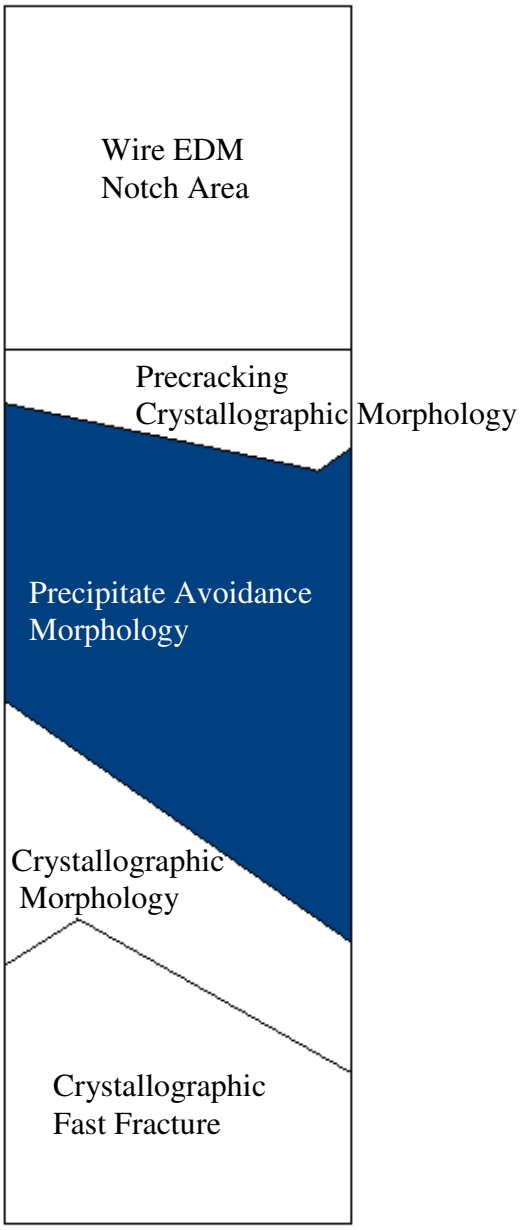

Figure 5.13: Typical Fracture Surface Morphology for PWA1484 Testing at 1 Hz, 649°C to 982°C for R=0.1 and R=0.7

The shortcoming of ΔK when used as the crack driving force in single crystal superalloys can be seen in Figure 5.14. This fracture surface and da/dN data are from isothermal constant amplitude testing at 982°C, 1 Hz and an R Ratio of 0.7. Crack branching and octahedral fracture can cause a decrease in the fatigue crack growth rate due to ΔK not being able to account for multiple fracture surfaces and planes of weakness. As is shown in Figure 5.14 the start of a decrease in crack growth rate is associated with the crack transitioning to octahedral fracture from transprecipitate non-crystallographic fatigue crack growth. The increase in crack growth rate can then be seen to correlate to the crack leaving an octahedral plane and returning to non-crystallographic fatigue crack growth until fast fracture is reached. The high R Ratio that this specimen was tested at would tend to promote crystallographic fracture even at high temperature and lower values of crack driving force.

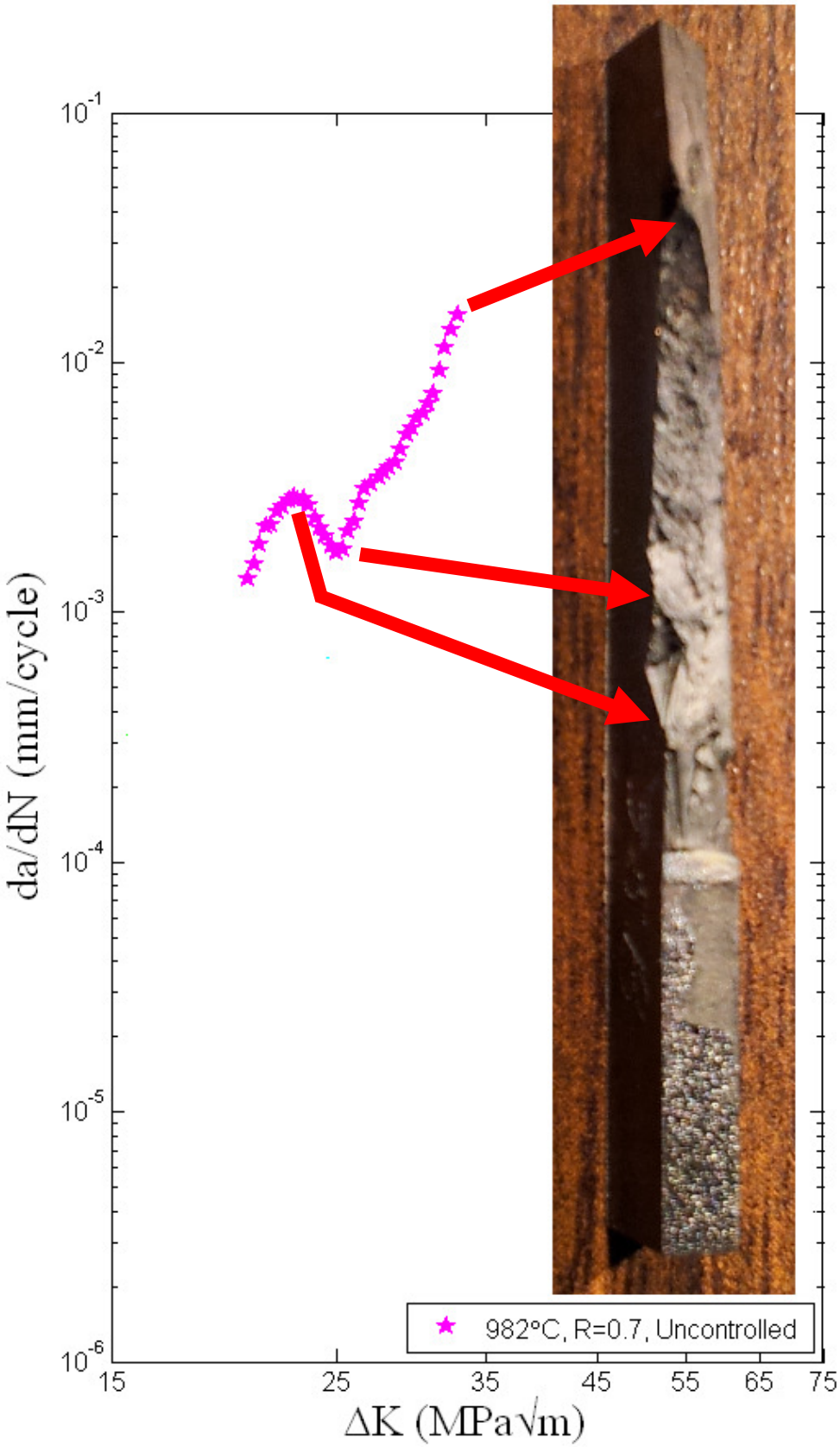

Figure 5.14: Fracture Surface Morphology Correlated to da/dN for 982°C and R=0.7

CHAPTER 6: MODELING

Monitoring the health of engine components and obtaining real time diagnostics is crucial for reducing life cycle costs and for implementation of retirement for cause. As aircraft engine complexity and performance requirements increase the pairing of in-situ component monitoring and the traditional process of regularly scheduled maintenance intervals has the promise to be advantageous and cost effective. Due to the increasing popularity of gas turbine telemetry to monitor engine components in-situ temperatures, strains and ultimately stresses it is extremely valuable to know what direction cracks would tend to propagate for ideal sensor placement [171-173]. In single crystal turbine blades often times the propagating crack will switch from cubic to octahedral planes several times before reaching fast fracture. An example of a crack growing crystallographically can be seen in Figure 6.1.

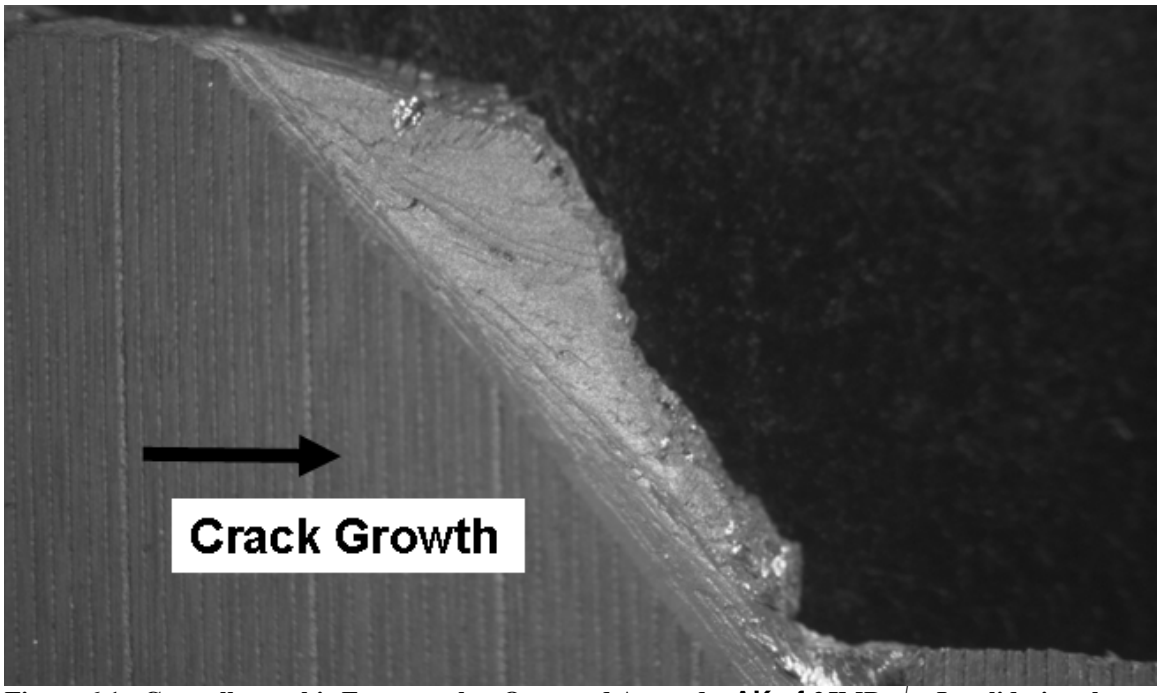

Figure 6.1: Crystallographic Fracture that Occurred Around a ΔK of 25MPa√m Invalidating the Fatigue Crack Growth Rate Test Results

6.1: Crack Path Trajectory

In order to understand why fatigue cracks in single crystal materials tend to propagate on crystallographic planes instead of perpendicular to the applied loads the normal and shear stresses on the octahedral planes need to be known. A Mathcad model developed by Stephen D. Antolovich was tested and verified using results from this study. With the primary and secondary orientations known through either dendritic determination or Laue back-reflection of X-rays this model can determine whether crack propagation will occur on crystallographic planes or perpendicular to the applied load. For many cases cracking follows {111} type planes even though the initial crack plane is usually of the {100} type. This means that the K solutions must be modified to take this deviation into account so that data is correlated with a proper forcing function. This crack trajectory model provides the orientation of {111} planes and <110> directions with respect to the specimen axes. It then transforms stresses in the specimen axis system to stresses normal to the {111} octahedral plane of interest and along the <110> direction of interest. Prediction of the likely fracture plane can then be accomplished by using either the sum or product of the normal and absolute values of the shear stresses.

As mentioned above the crack path trajectory model relates the specimen axes to the crystallographic axes as seen in Figure 6.2. X2 is the specimen axes while X is the crystallographic axes. With this relationship established the applied load can then be decomposed onto the octahedral crystallographic planes.

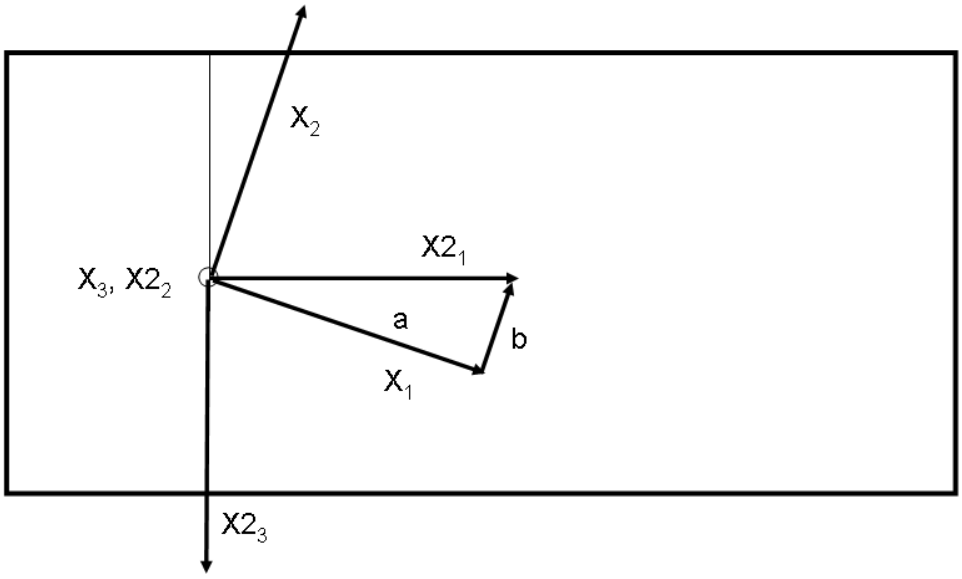

Figure 6.2: Assuming a Controlled Primary Orientation of [001] the Specimen Axes and Crystallographic Axes Can be Related by One Angular Measurement

The model gives the orientation of {111} planes and <110> directions with respect to the specimen axes as seen in Figure 6.3. With this information it then computes the tensile stress normal to any {111} plane and the shear stresses along the <110> directions on the plane of interest.

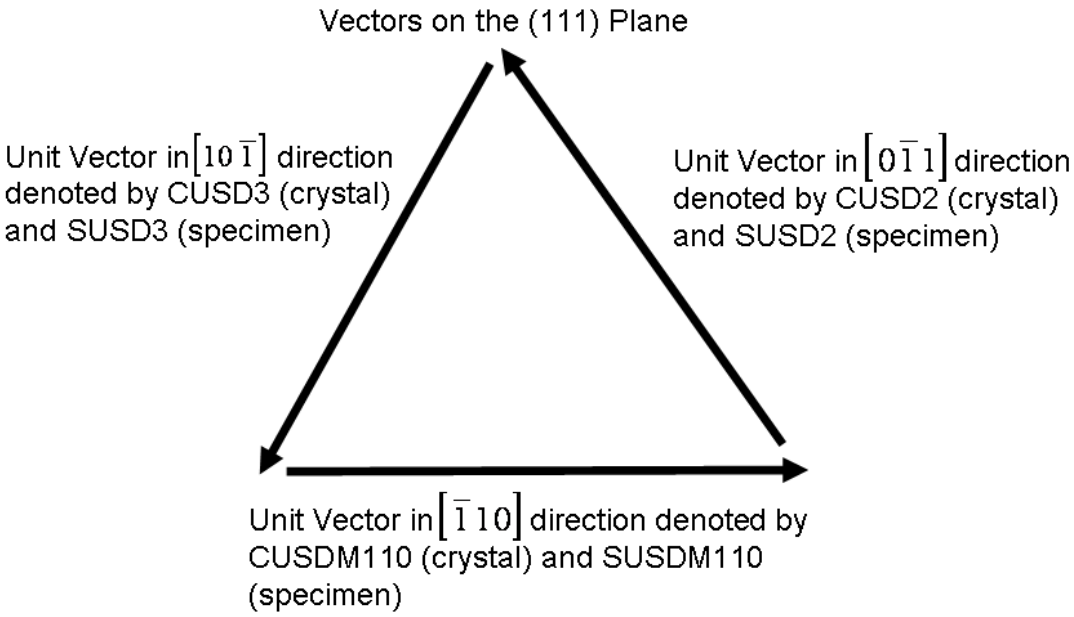

Figure 6.3: Crack Path Trajectory Model Definitions for Vectors on the (111) Plane

Initially the crystal directions and axis system of the specimen are defined in terms of X_i and $X2_i$, respectively. Next the transformation cosine matrix is computed to convert the crystallographic frame of reference to the specimen frame of reference as seen in Equation 6.1.

$$L = \begin{pmatrix} X2_1 \bullet X_1 & X2_1 \bullet X_2 & X2_1 \bullet X_3 \\ X2_2 \bullet X_1 & X2_2 \bullet X_2 & X2_2 \bullet X_3 \\ X2_3 \bullet X_1 & X2_3 \bullet X_2 & X2_3 \bullet X_3 \end{pmatrix} \quad \textbf{(6.1)}$$

The stress components normal to the octahedral planes and along the <110> directions are then calculated with equations s11 through s33 in the form of Equation 6.2.

$$s11(\theta) = \sum_i \sum_j \left(L_1, i \cdot L_1, j \cdot \sigma(\theta) i, j\right) \quad \textbf{(6.2)}$$

The crack path trajectory model predictions of normal and shear for slip plane (111) in the $[0\bar{1}1]$ direction is shown in Figure 6.4. These results show good correlation with three dimensional elastic anisotropic FEA results obtained by Arakere et al. [74] as seen in Figure 6.5. The square pink data points in the Arakere plot are for the same slip plane and slip direction as plotted in Figure 6.4. It has hypothesized that in the interest of modeling simplicity that isotropic calculations would be accurate enough for use as an engineering tool. This hypothesis appears to be correct in comparing these two charts.

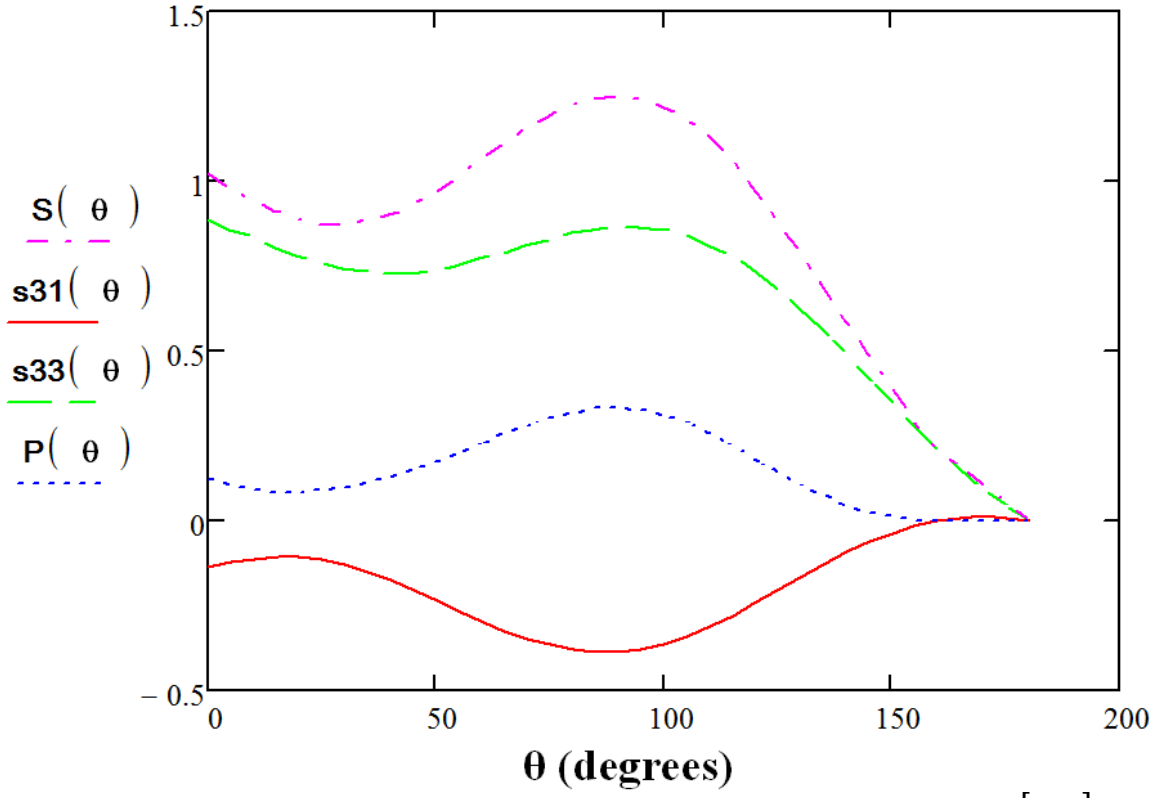

Figure 6.4: Crack Path Trajectory Model Normal and Shear Stress Predictions for $(111)[0\bar{1}1]$

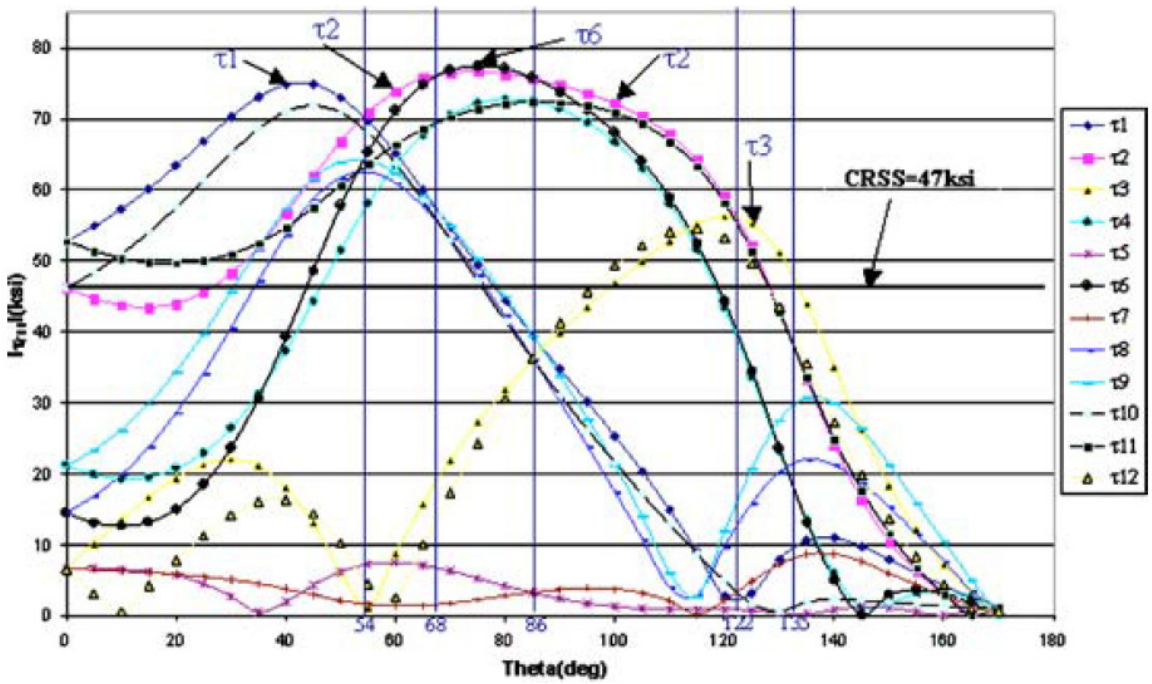

Figure 6.5: Three Dimensional Elastic Anisotropic RSS Values for the Twelve Slip Systems as a Function of Theta [74]

6.2: Crack Plane Determination Via SEM

The crack path trajectory model predicts that the highest stresses are on the octahedral planes when either calculated by the sum or product of the normal and shear stresses. The model is not able to take into account the effect of environment. With the added effect of environment during testing the γ' avoidance mechanism becomes more probable than the γ' shearing mechanism. In order to validate the crack path trajectory model several crystallographic fracture surfaces were verified by precision scanning electron microscope.

In all cases the planes were found to have interplanar angles between 50° and 60° relative to the cubic planes with most planes having interplanar angles right around 55°. This is a very strong indication that crystallographic fracture is occurring on {111} octahedral

planes (54.7°) [174]. These results correlate well with the crack path trajectory model, validating the model as an important tool in predicting likely crack growth directions in single crystal superalloys. Three SEM fractographs from testing at 816°C, R=0.7 and a frequency of 1 Hz used as part of the crack path trajectory model validation are shown in Figure 6.6, Figure 6.7 and Figure 6.8. Notice the octahedral crystallographic facets on the octahedral crystallographic plane in Figure 6.7.

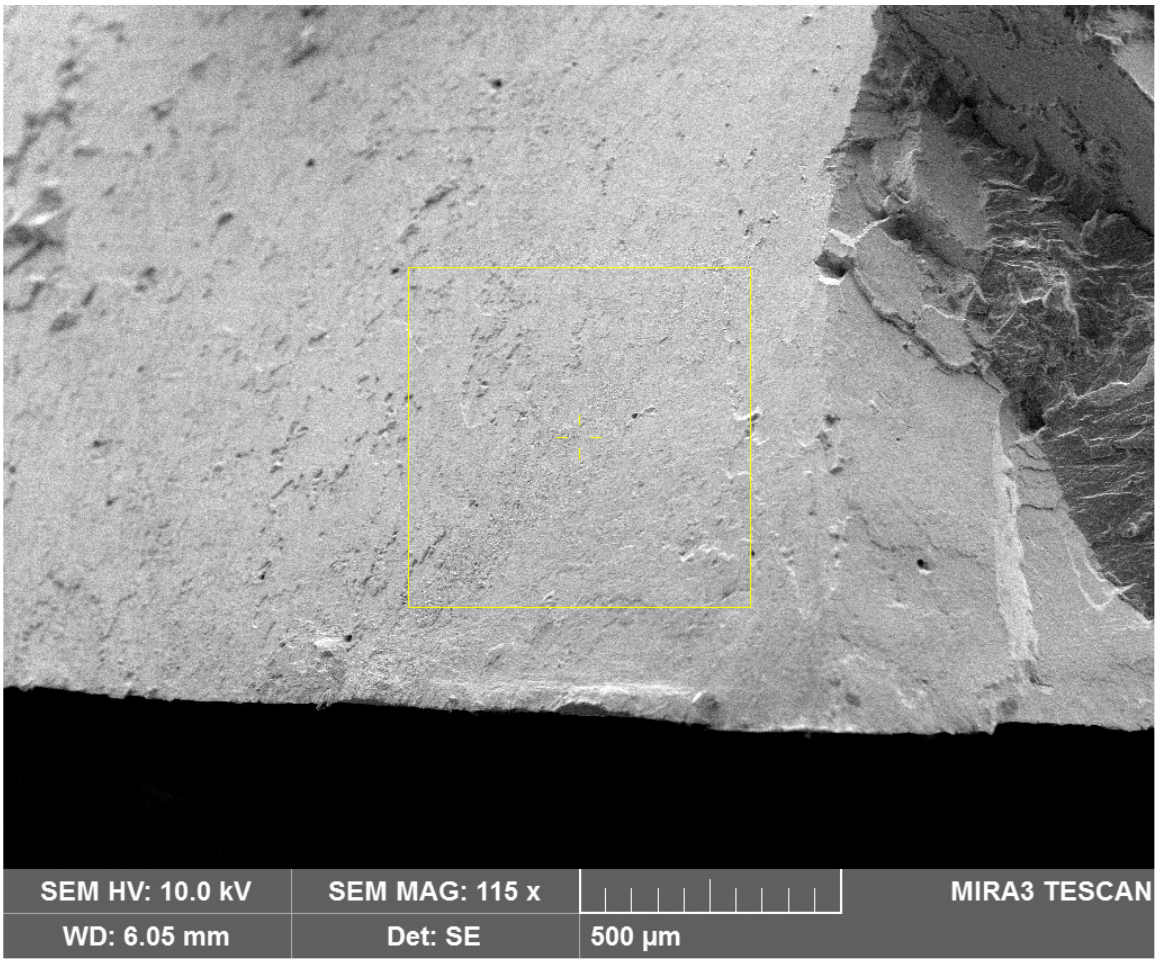

Figure 6.6: PWA1484 Fracture Surface Displaying Crystallographic Cracking at 1 Hz, 816°C and R=0.7, Crack Plane Determination Point 1

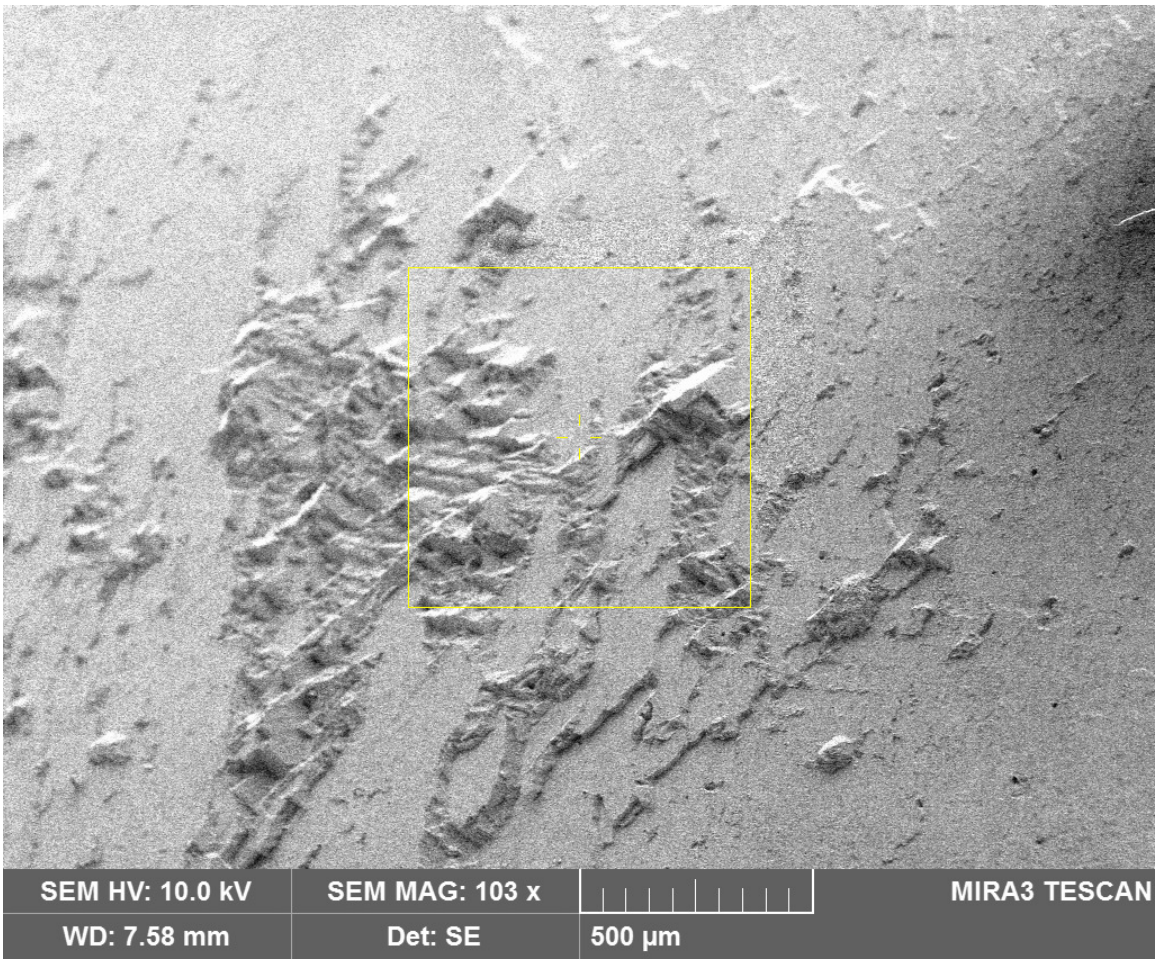

Figure 6.7: PWA1484 Fracture Surface Displaying Crystallographic Cracking at 1 Hz, 816°C and R=0.7, Crack Plane Determination Point 2

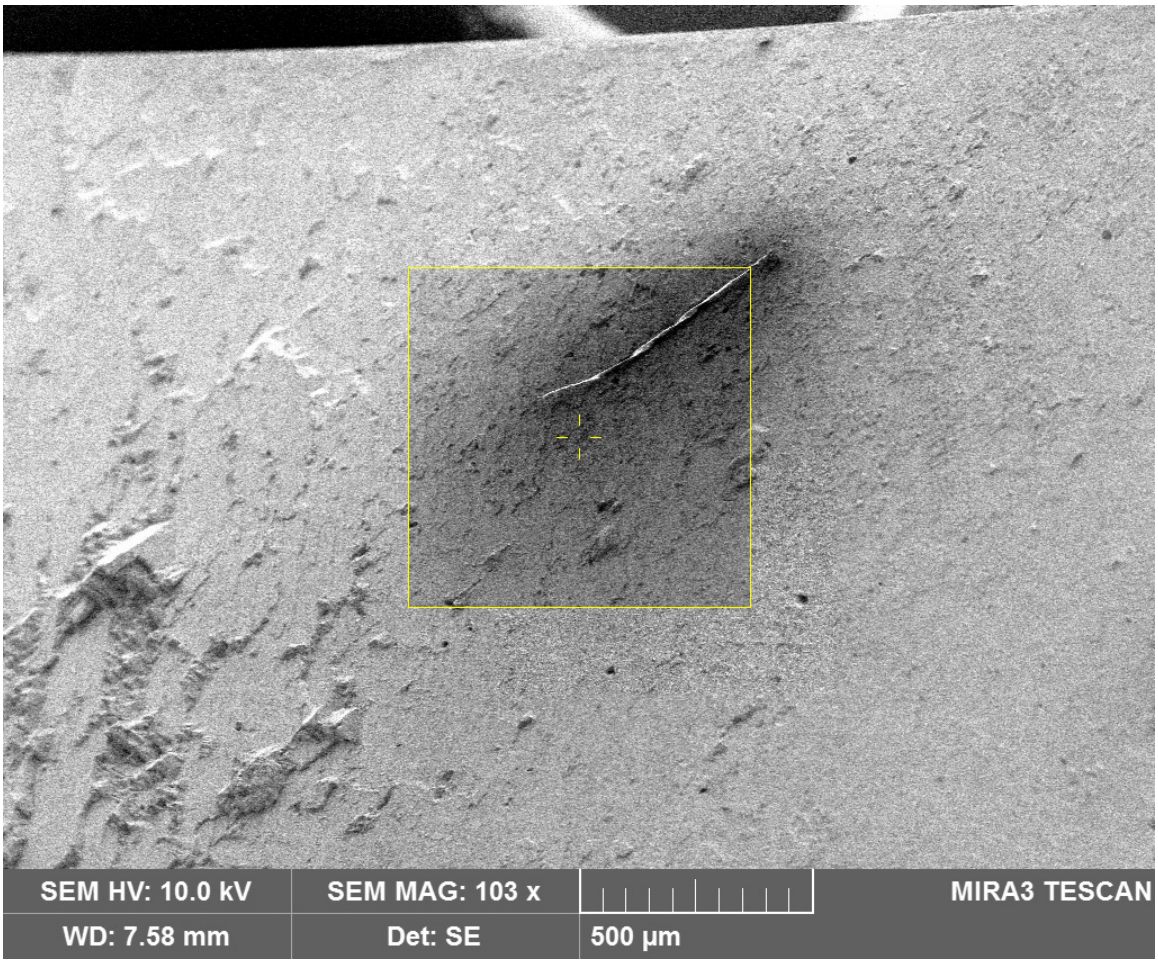

Figure 6.8: PWA1484 Fracture Surface Displaying Crystallographic Cracking at 1 Hz, 816°C and R=0.7, Crack Plane Determination Point 3

CHAPTER 7: CONCLUSIONS, RESEARCH SIGNIFICANCE AND RECOMMENDATIONS FOR FUTURE WORK

7.1: Conclusions

This research was conducted on PWA1484, a single crystal superalloy used by Pratt & Whitney for turbine blades. Initially, an isothermal constant amplitude fatigue crack growth rate database was developed, filling a void that currently exists in published literature. Through additional experimental testing, fractography, and modeling, the effects of temperature interactions, load interactions, oxidation and secondary crystallographic orientation on the fatigue crack growth rate and the underlying mechanisms responsible were determined. The conclusions from this work are as follows:

7.1.1: Isothermal Constant Amplitude Conclusions

- The effect of temperature on the crack growth rate becomes more pronounced as the crack driving force increases while the secondary orientation and R Ratio effects on the crack growth rate increase with increasing temperature.
- An R Ratio of 0.7 displays faster crack growth rates when compared to results at R=0.1.
- There was no significant effect on the crack growth rate due to aged microstructure for unstressed and stressed specimens at R Ratios of 0.1 and 0.7.
- The crack growth rate in an argon purged environment was almost identical to the rate seen in air. The fact that oxygen diffuses and reacts according to partial pressure not concentration appears to be responsible for these results.

7.1.2: Temperature Interaction Conclusions

- Number of alternating temperature cycles can determine whether retardation or acceleration is present. During alternating temperature cycling it was found that as the number of alternating temperature cycles increased, changes in the morphology (and hence deformation mode) caused changes in the environmental interactions thus demonstrating the sensitivity of the environmental interaction on the details of the deformation mode.
- During alternating temperature cycling it was shown that at a smaller number of alternating cycles, 649°C crack growth was accelerated due to crack tip embrittlement caused by 982°C cycling. At a larger number of alternating cycles the 649°C cycling quickly grew through the embrittled crack tip but then grew slower than expected due to γ' strengthening and the possible formation of Kear-Wilsdorf locks at 982°C.
- This transition from acceleration to retardation occurs between 10 and 20 alternating cycles for R = 0.1 and around 20 alternating cycles for R = 0.7 between temperatures of 649°C and 982°C.

7.1.3: Load Interaction Conclusions

- Overload interaction testing led to full crack retardation at 1.6x and 2.0x overloads for both 649°C and 816°C testing. The only growth seen during 1.6x and 2.0x overload testing was attributed to transient growth from the overload cycles.
- It was found that 1.3x overloads at 649°C and 816°C created retarded crack growth when compared with constant amplitude data at the same temperature. The crack growth during 1.3x overload testing at these two temperatures was found to be comprised of growth from both the 1.0x cycles and overload cycles.

- Load interaction testing showed that when the crack driving force is near K_{IC} the overload size greatly influences whether acceleration or retardation will occur at 982°C.

7.1.4: Semi-Realistic Spectrum Conclusions

- Semi-realistic spectrum testing demonstrated the extreme sensitivity that relative loading levels play on fatigue crack growth life. Under spectrum testing a 20% drop in load can lead to 5x the life.
- Life variability up to 40% was seen during spectrum testing for the same testing conditions. Probabilistic crack growth needs to be included in any spectrum life prediction models.
- The importance of dwell times in flight spectra were called into question. For the amount of time required the decrease in life was very minimal.

7.1.5: Crack Surface Morphology

- Two types of crack surface morphology were seen during fractography. The first is a precipitate avoidance (γ' avoidance) morphology that is rolling but still predominantly flat. In <001> primary oriented specimens this fracture mode tends to shift from cubic plane to cubic plane and the interdendritic region while staying mostly normal to the applied loads.
- The second mode is a form of cleavage (γ' shearing) and occurs predominantly on octahedral crystallographic planes.

7.1.6: Overall Conclusions

- Secondary orientation determination in single crystal superalloys can be determined with great success from secondary dendrite arm inspection.

- The effect of temperature on the crack growth rate becomes more pronounced as the crack driving force increases while the secondary orientation and R Ratio effects on the crack growth rate increase with increasing temperature.
- There is significant influence in changing temperature on resulting crack growth. This must be accounted for in any TMF crack growth life prediction model.
- There are significant load interaction (both retardation & accelerations) effects present in PWA1484 under TMF conditions. This also must be accounted for in TMF crack growth prediction models.
- A crack trajectory modeling approach using blade primary and secondary orientations was used to determine whether crack propagation will occur on crystallographic planes or normal to the applied load. Crack plane determination using a scanning electron microscope verified the crack trajectory modeling approach.

7.2: Research Significance

- The isothermal constant amplitude fatigue crack growth results fills a much needed void in currently available data.
- The temperature and load interaction fatigue crack growth results reveal the acceleration and retardation that is present in cracks growing in single crystal turbine blade materials under TMF conditions.
- This research provides a deeper understanding of the failure and deformation mechanisms responsible for crack growth during thermo-mechanical fatigue.
- Benefits of crack path trajectory modeling when a robust crack growth rate feature is added:
    - Will allow significant fidelity improvement in the input to designers of the next generation of single crystal gas turbine components.
    - Will play an integral role in rapid design iterations and the part/system optimization cycle.

- The realization of the cost efficiency through reduction in conservatism and weight savings.
- Enable engineers to evaluate interactions between different damage mechanisms resulting in design optimization.
- The allowance for a conditions based inspections and maintenance schedule.
- Enable "Retirement for Cause" to be used for critical turbine engine components, a drastic improvement over the standard "safe-life" calculations.
- Reduce the risk of catastrophic failure due to "chunk liberation" as a function of time.

- Provide an extensive building block for future research in this area such as time dependent deformation, i.e. creep and additional investigations into a local crack driving approach in single crystal superalloys.

7.3: Recommendations for Future Work

Since single crystal superalloys are highly anisotropic, both in an elastic and plastic sense, the applicability of conventional fracture mechanics approaches has been called into question. Stress based approaches thus far are limited to modifications of ΔK and as such are not totally appropriate when dealing with these materials. Global approaches on the other hand are more appropriate for orthotropic and isotropic materials but are difficult to incorporate into a crack growth life estimation model. The ideal route is to develop a "local approach" that can take into account anisotropy while taking into account planes of weakness and the normal and shear stresses on these planes. The crack path trajectory model focuses on the normal and shear stresses on the octahedral planes. An optimum way of combining these stresses was determined and can be used to calculate plans of weakness. In addition two crack surface morphologies have been

shown to correspond to two distinct mechanisms of crack advance which can be related to two fundamental dislocation/precipitate interactions; bypassing and shearing. Feeding this research into a Smith-Watson-Topper (SWT) and Fatemi-Socie parameter critical plane approach appears to be the optimal way to create a new crack force driving function in single crystals. SWT and the Fatemi-Socie parameter have shown great promise in the prediction of fatigue crack initiation life and can take into account mean stress effects and shear stress on critical planes. This new driving function could then be used to model crack growth in a way similar to how ΔK operates in isotropic materials.

Extensive fatigue crack growth rate testing, analysis and modeling were performed to add to the current body of knowledge for PWA1484. The results obtained from this study answered a lot of questions, yet much remains to be known to fully characterize the fatigue crack growth rate in PWA1484. The following recommendations, when coupled with the results from this study and existing literature, will greatly further the cause.

- Due to a limited number of specimens it was not possible to test at all desired temperatures, R ratios, and frequencies. Additional testing at frequencies between 1 and 20 Hz and at additional temperatures between 22°C and 649°C would be very beneficial to the PWA1484 isothermal constant amplitude fatigue crack growth rate database.
- Additional work should be performed looking into the PLC effect in PWA1484 to determine any detrimental effects on TMF crack growth rates.
- Performing single overload testing at additional overload ratios to pinpoint at what overload ratio acceleration begins and at which overload ratio full retardation initiates.

- Obtaining underload test data would be very beneficial for predicting flight spectrums.
- Creating 3D fracture surface maps that can be used to determine the average surface roughness would be very helpful for quantifying γ' avoidance and γ' shearing morphology changes.
- Testing performed in a vacuum would be very beneficial to separate the effect of environment from the fatigue crack growth rate.
- Develop plastic yield zone and crack closure approaches to predict FCGR for realistic TMF flight spectra.
- Additional work needs to be done to develop a "local approach" to the crack driving force in single crystal superalloys.

APPENDIX

A.1: Procedure for cold-mounting, grinding, polishing, and etching

Cold-mounting

1. Line plastic cup with release agent
2. Put paper cup on scale and zero scale
3. Add desired Epofix resin to paper cup
4. Multiply the mass of the resin by 3/25 (because its 25 parts resin, 3 parts hardener by mass) to determine required amount of hardener
5. Zero scale again and add calculated mass of Epofix hardener
6. Stir for a few minutes in paper cup and remove big air bubbles
7. Put specimen (and specimen holder clips if necessary) and add mount
8. Allow to harden for 12-24 hours

Grinding/Polishing

Step	Preparation Disc (Material)	Force (N)	Speed (RPM)	Suspension	Lubricant	Time (min)
Course Grind	320 AD (SiC)	30	150	None	Water	3+
Fine Grind I	1200 AD (SiC)	25	150	None	Water	5
Fine Grind II	4000 AD (SiC)	25	150	None	Water	5
Course Polish	MD Mol (Woven wool)	20	150	DiaPro Mol	None	8
Fine Polish	MD Chem-OP-S (Porous synthetic)	15	150	OP-S Suspension	None	2

** Thoroughly clean machine and the samples between each of the last 4 step!!!!!!
** If the polishing machine squeaks, put something nonmetallic (ex. folded up kimwipes) in between the sample and the force applicator or turn down the force

Etching

1.) Add 2 g of $CuCl_2$ to an empty beaker
2.) In the fume hood, add 40 mL of Ethanol
3.) Put on some gloves and add 40 mL of HCl
4.) Stir well
5.) Submerge specimen in etchant for 35-40 sec
6.) Immediately submerge in a beaker of water
7.) Rinse specimen with water and ethanol as necessary

A.2: Initial TMF Test Rig Startup Tasks

Water		Turn on induction heater's water supply (approx. 2 turns)
		Turn on water-cooled hydraulic grips' water supply (1.5 turns)
Open Station Manager		Start Station Manager program on TestStar IIs Computer
		Choose TMF-1.cfg configuration file
Turn On Hydraulics		Clear Interlock 1 by resetting it
		Power up HPS 1 to Power Low, then Power High
		Power up HSM 1 to Power Low, then Power High
Mount Specimen		Insert specimen so that it is properly positioned
		Manual Ctrl to Displacement, Enable Manual Control
		Move lower grip up (turn dial CCW) so top of specimen between top grip
		Make sure specimen aligned, Close lower grips on bottom of specimen
		Move lower grip up (turn dial CCW) so notch centered in coil gap
		Disable Manual Control, Auto Offset Force, Manual Ctrl to Force
		Enable Manual Control, Close upper grips on top of specimen
		Apply approx. 20lbf of tensile force (turn dial CW)
		Disable Manual Control
		Reposition induction heater heat station to center specimen in coil
Position Questar Microscope		Turn on light source and position so shining through coil gap from the side
		Toggle eye piece bypass switch to up (Enable eye piece use)
		Center notch tip in Questar view using positioning knobs and focus
		Toggle eye piece bypass switch to right (Disable eye piece use)
Questar RMS and Video Acquisition Startup		Switch on Power to RMS II system (two switches need to be turned on)
		Turn on surgeprotector to power up Video Processor and Questar Computer
		Open up RMS software on Questar Computer
		Open up Motion Platform and Encoder Position Windows
		Open Windows Movie Maker
		Click on Capture from video device, found under Capture Video heading
		New window will open up, Verify Dazzle DVC100 Video Device is selected
		Set video input source as Composite, Click Next to move forward
		Enter file name for video file, Choose Location to save file, Click Next
		Select Best Quality for Playback (default recommended setting), Click Next
		Use Video Processor and Motion Platform to enhance image in Preview
		Reposition light source to shine down through top of coils at incidence angle
		Use Video Processor and Motion Platform to enhance image again
Heating System Startup		Plug in power cord for temperature controller into 120Vac wall outlet
		Turn on power to heater by flipping power lever located on rear panel
		From now on, Do NOT touch coil or specimen until heater is turned off

[175]

A.3: TMF Test Procedure Setup and Initialization

MPT and Procedure Editor		Open MPT within Station Manager
		Open Procedure Editor within MPT
		When prompted, select procedure to run or create a new procedure to run
Specimen Selection		Back in MPT, select a previously created specimen -OR- choose to create new one
		In new window, select "Currently Loaded Procedure" and "Saved State: Reset"
Data File Setup		Toggle "Lock" icon back to Edit Mode ("lock" icon now displays open lock)
		Option 1: Erase "old" data file created in specimen folder: C:\tsiis\mpt\Specimens\<Selected Specimen Name>
		Option 2: In Data Acquisition Process for Procedure, change user data file name in Destination Tab to reflect new test
		Retoggle "Lock" icon back to Execute Mode
Start Test		Open any Scopes or Meters to display test data during test, setup as desired
		Position vertical crosshair of Questar image at notch/crack tip, zero Encoder Position
		Hit "Start" button on induction heater power supply front panel
		Simultaneously, Click "Program Run" in MPT on TestStar computer and "Start Capture" in Windows Movie Maker on Questar computer
		Readjust focus of Questar and image setting on Video Processor if needed
Acquire Data		For cyclic load tests: move vertical crosshair ahead of notch/crack 5mils, record cycle count for when crack reaches crosshair, then repeat
		For flight profile tests: at conclusion of every flight cycle, move vertical crosshair to crack tip, record Encoder Position values, then repeat

[175]

A.4: TMF Test Rig Shutdown Procedure

Shutdown		Click "Program Stop" in MPT on TestStar computer
		Click "Stop Capture" in Windows Movie Maker on Questar Computer
Remove Heating and Load with Function Generator		Go to Function Generator mode in Station Manager
		Select TempControl channel, setpoint & amplitude to 0.00V
		Click "Program Run," wait 5 seconds, click "Program Stop"
		Select Channel 1 channel & Force control mode, setpoint to 10lbf & amplitude to 0lbf
		Click "Program Run," wait 5 seconds, click "Program Stop"
Questar Microscope and Accessories Shutdown		Confirm video was captured and saved of the test on the Questar computer
		Close Windows Movie Maker on Questar computer
		Close Questar RMS II software on Questar computer
		Save any collected data and captured video from the Questar computer to an external hard drive
		Shut down Questar computer and power off the surge protector for the system
		Turn off power switches (two of them) for the Questar microscope RMS platform
		Turn off the light source
Turn off Heating		Turn off power switch for induction heater located on rear panel
		Unplug temperature controller once specimen temperature reaches approx. 100F
Remove Specimen from Grips		Manual Ctrl to Force, Enable Manual Control
		Lower load to a 5lbf tensile load by moving lower grip up (turn dial CCW)
		Disable Manual Control, Manual Ctrl to Displacement
		Open upper grips (turn lever CCW), Enable Manual Control
		Lower bottom grips to lowest level (turn dial CW), Disable Manual Control
		Open lower grips (turn lever CCW)
		Remove specimen from test frame
Shutdown Station Manager/ Retrieve Data		Power down HSM 1 to Power Low, then Power Off
		Power down HPS 1 to Power Low, then Power Off
		Close Station Manager
		Open folder: C:\tsiis\mpt\Specimens\<Selected Specimen Name>
		Save data file(s) saved there by Data Acquisition process(es) to a floppy
Water Off		Turn off induction heater's water supply
		Turn off water-cooled hydraulic grips' water supply

[175]

A.5: Semi-Realistic Spectrum #1 Loads and Temperatures

Running Time (seconds)	Min Load (N)	Max Load (N)	Temperature (°C)
1	2780	5004	532
300	2780	5004	532
301	2558	2780	552
600	2558	2780	552
601	2780	5004	582
900	2780	5004	582
901	2780	5004	612
1150	2780	5004	612
1151	2780	11121	982
1400	2780	11121	982
1401	8340	8340	982
1650	8340	8340	982
1651	7006	7228	982
2300	7006	7228	982
2301	6672	8340	982
2500	6672	8340	982
2501	6672	7228	982
2700	6672	7228	982
2701	7006	7228	982
2750	7006	7228	982
2751	5004	8896	972
2850	5004	8896	972
2851	5004	8896	962
2950	5004	8896	962
2951	5004	8896	952
3050	5004	8896	952
3051	5004	8896	942
3150	5004	8896	942
3151	8674	8896	932
3200	8674	8896	932
3201	5004	8896	922
3300	5004	8896	922
3301	8674	8896	912
3325	8674	8896	912
3326	5004	8896	902
3425	5004	8896	902
3426	8674	8896	892
3475	8674	8896	892

3476	4782	5004	882
3525	4782	5004	882
3526	5004	8896	872
3625	5004	8896	872
3626	8674	8896	852
3975	8674	8896	852
3976	5004	7228	842
4075	5004	7228	842
4076	7006	7228	832
4425	7006	7228	832
4426	7228	8896	982
4625	7228	8896	982
4626	7006	7228	882
5125	7006	7228	882
5126	7228	8896	932
5225	7228	8896	932
5226	8674	8896	982
5425	8674	8896	982
5426	8896	11121	982
5450	8896	11121	982
5451	7006	7228	782
6450	7006	7228	782
6451	2780	6672	632
6550	2780	6672	632
6551	6450	6672	982
7050	6450	6672	982
7150	6672	7228	982
7151	7006	7228	932
7200	7006	7228	932
7201	7228	8896	782
7225	7228	8896	782
7226	2780	8896	682
7275	2780	8896	682

A.6: Semi-Realistic Spectrum #2 Loads and Temperatures

Running Time (seconds)	Min Load (N)	Max Load (N)	Temperature (°C)
1	1334	13345	482.22
2	5560	5560	482.57
700	5560	5560	943.47
701	1334	13345	951.19
702	1334	13345	958.91
703	1334	13345	966.63
704	1334	1334	974.35
705	2313	23131	982.22
706	2313	23131	982.22
707	17793	17793	982.22
1054	17793	17793	982.22
1055	14457	14457	982.22
2204	14457	14457	982.22
2205	15569	22241	982.22
2206	15569	22241	982.14
2207	15569	22241	982.05
2208	15569	22241	981.97
2209	15569	22241	981.88
2210	15569	22241	981.79
2211	17793	17793	981.71
3362	17793	17793	883.05
3363	15569	22241	882.97
3364	15569	22241	882.88
3365	14457	14457	882.79
4867	14457	14457	902.83
4868	17793	17793	903.02
5216	17793	17793	948.02
5217	15569	23131	947.78
5218	15569	23131	947.78
5219	15569	23131	947.53
5220	14457	14457	947.29
6168	14457	14457	715.56
6169	1957	19572	715.56
6170	1957	19572	715.84
6171	13345	13345	716.12
7019	13345	13345	954.15
7020	14457	14457	954.43
7269	14457	14457	482.22

7270	1957	19572	478.89
7271	1957	19572	475.56

A.7: Semi-Realistic Spectrum #3 Loads and Temperatures

Running Time (seconds)	Min Load (N)	Max Load (N)	Temperature (°C)
1	1334	13345	482.22
2	1334	1334	510.00
13	1334	1334	815.56
14	1334	13345	843.33
15	1334	13345	871.11
16	1334	13345	898.89
17	1334	1334	926.67
23	1334	1334	982.22
24	2313	23131	982.22
25	2313	23131	982.22
26	15569	15569	982.22
30	15569	15569	965.56
31	15569	22241	960.00
32	15569	22241	954.44
33	15569	22241	948.89
34	15569	22241	943.33
35	15569	22241	937.78
36	15569	22241	932.22
37	15569	15569	926.67
53	15569	15569	837.78
54	15569	22241	832.22
55	15569	22241	860.00
56	15569	15569	887.78
66	15569	15569	948.89
67	15569	22241	943.33
68	15569	22241	937.78
69	15569	22241	932.22
70	15569	15569	926.67
107	15569	15569	721.11
108	1957	19572	715.56
109	1957	19572	715.56
110	1957	1957	743.33
127	1957	1957	948.89
128	1957	19572	943.33
129	1957	19572	937.78
130	1468	1468	932.22
211	1468	1468	482.22

REFERENCES

1. Rolls-Royce Ltd, *The Jet Engine*. 1996: Rolls-Royce.

2. Moran, M.J. and Shapiro, H.N., *Fundamentals of engineering thermodynamics*. 2000, New York: Wiley.

3. *Airplane Flying Handbook.* U.S. Department of Transportation, Federal Aviation Administation - Flight Standards Service, 2004. **FAA-H-8083-3A**.

4. Suresh, S., *Fatigue of materials*. 1998, Cambridge; New York: Cambridge University Press.

5. Blyth, N.R., *Examination of a Failed CFM56-3C-1 Turbofan Engine - Boeing 737-476, VH-TJN.* Technical Analysis Report 3/01 (Reference BE/200000023) (Canberra, Australia: The Australian Transport Safety Bureau), 2001.

6. Rosenker, M.V., *Safety recommendation, NTSB report on Los Angeles engine failure, safety recommendation.* 2006. **60-06 60-64**.

7. *Uncontained engine failure and air turn-back near San Francisco Airport, USA, 30 August 2010.* Australian Transport Safety Bureau, 2012.

8. Vardar, N. and Ekerim, A., *Failure analysis of gas turbine blades in a thermal power plant.* Engineering Failure Analysis, 2007. **14**(4): p. 743-749.

9. Barella, S., Boniardi, M., Cincera, S., Pellin, P., Degive, X., and Gijbels, S., *Failure analysis of a third stage gas turbine blade.* Engineering Failure Analysis, 2011. **18**(1): p. 386-393.

10. Smith, C.O. *Frank Whittle and the jet engine*. in *Proceedings of the 1995 ASME Design Engineering Technical Conference, September 17, 1995 - September 20, 1995*. 1995. Boston, MA, USA: ASME.

11. Reed, R.C., *The superalloys : fundamentals and applications*. 2008, Cambridge: Cambridge University Press. xv, 372 p.

12. Hartmann, I., Nagy, J., and Jacobson, M., *Explosive characteristics of titanium, zirconium, thorium, uranium and their hydrides*. 1951, United States Bureau of Mines: Washington, DC, United States. p. 16.

13. Smith, R.J., Lewis, G.J., and Yates, D.H., *Development and application of nickel alloys in aerospace engineering.* Aircraft Engineering and Aerospace Technology, 2001. **73**(2): p. 138-146.

14. Schulz, U., Leyens, C., Fritscher, K., Peters, M., Saruhan-Brings, B., Lavigne, O., Dorvaux, J.-M., Poulain, M., Mevrel, R., and Caliez, M., *Some recent trends in research and technology of advanced thermal barrier coatings.* Aerospace Science and Technology, 2003. **7**: p. 73-80.

15. Piearcey, B.J. and Versnyder, F.L., *Breakthrough in making turbine components.* Metal Progress, 1966. **90**(5): p. 66-71.

16. Strangman, T.E., Hoppin Iii, G.S., Phipps, C.M., Harris, K., and Schwer, R.E. *DEVELOPMENT OF EXOTHERMICALLY CAST SINGLE-CRYSTAL MAR-M 247 AND DERIVATIVE ALLOYS*. in *Superalloys 1980, Proceedings of the 4th International Symposium on Superalloys.* 1980. Champion, PA, USA: ASM.

17. DeLuca, D. and Annis, C., *Fatigue in Single Crystal Nickel Superalloys.* Office of Naval Research, Department of the Navy FR23800, August 1995.

18. Abe, F., Araki, H., Yoshida, H., and Okada, M., *ROLE OF ALUMINUM AND TITANIUM ON THE OXIDATION PROCESS OF A NICKEL-BASE SUPERALLOY IN STEAM AT 800°C.* Oxidation of Metals, 1987. **27**(1-2): p. 21-36.

19. Faber, G.H., *ROLE OF CHROMIUM IN CORROSION AND OXIDATION RESISTANT ALLOYS AND COATINGS.* 1978: p. 225-230.

20. Erickson, G.L. *Ni-based superalloy developments*. in *Proceedings from the Conference on Critical Issues in the Development of High Temperature Structural Materials, March 7, 1993 - March 14, 1993*. 1993. Kona, HI, USA: Publ by Minerals, Metals & Materials Soc (TMS).

21. Bondarenko, Y.A., Kablov, E.N., Surova, V.A., and Echin, A.B., *Effect of high-gradient directed crystallization on the structure and properties of rhenium-bearing single-crystal alloy.* Metal Science and Heat Treatment, 2006. **48**: p. 360-363.

22. Sims, C.T., *NICKEL ALLOYS. THE HEART OF GAS TURBINE ENGINES.* 1970.

23. Durand-Charre, M., *The microstructure of superalloys*. 1997. 170.

24. Morrissey, R.J., John, R., and John Porter Iii, W., *Fatigue variability of a single crystal superalloy at elevated temperature.* International Journal of Fatigue, 2009. **31**(11-12): p. 1758-1763.

25. Jackson, M.P.R.R.C., *Heat treatment of UDIMET 720Li: the effect of microstructure on properties.* Materials Science and Engineering: A Materials Science and Engineering: A, 1999. **259**(1): p. 85-97.

26. Yang, C., Liu, L., Zhao, X., Li, Y., Zhang, J., and Fu, H., *Dendrite morphology and evolution mechanism of nickel-based single crystal superalloys grown along*

the <001> and <011> orientations. Progress in Natural Science: Materials International, 2012. **22**(5): p. 407-413.

27. Yizhou, Z., *Formation of stray grains during directional solidification of a nickel-based superalloy.* Scripta Materialia, 2011. **65**(4): p. 281-4.

28. Cetel, A. and Duhl, D., *Second generation nickel-base single crystal superalloy.* A. D. Cetel, D. N. Duhl, Superalloys 1988, 1988: p. 235-244.

29. Wright, D.C. and Smith, D.J., *Forging of blades for gas turbines.* Materials Science and Technology, 1986. **2**(7): p. 742-747.

30. Whittaker, G.A., *Precision casting of aero gas turbine components.* Materials Science and Technology, 1986. **2**(5): p. 436-441.

31. McLean, M. and Metals, S., *Directionally solidified materials for hightemperature service*. 1983, London: Metals Society.

32. Beeley, P.R., Smart, R.F., and Institute of, M., *Investment casting*. 2008, Leeds, UK: Maney Publishing.

33. Arakere, N.K., *High-Temperature Fatigue Properties of Single Crystal Superalloys in Air and Hydrogen.* Journal of Engineering for Gas Turbines and Power, 2004. **126**(3): p. 590.

34. Nathal, M.V. *NASA and superalloys: A customer, a participant, and a referee*. in *11th International Symposium on Superalloys, Superalloys 2008, September 14, 2008 - September 18, 2008*. 2008. Champion, PA, United states: Minerals, Metals and Materials Society.

35. Kear, B.H. and Wilsdorf, H.G.F., *Dislocation configurations in plastically deformed polycrystalline Cu3Au alloys.* Metallurgical Society of American Institute of Mining, Metallurgical and Petroleum Engineers -- Transactions, 1962. **224**(2): p. 382-386.

36. de Bussac, A., Webb, G., and Antolovich, S.D., *Model for the strain-rate dependence of yielding in Ni3Al alloys.* Metallurgical transactions. A, Physical metallurgy and materials science, 1991. **22 A**(1): p. 125-128.

37. Shah, D.M. and Duhl, D.N., *The effect of orientation, temperature, and gamma prime size on the yield strength of a single crystal nickel base superalloy.* Superalloys 1984, Edited by M. Gell et al., TMS-AIME, Warrandale, PA., 1984, 1984.

38. Bettge, D. and Oesterle, W., *`Cube slip' in near-[111] oriented specimens of a single-crystal nickel-base superalloy.* Scripta Materialia, 1999. **40**: p. 389-395.

39. Milligan, W.W. and Antolovich, S.D., *YIELDING AND DEFORMATION BEHAVIOR OF THE SINGLE CRYSTAL SUPERALLOY PWA 1480.* Metallurgical transactions. A, Physical metallurgy and materials science, 1987. **18 A**(1): p. 85-95.

40. Arakere, N.K. and Swanson, G., *Effect of Crystal Orientation on Fatigue Failure of Single Crystal Nickel Base Turbine Blade Superalloys.* Journal of Engineering for Gas Turbines and Power, 2002. **124**(1): p. 161.

41. MacKay, R. and Maier, R., *The influence of orientation on the stress rupture properties of nickel-base superalloy single crystals.* Metallurgical and Materials Transactions A, 1982. **13**(10): p. 1747-1754.

42. Bannantine, J., Comer, J., and Handrock, J., *Fundamentals of Metal Fatigue Analysis*. 1990: Prentice Hall.

43. Wöhler, A., *Uber die Festigkeitsversuche mit Eisen und Stahl*. Vol. 20. 1870, Berlin: Ernst & Korn.

44. Wöhler, A., *Versuche über die Festigkeit der Eisenbahnwagenachsen.* Zeitschrift für Bauwesen, 1860. **10**: p. 160-161.

45. Coffin, L.F.J., *A STUDY OF THE EFFECTS OF CYCLIC THERMAL STRESSES ON A DUCTILE METAL.* Transactions of ASME, 1953. **76**: p. 931-950.

46. Manson, S.S., *BEHAVIOR OF MATERIALS UNDER CONDITIONS OF THERMAL STRESS*, in *Heat Transfer Symposium*. 1953: Unniversity of Michigan Engineering Research Institute. p. 9-75.

47. Romanoski, G.R., Antolovich, S.D., and Pelloux, R.M. *MODEL FOR LIFE PREDICTIONS OF NICKEL-BASE SUPERALLOYS IN HIGH-TEMPERATURE LOW CYCLE FATIGUE*. in *ASTM Spec Tech Publ 942, Low Cycle Fatigue, a Symp, September 30, 1987 - September 30, 1987*. 1987. Bolton Landing, NY, USA: ASTM.

48. Liaw, P.K., Saxena, A., and Perrin, J., *Life extension technology for steam pipe systems-I. Development of materials properties.* Engineering Fracture Mechanics, 1993. **45**(Copyright 1993, IEE): p. 759-86.

49. Domas, P.A. and Antolovich, S.D., *MECHANISTICALLY BASED MODEL FOR HIGH TEMPERATURE NOTCHED LCF OF RENE 80.* Engineering Fracture Mechanics, 1985. **21**(1): p. 203-214.

50. Boyer, H.E., *Atlas of fatigue curves*. 1986. 535.

51. Griffith, A.A., *The Phenomena of Rupture and Flow in Solids.* Philosophical Transactions of the Royal Society of London. Series A, Containing Papers of a Mathematical or Physical Character, 1921. **221**(582-593): p. 163-198.

52. Irwin, G.R., *Fracture Dynamics.* Fracturing of Metals, American Society for Metals, Cleveland, OH, 1948: p. 147-166.

53. Orowan, E., *Fracture and strength of solids.* Reports on Progress in Physics, 1949. **12**(1): p. 185.

54. Irwin, G.R., *Analysis of stresses and strains near the end of a crack traversing a plate.* Journal of Applied Mechanics, 1957. **24**: p. 361-364.

55. Tada, H., *The stress analysis of cracks handbook*. 3rd ed. ed, ed. P.C. Paris and G.R. Irwin. 2000, New York :: ASME Press.

56. Anderson, T.L., *Fracture mechanics : fundamentals and applications*. 3rd ed. ed. 2005, Boca Raton, FL :: Taylor & Francis.

57. Paris, P.C., Gomez, M.P., and Anderson, W.E., *A rational analytic theory of fatigue.* The Trend in Engineering, 1961. **1961**(13): p. 9-14.

58. Paris, P.C. and Erdogen, F., *A critical analysis of crack propagation la.* 1963(84.5): p. 528-534.

59. Walker, K., *The Effect of Stress Ratio during Crack Propagation and Fatigue for 2024-T3 and 7075-T6 Aluminum.* Effects of Environment and Complex Load History on Life, ASTM STP 462, American Society for Testing and Materials, 1970: p. 1.

60. Forman, R.G., Kearney, V.E., and Engle, R.M., *Numerical analysis of crack propagation in cyclic-loaded structures.* Transactions of the ASME. Series D, Journal of Basic Engineering, 1967. **89**(3): p. 459-464.

61. Beden, S.M., Abdullah, S., and Ariffin, A.K., *Review of Fatigue Crack Propagation Models for Metallic Components.* European Journal of Scientific Research, 2009. **28**(3): p. 364-397.

62. Rice, J.R., *TENSILE CRACK TIP FIELDS IN ELASTIC-IDEALLY PLASTIC CRYSTALS.* Mechanics of Materials, 1987. **6**(4): p. 317-335.

63. Rice, J.R. and Saeedvafa, M., *Crack tip singular fields in ductile crystals with Taylor power-law hardening. I. Anti-plane shear.* Journal of the Mechanics and Physics of Solids, 1988. **36**(2): p. 189-214.

64. Saeedvafa, M. and Rice, J.R., *Crack tip singular fields in ductile crystals with Taylor power-law hardening. II. Plane strain.* Journal of the Mechanics and Physics of Solids, 1989. **37**(6): p. 673-91.

65. Rice, J.R., Hawk, D.E., and Asaro, R.J., *Crack tip fields in ductile crystals.* International Journal of Fracture, 1990. **42**(4): p. 301-321.

66. Saeedvafa, M. and Rice, J.R., *Crack tip fields in a material with three independent slip systems: NiAl single crystal.* Modelling and Simulation in Materials Science and Engineering, 1992. **1**(1): p. 53-71.

67. Marchal, N., Flouriot, S., Forest, S., and Remy, L., *Crack-tip stress-strain fields in single crystal nickel-base superalloys at high temperature under cyclic loading.* Computational Materials Science, 2006. **37**(1-2): p. 42-50.

68. Haigh, J.R. and Skelton, R.P., *STRAIN INTENSITY APPROACH TO HIGH TEMPERATURE FATIGUE CRACK GROWTH AND FAILURE.* 1978. **36**(1): p. 133-137.

69. Shield, T.W., *Experimental study of the plastic strain fields near a notch tip in a copper single crystal during loading.* Acta Materialia, 1996. **44**(4): p. 1547-1561.

70. Schulson, E.M. and Xu, Y. *Notch-tip deformation of Ni3Al single crystals*. in *Proceedings of the 1996 MRS Fall Meeting, December 2, 1996 - December 5, 1996*. 1997. Boston, MA, USA: Materials Research Society.

71. Crone, W.C. and Shield, T.W., *Experimental study of the deformation near a notch tip in copper and copper-beryllium single crystals.* Journal of the Mechanics and Physics of Solids, 2001. **49**(12): p. 2819-2838.

72. Li, X.M., Chiang, F.P., Wu, J., and Dudley, M., *Experimental measurement of the crack tip strain field in a single crystal.* Engineering Fracture Mechanics, 1992. **43**(2): p. 171-184.

73. Shield, T.W. and Kim, K.S., *Experimental measurement of the near tip strain field in an iron-silicon single crystal.* Journal of the Mechanics and Physics of Solids, 1994. **42**(5): p. 845-873.

74. Arakere, N.K., Siddiqui, S., Magnan, S., Ebrahimi, F., and Forero, L.E., *Investigation of Three-Dimensional Stress Fields and Slip Systems for fcc Single-Crystal Superalloy Notched Specimens.* Journal of Engineering for Gas Turbines and Power, 2005. **127**(3): p. 629.

75. Sabnis, P.A., Maziere, M., Forest, S., Arakere, N.K., and Ebrahimi, F., *Effect of secondary orientation on notch-tip plasticity in superalloy single crystals.* International Journal of Plasticity, 2012. **28**(1): p. 102-123.

76. Arakere, N.K., Siddiqui, S., and Ebrahimi, F., *Evolution of plasticity in notched Ni-base superalloy single crystals.* International Journal of Solids and Structures, 2009. **46**(16): p. 3027-3044.

77. Naik, R.A., DeLuca, D.P., and Shah, D.M., *Critical plane fatigue modeling and characterization of single Crystal nickel Superalloys.* Transactions of the ASME. Journal of Engineering for Gas Turbines and Power, 2004. **126**(2): p. 391-400.

78. Fernandez-Zelaia, P., *THERMOMECHANICAL FATIGUE CRACK FORMATION IN NICKEL-BASE SUPERALLOYS AT NOTCHES*. 2012, Georgia Institute of Technology: Atlanta, GA.

79. Antolovich, B.F., Saxena, A., and Antolovich, S.D., *Fatigue crack propagation in single-crystal CMSX-2 at elevated temperature.* Journal of Materials Engineering and Performance, 1993. **2**(4): p. 489-496.

80. Antolovich, B.F., Saxena, A., and Antolovich, S.D., *Fatigue crack propagation in single-crystal CMSX- 2 at elevated temperature.* Journal of Materials Engineering and Performance, 1993. **2**(4): p. 489-495.

81. Boyd-Lee, A.D., Harrison, G.F., and Henderson, M.B., *Evaluation of standard life assessment procedures and life extension methodologies for fracture-critical components.* International Journal of Fatigue, 2001. **23**: p. S11-S19.

82. Goswami, T.K. and Harrison, G.F., *GAS-TURBINE DISK LIFTING PHILOSOPHIES - A REVIEW.* International Journal of Turbo & Jet-Engines, 1995. **12**(1): p. 59-77.

83. Claudio, R.A., Branco, C.M., Gomes, E.C., Byrne, J., Harrison, G.F., and Winstone, M.R., *Fatigue life prediction and failure analysis of a gas turbine disc using the finite-element method.* Fatigue and Fracture of Engineering Materials and Structures, 2004. **27**: p. 849-860.

84. Cowie, W.D., *TURBINE ENGINE STRUCTURAL INTEGRITY PROGRAM (ENSIP).* Journal of Aircraft, 1975. **12**: p. 366-369.

85. Johnson, W.S., *The history, logic and uses of the Equivalent Initial Flaw Size approach to total fatigue life prediction.* Procedia Engineering, 2010. **2**(1): p. 47-58.

86. DeLuca, D. and Cowles, B., *The fatigue and fracture of turbine blade alloys in high-pressure hydrogen.* JOM Journal of the Minerals, Metals and Materials Society, 1996. **48**(11): p. 61-64.

87. Telesman, J. and Ghosn, L.J. *Fatigue crack growth behavior of PWA 1484 single crystal superalloy at elevated temperatures*. in *Proceedings of the International Gas Turbine and Aeroengine Congress and Exposition, June 5, 1995 - June 8, 1995*. 1995. Houston, TX, USA: ASME.

88. Antolovich, S.D. and Antolovich, B.F., *The Effects of Microstructure, Deformation Mode and Environment on Fatigue* in *Fracture of Nano and Engineering Materials and Structures*, E.E. Gdoutos, Editor. 2006, Springer Netherlands. p. 1245-1246.

89. Arakere, N.K. and Moroso, J., *Fatigue failure in high-temperature single crystal superalloy turbine blades.* High Temperature Materials and Processes, 2001. **20**: p. 117-136.

90. Cunningham, S.E., DeLuca, D.P., and Haake, F.K., *crack growth and life prediction in single-crystal nickel superalloys Volume 2.* Wright Laboratory WL-TR-99-4048, August 1994.

91. Cunningham, S.E., DeLuca, D.P., and Haake, F.K., *crack growth and life prediction in single-crystal nickel superalloys Volume 1.* Wright Laboratory WL-TR-94-4089, February 1996.

92. Chan, K.S. and Cruse, T.A., *STRESS INTENSITY FACTORS FOR ANISOTROPIC COMPACT-TENSION SPECIMENS WITH INCLINED CRACKS.* Engineering Fracture Mechanics, 1986. **23**(5): p. 863-874.

93. Telesman, J. and Ghosn, L.J., *Unusual near-threshold FCG behavior of a single crystal superalloy and the resolved shear stress as the crack driving force.* Engineering Fracture Mechanics, 1989. **34**: p. 1183-1196.

94. Crompton, J.S. and Martin, J.W., *CRACK GROWTH IN A SINGLE CRYSTAL SUPERALLOY AT ELEVATED TEMPERATURE.* Metallurgical transactions. A, Physical metallurgy and materials science, 1984. **15 A**(9): p. 1711-1719.

95. Telesman, J. and Ghosn, L.J., *Crack growth and life prediction in single-crystal nickel superalloys.* Wright Laboratory WL-TR-99-4090, 1996. **3**.

96. Wen, Z. and Yue, Z., *Fracture behaviour of the compact tension specimens of nickel-based single crystal superalloys at high temperatures.* Materials Science and Engineering: A, 2007. **456**(1-2): p. 189-201.

97. Chan, K.S. and Leverant, G.R., *ELEVATED-TEMPERATURE FATIGUE CRACK GROWTH BEHAVIOR OF MAR-M200 SINGLE CRYSTALS.* Metallurgical transactions. A, Physical metallurgy and materials science, 1987. **18 A**(4): p. 593-602.

98. Chen, Q. and Liu, H.W., *Resolved shear stress intensity coefficient and fatigue crack growth in large crystals.* Theoretical and Applied Fracture Mechanics, 1988. **10**(2): p. 111-122.

99. Peach, M. and Koehler, J.S., *The forces exerted on dislocations and the stress fields produced by them.* Physical Review, 1950. **80**: p. 436-439.

100. Lerch, B.A. and Antolovich, S.D., *Fatigue crack propagation behavior of a single crystalline superalloy.* Metallurgical transactions. A, Physical metallurgy and materials science, 1990. **21 A**: p. 2169-2177.

101. Preuss, M., da Fonseca, J.Q., Grant, B., Knoche, E., Moat, R., and Daymond, M. *The effect of ' particle size on the deformation mechanism in an advanced polycrystalline nickel-base superalloy*. in *Superalloys 2008. Eleventh International Symposium on Superalloys, 14-18 Sept. 2008*. 2008. Warrendale, PA, USA: Minerals, Metals & Materials Society.

102. Wusatowska-Sarnek, A.M., Blackburn, M.J., and Aindow, M., *γ' Precipitation Kinetics in P/M IN100.* Materials Science Forum, 2003. **426-432**: p. 767-772.

103. Antolovich, S.D. and Jayaraman, N. *The effect of microstructure on the fatigue behavior of Ni base superalloys*. in *Fatigue. Environment and Temperature Effects. Proceedings of the 27th Sagamore Army Materials Research Conference, 14-18 July 1980*. 1983. New York, NY, USA: Plenum.

104. Antolovich, S.D. and Jayaraman, N., *Effects of environment and structural stability on the low cycle fatigue behaviour of nickel-base superalloys.* High Temperature Technology, 1984. **2**(Copyright 1984, IEE): p. 3-13.

105. Lerch, B.A., Jayaraman, N., and Antolovich, S.D., *A study of fatigue damage mechanisms in Waspaloy from 25 to 800C.* Material Science and Engineering, 1984. **66**(Copyright 1985, IEE): p. 151-66.

106. Bowman, R. and Antolovich, S.D., *EFFECT OF MELT SPINNING ON THE MICROSTRUCTURE AND MECHANICAL PROPERTIES OF THREE Ni-BASE SUPERALLOYS.* Metallurgical transactions. A, Physical metallurgy and materials science, 1988. **19 A**: p. 93-103.

107. Boyd-Lee, A.D., *Fatigue crack growth resistant microstructures in polycrystalline Ni-base superalloys for aeroengines.* International Journal of Fatigue, 1999. **21**: p. 393-405.

108. Gayda, J. and Miner, R.V., *FATIGUE CRACK INITIATION AND PROPAGATION IN SEVERAL NICKEL-BASE SUPERALLOYS AT 650°C.* International Journal of Fatigue, 1983. **5**: p. 135-143.

109. Telesman, J., Gabb, T.P., Garg, A., Bonacuse, P., and Gayda, J. *Effect of microstructure on time dependent fatigue crack growth behavior in a P/M turbine disk alloy*. in *Superalloys 2008. Eleventh International Symposium on Superalloys, 14-18 Sept. 2008*. 2008. Warrendale, PA, USA: Minerals, Metals & Materials Society.

110. Gabb, T.P., Telesman, J., Kantzos, P.T., and Garg, A., *Effects of Temperature on Failure Modes for a Nickel-Base Disk Superalloy.* Journal of Failure Analysis and Prevention, 2007. **7**(1): p. 56-65.

111. Murakumo, T.K.T.K.Y.H.H., *Creep behaviour of Ni-base single-crystal superalloys with various g volume fraction.* Acta Materialia Acta Materialia, 2004. **52**(12): p. 3737-3744.

112. Pineau, A. and Antolovich, S.D., *High temperature fatigue of nickel-base superalloys – A review with special emphasis on deformation modes and oxidation.* Engineering Failure Analysis, 2009. **16**(8): p. 2668-2697.

113. Bowman, R.R., *The Effect of microstructure on the fatigue crack growth resistance of nickel-base super alloys*. 1988, Georgia Institute of Technology.

114. Martínez-Esnaola, J.M., Martín-Meizoso, A., Affeldt, E.E., Bennett, A., and Fuentes, M., *HIGH TEMPERATURE FATIGUE IN SINGLE CRYSTAL SUPERALLOYS.* Fatigue & Fracture of Engineering Materials & Structures, 1997. **20**(5): p. 771-788.

115. Larsen, J.M., Rosenberger, A.H., Hartman, G.A., Russ, S.M., and John, R., *The Role of Spectrum Loading in Damage-Tolerance Life-Management of Fracture Critical Turbine Engine Components.* 2003.

116. Henderson, M.B. and Martin, J.W., *Influence of crystal orientation on the high temperature fatigue crack growth of a Ni-based single crystal superalloy.* Acta Materialia, 1996. **44**: p. 111-126.

117. Reed, P.A.S., *Fatigue crack growth mechanisms in superalloys: overview.* Materials Science and Technology, 2009. **25**(2): p. 258-270.

118. Chen, Q.Z., Jones, N., and Knowles, D.M., *The microstructures of base/modified RR2072 SX superalloys and their effects on creep properties at elevated temperatures.* Acta Materialia, 2002. **50**(5): p. 1095-1112.

119. Moss, S.J., Webster, G.A., and Fleury, E., *Creep deformation and crack growth behavior of a single-crystal nickel-base superalloy.* Metallurgical and Materials Transactions A: Physical Metallurgy and Materials Science, 1996. **27 A**(4): p. 829-837.

120. Antolovich, S.D., Domas, P., and Strudel, J.L., *LOW CYCLE FATIGUE OF RENE 80 AS AFFECTED BY PRIOR EXPOSURE.* Metallurgical transactions. A, Physical metallurgy and materials science, 1979. **10 A**(12): p. 1859-1868.

121. Liu, H.W. and Oshida, Y., *Grain boundary oxidation and fatigue crack growth at elevated temperatures.* Theoretical and Applied Fracture Mechanics, 1986. **6**(2): p. 85-94.

122. Wei, R.P., Miller, C., Huang, Z., Simmons, G.W., and Harlow, D.G., *Oxygen enhanced crack growth in nickel-based superalloys and materials damage prognosis.* Engineering Fracture Mechanics, 2009. **76**(5): p. 715-727.

123. de Bussac, A. and Antolovich, S., *The Effects of Microstructure and Environment on the Fatigue Crack Propagation Behaviour of a Ni-Base Alloy.* Fatigue 2006, 2006.

124. Hancock, P., *The influence of environment on the fatigue behaviour of superalloy components at high temperatures.* Corrosion Science, 1989. **29**(6): p. 657-671.

125. Hoffelner, W. *Effects of environment on crack growth behaviour of superalloys under various loading conditions*. in *Mechanical Behaviour of Superalloys, 10-11 June 1986*. 1987. UK.

126. Andrieu, E., Molins, R., Ghonem, H., and Pineau, A., *Intergranular crack tip oxidation mechanism in a nickel-based superalloy.* Materials Science and Engineering A, 1992. **A154**: p. 21-28.

127. Adair, B.S., Johnson, W.S., Antolovich, S.D., and Staroselsky, A., *Identification of fatigue crack growth mechanisms in IN100 superalloy as a function of temperature and frequency.* Fatigue and Fracture of Engineering Materials and Structures, 2013. **36**(3): p. 217-227.

128. Mercer, C., Shademan, S., and Soboyejo, W.O., *An investigation of the micromechanisms of fatigue crack growth in structural gas turbine engine alloys.* Journal of Materials Science, 2003. **38**: p. 291-305.

129. Krueger, D.D., Antolovich, S.D., and Van Stone, R.H., *EFFECTS OF GRAIN SIZE AND PRECIPITATE SIZE ON THE FATIGUE CRACK GROWTH BEHAVIOR OF ALLOY 718 AT 427°C.* Metallurgical transactions. A, Physical metallurgy and materials science, 1987. **18 A**(8): p. 1431-1449.

130. Skorupa, M., *Load interaction effects during fatigue crack growth under variable amplitude loading - a literature review. Part I: Empirical trends.* Fatigue and Fracture of Engineering Materials and Structures, 1998. **21**: p. 987-1006.

131. Skorupa, M., *Load interaction effects during fatigue crack growth under variable amplitude loading - a literature review. Part II: qualitative interpretation.* Fatigue and Fracture of Engineering Materials and Structures, 1999. **22**: p. 905-926.

132. *METHODS AND MODELS FOR PREDICTING FATIGUE CRACK GROWTH UNDER RANDOM LOADING.* ASTM Special Technical Publication, 1981.

133. Macha, D.E., *FATIGUE CRACK GROWTH RETARDATION BEHAVIOR OF IN-100 AT ELEVATED TEMPERATURE.* Engineering Fracture Mechanics, 1979. **12**: p. 1-11.

134. Larsen, J.M., Schwartz, B.J., Annis, C.G., and Air Force Materials, L., *Cumulative damage fracture mechanics under engine spectra*. 1980, Wright-Patterson Air Force Base, Ohio: Air Force Materials Laboratory.

135. Nicholas, T., Haritos, G.K., Hastie Jr, R.L., and Harms, K., *Effects of overloads on sustained-load crack growth in a nickel-base superalloy. Part II. Experiments.* Theoretical and Applied Fracture Mechanics, 1991. **16**: p. 51-62.

136. Gemma, A.E., *HOLD-TIME EFFECT OF A SINGLE OVERLOAD ON CRACK RETARDATION AT ELEVATED TEMPERATURE.* Engineering Fracture Mechanics, 1979. **11**: p. 763-774.

137. Kanesund, J., Moverare, J.J., and Johansson, S., *Deformation and damage mechanisms in IN792 during thermomechanical fatigue.* Materials Science and Engineering A, 2011. **528**: p. 4658-4668.

138. Zhang, J.X., Harada, H., Ro, Y., Koizumi, Y., and Kobayashi, T., *Thermomechanical fatigue mechanism in a modern single crystal nickel base superalloy TMS-82.* Acta Materialia, 2008. **56**(Copyright 2008, The Institution of Engineering and Technology): p. 2975-87.

139. Jung, A. and Schnell, A., *Crack growth in a coated gas turbine superalloy under thermo-mechanical fatigue.* International Journal of Fatigue, 2008. **30**(2): p. 286-291.

140. Okazaki, M. and Sakaguchi, M., *Thermo-mechanical fatigue failure of a single crystal Ni-based superalloy.* International Journal of Fatigue, 2008. **30**(2): p. 318-323.

141. Nissley, D.M., *Thermomechanical fatigue life prediction in gas turbine superalloys: A fracture mechanics approach.* AIAA Journal, 1995. **33**(6): p. 1114-1120.

142. Cailletaud, G. and Chaboche, J.L., *MACROSCOPIC DESCRIPTION OF THE MICROSTRUCTURAL CHANGES INDUCED BY VARYING TEMPERATURE: EXAMPLE OF IN100 CYCLIC BEHAVIOUR.* Proceedings - Computer Networking Symposium, 1980. **2**: p. 23-32.

143. Adair, B.S., Johnson, W.S., Antolovich, S.D., and Staroselsky, A. *Temperature and load interaction effects on the fatigue crack growth rate and fracture surface morphology of IN100 superalloy*. in *38th National Symposium on Fatigue and Fracture Mechanics, May 18, 2011 - May 20, 2011*. 2012. Anaheim, CA, United states: American Society for Testing and Materials.

144. Barker, V.M., Johnson, W.S., Adair, B.S., Antolovich, S.D., and Staroselsky, A., *Load and temperature interaction modeling of fatigue crack growth in a Ni-base superalloy.* International Journal of Fatigue, 2013. **52**: p. 95-105.

145. Kiyak, Y., Fedelich, B., May, T., and Pfennig, A., *Simulation of crack growth under low cycle fatigue at high temperature in a single crystal superalloy.* Engineering Fracture Mechanics, 2008. **75**(8): p. 2418-2443.

146. Anton, D.L., *Low cycle fatigue characteristics of <001> and randomly aligned superalloy single crystals.* Acta Metallurgica, 1984. **32**(10): p. 1669-1679.

147. Chan, K.S., Feiger, J., Lee, Y.D., John, R., and Hudak Jr, S.J. *Fatigue crack growth thresholds of deflected mixed-mode cracks in PWA1484*. 2005: American Society of Mechanical Engineers.

148. Seetharaman, V. and Cetel, A.D. *Thickness debit in creep properties of PWA 1484*. in *SUPERALLOYS 2004 - Tenth International Symposium on Superalloys, September 19, 2004 - September 23, 2004*. 2004. Champion, PA, United states: Minerals, Metals and Materials Society.

149. Le Bihan, Y., Joubert, P.Y., and Placko, D., *Wall thickness evaluation of single-crystal hollow blades by eddy current sensor.* NDT and E International, 2001. **34**(5): p. 363-368.

150. Skinn, D.A., Gallagher, J.P., Berens, A.P., Huber, P.D., Smith, J., and Dayton Univ Oh Research, I. *Damage Tolerant Design Handbook. Volume 2. Chapter 5*. 1994; Available from: http://handle.dtic.mil/100.2/ADA311690.

151. Wu, Newman, Zhao, Swain, Ding, and Phillips, *SMALL CRACK GROWTH AND FATIGUE LIFE PREDICTIONS FOR HIGH-STRENGTH ALUMINIUM ALLOYS: PART I—EXPERIMENTAL AND FRACTURE MECHANICS ANALYSIS.* Fatigue & Fracture of Engineering Materials & Structures, 1998. **21**(11): p. 1289-1306.

152. Tan, P.W., Raju, I.S., and Newman, J.C., Jr., *Boundary force method for analyzing two-dimensional cracked bodies.* Fracture Mechanics: Eighteenth Symposium. ASTM STP 945, 1988: p. 259-277.

153. Blatt, D., John, R., and Coker, D., *Stress intensity factor and compliance solutions for a single edge notched specimen with clamped ends.* Engineering Fracture Mechanics, 1994. **47**(4): p. 521-532.

154. John, R. and Rigling, B., *Effect of height to width ratio on K and CMOD solutions for a single edge cracked geometry with clamped ends.* Engineering Fracture Mechanics, 1998. **60**(2): p. 147-156.

155. Jones, I., *A wide range weight function for a single edge cracked geometry with clamped ends.* International Journal of Fracture, 1998. **89**(1): p. 1-18.

156. Mattoni, M. and Zok, F., *A method for determining the stress intensity factor of a single edge-notched tensile specimen.* International Journal of Fracture, 2003. **119**(1): p. L3-L8.

157. Adair, B., *Thermo-Mechanical Fatigue Crack Growth of a Polycrystalline Superalloy*, in *Woodruff School of Mechanical Engineering*. 2010, Georgia Institute of Technology: Atlanta.

158. *Standard Test Method for Measurement of Fatigue Crack Growth Rate.* ASTM Standard E647, 2013. **03.01**.

159. *Standard Test Method for Linear-Elastic Plane-Strain Fracture Toughness KIc of Metallic Materials.* ASTM Standard E399, 2006.

160. Portevin, A. and Le Chatelier, F., *Sur un phenomene observe lors de l'essai de traction d'alliages en cours de transformation.* Academie des Sciences -- Comptes Rendus des Seances, 1923. **176**(8): p. 507-510.

161. Garat, V., Cloue, J.M., Viguier, B., and Andrieu, E. *Influence of portevin-Le Chatelier effect on rupture mode of alloy 718 specimens*. in *6th International Symposium on Superalloys 718, 625, 706 and Derivatives, October 2, 2005 - October 5, 2005*. 2005. Pittsburgh, PA, United states: Minerals, Metals and Materials Society.

162. Fournier, L., Delafosse, D., and Magnin, T., *Oxidation induced intergranular cracking and Portevin-Le Chatelier effect in nickel base superalloy 718.* Materials Science and Engineering A, 2001. **316**(1-2): p. 166-173.

163. Hayes, R.W. and Hayes, W.C., *ON THE MECHANISM OF DELAYED DISCONTINUOUS PLASTIC FLOW IN AN AGE-HARDENED NICKEL ALLOY.* Acta Metallurgica, 1982. **30**(7): p. 1295-1301.

164. *High Temperature High Strength Nickel Base Alloys*. 1995, Nickel Development Institute.

165. Li, S.X., Ellison, E.G., and Smith, D.J., *Influence of orientation on the elastic and low cycle fatigue properties of several single crystal nickel base superalloys.* Journal of Strain Analysis for Engineering Design, 1994. **29**(2): p. 147-153.

166. Lahrman, D.F., Field, R.D., and Darolia, R. *The effect of strain rate on the mechanical properties of single crystal NiAl*. in *High-Temperature Ordered Intermetallic Alloys IV. Symposium, 27-30 Nov. 1990*. 1991. Pittsburgh, PA, USA: Mater. Res. Soc.

167. Hudak, S.J.W.E.C.R. and Development Center, A.F.M.L., *Development of standard methods of testing and analyzing fatigue crack growth rate data*. 1978, Wright-Patterson Air Force Base, Ohio: Air Force Systems Command, Air Force Materials Laboratory.

168. Milonopoulou, V., Forster, K.M., Formica, J.P., Kulik, J., Richardson, J.T., and Luss, D., *Influence of oxygen partial pressure on the kinetics of YBa2Cu3O7-x formation.* Journal of Materials Research, 1994. **9**(2): p. 275-285.

169. Wang, S., Verma, A., Yang, Y.L., Jacobson, A.J., and Abeles, B., *The effect of the magnitude of the oxygen partial pressure change in electrical conductivity relaxation measurements: Oxygen transport kinetics in La0.5Sr0.5CoO3.* Solid State Ionics, 2001. **140**(1-2): p. 125-133.

170. Antolovich, B., *Fatigue crack propagation in single crystal CMSX-2 at elevated temperature*, in *Materials science and engineering*. 1993, Georgia Institute of Technology: Atlanta.

171. Long, S.A., Edney, S.L., Reiger, P.A., Elliott, M.W., Knabe, F., and Bernhard, D., *Telemetry system integrated in a small gas turbine engine.* Journal of Engineering for Gas Turbines and Power, 2012. **134**(4).

172. Keyes, B., Brogan, J., Gouldstone, C., Greenlaw, R., Yang, J., Fraley, J., Western, B., and Schupbach, M. *High temperature telemetry systems for in situ monitoring of gas turbine engine components*. in *2009 IEEE Aerospace Conference, March 7, 2009 - March 14, 2009*. 2009. Big Sky, MT, United states: IEEE Computer Society.

173. Mitchell, D., Kulkarni, A., Roesch, E., Subramanian, R., Burns, A., Brogan, J., Greenlaw, R., Lostetter, A., Schupbach, M., Fraley, J., and Waits, R. *Development and F-class industrial gas turbine engine testing of smart components with direct write embedded sensors and high temperature wireless telemetry*. in *2008 ASME Turbo Expo, June 9, 2008 - June 13, 2008*. 2008. Berlin, Germany: American Society of Mechanical Engineers.

174. Cullity, B.D., *Elements of x-ray diffraction*. 2nd ed. 1978, Reading, Mass.: Addison-Wesley Pub. Co.

175. Woodworth, B., *Development of a Thermo-Mechanical Fatigue test apparatus with crack growth monitoring capability.* 2009: p. 110.